The University Of Sheffield.

Analysis, Design and Control of DC-DC Resonant Converter for On-board Bidirectional Battery Charger in Electric Vehicles

By

Chaohui Liu

A thesis submitted for the degree of Doctor of Philosophy

Department of Electronic and Electrical Engineering

Faulty of Engineering

The University of Sheffield

February 2017

Abstract

The combustion of fossil fuels, a non-renewable and finite resource, has caused increasing air pollution, ozone damage, acid rain and global warming. Electric vehicles (EVs) are eco-friendly with the attractive properties of lower greenhouse emissions, lower fuel usage and reduced air pollution. Battery and charger is one of the vital elements to analyse and develop for EVs. This research focuses on the bidirectional on-board battery charger with the emphasis on the design and analysis of the DC-DC converter.

Firstly, a LLC resonant topology is selected as the initial design candidate of the DC-DC resonant converter owing to the preferred soft-switching features. Single phase chargers suffer from a second harmonic voltage/current ripple which can lead to reduction of battery life. A feedforward-proportional-integral-resonant (FF-PIR) controller has been proposed and tested for suppressing this low-frequency current ripple in the LLC resonant converter employed in EV battery chargers.

Secondly, the recent developments in smart-grid technology necessitates bi-directional power flow from distributed energy storages like EV to support grid in the vehicle-to-grid (V2G) application. To achieve bi-directional power flow capability, the conventional uni-directional LLC topology is modified into bidirectional CLLC resonant converter. The characteristics have been analysed and validated by extensive simulations and experimental tests.

Further improvement has been implemented to increase the power efficiency under varying battery voltages. An optimum-resonant-frequency tracking scheme is proposed and tested to maintain the operation close to the maximum efficiency point over a wide battery voltage range.

Finally, in order to predict the converter efficiency accurately, this thesis presents a prediction method employing 2D and 3D finite element analysis (FEA) for calculating the power losses of magnetic components with litz wire in the converter.

Acknowledgement

Firstly. I would like to thank my supervisor Professor Jiabin Wang, for his consistent supervision, support and patience. His guidance on academic writing and critical thinking is invaluable. I would like to express my gratitude to my second supervisor Professor Dave Stone for the support and help. I am grateful to Dr. Chris Gould for the help on resonant converter and the hardware prototype. I am thankful to Professor Martin Poster, Dr. Daniel Gladwin and Dr. Antonio Griffo for the great help and guidance on hardware design and practise. Thanks Professor Zi-Qiang Zhu, the EMD Group leader, for the helpful encouragement. Thanks Mrs Weiya Wang for the encouragement and motivation.

My sincere thanks to Dr. Kalhana Colombage for the kind help on MATLAB coding, and especially for the encouragement and support. Special thanks goes to Dr. Bhaskar Sen for the invaluable help on hardware testing, controller optimization as well as the motivation. The days we worked together overnight in the office, and the time in Beehive would be memorial for long.

I would like to express my eternal gratitude to Dr Xiao Chen, for the help on the FEA and FLUX modelling. Special thanks for his encouragement, inspiration, accompany and support. I would also like to thank all the colleagues in office F26 for the knowledgeable discussion. They are Abdullah K Shanshal, Bing Liu, Bo Wang, Dr. Mikail Koc, Dr. Sreeju S Nair, Dr. Tianfu Sun, Liang Chen, Panos, Rongguang Hu and Yanwen Shi,

Thanks my colleagues in the EMD group for the help and support. Special thanks goes to the lab technicians Mr. John Wilkinson, Mr. Richard Garraway, Mr Lawrence Obodo and Mr. Andrew Race for their technical supports.

Heartfelt thanks to Mr Bin Cao and Mrs Xinhua Li, for the support, encouragement and motivation.

Finally, my eternal gratitude goes to my parents and family for their unlimited support, encouragement and love, without which the journey would not have come to an end.

Table of Contents

CHAPTER 1
Research Background and Introduction

This chapter introduces electric vehicles, automotive batteries, their chargers and design requirements. The motivations to carry out the research is described followed by the main contributions of the doctoral research work and the outline of the thesis.

1.1 Electric Vehicles

The world energy consumption due to the transport sector is expected to show dramatic growth of around 44% from 2008 to 2035 [1]. This consumption is responsible for the largest share (63%) of the total increase in petroleum and other fossil fuels usage from 2010 to 2040. The combustion of fossil fuels, a non-renewable and finite resource, has caused increasing air pollution, ozone damage, acid rain and global warming. Therefore, new technologies for alternative vehicles are of great interest to researchers, industry, governments and general public nowadays [2, 3].

Electric vehicles (EVs) use electric motors for propulsion and are directly powered from an energy store rather than indirectly via internal combustion engines (ICEs) [2, 3]. Compared with the traditional fossil fuel-powered vehicles, EVs are more eco-friendly with the attractive properties of lower greenhouse emissions, lower fuel usage and reduced air pollution [4]. There is thus a growing interest in EVs globally.

Besides the potential to solve environmental deterioration and fossil fuel crisis, another benefit of EVs is that they can be used as energy storage units in the vehicle-to-grid (V2G) application when they are plugged in to their charging sockets, as well as the conventional grid-to-vehicle (G2V) charging [5, 6]. The main idea of V2G technology is to use vehicles as the energy storage units and provide power to the grid for supporting the grid during voltage sags and frequency dips [7, 8]. This support may become crucial when a large percentage of grid power is generated from renewable energy sources, such as wind, solar and wave/tide, which have a large degree of fluctuation.

1.2 Battery for EVs

Although there are advantages of EVs, technology barriers such as higher cost compared to equivalently sized petrol vehicles, lengthy charging time, limited battery life

and limited travel distance on one charge still remain [9]. To overcome the obstacle, battery is one of the vital elements to analyse and develop.

The main concerns of EV battery are safety, power density (power, volume and weight), cost, reliability and life span. Firstly, safety is always the priority for the EV [10]. The key protection conditions include galvanic isolation as well as the protection operation such as over-voltage, over current, deep discharge, over temperature and cell charge balancing. Secondly, since the space is limited in EV, power density is more of a concern. In an EV battery, the energy stored is measured in amp-hour (Ah) and determines the drive range of EV. The power rating of battery, with the unit of watt (W), determines the rate of charging and discharging. Thirdly, the battery life span can be measured in two specifications: the minimum calendar life and the total charging-discharging cycle life [11]. A vehicle battery is generally supposed to last for the calendar life of 10-15 years with a specified capacity [12]. Overall, although trade-off must be taken into considerations, EV battery should meet all these requirements with a reasonable cost, since the high cost of battery has already been a prime barrier that prevents the widespread of EV [13].

Currently, three main battery technologies are widely used for EVs: the lead-acid battery, the nickel metal hydride (NiMH) battery and the Lithium-ion (Li-ion) battery technologies, whose key features are shown in Table 1-1 [14].

Table 1-1 The comparison of different batteries for EVs [14]

Type	Discharge power capacity	Cost	Energy density	Self-discharge rate	Life span
Lead-acid	Good	Affordable	Low	High	Short
NiMH	Good	High	High	High	Long
Li-ion	Good	Reasonable	High	Low	Long

The lead-acid battery used to power early EVs such as GM EV1 [15, 16]. It has the advantages of good discharge power capacity enabling the fast response to the load changes. Meanwhile the cost is affordable due to the mature development of the technology. However, the low energy density, heavy weight and short life span due to the deep discharging deterioration make it not suitable for the latest EVs.

The NiMH batteries are employed in Toyota Prius [17] and Honda Insight [18]. Compared to the lead-acid, a NiMH battery has higher power density, due to simpler charger/discharge reactions. With the high density characteristic, the EV with NiMH

battery has twice drive range than the one with the counterpart lead-acid battery [19]. Also, a NiMH battery can tolerate moderate overcharges and deep discharges thus has a longer life cycle. The charging efficiency is higher because the NiMH battery has low internal resistance and much higher charge acceptance capability. However, the main disadvantage of NiMH is the high self-discharge rate which means the battery will lose charge when not used. Also, it has higher cost and low charge acceptance capability in high temperature conditions which reduces the charging efficiency.

Lithium-ion (Li-ion) battery has become one of the preferred energy storage units for recent generation of EVs such as Nissan leaf [20, 21]. Although the Li-ion battery has the issues need to be improved such as cell life, cell balance, cooling operation, cost and safety, compared to other rechargeable batteries, Li-ion has the attractive features of higher energy density, higher power rating (high cell voltage and output power), lower weight and great discharging power for faster acceleration. And the advantages can be summarized as follows [12, 22-25]:

(1) The superior power density is one of the most favourable advantages. To provide the same amount of capacity, Li-ion batteries have much lighter weight than other type of batteries. For example, to provide the identical energy (16kWh), Chevrolet Volt's AC Delco lead-acid battery pack weights 590 kg while with the new Li-ion battery pack the weight has been reduced to 170 kg which is only 28.81% of the original solution.

(2) The self-discharge rate of Lithium-ion cells is 2% to 3% per month, which is much lower than Lead Acid (4% to 6% per month) and NiMH (30% per month). Thus, the life time span of the Lithium-ion battery is much competitive than other types of batteries. In addition, the discharge curve of Lithium-ion battery is fairly flat. It is well known that if the power delivered from the battery falls rapidly during the discharge cycle, hazardous issue occurs at the end of cycle especially for high power applications. As shown in Fig. 1-1, the Lithium-ion battery delivers approximately constant voltage (corresponding stable power) during 80% of the whole discharge cycle.

(3) The Li-ion battery pack consists of large numbers of cells inside [26]. For example, 48 modules each containing 4 cells compose the 196 cells in total in Nissan Leaf battery pack [27, 28]. This structure makes the charging process much faster and efficient.

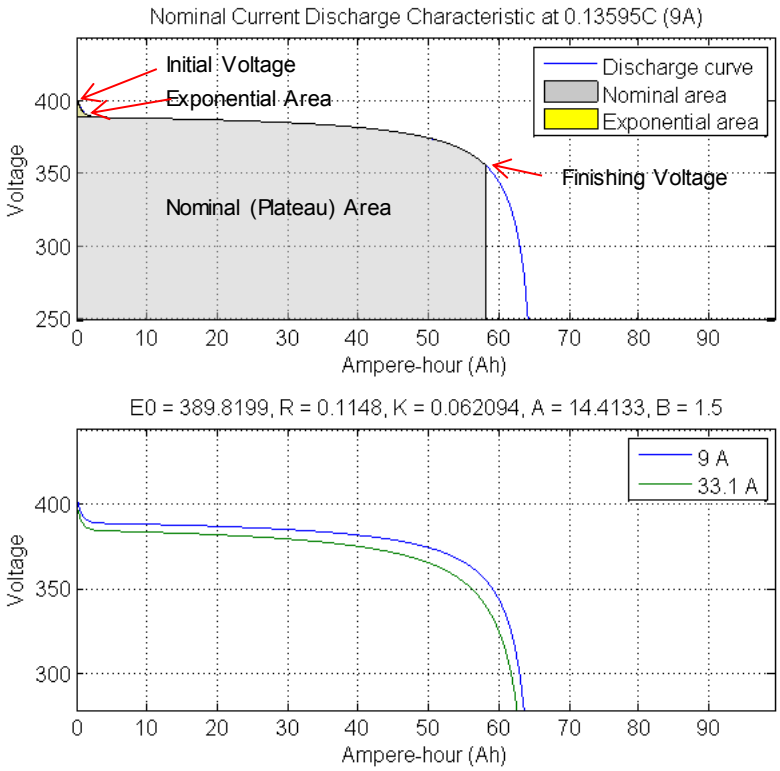

Fig. 1-1 The Lithium-ion battery discharge characteristics [24, 30]

1.3 Battery Charging Technology

The battery performance is affected by not only the battery design, but also the charging and discharging regulation. Therefore the operation and control of battery charge and discharge are essential technologies in the whole EV system [29].

1.3.1 Charging strategy

There are different charging approaches including constant current (CC) [30], constant voltage (CV) [31], constant power, taper current, etc [32]. The constant voltage charger is the simplest method which charges the battery by supplying required current to obtain the constant battery voltage. Basically it needs additional circuit to protect the battery. Constant current charger supplies a fixed current (usually the maximum current to get fast charging) into the battery and the battery voltage increases linearly during the period. Constant power charger, is usually preferred for giant and costly batteries in slow charging approach. It is worth noting that the main limitation, when charging in domestic environment, is the maximum current which should be less than the single phase outlet fuse current.

For the Li-ion battery, the constant current-constant voltage (CC-CV) charging scheme is usually employed [33, 34]. In this CC-CV charging profile, the charging process include two stages: the CC mode and CV mode. The first stage is the CC mode, during which the current should be regulated at a fixed value (usually the maximum current which the battery tolerates without causing damage) while the battery voltage increases rapidly to its rated maximum level. After that, further continuing the constant current charging will cause overcharging and excessive heating which might damage the battery. In order to avoid this, when the battery voltage reaches the threshold voltage (nearly fully-charged voltage), the charging process is switched to the CV mode, during which the battery voltage is maintained at a constant value while the battery is slowly charged. Meanwhile, the battery charging current decreases to avoid over-charging of the battery until the current reaches a specific low value at which the charging process is terminated. For instance, the Li-ion battery cell usually has a maximum charging voltage of 3.6V or 4.2V. When the battery voltage reaches 90% state of charging (SOC), the CV stage starts and the current begins to decrease [35].

1.3.2 Charging power levels

According to different power ratings and charging time, battery chargers are classified into three levels [36, 37]: Level 1 which is the slow (domestic) charging, Level 2 which is the primary charging and Level 3 which is the fast charging approach (usually with DC voltage) [9], as shown in Table 1-2.

Table 1-2 The comparison of the three charging power levels [36, 38]

Type	Classification	Voltage	Power level	Charging time
Level 1	*slow charging*	standard domestic outlets (120 V ac in US and 230 V ac in EU)	2 kW	10-12 hours
Level 2	*primary charging*	240 V ac (in US) or 400 V ac (in EU)	19.2 kW	4 hours
Level 3	*DC fast charging*	480V DC or higher	50-150 kW	less than 1 hours

With Level 1 solution, the EVs can use the standard domestic outlets (120 V ac in US and 230 V ac in EU) for slow charging, thus no additional infrastructure is needed. Another advantage is the low off-peak electricity rate at night. For example, Nissan Leaf can be plugged into the convenience outlet at home with the 2.2kW/10A charger and it is capable of fully charging the 24 kWh battery pack in a relatively long time of 10-12 hours.

Level 2 charging approach is usually considered as one of the primary solutions to be employed in both domestic and public applications. This method employs standard 3-phase 240 V ac (in US) or 400 V ac (in EU) power outlet capable of delivering continuous current rated from 16 to 80 A [39]. Usually a special connection with dedicated devices need to be installed at home or in the public area. For instance, to get Level 2 charging, the Nissan Leaf needs to use the Electric Vehicle Supply Equipment (EVSE) cable, with which it is able to fully charge its battery pack (rated 24 kWh) in less than 8 hours with a 3.6 kW/16A charger. It also offers a 6.6 kW/32A solution to charge the battery from empty to 100% SOC in less than 4 hours.

Level 3 charging is usually the DC fast charging approach and typical used in the commercial stations, while Level 1 and Level 2 are usually single phase and used at home or work place [40]. Level 1 and Level 2 chargers provide ac power to the on-board charger in the vehicle, while there is usually an AC-DC converter in the station to convert three-phase ac voltage to dc voltage which can bypass the on-board charger and is connected directly to the vehicles. It typically operates at 480 V DC or higher voltage offering fast charging less than one hour. For example, in a 500 V DC rapid charger station, it only takes approximately 30 minutes to charge a Nissan Leaf battery from zero to 80% capacity. However, the drawback of high power fast charging is also considerable. For instance, it might aggravate the peak demand and overload quickly in the local distribution equipment at peak times which will influence the whole grid [41]. Thus the integration of large numbers of EVs charging stations to the public network need to be analysed. Another disadvantage of Level 3 fast charging is the investment and public construction due to high cost to build charging stations. In addition, researchers are also trying to find out whether the damping of the big amount of electrons into the battery pack in such a short time would reduce the battery life.

1.3.3 On-board and off-board charger

Typically, the battery chargers for EVs are usually categorised into on-board chargers and off-board chargers, as shown in Table 1-3. Off-board chargers, also known as stand-alone fast charging stations, act like filling stations for liquid fuel vehicles to provide rapid charge at high power [9]. Off-board charger stations are usually installed in public areas such as shopping centres, car parks and motorway services which can greatly extend the range of pure-battery EVs [42]. There are reduced constrains of size, weight or space

to develop such an off-board station; however, these stations need significant investment and long-term construction time.

Table 1-3 The comparison of on-board and off-board chargers

Classification	Size limit	Weight limit	Space limit	Construction requirement	Power rating	Level type	Typical charging time
Off-board	less	less	less	yes	50 kW	3	fast charging 1 hour
On-board	yes	yes	yes	less	2-20 kW	1,2	slow charging 4-12 hours

In contrast, on-board chargers are integrated into the vehicles, and offer slow charging within 6-16 hours in low power as 2-20 kW [9]. On-board chargers provide simple charging at domestic user dwellings overnight when the EVs are plugged into a household utility outlet. As the charger can be built into the EV, it will not require significant extra cost compared to off-board charger station. Despite of the constraints such as size, weight and space limit the input power level and hence slow charging, on-board charging is still a promising solution due to its compact structure, simplicity of usage and low cost. Two technologies are available for the On-board charger, including the conductive method and inductive approach depending on the direct electrical contact between the grid and the vehicle [43]. As most EVs are being designed with plug-in battery connector, conductive battery system is a more common solution.

According to the SAE J1772 standard [26], on-board charger usually adopts Level 1 and Level 2 which are supposed to be installed in the vehicle, and Level 3 is usually employed in the off-board charger.

1.3.4 On-board Bidirectional charger

(1) Grid-to-vehicle (G2V) Charging

The traditional unidirectional on-board battery charger operates only in grid-to-vehicle (G2V) mode, in which the power only flows from the grid to the EV battery pack. The benefits of this unidirectional charger include low cost, simple control and fewer system components [1].

Fig. 1-2 shows the schematic of a typical unidirectional charger which is only capable of delivering energy from the power grid to the battery pack because it usually employs diode bridges rather than active switches in the output side [9]. The charger only works

in G2V mode, thus it cannot provide power back to the grid and contribute to the energy storage [44]. However, this makes the controller design simpler, cheaper, has fewer active components and less losses, all of which are attractive features [45].

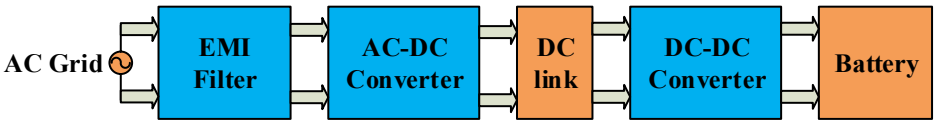

Fig. 1-2 Unidirectional battery charger architecture (arrow indicated power flow direction)

(2) Vehicle-to-grid (V2G) Discharging

In general, a vehicle is parked during most of the life time (more than 15 hours a day) [46]. When the EV is parked, the battery in EV can act as an energy resource, which implies that a large amount of widespread EVs being plugged into the network provide good opportunity of acting as distributed energy storage to feed energy back to the grid [47].

For this reason, the EV should be equipped with not only a powerful battery pack but also a bi-directional converter for charging and discharging. In charging mode, the grid charges the battery, and during the discharge mode the battery feeds the energy back to the grid. By this way, the battery charger has the capability to deliver power from the traction battery back to the power grid, which provides the benefit of ancillary support including the spinning reserves and the frequency/voltage compensation by peak shaving and valley filling [46]. Moreover, in the night, the battery can be charged when the electricity price is low; while during the daytime when the grid power demand is high, the battery can be discharged and feed the power back to the network. Thus EV owners can benefit from participation in the power energy market and potentially reap financial benefits; while the grid authorities also benefit because the integration of EVs buffering can be used to balance energy quality and consumption, as well as improving the grid network stability [43]. Therefore, the EVs with bi-directional battery chargers can be integrated into the smart grid, and will greatly change the energy market [48]. Thus the grid-connected bidirectional charger is considered a key research area in the future [49, 50].

1.4 Design Requirement

A typical bidirectional on-board battery charger usually employs two-stage topology including an frontend AC-DC converter stage connected to a DC-DC converter, as shown

in Fig. 1-3. As can be seen, the AC-DC converter acting as the front-end power factor corrector (PFC) stage rectifies the power from the grid to the battery load through the dc link capacitor followed by the DC-DC converter.

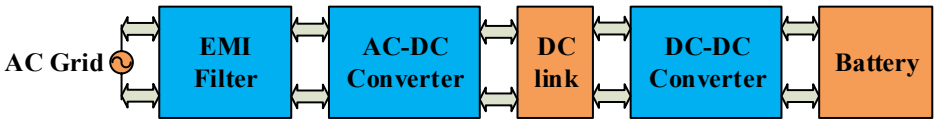

Fig. 1-3 Typical architecture of an on-board bidirectional battery charger (arrow indicated power flow direction)

This research work will mainly focus on the DC-DC converter part. And the priorities considered when designing the chargers are:

- Safety
- Power density
- Low cost
- Small size/volume
- High efficiency
- Bidirectional power flow

1.4.1 Galvanic isolation

Safety is of paramount importance in EV system. According to ISO 6469-3:2011-2012 [51] and UL2231-1:2002-05 [52], insulation and galvanic separation must be maintained throughout the battery charger service life under all the operating conditions. Thus an isolated transformer is usually employed between the grid side and battery pack to provide galvanic isolation and safety operation [53]. Therefore, the basic non-isolated DC-DC converter such as buck converter and boost converter [54] will not be used in this research, despite of the advantages of simple structure, low cost, fewer components, small size and light weight [42]. In addition, with different turns ratio of the transformer, isolated converter has the potential to provide a wider output voltage to cope with the wide variety of battery voltages in the battery charging system [55].

1.4.2 High power density

Employing a transformer in a full-bridge voltage/current source DC-DC converter can provide galvanic isolation and increase reliability, but also result in bulky system with extra weight, size and cost compared to the non-isolated chargers [9]. Since at high frequency, the volume of the magnetic components (such as the transformer) and passive

components (such as capacitors) could be minimised, thereby reducing the total cost and volume of the converter. Thus the most effective method of obtaining higher power density in the isolated DC-DC converter relies on higher switching frequency.

There are many topologies available for the isolated DC-DC converters, such as flyback converter [56], forward converter [57], active clamp forward converter [58], push-pull converter [59], half-bridge converter [60] and full-bridge converter. However, the transformer in these topologies tends to be bulky for higher power rating applications, so usually for power rates higher than 500 W, full-bridge converters are generally the favourable type [55]. Therefore full-bridge high frequency galvanic isolated DC-DC converter is usually employed for the on-board chargers [61].

1.4.3 Soft-switching

The conventional PWM DC-DC converters are usually regulated by generating gate drives for the switch devices, i.e. regulating the output voltage or current by turning on diagonal pairs of power switches during the ON stage and turning off all the switches during the OFF time. When any pair of the diagonal switches are turned on, the rectifier diodes in another side of the transformer are conducted to enable the power flow [62].

Since the power losses during the switching on/off period increase with switching frequency, high switching frequencies would result in high switching losses of the power devices and electromagnetic interference (EMI) emissions, and then limit the conversion efficiency. To mitigate this issue, soft-switching technology, i.e., zero-voltage-switching (ZVS) and zero-current-switching (ZCS) is usually employed [63].

The basic concept of ZVS is that during the turn-on transient, the device voltage fails to a small value near zero before the current going through the device; while in the ZCS transistors turn-off transition occurs at zero current. For high frequency power conversion where power MOSFETs are applied as semiconductor devices, ZVS operation is more preferred, because the considerable turn-on loss caused by the energy circulating in the MOSFET output capacitance during the charging/discharging period. ZCS operation however is more preferred for the insulated-gate bipolar transistors (IGBT) devices, to depress the large power loss caused by the current tail during turn-off period [64].

1.4.4 Wide operation range

Extensive research has been performed on full-bridge soft-switching converters, such as the dual active bridge (DAB) converter [65-67]. DAB converter has advantages such as symmetric structure, galvanic isolation and bidirectional power transfer capability. However, as the load lightens, the operating region in which the circuit maintains ZVS becomes narrow, thus the ZVS may be lost under light load, which is a drawback of DAB topology [68]. In addition, large turn-off current and large circulating energy in the DAB circuit results in high power loss and reduce efficiency [69].

Resonant converters, featuring high efficiency and low electromagnetic interference (EMI), can be used to achieve low switching loss with ZVS and ZCS [70-74]. Different numbers of resonance elements are usually used to form the resonant tank and resonant with each other to realise the zero-crossing of the voltage or current. Various topologies of resonant converters have been analysed, of which the conventional types are series resonant converter (SRC) which contains two resonant elements in series, parallel resonant converter (PRC) which contains two resonant elements in parallel and Series Parallel Resonant Converter (SPRC) which has three resonant elements, as shown in Fig. 1-4.

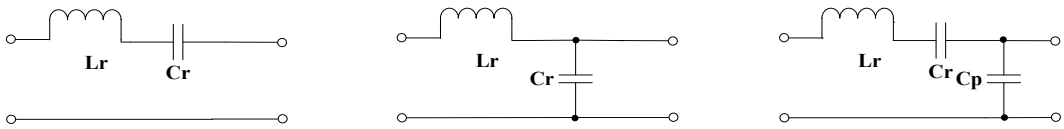

Fig. 1-4 Basic resonant circuit topologies

In an SRC converter [75, 76], ZVS operation occurs at operating frequencies above the series resonant frequency (determined by the two resonant elements); otherwise the converter works at ZCS. When operating at light load or high input voltage, the frequency needs to be increased to a very high level, therefore causing more energy circulating back to the input source. The PRC, with narrow operating frequency range, can keep the output voltage regulated even with light load [77]. However, the power loss during turn-off and the conduction loss due to the energy circulating in the resonant tank are still major problems. The SPRC achieves the good characteristics of the previous two converters, while the conduction loss is still high when the input voltage varies widely [78-80].

Overall, the SRC, PRC and SPRC will have high circulating energy, high conduction losses and switching losses in wide input range and light load condition, which limits the capability to achieve high efficiency.

1.4.5 LLC resonant converter

A LLC resonant topology contains a series inductor, a series capacitor and a parallel (magnetizing) inductor together referred to as the resonant tank, as shown in Fig. 1-5 [81]. Due to the three components in the resonant tank, over the whole operation range there are two resonant frequencies, one of which is related to the series inductor and capacitor (series resonant frequency), while the other is determined by all the three elements (fundamental resonant frequency) [82]. The LLC resonant converter has similar characteristics to a SRC at operating range above the series resonant frequency. Otherwise, it performs like a PRC when the load is light and a SRC under heavy load conditions. The peak gain occurs at system resonant frequency which is between the series resonant frequency and the fundamental resonant frequency. When the operation is in the range above the system resonant frequency, the resonant converter can achieve soft-switching features (ZVS and ZCS) therefore reducing the switching losses and conduction losses greatly [61, 83, 84] . This feature will be analysed in detail in Chapter 3.

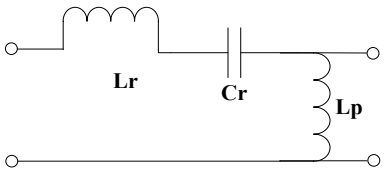

Fig. 1-5 Typical LLC resonant circuit topology

With the LLC resonant tank in the DC-DC converter, ZVS in the primary side active switches and ZCS in the rectifier diodes can be achieved over the entire load conditions, or even no load [85, 86]. Therefore, it is clear that, with all these advantages, LLC resonant converter is a promising topology and therefore will be used as the initial design candidate in this research.

1.5 Current state-of-the-art in bi-directional EV charges

In this section, a brief overview of the state-of-the-art in bi-directional EV chargers is presented. The main topology considered is the galvanic isolated full-bridge DC-DC

converter with bi-directional power flow capability to facilitate the V2G operation and high efficiency owing to the soft-switching features and low harmonics distortions. Further detailed literature reviews are given in each chapter where a specific issue is addressed.

1.5.1 Current state-of-the-art

Numerous different bi-directional DC-DC converter topologies for EV chargers have been presented. Full-bridge voltage-source and current-source DC-DC converters are presented in [87]. Since the converter operates in hard switching mode, active-clamped snubbers or passive-clamped snubbers are necessary to reduce switching loss and EMI. Although high efficiency is achieved over wide load conditions, the extra snubber circuit increases the size, volume and cost. Dual active bridge (DAB) converter and series resonant converter (SRC) are investigated and compared in [86] in terms of the modulation method, power loss, volume, and efficiency. Although high efficiency can be achieved with high operating frequency and reduced volume/size, the disadvantage of the DAB and SRC converters is the narrow soft switching operation range, as illustrated in the previous section.

In [64], a bidirectional DC-DC converter employing a four-element CLLC resonant tank based on the combination of two LLC resonant topologies is proposed. The resonant converter achieves higher efficiency than the conventional LLC resonant converter. However, the transformer features a large turn ratio in order to cope with large difference between the input and output voltage, which makes it unsuitable for EV battery charging system. Although the transformer turns ratio can be easily adjusted to cope with different input/output voltage combinations, the design method of the resonant tank is challenged in order to attain the similarly of the two separate LLC resonant tanks [88]. Reference [89] proposes a symmetric full-bridge CLLC topology, featuring ZVS and ZCS in both the charging and the reverse discharging modes. Due to the symmetric topology, the operation and the converter efficiency in forward charging mode is the same as that in the reverse mode. Comprehensive analysis are presented in [90] on the DAB DC-DC converter and the symmetric CLLC DC-DC resonant converter. The design methodology, soft-switching region, component selections and the power density are compared.

A CLLLC resonant topology is analysed and employed in a full bridge bidirectional DC-DC converter in [91]. Two separate capacitors are employed on each side of the

transformer to form a new 5-element resonant tank. The reported efficiency was 94.5% at 3.3 kW power rating.

All of the chargers mentioned so far are conductive chargers, which mean the charger inlet is directly connected to the connector on EV. This type of battery charger is the most common technology and widely employed in the market. Another topology being explored is the inductive power transfer (IPT) which transfers power wirelessly thus also called contactless inductive charger. The advantages are convenient charging, isolation and safety. The drawback includes low efficiency, low power density and investment of infrastructure. For example, a wireless EV charger with large airgap is presented in [92]. Self-resonance PWM control method is used for wide operation range. Large air-gap results in higher conversion gain and thus the capability of transferring higher power. However, the total efficiency is still a problem.

1.5.2 Main challenges

Although significant progress has been made by the researchers, challenges still exist [9]. First, the conversion efficiency can be further boosted by reducing the power losses in the active components, passive components, winding and core. Secondly, the power density should be improved due to the wide use of transformers and inductors in the chargers. In addition, more potential topologies should be investigated for the improvement of the reliability, durability of the chargers. The capability of high-efficiency power flow in the V2G mode and the influence of the large-amount of vehicle plugged in the grid need further research and investigation. For example, the battery degradation because of the charging/discharging cycles in the frequent V2G and G2V operations need to be overcome. Safety monitoring and protection are required in the charging/discharging system. Anti-islanding protection and other issues associated with the interconnection of the DC-DC converter stage to the front-end stage must also be addressed.

1.6 Motivation

The main concern of this research is an on-board bidirectional charging system for electric vehicles that operates at high frequency and over wide battery voltage conditions. The LLC resonant converter, as mentioned before, will be employed as the initial design candidate. The main aim is to enhance the DC-DC power conversion efficiency through extensive work in the following areas:

(1) Analysis and development of the LLC resonant topologies

In order to design an optimal bidirectional battery charger, the LLC resonant topology should be analysed and developed to select the optimal components. Analytical investigation, design approach, simulation study and experimental tests will be implemented.

(2) Control design

In the battery charging system, battery voltage and SoC usually varies in a wide range during the charging/discharging process. For example, in Nissan Leaf battery pack, the voltage changes from 240V to 403V, corresponding to 68% and 112% of the nominal voltage (350V), respectively. In order to cope with this variation, the battery charger should be capable of regulating charging current and the output voltage in a wide range under varying load condition. Therefore, it is critical to design an optimally tuned controller in order to handle the varying load conditions.

(3) Ripple current reduction

Ripple in charging current can reduce battery life due to higher losses and hence higher temperature of battery during charging. However, in single phase chargers, a second harmonic voltage/current ripple is inevitable due to inherent ripple in power flow. Therefore, a control approach that reduces this ripple current is desirable.

(4) Application of new converter topology

The analysis and application of new DC-DC converter topology is essential for the bidirectional power flow capability. High efficiency, soft-switching and side load condition range should be taken into consideration.

(5) Control technique for high efficiency operation

Based on the designed charger with the selected converter topology, the control scheme is crucial in the voltage/current regulation, current waveform shaping, harmonic depression. A well-designed controller will further boost the efficiency of the battery charger.

(6) Power loss evaluation

The main target of the battery charger is to improve the efficiency. Even fractional improvement of efficiency has big impact on yearly energy consumption and hence power loss is important to be analysed, evaluated and quantified in a reasonable accuracy. Moreover, the use of litz wire in the magnetic components

also brings challenges for the power loss evaluation, because the complex structure of litz wire is not easy to be modelled.

1.7 Main Contributions of the Thesis

With a focus on the development of high-frequency/high-efficiency on-board bidirectional battery charger for EVs, the main contributions of the doctorial work that will be presented in this thesis are outline as follows:

(1) A feedforward-proportional-integral-resonant (FF-PIR) control scheme has been developed for suppressing the low-frequency current ripple in an LLC resonant converter employed in EV battery chargers.

(2) A systematic design method and procedure is presented based on the comprehensive investigation on bidirectional CLLC DC-DC resonant topology in both the G2V and the V2G modes. A comprehensive approach of selecting the secondary side capacitance is presented. Extensive experimental tests have been implemented to validate the performance, and illustrated that 10% efficiency improvement has been achieved in the reverse mode.

(3) An optimum-resonant-frequency tracking scheme is proposed to maintain the operating frequency close to the optimum resonant frequency corresponding to the maximum efficiency point in both the G2V and V2G modes. Experimental tests have validated that the efficiency has been enhanced further by 2%.

1.8 Outline

The thesis is organized in 6 chapters. Each of the chapters can be summarised as follows:

Chapter 1 presents the background knowledge of the EV and battery charger. Basic requirements for EV charger are briefly outlined and candidate charger topologies are assessed. The LLC resonant converter topology is initially selected as the candidate for the bi-directional chargers.

Chapter 2 describes a feedforward-proportional-integral-resonant (FF-PIR) controller employed to suppress the low-frequency current ripple in an LLC resonant converter. A small-signal model of the LLC resonant converter based battery charging system has been established from time-domain simulations. A FF-PIR controller is subsequently designed and the control performance is analysed. The performance of the

proposed resonant controller on suppressing the harmonic current is assessed by extensive simulations and experimental tests.

In **Chapter 3** a CLLC resonant converter is analysed for the use of bi-directional battery charger. While a LLC converter has good performance in charging (forward) mode of operation, its performance deteriorates significantly in discharging (reverse) mode (V2G mode). By adding an extra series capacitor in the transformer secondary side, the conventional three-element LLC resonant converter has been reshaped into four-element resonant converter. In both G2V and V2G modes, the resonant tank possesses almost the same operational characteristics of the conventional LLC resonant tank. Thus the ZVS+ZCS soft switching can be achieved both in forward and reverse modes and the switching losses can be minimized, hereby improving the charger efficiency. The circuit topology, operation principle and DC gain characteristics are analysed. Design procedure is described. Performance of the designed CLLC resonant converter in both forward and reverse modes are assessed by extensive experimental tests. Power loss analysis shows that the efficiency of CLLC improves between 1% to 10.02 % in the whole operating range compared with conventional LLC converter.

Chapter 4 presents an optimum-resonant-frequency-tracking scheme for further enhancing the efficiency of the 4-element CLLC resonant converter proposed in Chapter 3. The operation and characteristics of the CLLC resonant tank is analysed to identify the optimal operating frequency for this converter. In order to maintain the operating frequency close to the optimum resonant frequency corresponding to the maximum efficiency point in a wide battery voltage range, the DC link voltage is adjusted accordingly when the battery voltage varies. Thus, the resonant converter is always operating with less circulating current in the resonant tank and transformer, less turn-off current in the primary side MOSFETs and less di/dt in the secondary side diodes. Simulations, tests and comparison with the conventional fixed DC link voltage are presented to verify the effectiveness of the proposed control scheme.

Chapter 5 proposes a method employing 2D and 3D finite element (FE) method to calculate the power losses for magnetic components in the converter. The features of litz wire coil are taken into consideration. The FE model is built with the definitions of the geometries, meshes, materials, electric circuits, boundary conditions and load conditions. The flux density is calculated via finite element analysis (FEA) at the given load condition. Then, the power loss of each element is calculated using the obtained nodal flux densities

and power loss density function. Finally, the total loss is the sum of the power losses of all the elements. Compared to the conventional method described in Chapter 4, the FEA approach can predict the flux density more accurately, owing to a detailed model with all the geometric parameters and thus the flux leakage and end-winding effects can be considered. In addition, the nonlinear effect of the core material can be considered in the B-H curve definition in FEA. The 3D FEA approach can predict more accurate winding flux density and thus more accurate proximity loss. Experimental measurements have been performed to assess the proposed calculation method.

Chapter 6 summarise the research work on on-board bi-directional battery charger for EVs, followed by the future scope of work that can be continued for further optimisation and improvement of the battery charger.

CHAPTER 2
Modelling and Control Design of Electric Vehicle On-Board Battery Charger with Current Ripple Reduction Employing FF-PIR Controller

This chapter describes a feedforward-proportional-integral-resonant (FF-PIR) controller employed to suppress the low-frequency current ripple in an EV battery charger based on a LLC resonant converter. A small-signal model of the DC-DC converter with 3-element LLC resonant tank is established from time-domain simulations by injecting a small perturbation signal into the converter operating frequency. A FF-PIR controller is subsequently designed and the control performance is analysed. The effectiveness of the proposed resonant controller on suppressing the harmonic current is assessed by extensive simulations and experimental tests.

Part of the contents in this chapter has been published in [93] by the author.

2.1 Introduction

As described in Chapter 1, in the DC-DC stage of a typical on-board EV battery charging system, as shown in Fig. 2-1 [9], full-bridge DC-DC converters that employ a high-frequency galvanic isolated transformer and active power switches are often used as the interface between the front end converter and the EV battery [61], to provide galvanic isolation and flexibility of installation on the EVs.

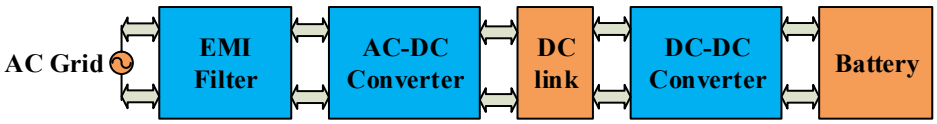

Fig. 2-1 Typical on-board EV battery charging system

The LLC resonant converter described in Chapter 1 is a promising candidate for the DC-DC stage in an on-board EV battery charging system. However, when combing with the front-end and connecting to the AC Grid, the charging system suffers from the second order mains frequency harmonic.

2.1.1 Influence of second order mains frequency harmonic on battery charging system

In the EV battery charging operation, a typical charging cycle of EV battery contains part or full of the two stages: constant current stage and constant voltage (CC-CV) stage. During CC stage, the charging current is controlled to be fixed at a desirable constant value for optimal performance. However, when the single-phase grid side AC voltage (50

or 60 Hz) is rectified, a second order mains frequency harmonic (100 or 120 Hz) will be present in the DC link voltage. This voltage harmonic in turn results in a low frequency current ripple during battery charging as shown schematically in Fig. 2-2.

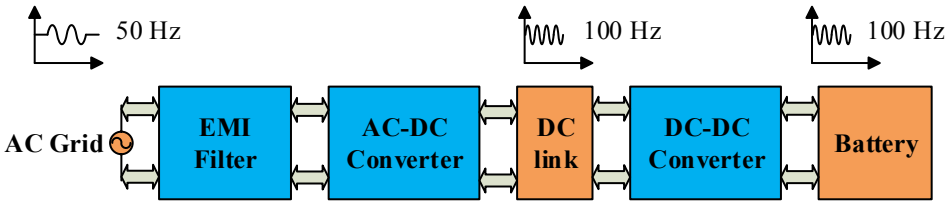

Fig. 2-2 Second order voltage and current harmonic in the charging system

The ripple current can be relatively high, due to low internal impedance of the battery. This low frequency current ripple is not desired as it causes additional losses, resulting in an increase in battery temperature, which in turn reduce the battery lifetime and EV driving range [94].

Additionally, the temperature increase may give rise to internal heat generation of the battery and potential safety issues. Thus, most battery manufacturers recommend the current ripple should not exceed 5% of the total battery Ampere-hour capacity [95].

In the EV battery dis-charging operation, battery deliveries power to the grid through the converter. The second order mains frequency harmonic on DC link side has negligible effect on dis-charging current because the overall impedance of the converter in the reverse power flow mode is comparatively large. In addition, the LLC resonant converter is not usually used for the reverse mode operation which will be further explained in next chapters. Thus, only the forward charging mode is discussed in this chapter.

2.1.2 Conventional ripple reduction methods

To suppress this 100/120 Hz current ripple, a large DC-link capacitor or L-C filter may be used. However this will lead to a bulky system [96]. A compensator network is used in [97] and [98] to reduce the current ripple while in [99] low-ripple output current is achieved by storing the ripple energy in an extra inductor. The voltage ripple may also be suppressed by feedforward compensation [100]. However, all these methods require additional ac circuits which increase the overall volume, weight and cost.

A resonant controller, featuring high loop gain at its resonant frequency, is a preferred option which has widely been used for the grid current harmonic compensation in active filters [101, 102], photovoltaic power conditioning systems with PWM inverters [103]

and wind power converters [104] to achieve zero steady-state current control error. Steady-state characteristic and dynamic behavior of the low-frequency current ripple is evaluated in [105] for a single-phase inverter. Based on the input-to-output current gain, a proportional-resonant filter is presented to suppress the ripple of the charging current in the inverter. A frequency-adaptive filtering approach is proposed in [106] to reduce the current ripple in power conditioning systems of the fuel cell. More ripple cancellation methods are analysed and developed in [107-110].

However, all these control schemes, based on varying duty ratio constant frequency PWM operation, are, not suitable for constant duty cycle LLC resonant converters whose outputs are controlled by adjusting switching frequency. In addition, in order to achieve high efficiency, LLC converter is usually operating close to its resonant frequency and the voltage gains of the converter over its operating frequency range is usually quite high. Thus, a small DC-link voltage ripple could result in a large current ripple during charging.

Whilst a resonant controller has been proposed to reduce 120 Hz voltage ripple in the half-bridge LLC DC-DC resonant converter in [111], its effect on the system performance has not been quantified, nor have the detailed design procedures on determining the controller parameters been presented. In [112] a PIR controller is designed after the quantitative propagation analysis of the relationship of the input-to-output voltage ripple. Although the LLC DC-DC resonant converter is used for an EV battery charger, the issues associated with modelling (ac input voltage ripple to charging current ripple) of battery chargers have not been addressed.

2.1.3 Objective

This chapter describes an effective approach to suppression of battery harmonic current in a 4 kW LLC resonant converter based EV battery charger. The advances over the current state-of-the art are: 1) the influence of the battery State-of-Charge (SOC) on dynamic behavior is taken in to consideration in both the modelling and the control design of the battery charger; 2) control robustness to the grid frequency variations is addressed.

The chapter is organized as follows. In Section 2.2, the basic operation of the LLC resonant converter is analysed and explained. In Section 2.3, the small-signal transfer function of the battery charger is analyzed and established. Based on this, the DC gain characteristic is analyzed and the PI based resonant controller capable of reducing the current ripple at 100 Hz is designed and evaluated in Section 2.4. Simulation and

experimental tests are presented and discussed in Section 2.5 and Section 2.6, respectively to verify the control performance.

2.2 Operation of the LLC Resonant Converter

2.2.1 Converter Topology

As shown in Fig. 2-3, a typical LLC resonant converter consists of input voltage source V_{in}, inverter stage S_1~S_4, LLC resonant tank, transformer, rectifier stage D_1~D_4, output filter C_f and the load. The resonant tank includes the series inductor L_s, the series capacitor C_s, the magnetizing inductor L_m. Power flows from the input voltage source to the battery load through the transformer.

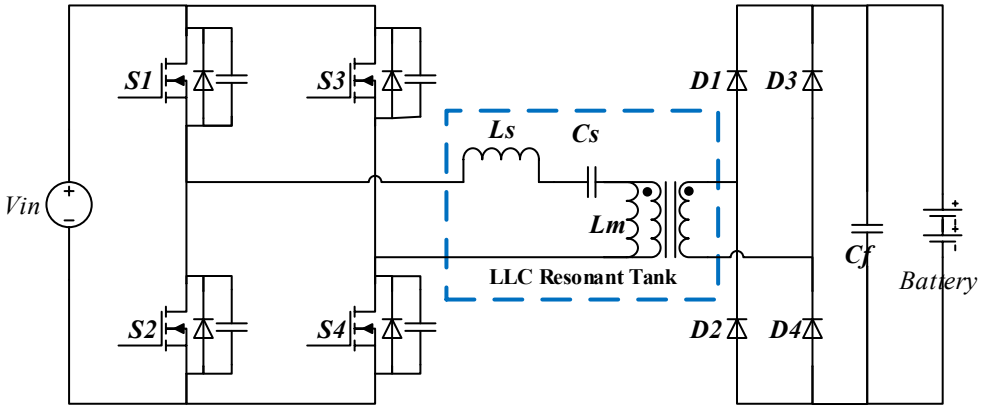

Fig. 2-3 A typical uni-directional LLC resonant converter diagram

The series inductor L_s and series capacitor C_s constitute a series resonant tank, which has a minimum impedance to the sinusoidal current at the series resonant frequency defined in Equation (2-1). Changing the frequency of the input voltage away from this frequency, the impedance of the resonant circuit increases. As a result, the amount of current circulated in the resonant tank and the energy delivered to the load vary accordingly.

$$f_{sr} = \frac{1}{2\pi\sqrt{L_s \cdot C_s}} \tag{2-1}$$

With the second inductance L_m anticipated in the resonance operation, a new resonant frequency called system resonant frequency f_s exists in the LLC resonant tank which is described in Equation (2-2).

$$f_s = \frac{1}{2\pi\sqrt{(L_s + L_m) \cdot C_s}} \tag{2-2}$$

The peak resonant frequency f_p at which the resonant gain reaches the highest level, moves within the range of f_s and f_{sr} determined by the load condition. At no load condition, the peak resonant frequency f_p is equal to the system resonant frequency f_s, and when the load increases, the peak resonant frequency moves towards to series resonant frequency f_{sr}. At short circuit, peak resonant frequency f_p is equal to the series resonant frequency f_{sr}.

2.2.2 FHA Model

If the LLC resonant operates close to the series resonant frequency, the circulating current can be assumed as a pure sinusoidal current. First-Harmonic Approximation (FHA) [113] can be used to analyse the circuit.

Since the main composite of circulating current in the resonant tank is a pure sinusoidal current, it is assumed that only the fundamental of the current transfer real power to the load, and all the high order harmonics are ignored, which is the principle of FHA method. The ac equivalent model of the LLC resonant converter can be obtained and shown in Fig. 2-4 based on the following assumptions: (1) The input voltage is modelled as an ideal sinusoidal voltage source, which represents only the fundamental component ignoring all the higher-order harmonics; (2) The output filter capacitor and the secondary side leakage inductance of the transformer are ignored; (3) Refer the secondary side variables to the primary side.

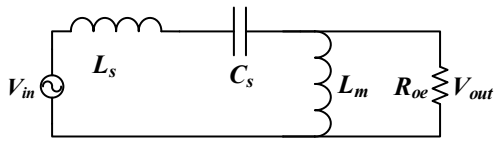

Fig. 2-4 AC equivalent circuit of the LLC resonant converter from FHA

V_{in} and V_{out} are the RMS values of the fundamental component of the input and output voltages of the resonant tank in the forward mode, respectively. R_{oe} given in Equation (2-3) is the equivalent resistive load representing the rectified diode, filter capacitor and battery load referred to the transformer primary side from the transformer secondary side.

$$R_{oe} = N^2 \cdot \frac{8}{\pi^2} \frac{V_{out}^2}{P_{out}} \tag{2-3}$$

Then the voltage gain transfer function can be normalized as Equation (2-4).

$$M(f_n, l_n, Q) = \left| \frac{l_n \times {f_n}^2}{[(l_n + 1) \times {f_n}^2 - 1] + j[({f_n}^2 - 1) \times f_n \times Q \times l_n]} \right| \tag{2-4}$$

where

$$f_n = \frac{f_{sw}}{f_{sr}} \tag{2-5}$$

$$l_n = \frac{L_m}{L_s} \tag{2-6}$$

$$Q = \frac{\sqrt{L_s/C_s}}{R_{oe}} \tag{2-7}$$

And the relationship between input and output voltages is:

$$V_{out} = M(f_n, l_n, Q) \times \frac{1}{N} \times V_{in} \tag{2-8}$$

With the transfer function, the DC/DC voltage gain of the resonant tank can be obtained and shown in Fig. 2-5.

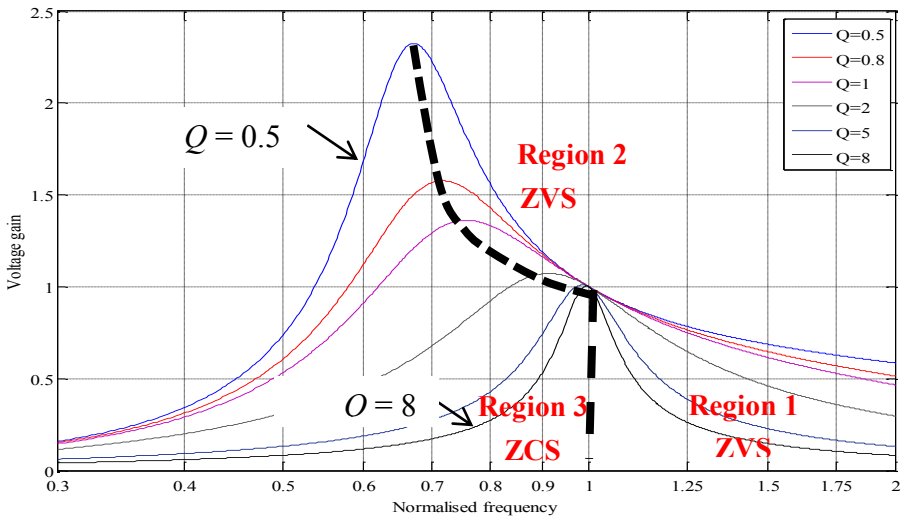

Fig. 2-5 DC gain characteristics of the LLC resonant converter

It can be seen that the voltage gain is a function of the frequency with the variations of loads. As the load resistor is in parallel to the magnetizing inductor L_m, reduction of

the load resistor will reduce the effect of L_m, thus increase of the quality factor Q causes narrow curve with a smaller peak gain. At open load, the load resistance is infinite and $Q = 0$, the gain peak very high and can be infinite in theory. While when the load is shorted, load resistance is zero, and Q is infinite. In this condition, the magnetizing inductor L_m is shorted and the effect of L_m on the gain disappear.

Regardless of the value of Q (representing the load conditions), all the gain curves go through one point which means that this is independent of the load. At this point, the nominalized frequency is 1 and the switching frequency the series resonant frequency. The impedance of the series resonant circuit is zero, and the voltage drop across series inductor and series capacitor is zero, thus the input voltage is applied directly to the output load, resulting a unity voltage gain of $M(f_n, l_n, Q) = 1$.

When the DC gain curve slope is negative, the converter is working under zero voltage switching (ZVS) with inductive input impedance; while when the slope is positive, the converter works under zero current switching (ZCS) with capacitive input impedance. Thus the whole area can be divided to three regions as shown in the figure. Region 1 and Region 2 are the ZVS regions while region 3 is the ZCS region. As ZVS is preferred for MOSFET devices to reduce the turn-on losses, the operate region should be in region 1 and region 2. Fig. 2-6 shows the ZVS operation of the LLC resonant converter.

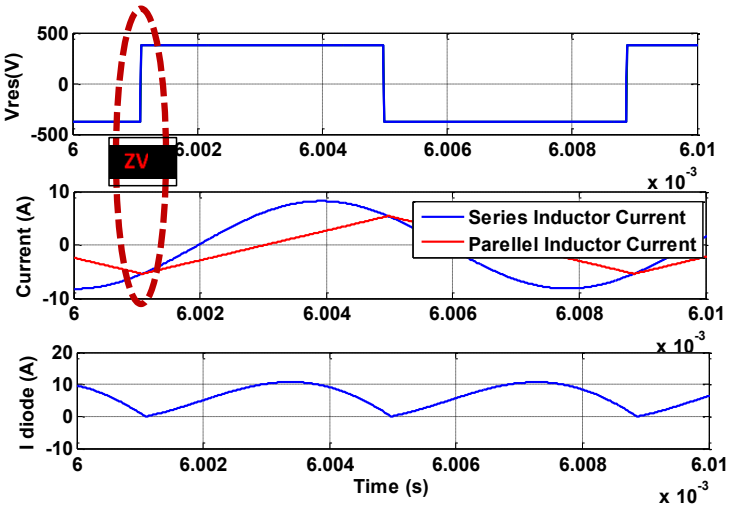

Fig. 2-6 Circuit operation of the LLC resonant converter

2.2.3 Design of the LLC resonant converter

This thesis will not focus on the design procedure of the LLC resonant tank since it is based on an existed design in [61], thus only the design principle is outlined in this section. Generally, a typical design procedure starts with the design of transformer. The transformer turns ratio can be calculated through the input-output relationship at the series resonant frequency (based on FHA method) and full load condition. With the designed transformer, voltage conversion ratio can be determined according to the input voltage and output voltage. Then the inductor ratio and quality factor should be determined to meet the limit in DC gain curve.

It should be noted that there are many trade-offs of the combination of l_n and Q that affect the design. A small l_n provides narrow frequency range and high peak gain, which help to attain ZVS; however, the turn off current of MOSFETs would be large, and the high magnetizing current will increase the conduction loss. A small Q makes the peak gain higher while increase the frequency variation range. A large Q results a very low peak gain, which may not meet the design requirements. Generally, the initial value can be selected around 5 for l_n and around 0.5 for Q, then check the DC gain is between maximum and minimum gain or not. Reiteration is needed after the initial selection. With the inductor ratio, quality factor and equivalent output, the resonant tank can be designed.

The power rating in the converter can be calculated to help analyse the power loss and select components (the input filter capacitor, MOSFETs, output rectifier and output-filter capacitor).

2.3 Modelling of the LLC Resonant Converter

In order to devise an effective control scheme for suppression of the ripple component, it is essential to establish a representative dynamic model of the LLC resonant converter.

2.3.1 Modelling methods

Generally, in PWM converters, the state space average method is widely employed to generate small signal models. However, it is not applicable to a frequency-controlled resonant converter because the operating frequency is not constant and the energy is mostly transferred through the fundamental components of the voltage and current waveforms [114]. In [115] an extended describing function (EDF) method is used to obtain the voltage transfer functions. This method however is too complicated to be

applicable to an LLC resonant converter with multiple operating modes [81]. To solve this problem, small signal characteristics of the LLC resonant converter is analysed from a simulation method with the function of simulated impedance analyzer [116]. Here, time domain simulation is used to extract the small signal model by injection of small signal perturbations at the nominal switching frequency.

2.3.2 Time-Domain Simulink model

A time-domain simulation model of the LLC resonant converter is built in MATLAB/Simulink software as shown in Fig. 2-7 and Fig. 2-8. The parameters is based on [61] and shown in Table 2-1. L_s, L_m *and* C_s are the series inductor, parallel inductor and series capacitor which form the LLC resonant tank; C_f is the output filter capacitor. The transformer turns ratio is 1.66. The series resonant frequency of the converter is 128 kHz. The converter operates at a DC link voltage of 380 V and variable battery voltages from 240 V (SOC 2.65%) to 402 V (SOC 99.8%) to enable modelling of a typical Li-ion battery pack as used in a Nissan Leaf [117]. The battery has a rated capacity of 66.2 Ah and its charging/discharging current I_{bat} is set to 9 A for maximum power transfer efficiency.

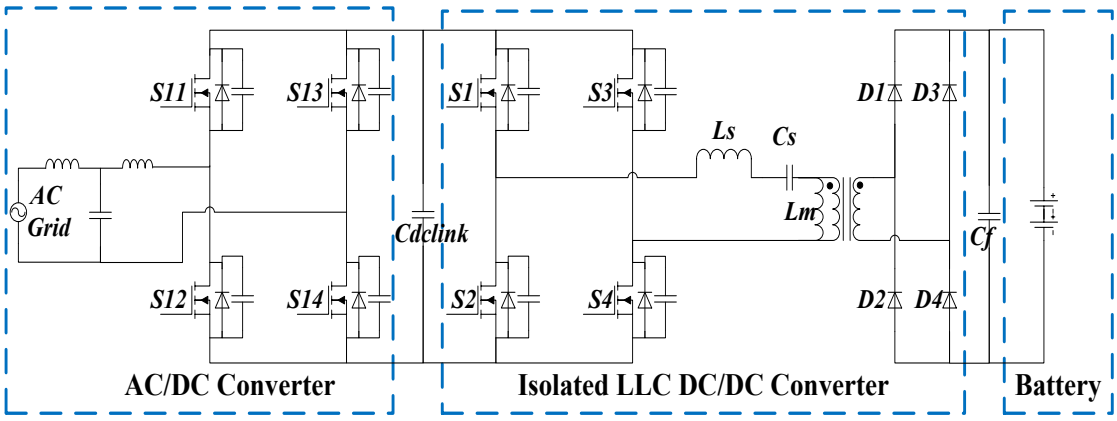

Fig. 2-7. Typical EV on-board battery charger architecture based on LLC resonant converter

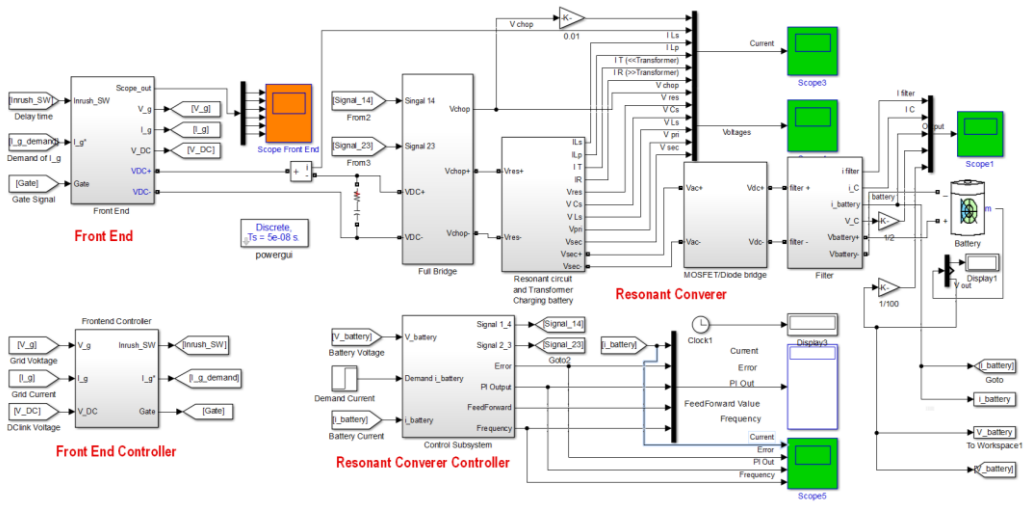

Fig. 2-8 MATLAB/Simulink model of the battery charger

Table 2-1 The designed LLC resonant converter specification

Parameters	Symbol	Value	Unit
Series inductor	L_s	97.0	μH
Parallel inductor	L_m	136.5	μH
Series capacitor	C_s	15.8	nF
Output filter capacitor	C_f	330	μF
DC link voltage	V_{dc}	380	V
Battery charging current	I_{bat}	9.0	A
Battery internal resister	R_{bat}	0.1148	Ω
Battery rated capacity	$A \cdot h$	66.2	Ah
Battery fully charged voltage	V_{max}	403.2	V
Battery initial voltage	V_{min}	240	V

2.3.3 Small signal model at nominal battery voltage

Under a given battery voltage and switching frequency f_s, a small sinusoidal perturbation signal is injected to the switching frequency, $f_{sp} = f_s + \Delta F sin(2\pi ft)$, where ΔF and f are the amplitude (100 Hz) and frequency of the perturbation, respectively. The resultant output current will contain a small ripple of the same frequency (f). The magnitude and phase of the resultant current ripple is extracted by Fourier analysis. The magnitude and phase variations with the perturbation frequency can be established. Fig. 2-9 (a) shows the Bode plots for 6 switching frequencies ranging from 109 kHz to 111 kHz in 0.4 kHz step at 320 V battery voltage (SOC 5.5%). As can be seen, apart from the DC gain and corner frequency, the frequency responses at different switching frequencies exhibit the characteristics of a second order system. The small signal transfer function of the battery current against perturbation frequency is therefore derived from the simulation data through curve fitting. By way of example, Equation (2-9) shows the transfer function at the nominal frequency of 109.37 kHz (at which the charging current is 9A) and the nominal battery voltage of 320 V (SOC 5.5%).

$$G_{p\_320}(\mathrm{s}) = \frac{\Delta I_b(s)}{\Delta f_s(s)} = \frac{5.613s - 835400}{s^2 + 30390s + 118700000} \tag{2-9}$$

After obtaining this transfer function, the Bode plot is compared with the simulation results in Fig. 2-9 (b) and a very good match between the two can be observed.

It should be noted that the coefficients of the s-polynomials in Equation (2-9) vary with operating switching frequency (or battery charging current). The variation of the DC gain of the transfer function represents the controllability of the LLC converter for regulating the charging current by adjusting the switching frequency.

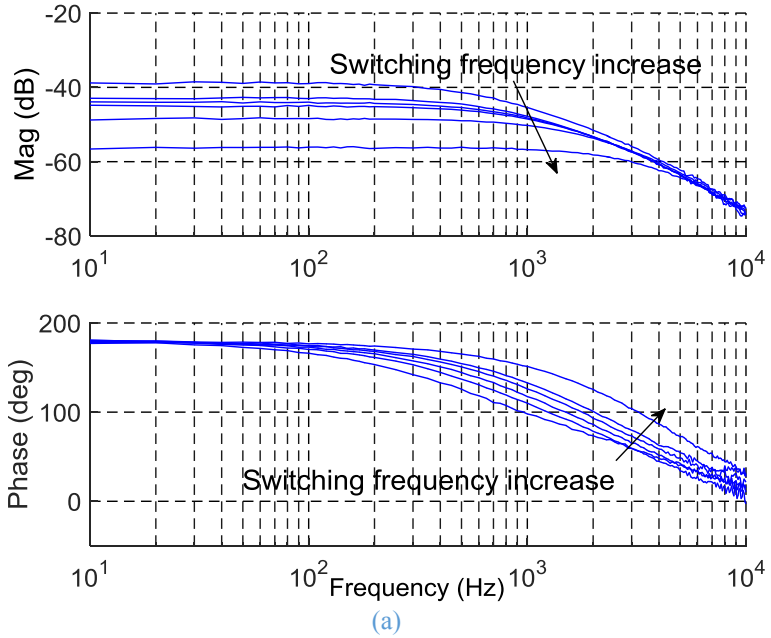

(a)

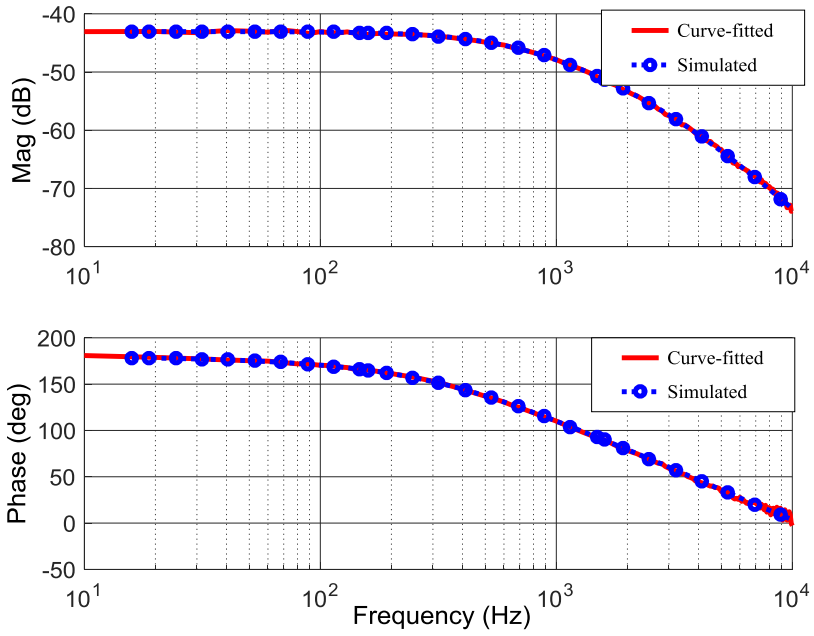

(b)

Fig. 2-9. Small signal frequency response of LLC converter based charging system at the nominal 320 V battery voltage. (a) variations with switching frequencies. (b) comparison of simulated and derived frequency responses at 109.37 kHz switching frequency.

2.3.4 Small signal model at low/high battery voltages

Small signal transfer functions for different battery voltages and charging currents can be similarly derived. Equation (2-10) and (2-11) show the transfer functions at the nominal frequency for 9.0 A charging current at 240 V (SOC 2.65%) and 402 V (SOC 99.8%) battery voltages respectively. Simulated and derived Bode plots in each condition are compared in Fig. 2-10 and Fig. 2-11, respectively. As can be seen, they all exhibit the characteristics of the second order system in Equation (2-9) while the coefficients are dependent on the battery voltage and current.

$$G_{p\_240}(\mathrm{s}) = \frac{\Delta I_b(s)}{\Delta f_s(s)} = \frac{4.765s - 868000}{s^2 + 26480s + 67560000} \tag{2-10}$$

$$G_{p\_402}(s) = \frac{\Delta I_b(s)}{\Delta f_s(s)} = \frac{8.477s - 712400}{s^2 + 31530s + 164200000} \tag{2-11}$$

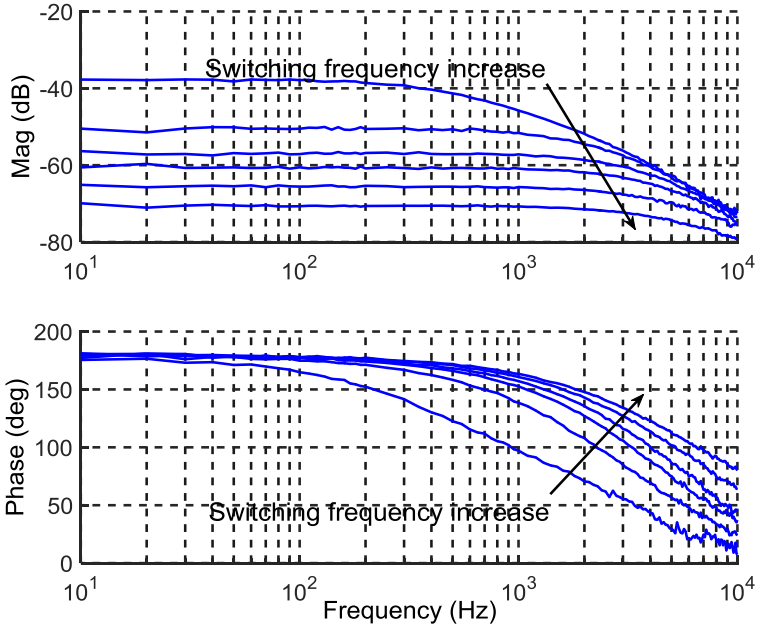

(a)

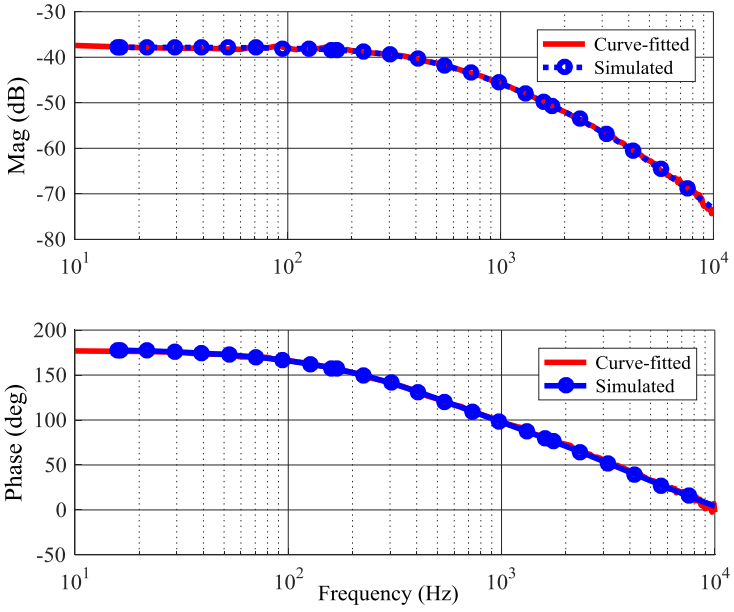

(b)

Fig. 2-10. Small signal frequency response of the charging system at 240 V battery voltage. (a) variation of switching frequencies; (b) comparison of simulated and derived frequency responses at 124.04 kHz.

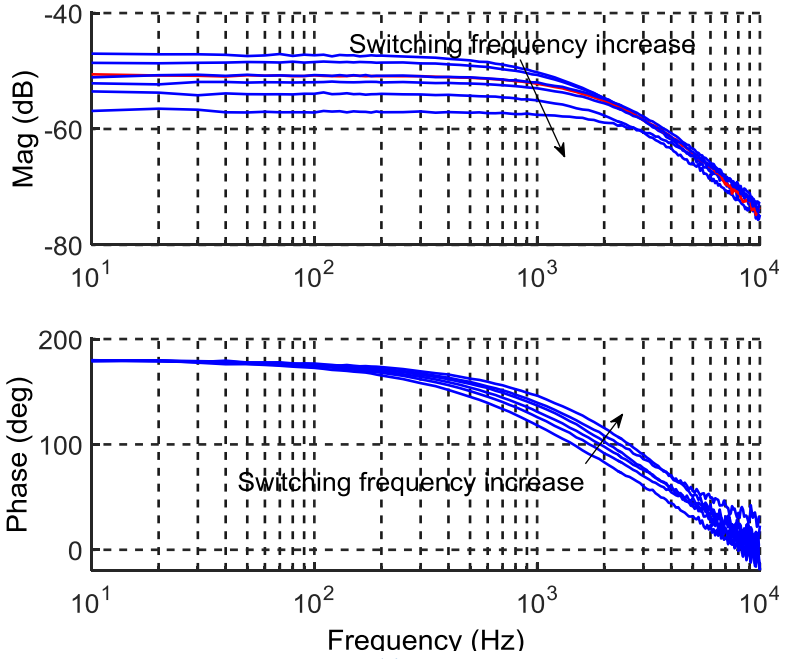

(a)

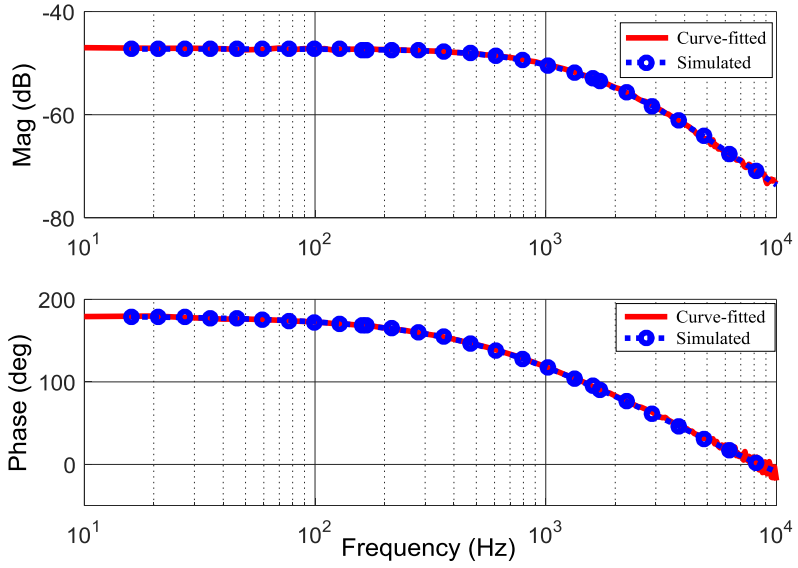

(b)

Fig. 2-11. Small signal frequency response of the charging system at 402 V battery voltage. (a) variation of switching frequencies; (b) comparison of simulated and derived frequency responses at 101.7 kHz.

2.4 FF-PIR Control Design

2.4.1 Frequency control characteristics

The steady state relationship between average charger current and converter switching frequency for a given battery voltage can be determined by sweeping the operating

frequency in an appropriate range. The resultant average battery current variations with switching frequency at three representative battery voltages of 240 V (SOC 2.65%), 320 V (SOC 5.5%) and 402 V (SOC 99.8%) are illustrated in Fig. 2-12 (a).

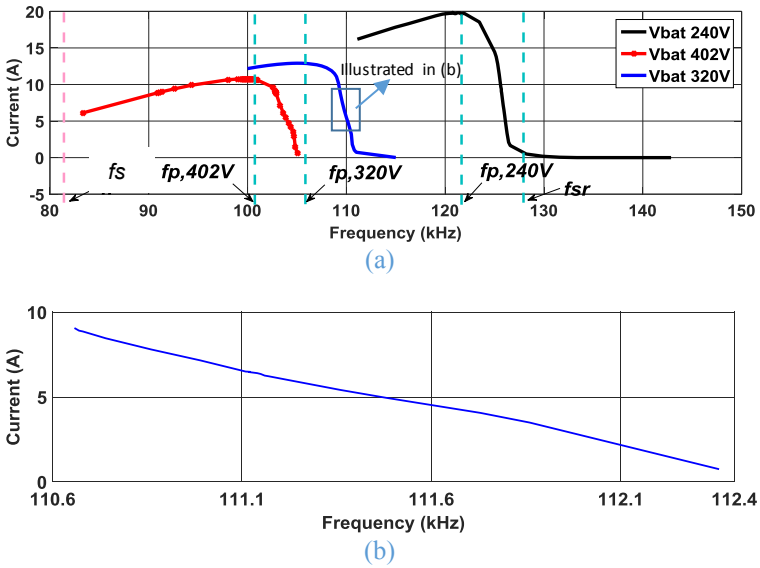

Fig. 2-12. Operational characteristics of the DC-DC LLC resonant converter. (a) variations of averaged battery current with switching frequency and battery voltages at different battery voltage; (b) at 320 V battery voltage.

For an LLC resonant converter, the series inductor and series capacitor constitute a series resonant branch, which has resistive impedance at the series resonant frequency given previously in Equation (2-1). With the presence of the second inductor, the system resonant frequency, at which the whole impedance of the LLC resonant tank is predominantly resistive, is determined by Equation (2-2). In this design, with the parameters shown in Table 2-1, the series resonant frequency f_{sr} and the system resonant frequency f_s can be calculated as 128.560 kHz and 82.86 kHz, respectively.

As illustrated in Fig. 2-5 and Fig. 2-12, the battery current reaches a peak value at the peak resonant frequency f_p which is sensitive to the load variations. Operating below the peak resonant frequency f_p will produce ZCS of the MOSFET in a capacitive mode, i.e., the current leads the voltage; while switching above will attain ZVS in an inductive operation, which is preferable for MOSFET devices to avoid excessive voltage stress. Since the peak resonant frequency f_p is dependent on battery voltage, the preferable ZVS operating switching frequency range also varies with the battery voltage. As an instance, Fig. 2-12 (b) shows zoomed view of the battery current variation with switching frequency over the operating switching frequency range at 320 V battery voltage. It is evident that the battery charging current can be regulated by varying the operating

frequency. The rate of change in the current with regard to switching frequency, i.e., the DC gain, is almost constant for a given battery voltage.

2.4.2 FF-PIR control structure

The battery charging current is controlled through the feedforward-proportional-integral-resonant (FF-PIR) control system shown in Fig. 2-13. The controller consists of a feedforward compensator to cope with battery voltage variations, and a feedback controller including a conventional PI controller in parallel with a resonant controller which is employed to eliminate the 100/120 Hz current ripple. The plant model is the small-signal model derived in Section 2.3.

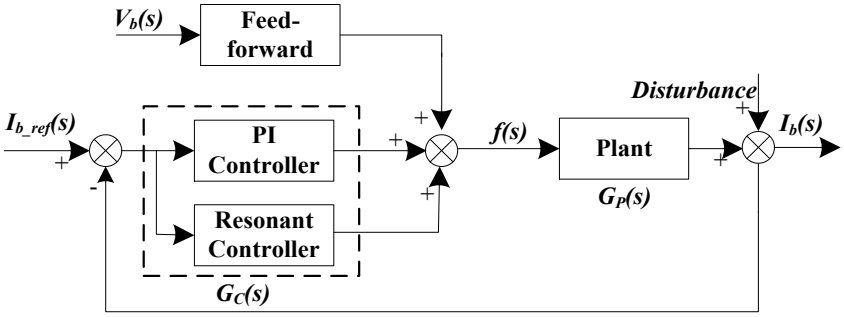

Fig. 2-13. Block diagram of the feedback control system

The transfer function of the feedback controller is given in Equation (2-12), where K_p, K_i, K_r are the proportional gain, integral gain and resonant gain, respectively. The quality factor Q represents the damping effect of the resonant control.

$$\begin{cases} G_c(s) = K_p + \dfrac{K_i}{s} + G_R(s) \\ G_R(s) = \dfrac{K_r \omega_n s}{s^2 + \dfrac{\omega_n s}{Q} + {\omega_n}^2} \end{cases} \tag{2-12}$$

2.4.3 Feed-forward control design

Since the preferable operating range is dependent on battery voltages, the switching frequency varies to attain constant battery current during the charging process. Based on the model obtained, the desired switching frequencies at different battery voltages (i.e. different SOC) can be shown in Fig. 2-14. This relationship of frequency range variation with battery voltage is stored in a look-up table and compensated through feed-forward. With the feed-forward control, the charging current can be regulated to steady-state fast and the controller achieves better dynamic performance. It should be noted that even without the feed-forward control, the controller is still able to achieve steady-state

gradually however with a worse dynamic response. Since the desired switching frequencies shown in Fig. 2-14 are within the region 1 and region 2, the ZVS features can be obtained at all the load conditions, thus the feed-forward control will not compromise the soft-switching operations.

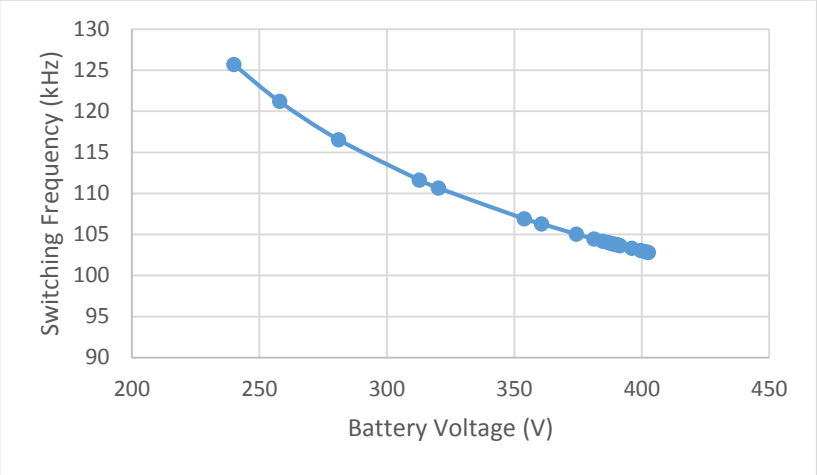

Fig. 2-14. Desired switching frequency at different battery voltages to attain constant charging current

2.4.4 PIR control design

The feed-forward control parameters are obtained from the large-signal model in Section 2.3.2 and Section 2.4.1. While for the PIR control parameters K_p and K_i are determined according to the small-signal transfer function model to obtain a desirable closed loop response and steady-state performance. With ω_n being set to $100 \cdot 2\pi$ or $120 \cdot 2\pi$, the resonant control gain K_r and quality factor Q are determined against the requirement for the current ripple attenuation.

Fig. 2-15 shows the effects of Q and K_r on the frequency responses of the PIR controller. A high K_r leads to better ripple current rejection but a smaller phase margin [101, 102], therefore the maximum value of K_r can be defined according to the desired phase margin. A higher quality factor Q increases the peak amplitude at the target frequency, corresponding to higher gain and greater ripple attenuation. A small quality factor Q gives rise to a wider bandwidth at the target frequency. The controller is less sensitive to mains frequency variation, but yields low ripple attenuation [112]. In [111], the damping element design makes the infinite gain only occurs at 100 Hz. However, in reality, the ac grid frequency of power system is not constant at 50Hz but fluctuates in a range between 49.5 Hz to 50.5 Hz, which corresponds to 99Hz to 101Hz in the DC link and the same in the DC-DC converter side [118, 119]. This requires certain degree of

freedom for the ripple depression capability to increase the robustness by reducing the controller sensitivity to the grid frequency variations.

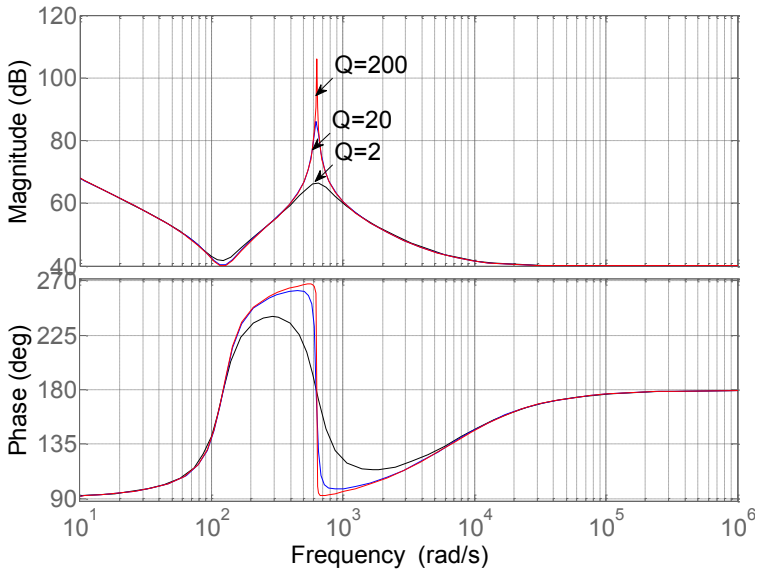

(a)

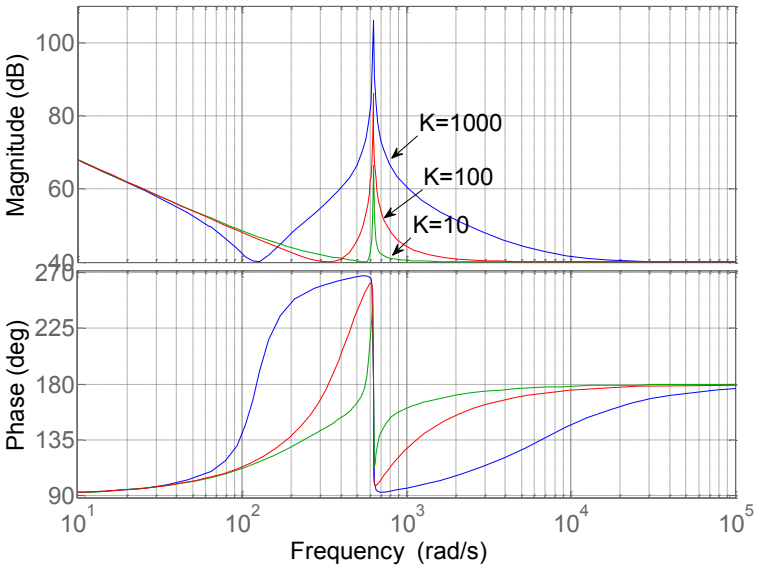

(b)

Fig. 2-15. Effects of resonant controller parameters on frequency responses of PIR controller. (a) effect of Q; (b) effect of Kr

2.4.5 Controller performance analysis

Based on the system requirement for the current control bandwidth of 1.5 kHz and 30 dB attenuation of 99Hz to 101Hz second harmonic ripple, the controller parameters are chosen as: K_p=100, K_i=25000, K_r=1000, Q=200. The Bode diagrams of the open- and closed- loop systems are shown in Fig. 2-16 for the operating condition of 320 V and 9

A. It should be noted that the small signal transfer function, $G_p(s)$, of the LLC converter based battery charging system is a non-minimum phase system as it has a zero on the right hand side of the s-plane. Nevertheless, the Bode plot of the open-loop system, given by $G_c(s)*G_p(s)$, shows that phase margin of the system is 69.3º, and the gain margin is 32.5 dB. Hence, the closed-loop system exhibits good stability as is evident from Fig. 2-16 (b).

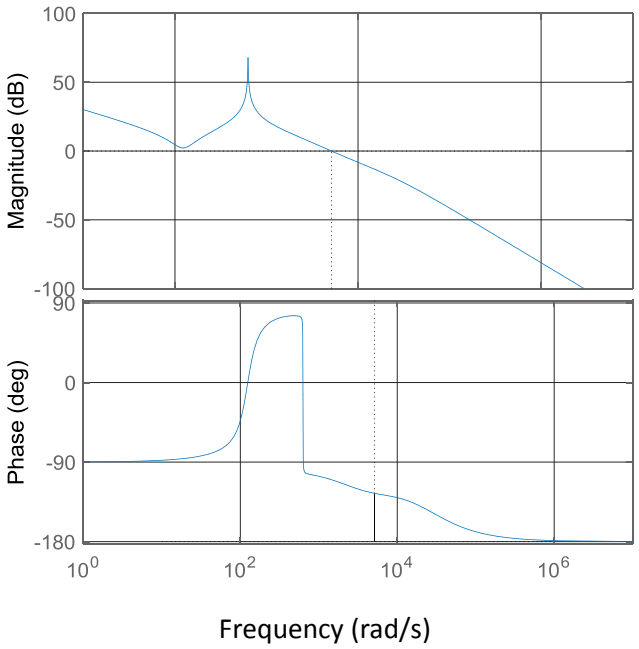

(a)

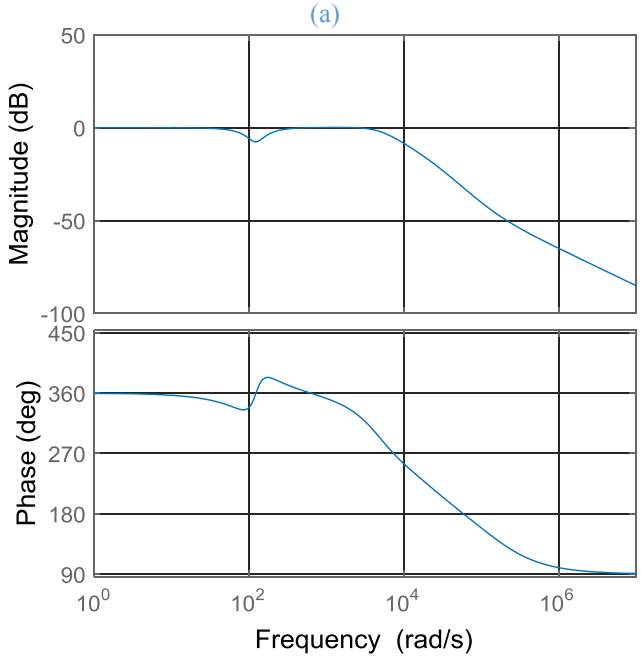

(b)

Fig. 2-16. Bode plots of the control systems with designed PIR controller at nominal 320V battery voltage. (a) Open Loop; (b) Closed loop

The Bode plot of the disturbance rejection property of the closed-loop system, denoted by $1/((1+G_c(s)*G_p(s))$, is shown in Fig. 2-17. It is clear that the attenuation at 100 Hz (628 rad/s) is more than 60 dB. Also, as illustrated in Fig. 2-17 (b), it has enough coverage of the ac grid frequency variations from 99 Hz (622 rad/s) to 101 Hz (634 rad/s). Similar frequency domain analyses are performed against other operating conditions, as shown in Fig. 2-18 and it can be shown that the proposed controller is robust to variations of operating conditions.

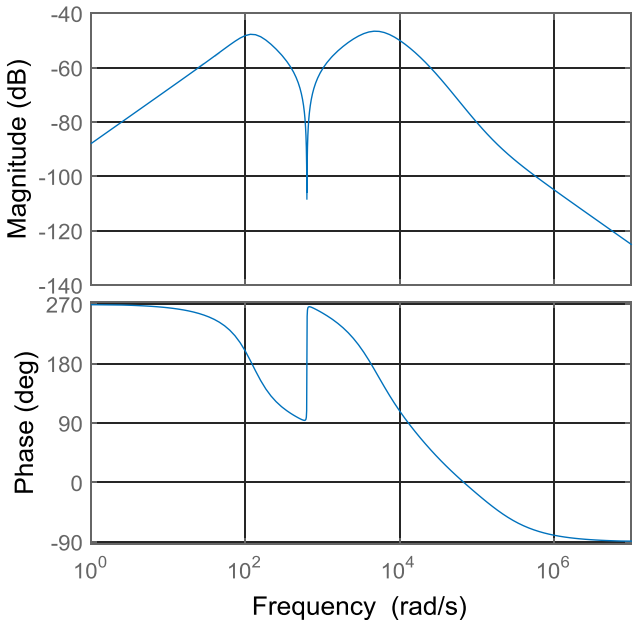

(a)

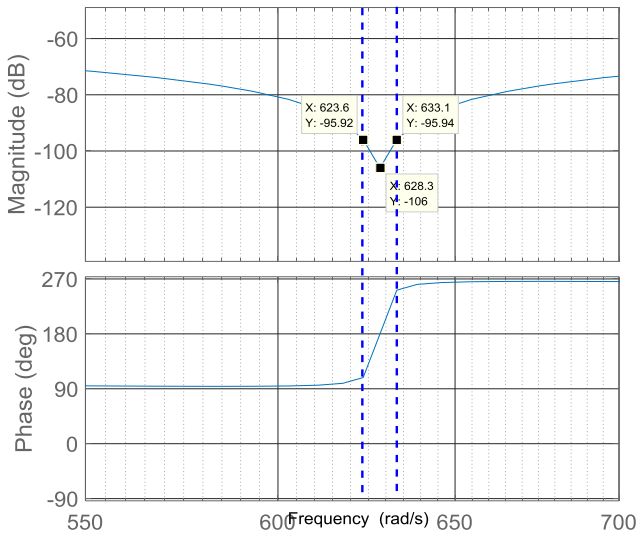

(b)

Fig. 2-17. Disturbance bode plot with the frequency variation from 99Hz to 101Hz, corresponding to 622 rad/s to 634 rad/s. (a) frequency response; (b) zoom-in in the frequency variation range

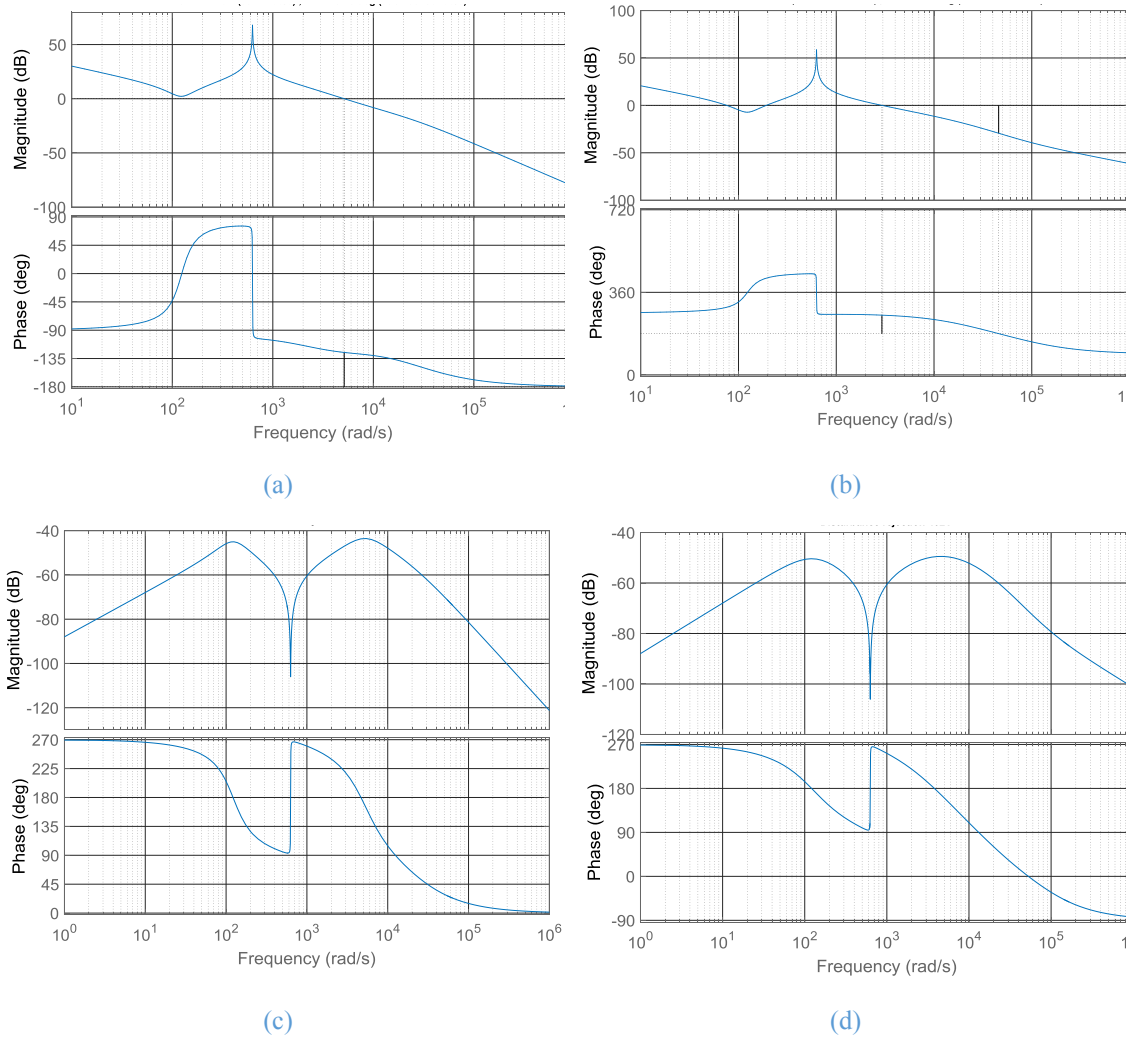

Fig. 2-18. Control performance at high and low battery voltages (a) open loop bode plot at 240V; (b) open loop bode plot at 402V; (c) disturbance bode plot at 240V; (d) disturbance bode plot at 402V

2.5 Simulation Study

Extensive simulations have been implemented to assess the performance of the developed controller with varying battery voltages and loads. In order to save simulation time, the primary DC link voltage is injected with an ideal 100Hz sin wave with 12 V peak-to-peak ripple (3%). Fig. 2-19 (a) compares the steady state battery current at 320 V battery voltage which results with conventional PI and the proposed PIR controllers. With 3% 100 Hz DC link voltage ripple, the peak-to-peak current ripple with the PI controller reaches 5.26 A or 58% while that with the PIR controller is 6 mA, which clearly demonstrates the effectiveness of the proposed controller in elimination of the current ripple.

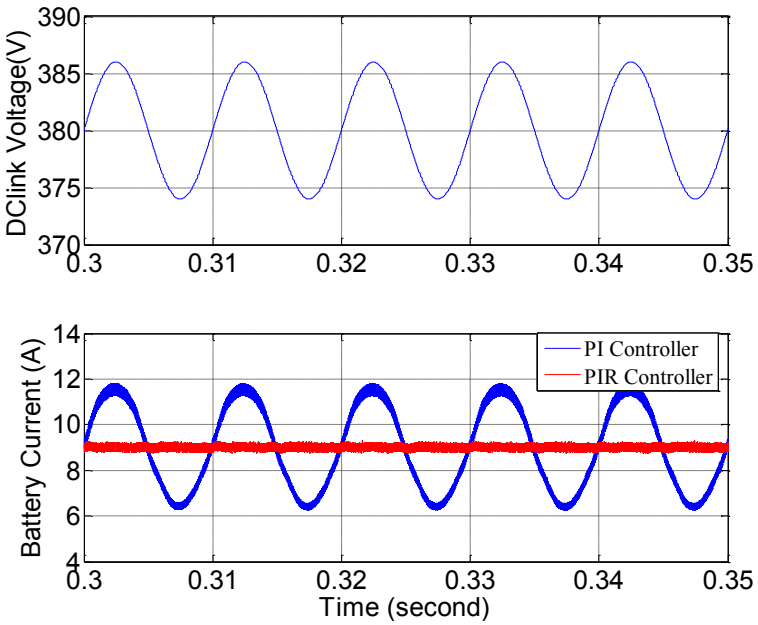

(a)

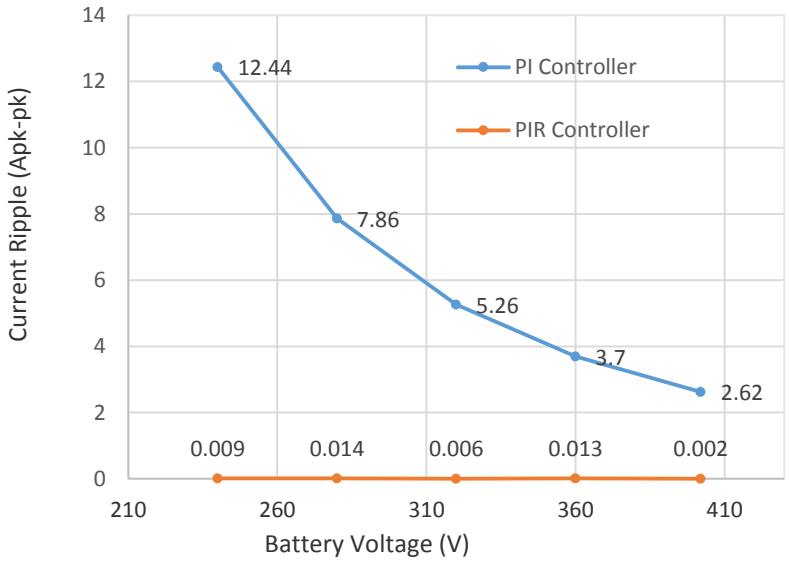

(b)

Fig. 2-19. Simulation results with PI controller and PIR controller. (a) the battery charging current at 320 V battery voltage; (b) FFT current ripple at different battery voltages

The results with different battery voltages covering the whole operating range is shown in Fig. 2-19 (b). When the fixed gain PI controller is used, the resultant peak-to-peak current ripple becomes 12.44 A at 240 V battery voltage and 2.64 A at 402 V battery voltage. With the fixed gain PIR controller in contrast, the current ripple can be attenuated to a very low level over the entire operating range.

2.6 Experimental Verification

To verify the modeling and control strategy described in previous sections, a prototype of battery charging system including a front end AC-DC converter and LLC DC-DC resonant converter has been constructed with the specifications shown in Table 2-2.

Table 2-2 OBBC battery charger prototype specification

Parameters	Symbol	Value	Unit
AC input mains voltage	V_{grid}	240	Vrms
DC link voltage	V_{dc}	380	V
Battery internal resister	R_{bat}	0.6	Ω
Battery fully charged voltage	V_{max}	403.2	V
Battery initial voltage	V_{min}	240	V

2.6.1 Experimental system

The prototype bidirectional charger and the battery load are shown in Fig. 2-20. A variac is used to deliver an adjustable AC voltage to the charger. A front end AC-DC converter converts AC into DC and vice versa. The DC voltage across the DC link capacitor is regulated to 380 V. In the DC-DC stage, the DC power is controlled by the LLC resonant converter during the battery charging/discharging operations. SCH2080KE N-channel Silicon Carbide (SiC) power MOSFETs are used for the full bridge devices. Both the front-end and LLC resonant converters are controlled by the NI Compact RIO 9082 digital controller from National Instruments. The testing load is a Honda Civic NiMH battery which is in “second life” service [120].

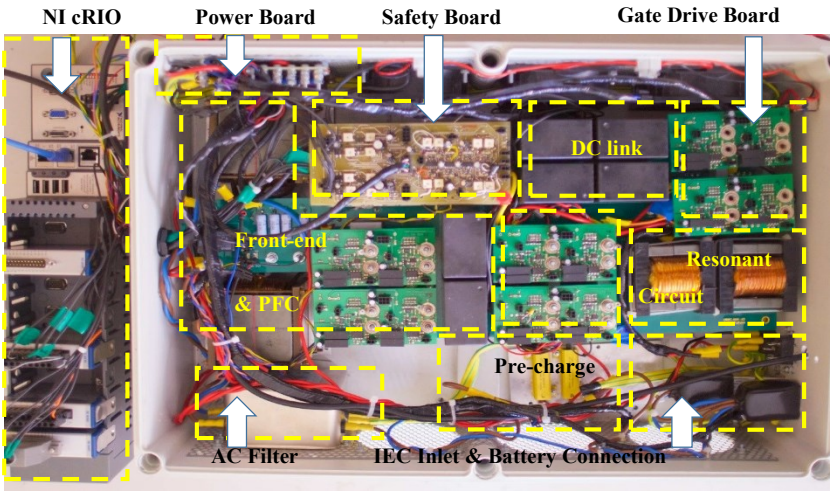

(a)

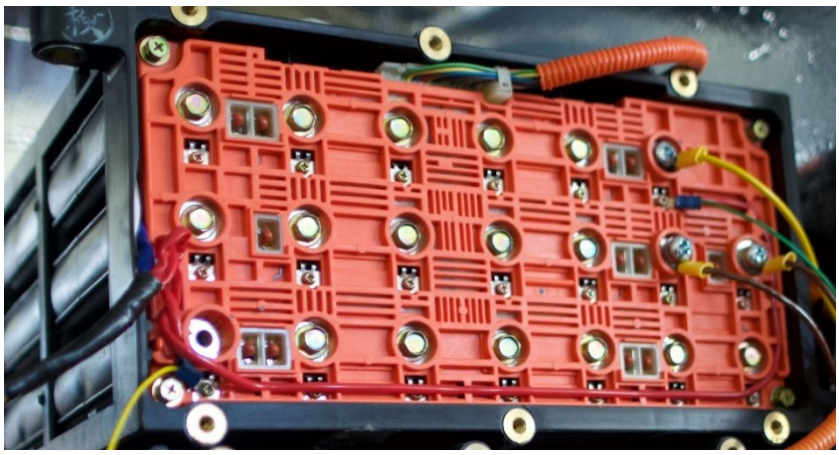

(b)

Fig. 2-20. The prototype battery charger and the battery load. (a) prototype of the bidirectional charger; (b) battery load

2.6.2 ZVS/ZCS operation

Fig. 2-21 and Fig. 2-22 show the testing operation waveforms of the converter in light and heavy resistive load, respectively. As can be seen in both cases, I_{Ls} lags the chopped voltage in the transformer primary side. It is negative before positive voltage provided across the devices, which ensures that the Drain-Source voltage V_{DS} decrease to zero first and then the switch turns on. By this way, the ZVS operation can be achieved. Furthermore, in the secondary side rectifier bridge, diode current decreases to zero when turning off, thus the ZCS operation is achieved in the turns-off, with a low *di/dt*.

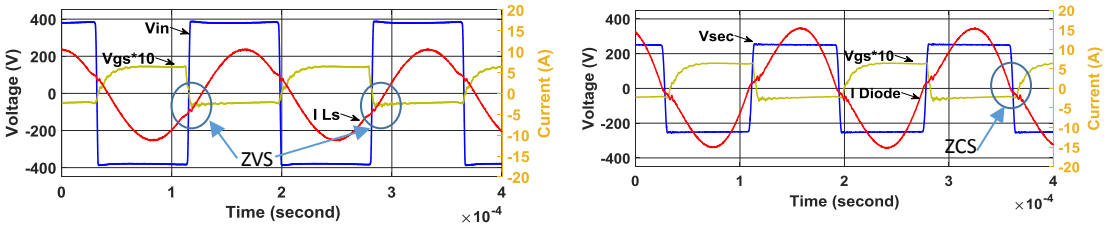

(a) (b)

Fig. 2-21. Experimental results at 240 V battery voltage (a) voltage and current of resonant tank in the primary side; (b) diode current

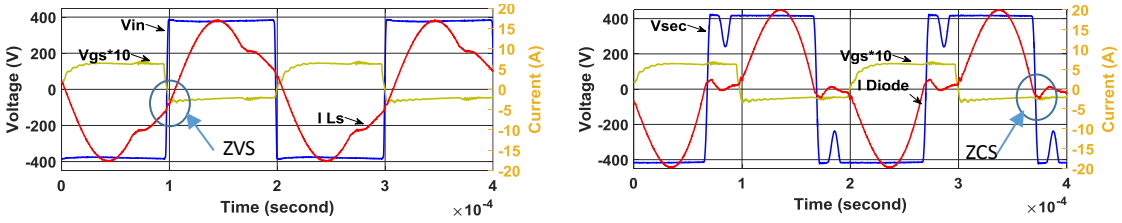

(a) (b)

Fig. 2-22. Experimental results at 410 V battery voltage (a) voltage and current in the primary side; (b) diode current

When the battery side voltage is 240 V, the converter is operating close to the series resonant frequency (128 kHz). However, in order to reach 9 A nominal charging current at 410 V, the converter is operating at 99 kHz, far below the series resonant frequency. This corresponds to discontinuous current mode (DCM) of operation. Consequently, the current waveforms on both the primary and secondary are distorted. A small reverse recovery current in the secondary diodes is also visible.

2.6.3 Current ripple reduction

Fig. 2-23 and Fig. 2-24 illustrate steady-state simulation and experimental results of the battery charging system under the nominal operating condition at 320 V battery voltage employing PI controller and PIR controller, respectively.

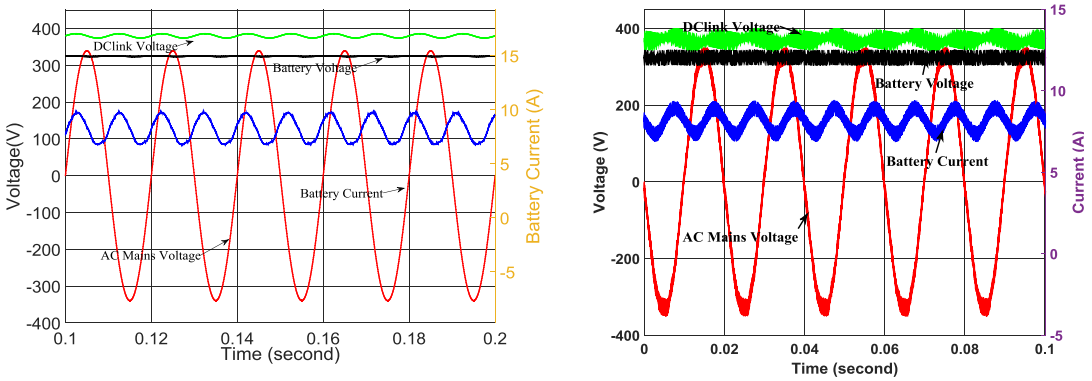

(a) (b)

Fig. 2-23. Results with PI controller at 320 V. (a) simulation; (b) experimental test results.

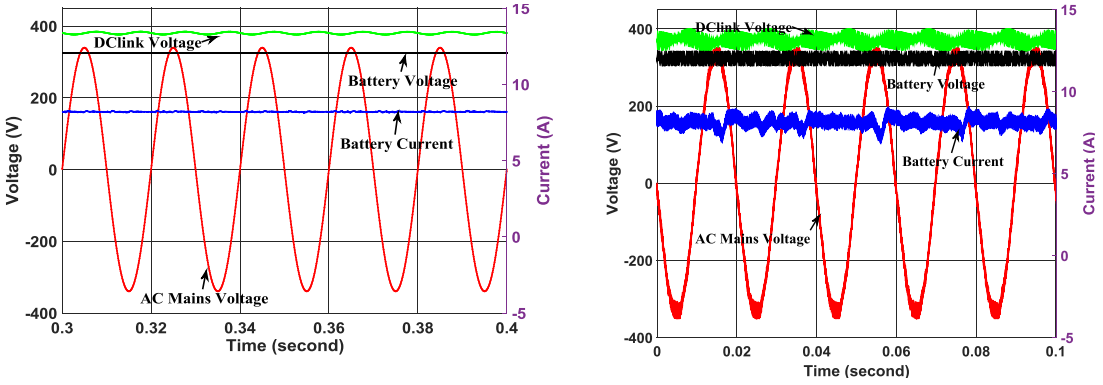

(a) (b)

Fig. 2-24 Results with PIR controller at 320 V. (a) simulation; (b) experimental test results.

Four traces, namely, AC mains voltage, DC link voltage, battery voltage and battery current, are shown in each of the figures. Since the battery used in the tests differs from those in the previous simulation study, the Simulink model is modified with measured

battery off-line impedance and includes parasitic resistance and inductance of the cables. The front-end AC-DC converter is combined with the LLC resonant converter and battery models for simulation study of the whole system. It is observed that the simulation waveforms agree well with the experimental results. It should be noted that, in the experimental tests results, the AC-DC converter in the front-end was included thus this converter switching operation leads to high-frequency noise in the DC link voltage waveforms. However, the DC link voltage waveforms in the time-domain simulations are relatively clean. This is because in order to save simulation time, the primary DC link voltage is injected with an ideal 100Hz sin wave with 12 V peak-to-peak ripple (3%).

Fig. 2-25 shows the harmonic distributions of the measured battery current waveforms which result with the PI and PIR controllers. The simulated and measured DC link voltage and charger current ripples are compared in Table 2-3. With the conventional PI controller, the simulated and measured peak-to-peak DC link voltage ripple is 6.983 V (1.83%) and 10.18 V (2.67%), respectively. The resultant 100 Hz harmonic in the battery current, is 1.758 A (21.4%) peak-to-peak and 1.571 A (19.2%). By applying the resonant controller, the 100 Hz current ripple is suppressed considerably both in the simulation and experimental results, and the resultant 100Hz current ripples are 0.002A (0.02%) in the simulation and 0.226 A (2.7%) in the test, respectively. It can be observed that the 100 Hz harmonic is attenuated by 99% in the simulation and 86% in the experiment. The ripple suppression effect in the test is less than that predicted in simulation due to the impedance change in the real battery system. It should also be noted that the harmonic currents at integer multiple of 100Hz are slightly increased when the PIR control is applied since the attenuation at these frequencies is much lower.

It is worth noting that, since the DC-DC converter together with the battery can be considered as a load branch in parallel with the DC link branch, larger impedance in the load side leads to a comparatively smaller impedance in the DC link side thus more energy is circulating across the DC link. Therefore, after applying the resonant controller, although the battery current ripple decreases, higher ripple level is seen in the DC link voltage, as evidenced in Table 2-3. Also, a high frequency harmonic in the battery current can be seen in Fig. 2-24 (b). This may because the saturation of the controller at high power and the nonlinear characteristics of the battery.

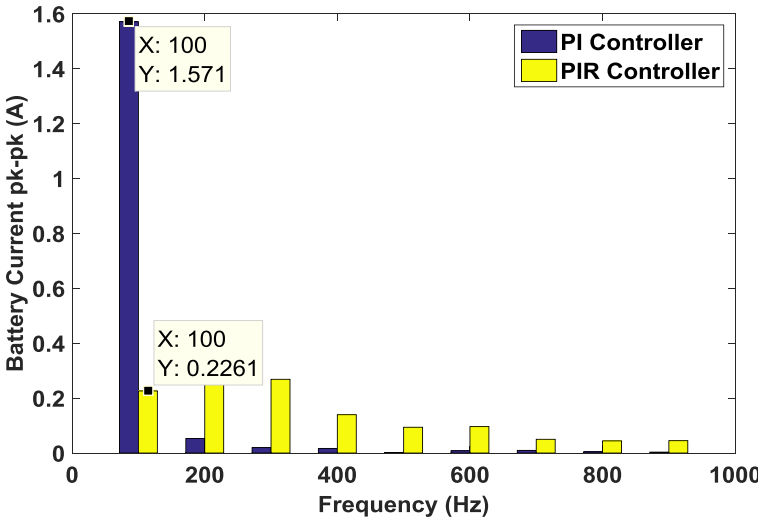

Fig. 2-25. FFT analysis of battery current ripple with PI and PIR controller at 320 V battery voltage in the experimental test

Table 2-3 Comparison of Simulation and Test Result at 320V

Parameters	SIMULATION		TEST		Unit
	PI	PIR	PI	PIR	
V_{dc} ripple p-p	6.983	7.779	10.18	10.58	V
I_{bat} ripple p-p	1.758	0.002	1.571	0.226	A
I_{bat} ripple percentage	21.4	0.02	19.2	2.7	%

Further testing was performed at charging current 6.5 A at 270 V battery voltage. Fig. 2-26 demonstrates simulation and experimental results employing PI controller under this condition. It is clear that the simulated and measured peak-to-peak currents are 1.442 A (22.1%) and 1.834 A (28.2%), respectively. However, when the PIR controlled is employed, the ripples have been reduced to 0.008 A (0.12%) in the simulation and 0.027 A (0.43%) in the measurement, as presented in Fig. 2-27. FFT analysis result of the measured current is displayed in Fig. 2-28. The simulated and measured voltage and current ripples are compared in Table 2-4. It can be seen that the 100 Hz harmonic current is attenuated by 99% in the simulation and 98.6% in the measurement, demonstrating that the proposed controller is able to eliminate the current ripple effectively.

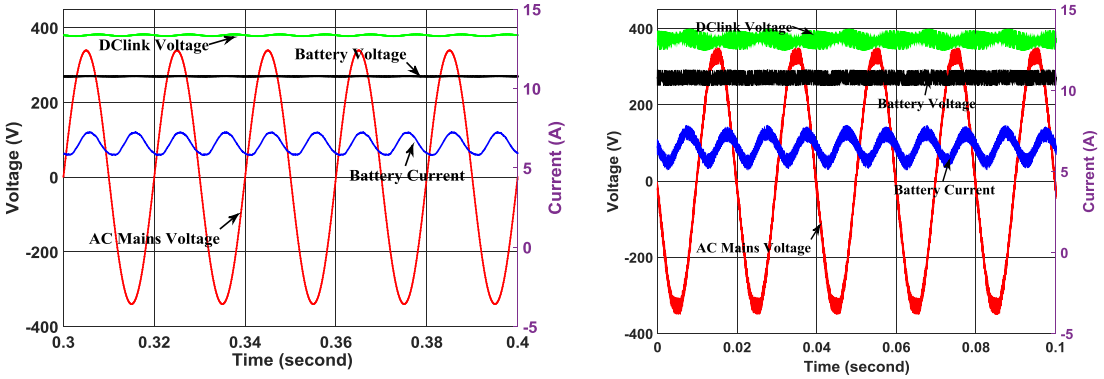

(a) (b)

Fig. 2-26. Results with PI controller at 270 V. (a) simulation; (b) experiment

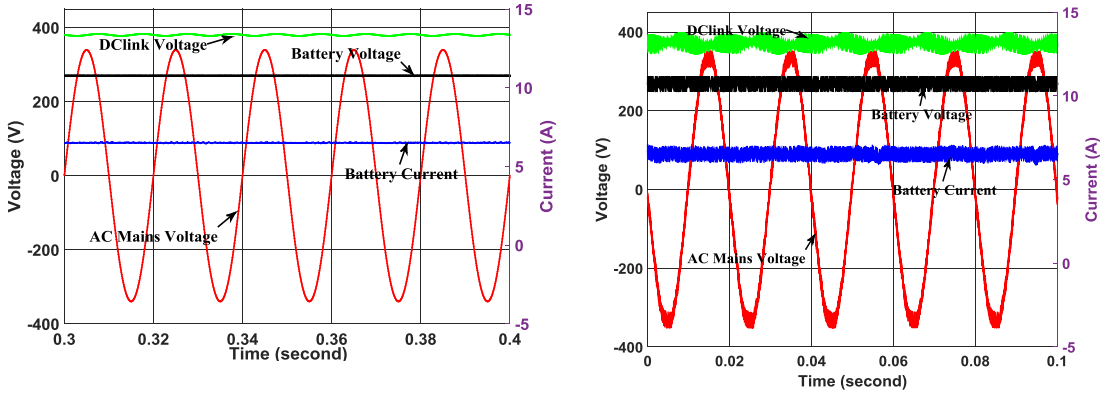

(a) (b)

Fig. 2-27. Results with PIR controller at 270 V. (a) simulation; (b) test.

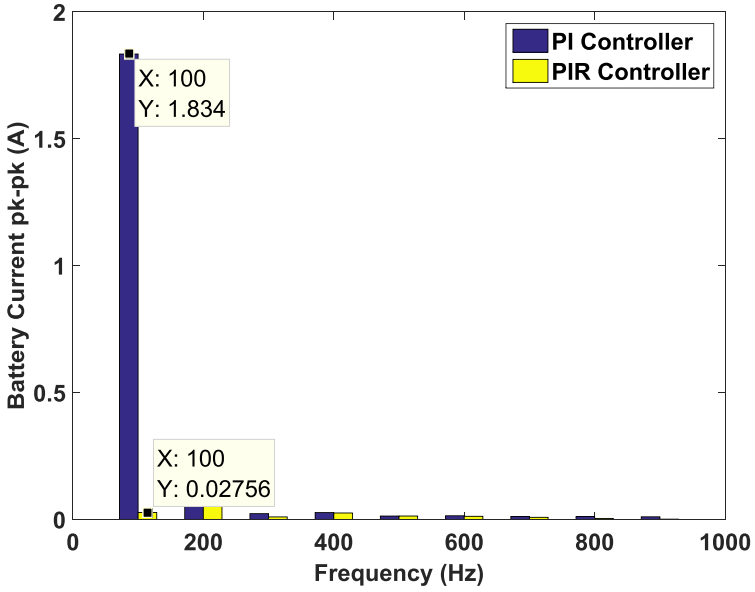

Fig. 2-28. FFT analysis of battery current ripple with PI and PIR controller at 270 V battery voltage in the experimental test

Table 2-4 Comparison of Simulation and Test Result at 270V

Parameters	SIMULATION		TEST		Unit
	PI	PIR	PI	PIR	
V_{dc} ripple p-p	4.604	5.174	7.271	7.341	V
I_{bat} ripple p-p	1.442	0.008	1.834	0.027	A
I_{bat} ripple percentage	22.1	0.12	28.2	0.43	%

2.7 Summary

A feedforward-proportional-integral-resonant control strategy has been described to suppress the low-frequency current ripple in an LLC resonant converter for EV battery chargers. The DC gain of the LLC resonant converter is analyzed and quantified. A small-signal transfer function is derived in time-domain simulations by injecting a small perturbation signal into the converter switching frequency. With the derived model, the FF-PIR controller is designed. Stability and robustness of the controller is analyzed by employing frequency domain techniques. The effectiveness of the proposed resonant controller on suppressing the harmonic current is verified by simulations and experimental tests. Therefore, this control strategy can be used in grid-connected EV onboard charger to improve charger performance and hence enhancing battery performance, efficiency and lifetime.

CHAPTER 3
Design and Power Loss Analysis of CLLC Resonant Converter for EV Bidirectional Charger

This chapter describes a CLLC resonant converter for a bi-directional battery charger. By adding an extra capacitor in the transformer secondary side, the conventional three-element LLC resonant converter has been reshaped into a four-element resonant converter. In both forward and reverse modes, the resonant tank possesses almost the same operational characteristics of the conventional LLC resonant tank. Thus the ZVS+ZCS soft switching can be achieved both in forward and reverse modes and the switching losses can be minimized, hereby improving the charger efficiency. The circuit topology, operation principle and DC gain characteristics are analysed. A systematic design procedure is described and a comprehensive approach for designing the secondary side capacitor is presented. Performance of the designed CLLC resonant converter in both forward and reverse modes are assessed by extensive experimental tests. Power loss analysis shows that the efficiency of CLLC improves between 1% to 10.02 % in the whole operating range compared with conventional LLC converter.

Part of the contents in this chapter has been published in [121] by the author.

3.1 Introduction

As described in the previous chapters, among the various DC-DC converter topologies proposed in literature, a LLC resonant converter, which employs a series inductor and capacitor along with the parallel magnetizing inductance of high frequency transformer to form the three-element resonant tank, exhibits high efficiency due to zero-voltage switching (ZVS) in the primary side and zero-current switching (ZCS) in the secondary side, and hence is a promising candidate topology for charging applications [70, 81, 83, 122-124].

However, LLC resonant converters lose the soft switching features in the reverse (V2G) mode, thereby compromising the efficiency and limiting the capabilities of bidirectional power transfer. This limitation may be overcome by a bidirectional CLLC resonant converter which has an extra series capacitor to form a four-element resonant tank. In [64], a bidirectional DC-DC converter based on the combination of two LLC resonant topologies is proposed. The resonant converter achieves higher efficiency than the conventional LLC resonant converter. However, the transformer features a large turn ratio in order to cope with large difference between the input and output voltage, which makes it not suitable for EV battery charging system [88]. Reference [89] proposes a symmetric full-bridge CLLC topology, featuring ZVS and ZCS in both the forward and the reverse modes. Due to the symmetric topology, the operation characteristics and the converter efficiency is equivalent in both the forward and the reverse modes. However,

since in the symmetric topology the turns ratio is limited to 1:1, the converter voltage gain is low therefore reducing zero switching range and makes it difficult to cope with wide battery voltage variation.

This chapter presents an asymmetric CLLC structure suitable for bi-directional battery charger and its content is organized as follows. Section 3.2 presents the topology and the operation principle of the CLLC resonant converter at different operation ranges in both forward and reverse modes. The operational characteristics of the CLLC resonant network is analysed in Section 3.3 using fundamental harmonic approximation (FHA) method in both G2V and V2G modes. A design procedure for the CLLC resonant converter is discussed and evaluated in Section 3.4. Time-domain simulation and the power loss evaluation is presented in Section 3.5 and Section 3.6. Experimental tests, power loss measurement and comparisons are presented in Sections 3.7 and Section 3.8 to validate the performance of the proposed converter.

3.2 CLLC Resonant Converter

3.2.1 Circuit topology

The LLC resonant converter has advantages of ZVS in the primary side and ZCS in the secondary side. However, when the LLC resonant converter operates in the reverse mode, the magnetic inductance of the transformer which is in parallel with the load is clamped by the battery. Thus only the series resonant inductor and series resonant capacitor participate in the resonance as a L-C series resonant converter (SRC) which has the following issues:

1) In SRC, the resonant tank component, connected in series with the equivalent load, acts as a voltage divider of the input voltage. Thus the DC gain of SRC cannot be higher than unity, which makes the topology not suitable for the EV battery charging applications due to the wide input and output voltage ranges.
2) The DC gain curve of SRC against switching frequency at different load conditions (in the figure represented as R_{ac} which is the equivalent ac load in the FHA model) is displayed in Fig. 3-1. As can be observed, the maximum DC gain of SRC is achieved at the series resonant frequency. In the regions below this frequency, the converter operates under ZCS operation in which the MOSFETs suffer from significant power losses in the body diodes. Thus the ZVS operation (further illustrated in Section 3.2.2 with voltage and current

waveforms) is preferred for reducing the turn on losses. However the ZVS operation can only be realized in the region above the series resonant frequency [89]. Consequently, the soft switching features cannot be attained under all load conditions and wide input/output voltage ranges. Furthermore, in the ZVS region, in order to keep regulating the output voltage at light load conditions, the negative slope of the DC gain curve leads to the operation far above the series resonant frequency. In this condition, large current circulating in the resonant tank increases the converter loss.

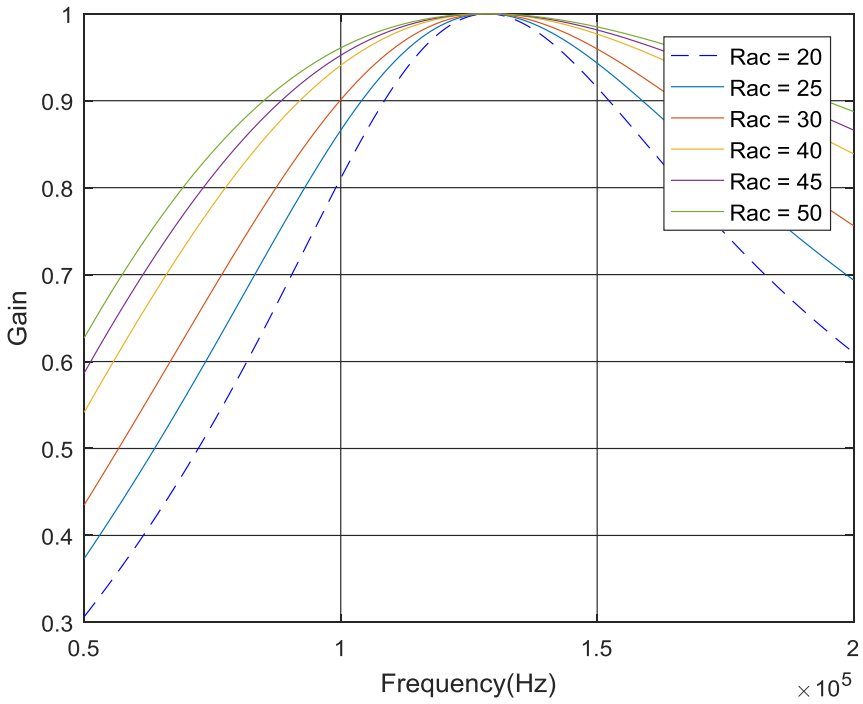

Fig. 3-1 DC gain curve of the SRC resonant converter

By adding a capacitor (C_{s2}) in the secondary side, the LLC resonant tank has been reshaped into a four-element CLLC resonant tank, as shown in Fig. 3-2. In both forward and reverse modes, the resonant tank possesses almost the same operation characteristics of the conventional LLC resonant tank [11]. Thus the ZVS+ZCS soft switching can be achieved both in forward and reverse modes and the switching losses can be minimized, thereby improving the charger efficiency.

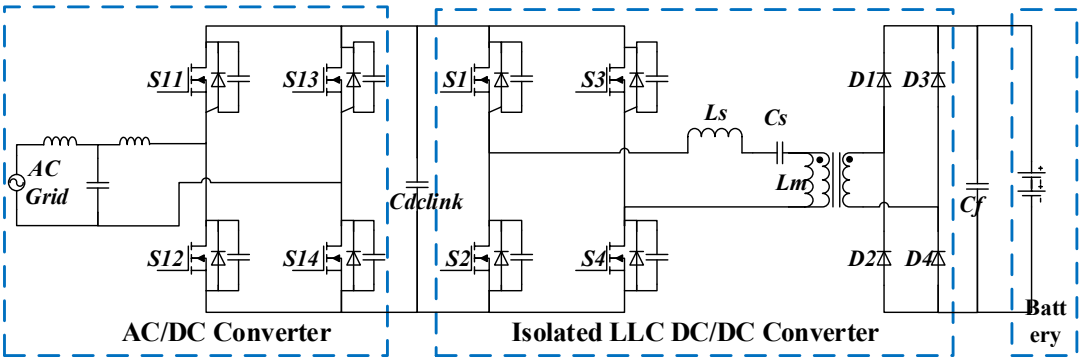

(a)

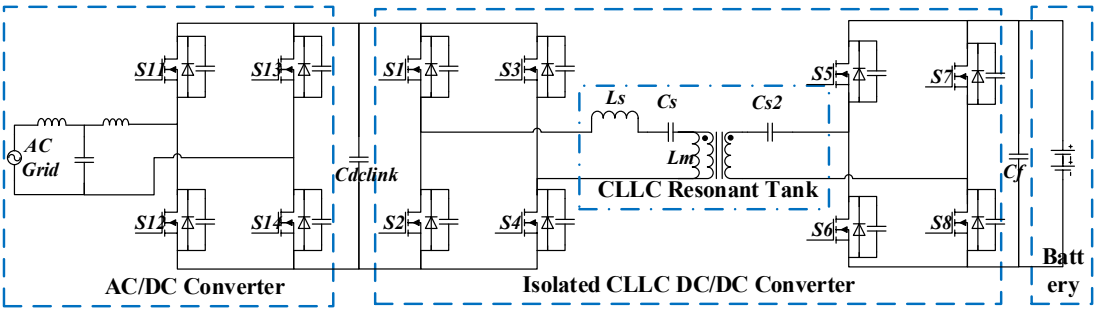

(b)

Fig. 3-2. Typical EV on-board battery charger architecture based on the DC-DC converter employing (a) LLC uni-directional resonant tank; (b) CLLC bidirectional resonant tank

3.2.2 Operation principle

In this section, the operating principle of the CLLC resonant converter in each operating mode is analysed. For the sake of convenience, the AC-DC front end is omitted here. and only the DC-DC resonant converter is analysed.

(1) Forward CLLC

In the forward mode, the power flow is from the DC link to the battery. In the primary side, the active switches driven by 50% duty cycle square wave. In the secondary side, the switches are turned off but the bode diodes operate as a rectifier bridge. During one switching cycle, the converter operation has eight stages as shown in Fig. 3-3. Stage (a) – stage (d) in the first half cycle repeats in the second half cycle (stage (e) to stage (h)).

Stage (a) and stage (e) are resonance stages with power transferring from primary to the secondary; stage (b) and stage (f) are discontinuous stages during with no power transferred; stage (c) – (d) and stage (g)- (h) correspond to the dead time period. Stage (c) and stage (g) are associated with the capacitor charging and discharging stages while stage (d) and stage (h) are the diode commuting stages which facilities the ZVS operation.

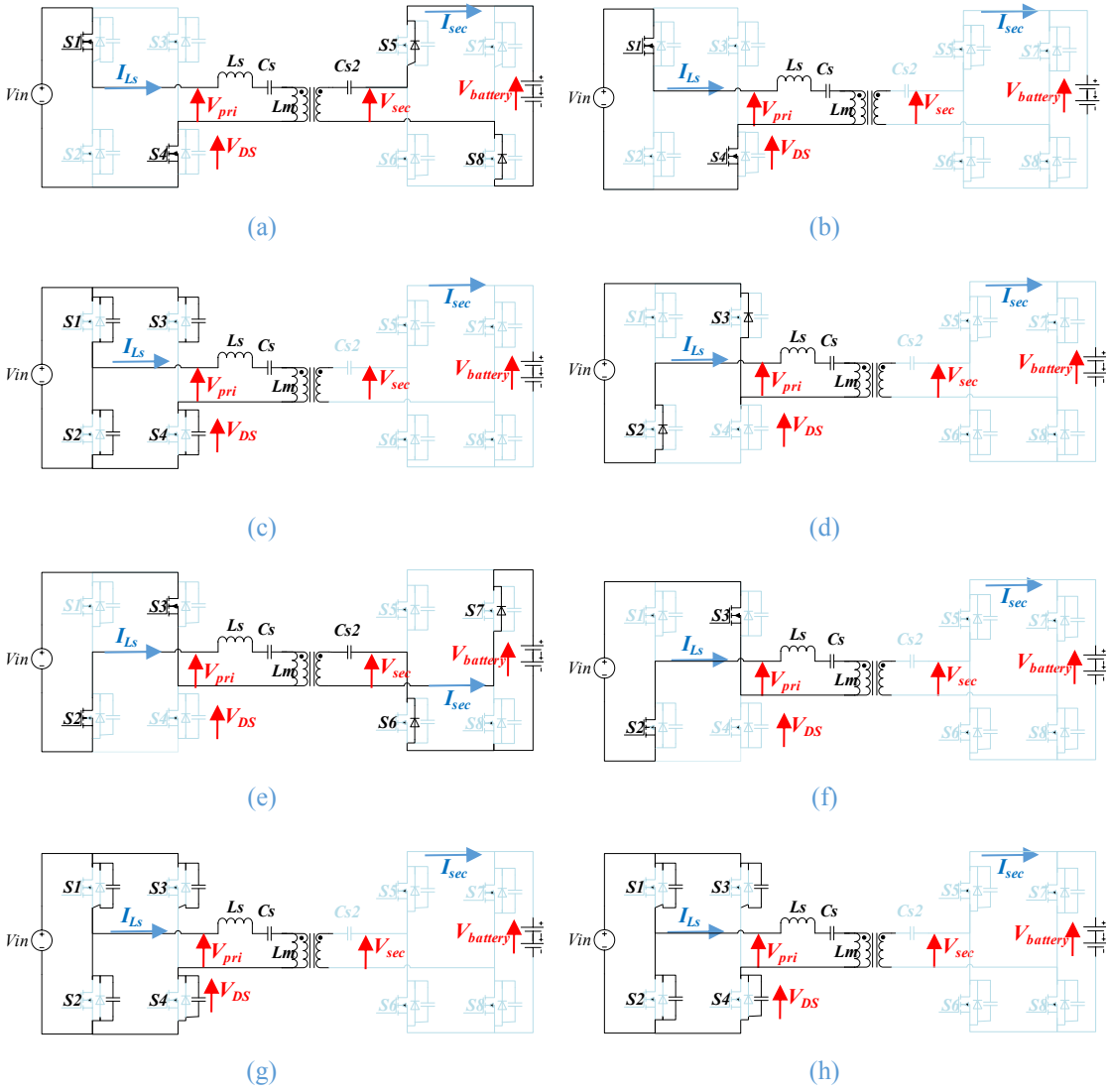

Fig. 3-3 Operational stages of the CLLC DC-DC resonant converter in forward mode

The ideal waveforms can be shown in Fig. 3-4. And the detailed explanations of the operation are described as follows:

Stage (a) [$t_0 - t_1$]: the resonance stage. On the primary side, with the switches S1 and S4 turned on, the chopped voltage Vin forces resonant current i_{Ls} to increase in a sinusoidal wave through S1 and S4. The power transfers from the primary side of the transformer to the load. The L_m is in parallel with the transformer and clamped by the output voltage thus only acts as a passive load instead of participating in the resonance. The current through the magnetizing inductance i_{Lm} also increases during this stage in a triangle shape and is lower than i_{Ls}. Meanwhile, the voltage across the transformer secondary side forces the diodes of switches S5 and S8 forward biased and the current

through the rectifier bridge to the output battery. This stage ends when the magnetizing inductance current i_{Lm} meets the resonant current i_{Ls}.

Stage (b) [t_1 – t_2]: the discontinuous non-resonance stage. When the inductance current i_{Lm} dropped to the same value of i_{Ls}, there is no net current flowing into the transformer thus the rectifier current in the transformer secondary side becomes zero accordingly. The magnetizing inductor is anticipating the resonance together with the series capacitor and series inductor. The resonant capacitor C_{s2} in the secondary side reaches to the peak point and remains unchanged as there is no rectifier current through it. The rectifier diodes of switches S5 and S8 turn off at the Zero Current Switching condition. As the current in the rectifier is not continuous any more, the stage is called discontinuous current mode. During this mode, there is no power transfer between the primary and the secondary side.

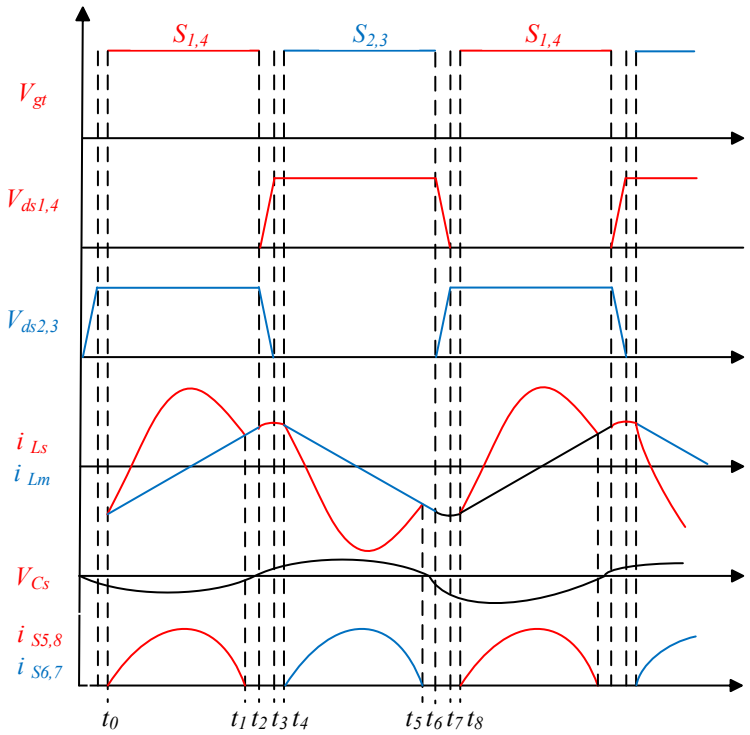

Fig. 3-4 Typical theoretical operation principles of CLLC resonant converter in forward mode

Stage (c) [t_2 – t_3]: dead time and capacitor charging/discharging stage. When the switches S1 and S4 are conducting, the parasitic capacitors are fully discharged. At time t_2, the switches S1 and S4 turn off, and i_{Ls} does not change flowing direction thus charging the parasitic capacitors of S1 and S4, while discharging parasitic capacitors of S2 and S3 simultaneously. This charging/discharging time is much shorter compared with the whole

switching cycle, because the parasitic capacitor is rather smaller than the series capacitor C_s.

Stage (d) [t_3 – t_4]: dead time and diode freewheeling stage. When the parasitic capacitors of switches S1 and S4 are fully charged and those of S2 and S3 are fully discharged, the resonant current passes through the antiparallel diodes of S2 and S3 immediately, guaranteeing the zero voltage switching for the turn-on event in the next stage. This period is also short compared to the whole switching cycle.

Stage (e) [t_4 – t_5]: At the end of stage (d), switches S2 and S3 turn on with zero voltage switching operation. The drain-source voltages of S1 and S4 reach the input voltage V_{in}, and the drain-source voltages of S2 and S3 become zero. The voltage after the H-bridge applied to the resonant circuit changes to its opposite direction. The input voltage Vin forces the resonant current i_{Ls} to decrease initially and then increase in a sinusoidal wave, in the opposite direction, through S2 and S3. The power transfers through the transformer. The magnetic energy in the magnetizing inductance changes linearly so the L_m does not participate in the resonance. Current through magnetizing inductance i_{Lm} also increases in the opposite direction with respect to stage (a). On the secondary side, the voltage across the transformer secondary side forces the diodes of switches S6 and S7 forward biased and the current through the rectifier bridge to the output battery. This stage ends when the magnetizing inductance current i_{Lm} equals the resonant current i_{Ls}.

Stage (f) [t_5 – t_6]: the discontinuous non-resonance stage. This stage is similar to stage (f). There is no current going through the transformer and the rectifier current in transformer secondary side becomes zero. L_m is anticipating the resonance together with the series capacitor and series inductor. However, the difference is that the rectifier diodes of switches S6 and S7, rather than S5 and S8 turn off under the Zero Current Switching condition.

Stage (g) [t_6 – t_7]: dead time and capacitor charging/discharging stage. This is similar to stage (d), the parasitic capacitors of S1 and S4 are being charged while those of S2 and S3 discharged simultaneously.

Stage (h) [t_7 – t_8]: dead time and diode freewheeling stage. This stage is similar to stage (d), however, the resonant current passes through the antiparallel diodes of S1 and S4, which leads the zero voltage switching for S1 and S4 to be turned on in the next stage.

The operation modes of the switches and the anti-parallel diodes are presented in Table 3-1:

Table 3-1 Typical operation of the switches and anti-parallel diodes in one switching cycle

Stages	S1,S4	D1,D4	S2,S3	D2,D3	S5-S8	D5,D8	D6,D7
(a) Resonance stage	ON	OFF	OFF	OFF	OFF	ON	OFF
(b) Discontinuous stage	ON	OFF	OFF	OFF	OFF	OFF	OFF
(c) Dead time- capacitor stage	OFF	OFF	OFF	OFF	OFF	OFF	OFF
(d) Dead time- diode stage	OFF	OFF	OFF	ON	ON	OFF	OFF
(e) Resonance stage	OFF	OFF	ON	OFF	OFF	OFF	ON
(f) Discontinuous stage	OFF	OFF	ON	OFF	OFF	OFF	OFF
(g) Dead time- capacitor stage	OFF	OFF	OFF	OFF	OFF	OFF	OFF
(h) Dead time- diode stage	OFF	ON	OFF	OFF	OFF	OFF	OFF

(2) Reverse mode CLLC

In the reverse mode, the power flow is from the battery load to the DC link. Active switches in the transformer secondary side are driven by 50% duty cycle signals; while in the primary side the switches are turned off but the antiparallel body diodes operating as a rectifier bridge. Similar to the operation in the forward mode, one switching cycle of the converter includes eight stages as shown in Fig. 3-5. Stage (a) - stage (d) in the first half cycle repeats in the second half cycle denoted as stage (e) to stage (h).

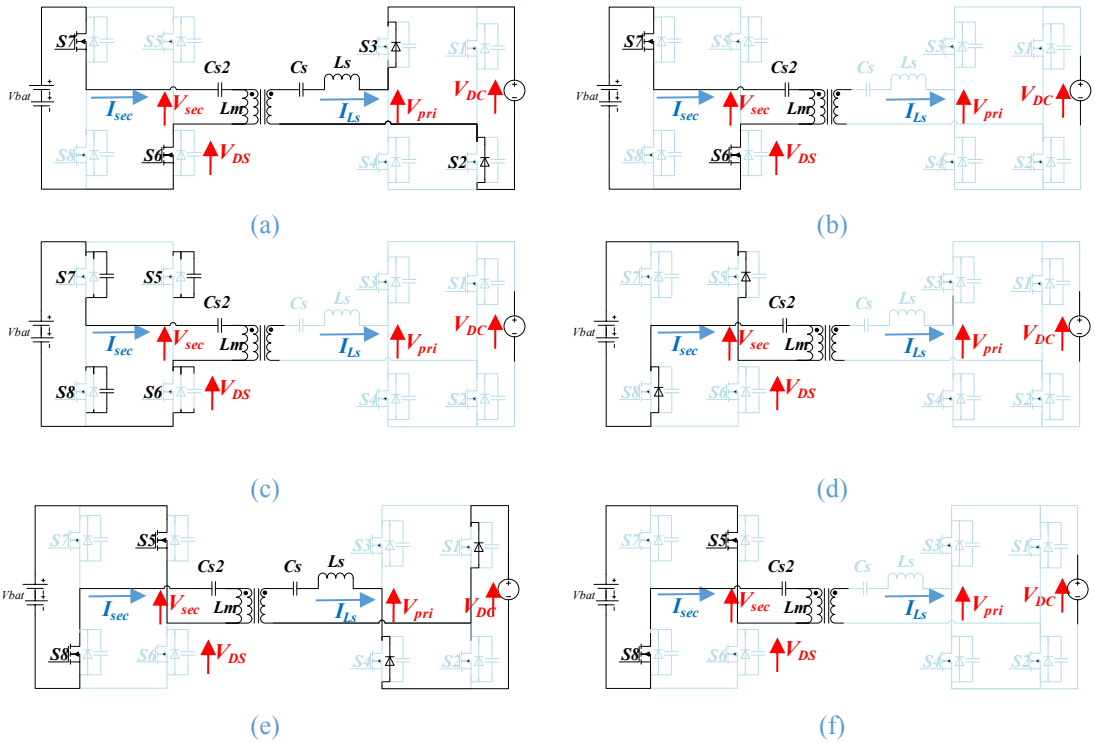

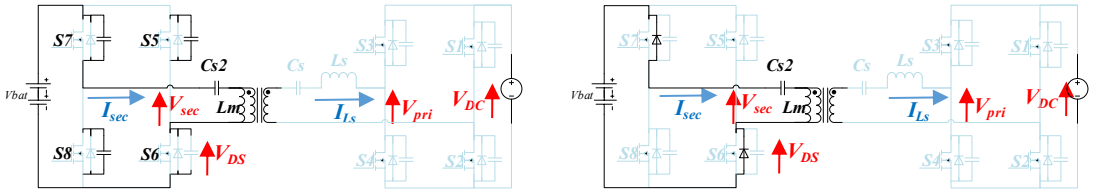

(g) (h)

Fig. 3-5 Operational stages of the CLLC DC-DC resonant converter in reverse mode

Stage (a) and stage (e) are resonance stages with power transferring from the battery to the DC link; stage (b) and stage (f) are discontinuous stages during which no power is transferred; stage (c) – (d) and stage (g)- (h) correspond to the dead time period. Stage (c) and stage (g) are associated with the capacitor charging and discharging while stage (d) and stage (h) coincide with diode commutation which allows for ZVS operation. The switches status in one switching cycle are summarised in Table 3-2.

Table 3-2 Typical operation of the switches and anti-parallel diodes in one switching cycle

Stages	S6,S7	D6,D7	S5,S8	D5,D8	S1-S4	D2,D3	D1,D4
(a) Resonance stage	ON	OFF	OFF	OFF	OFF	ON	OFF
(b) Discontinuous stage	ON	OFF	OFF	OFF	OFF	OFF	OFF
(c) Dead time- capacitor stage	OFF	OFF	OFF	OFF	OFF	OFF	OFF
(d) Dead time- diode stage	OFF	OFF	OFF	ON	ON	OFF	OFF
(e) Resonance stage	OFF	OFF	ON	OFF	OFF	OFF	ON
(f) Discontinuous stage	OFF	OFF	ON	OFF	OFF	OFF	OFF
(g) Dead time- capacitor stage	OFF	OFF	OFF	OFF	OFF	OFF	OFF
(h) Dead time- diode stage	OFF	ON	OFF	OFF	OFF	OFF	OFF

The ideal waveforms are shown in Fig. 3-6. As observed from in Fig. 3-5 and Fig. 3-6, the reverse mode operates in a similar manner to the forward mode.

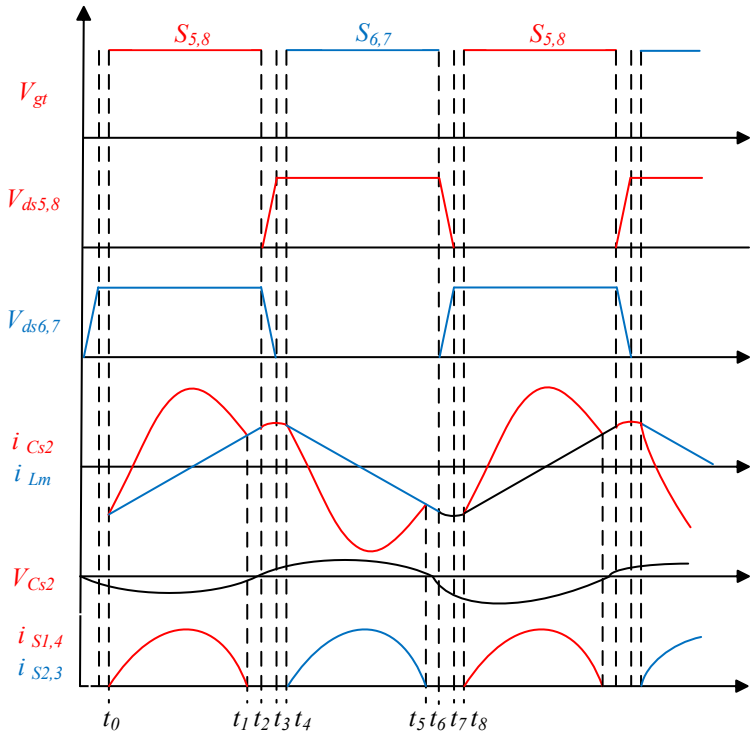

Fig. 3-6 Typical theoretical operation principles of CLLC resonant converter in the reverse mode

3.3 DC Gain Characteristics

The DC/DC voltage gain of the converter as a function of switching frequency in both forward and reverse modes can be derived using FHA method [88].

3.3.1 Forward mode

The equivalent circuit of the CLLC resonant converter in the forward mode using FHA method is shown in Fig. 3-7.

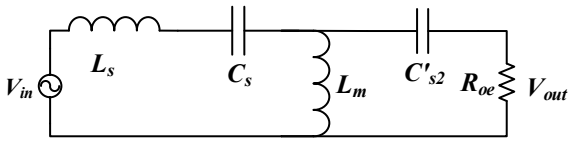

Fig. 3-7 Equivalent circuit of CLLC resonant converter in forward mode

V_{in} and V_{out} are the RMS values of the fundamental component of the input and output voltages of the resonant tank in the forward mode, respectively. C'_{s2} given by Equation (3-1) is the equivalent value of C_{s2} referred to the transformer primary side from the transformer secondary side. R_{oe} given in Equation (3-2) is the equivalent resistive load representing the rectified diode, filter capacitor and battery load referred to the transformer primary side from the transformer secondary side.

$$C'_{s2} = \frac{C_{s2}}{N^2} \tag{3-1}$$

$$R_{oe} = N^2 \cdot \frac{8}{\pi^2} \frac{V_{out}^2}{P_{out}} \tag{3-2}$$

The forward transfer function of the resonant tank can be derived and shown in Equation (3-3).

$$\begin{aligned} G(s), forward &= \frac{V_{out}(s)}{V_{in}(s)} \\ &= \frac{Z_0(s)}{(sC_s)^{-1} + sL_s + Z_0(s)} \cdot \frac{R_{oe}}{(sC'_{s2})^{-1} + R_{oe}} \end{aligned} \tag{3-3}$$

where s is Laplace's operator. The equivalent input impedance of the resonant network and load, Z_O is given in Equation (3-4).

$$Z_0(s) = \frac{sL_m \cdot ((sC'_{s2})^{-1} + R_{oe})}{sL_m + (sC'_{s2})^{-1} + R_{oe}} \tag{3-4}$$

The series resonant frequency f_{sr}, the nominal frequency f_n, the switching frequency f_s, the quality factor Q, the inductance ratio k, and the capacitor ratio g are defined in Equation (3-5)

$$\begin{aligned} \omega_{sr} = 2\pi f_{sr} = \frac{1}{\sqrt{(L_s \cdot C_s)}}, f_n = \frac{f_s}{f s_r} \\ Q = \frac{Z_r}{R_{o,e}}, \; Z_r = \sqrt{\frac{L_s}{C_s}}, \; k = \frac{L_s}{L_m}, g = \frac{C'_{s2}}{C_s} \end{aligned} \tag{3-5}$$

The DC/DC conversion gain of the resonant tank as a function of switching frequency in the forward mode can be obtained and expressed in Equation (3-6).

$$|G(s)|, forward = \frac{1}{\sqrt{A^2 + B^2}} \tag{3-6}$$

where,

$$A = \frac{k - k \cdot f_n^2 + f_n^2}{f_n^2} \tag{3-7}$$

$$B = \frac{Q}{f_n}(1 - f_n^2 + \frac{k+1}{g} - \frac{k}{g \cdot f_n^2}) \tag{3-8}$$

Based on Equations (3-6), (3-7) and (3-8), the voltage gain curves of the CLLC resonant converter as a function of switching frequency under varying load conditions indicated by Q factor in the forward mode is shown in Fig. 3-8.

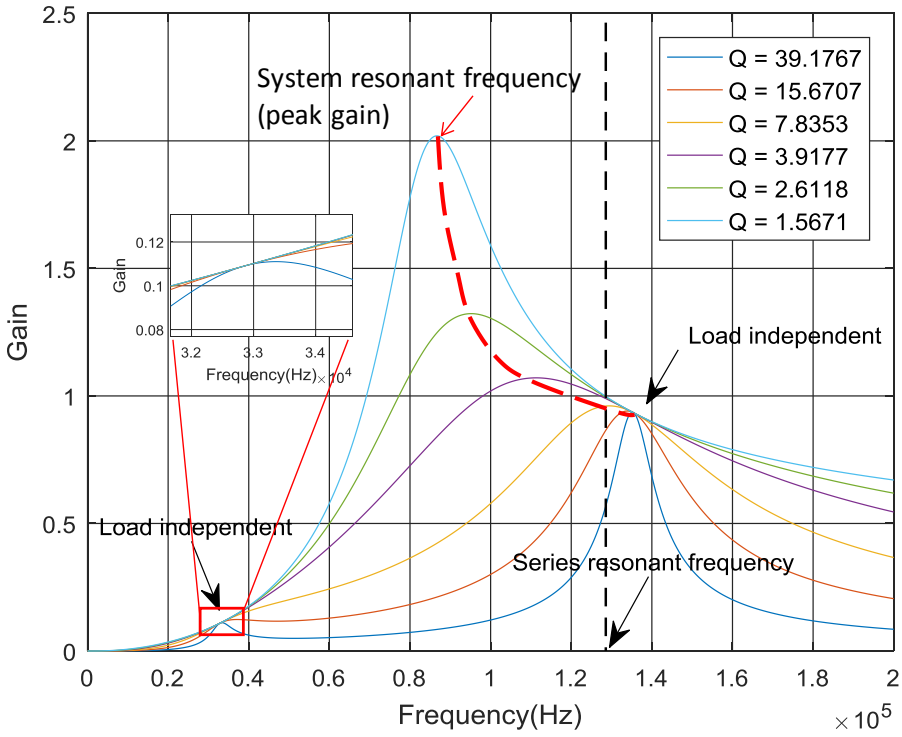

Fig. 3-8 Voltage gain characteristics of CLLC resonant converter in the forward mode

As shown in the figure, for a given load condition, the maximum voltage gain is reached at the system resonant frequency. As the load (represented with Q in the figure) increases, the system resonant frequency increases while the peak gain decreases. The DC gain characteristics is discussed as follows:

(1) The system resonant frequency varies at different load conditions and the resonant tanks. At lighter load, the peak gain is higher and the resonant tank behaves like a parallel resonant converter; while when the load becomes heavier, the peak gain decreases and the resonant tank exhibits series resonant converter characteristics.

(2) While the converter is operating at switching frequency greater than the system resonant frequency under a given load condition, the resonant tank acts like a series resonant converter in both high loads and light loads and exhibits inductive feature with negative gain slope. Consequently ZVS is achieved in the converter [81]. In contrast, in the regions with the switching frequency lower than the system resonant frequency, capacitive feature of the resonant tank results in ZCS

condition which should be avoided because it incurs high switching losses, as explained in Section 2.2. This feature has no difference with the LLC resonant converter. Since the system resonant point varies with load conditions, the ZVS region also changes with loads.

(3) The LLC resonant converter has unity gain at the series resonant frequency and the voltage across L_s cancels the voltage across L_m thus all the input voltage will drop to the load [125]. However, in the CLLC, although the series resonant frequency f_{sr} is fixed when the resonant tank is designed, the unity gain point varies with load conditions because the secondary side capacitor C_{s2} participates in the resonance.

(4) When the converter is operating at or close to the load independent point, the switching frequency does not need to be regulated in such a wide range when the load changes. Thus it is preferred for the application with varying battery voltages. The CLLC resonant converter has two load independent points. Based on the converter gain equation, the load independent frequency can be derived by setting the coefficient of Q in Equation (3-8) equal to zero, as shown in Equation (3-9). Thus the two load independent frequency f_{in_1} and f_{in_1} are obtained and shown in Equations (3-10) and (3-11), which are also displayed in Fig. 3-8. It is obvious that the load independent point where the frequency is lower than the system resonant frequencies with lower gain is of little practical use, due to large volumes/size of the magnetic components at lower frequency.

$$B = \frac{Q}{f_n}\left(1 - f_n^2 + \frac{k+1}{g} - \frac{k}{g \cdot f_n^2}\right) = 0 \tag{3-9}$$

$$f_{in\_1} = \frac{f_{sr}}{\sqrt{2}} \cdot \sqrt{\left(1 + \frac{k}{g} + \frac{1}{g}\right) - \sqrt{\left(1 + \frac{k}{g} + \frac{1}{g}\right)^2 - 4\frac{k}{g}}} \tag{3-10}$$

$$f_{in\_2} = \frac{f_{sr}}{\sqrt{2}} \cdot \sqrt{\left(1 + \frac{k}{g} + \frac{1}{g}\right) + \sqrt{\left(1 + \frac{k}{g} + \frac{1}{g}\right)^2 - 4\frac{k}{g}}} \tag{3-11}$$

3.3.2 Reverse mode

The equivalent circuit of the CLLC resonant converter in reverse mode using FHA method is shown in Fig. 3-9. V'_{in}, and V'_{out} are the RMS values of the fundamental

component of the input and output voltages of the resonant tank, respectively. L'_s, C'_s, L'_m and R'_{oe} represent the equivalent L_s, C_s, L_m and R_{oe} respectively referred to the transformer secondary side from the transformer primary side.

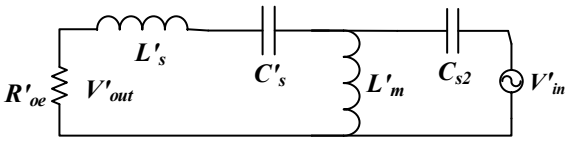

Fig. 3-9 Equivalent circuit of CLLC resonant converter in the reverse mode

$$L'_s = \frac{L_s}{N^2} \tag{3-12}$$

$$C'_s = N^2 \cdot C_s \tag{3-13}$$

$$L'_m = \frac{L_m}{N^2} \tag{3-14}$$

$$R'_{oe} = \frac{1}{N^2} \cdot \frac{8}{\pi^2} \frac{V_{in}^2}{P_{in}} \tag{3-15}$$

The voltage conversion gain in the reverse mode is similarly derived and given in Equations (3-16) - (3-19). The gain variations with load and frequency are plotted in Fig. 3-10.

$$|G(s)|, reverse = \frac{1}{\sqrt{C^2 + D^2}} \tag{3-16}$$

$$C = \frac{f_n^2 - k}{f_n^2} \tag{3-17}$$

$$D = \frac{Q}{f_n}(1 - f_n^2 + k + g - \frac{g \cdot k}{f_n}) \tag{3-18}$$

$$\omega_{sr} = 2\pi f_{sr} = \frac{1}{\sqrt{(L_s \cdot C_s)}}, f_n = \frac{f_s}{f_{sr}}$$
$$Q = \frac{Z_r}{R'_{o,e}}, \ Z_r = \sqrt{\frac{L_s}{C_s}}, \ k = \frac{L_s}{L_m}, g = \frac{C'_{s2}}{C_s} \tag{3-19}$$

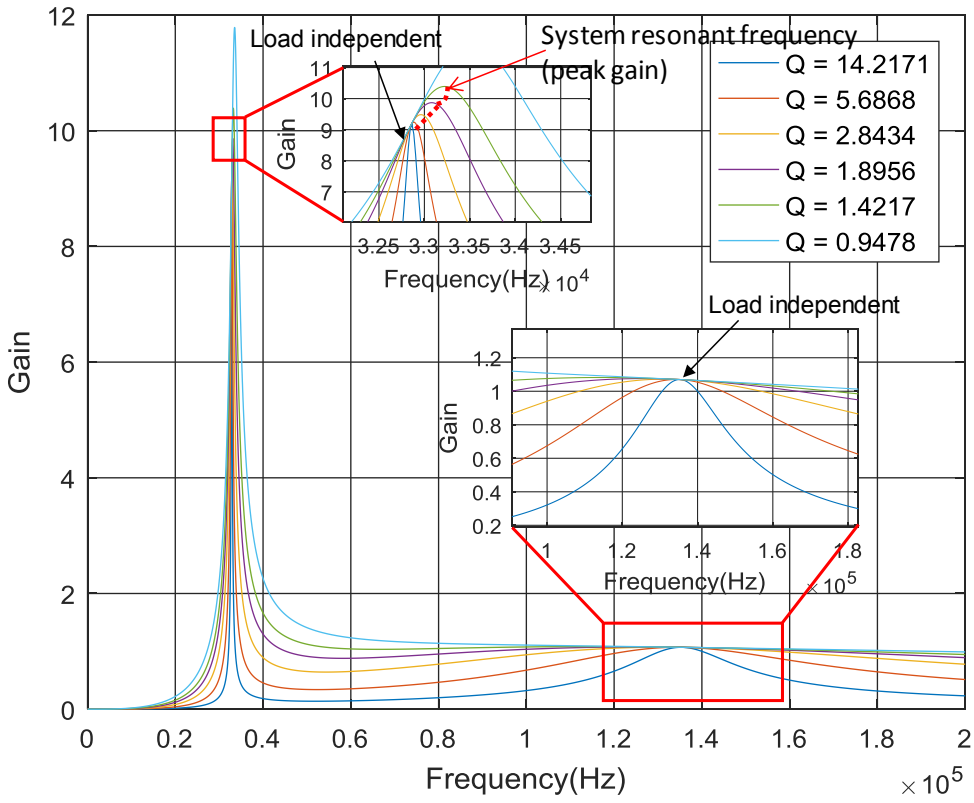

Fig. 3-10 Voltage gain characteristics of the CLLC resonant converter in the reverse mode

As shown in the figure, in the reverse mode, similar characteristics to the forward mode are exhibited in the CLLC resonant converter. Overall, for a given load condition, the peak gain occurs at the system resonant frequency. As the load (represented by Q in the figure) increases, the system resonant frequency increases and the peak gain also increases. The detailed characteristics can be summarized as follows:

(1) Similar to the characteristics in the forward mode, the peak gains correspond to the system resonance and they vary with load conditions. At heavy load, the peak gain is lower and it behaves like a series resonant converter; while when the load becomes lighter, the peak gain increases and the resonant tank exhibits parallel resonant converter characteristics. This feature is similar to series-parallel resonant converter (SPRC or LCC) analysed in [126] and the gain curve mirrors that of the LLC resonant converter in the forward mode.

(2) When the converter operating frequency goes greater than system resonant frequency under a given load condition, the resonant tank acts like a series resonant converter in both high loads and light loads and exhibits inductive feature with negative gain slope. Consequently ZVS is achieved in the converter [81]. In

contrast, in the regions with the switching frequency lower than the system resonant frequency, capacitive feature of the resonant tank results in ZCS condition which should be avoided because it incurs high switching losses. Since the system resonant point varies with load conditions, the ZVS region also changes with load conditions.

(3) Similar to the forward mode, two load independent points are observed in the reverse mode in Fig. 3-10. The load independent frequency can be derived by Equation (3-19) and Equation (3-20), thus the two load independent frequency f_{in_3} and f_{in_4} are obtained and shown in Equation (3-20) and Equation (3-21), where the function components A and B are shown in Equation (3-23) and Equation (3-24), respectively. It is obvious that the load independent point where the frequency is lower than the system resonant frequencies is of little practical use due to the ZCS operation, despite of the large gains.

$$D = \frac{Q}{f_n}\left(1 - f_n^2 + k + g - \frac{g \cdot k}{f_n}\right) = 0 \tag{3-20}$$

$$f_{in\_3} = \sqrt[3]{A + B} + \sqrt[3]{A - B} \tag{3-21}$$

$$f_{in\_4} = \left(-\frac{1}{2} - \frac{\sqrt{3}}{2}i\right) \cdot \sqrt[3]{A - B} + \left(-\frac{1}{2} + \frac{\sqrt{3}}{2}i\right) \cdot \sqrt[3]{A + B} \tag{3-22}$$

$$A = -\frac{gk}{2} \tag{3-23}$$

$$B = \sqrt{\frac{g^2 \cdot k^2}{4} - \frac{1}{27}(1 + k + g)^3} \tag{3-24}$$

The analysis of the DC gain characteristics in both the forward mode and reverse modes is essential for designing the CLLC resonant converter. From the above discussion, the conclusion is that although different features exist, the similarity of the gain characteristics in the two modes are obvious. This implies that the converter can be operated in similar conditions in both V2G and G2V modes, with a carefully designed resonant tank.

3.4 Design Procedure of CLLC

The four-elements resonant tank in the CLLC resonant converter can be designed with different methods described in [89, 127]. Due to the wide output battery voltage ranges in the bidirectional charger applications, the design processes proposed in the references are complex to be applied.

Due to the complexity in optimization with the four resonant elements together, in the design described below, the CLLC resonant tank is treated as an extra capacitor being added on the conventional three-element LLC resonant tank. Thus the CLLC resonant tank can be designed in two stages. As the design methods of LLC resonant converter have been widely analysed and extensively presented [70, 128-135], it is convenient to first design the LLC resonant tank according to the output voltage range, soft switching requirement and power rating and then sizing the secondary side capacitor based on gain analysis and system constraints. This method has the advantage of alleviating the difficulties of designing the four-element resonant tank.

The design of CLLC resonant tank in this chapter is based on the LLC resonant tank discussed in Chapter 2. Thus the only design problem is the sizing of a series capacitor C_{s2} in the secondary side. A proper value of C_{s2} should be chosen such that the voltage gain curves in the forward and reverse modes are alike both in the shape and amplitude, while meeting the resonant gain requirement, ZVS operation requirement, load independent requirement and power factor requirement.

In this study, a CLLC resonant converter is designed on the base of the LLC resonant circuit described in Chapter 2. The DC-DC converter specifications and the designed LLC resonant tank parameters are shown in Table 3-3. The design procedure involves the following steps as shown in Fig. 3-11.

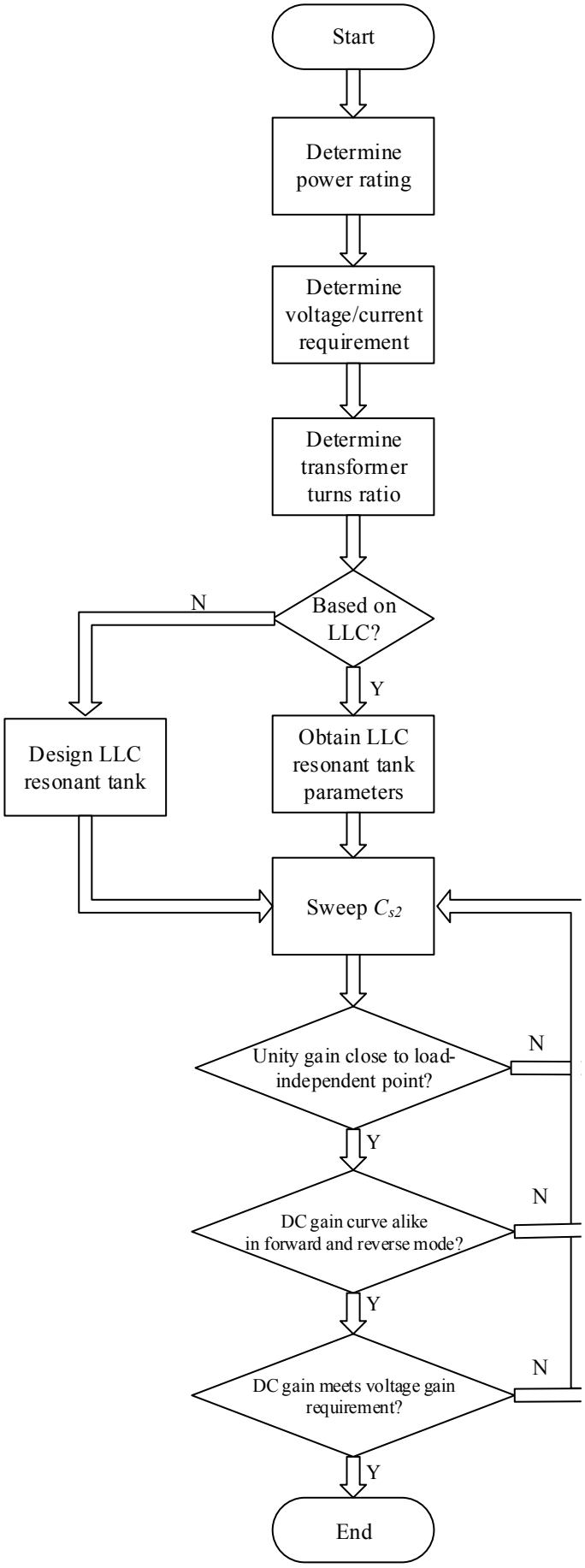

Fig. 3-11 Design procedure of CLLC resonant tank

Table 3-3 The DC-DC converter requirement specification

Parameters	Symbol	Value	Unit
Input DC link voltage	V_{dc}	380	V
Input power rating	P_{in}	4.0	kW
Battery charging current	I_{bat}	9.0	A
Minimum efficiency requirement	η	90	%
Switching frequency range	f_{sw}	100-200	kHz
Battery fully charged voltage	V_{max}	403.2	V
Battery initial voltage	V_{min}	240	V
Series inductor	L_s	97.0	µH
Parallel/magnetic inductor	L_m	136.5	µH
Primary side series capacitor	C_s	15.8	nF

(1) Design of the resonant tank starts with the system power rating and input/output requirement. The transformer turns ratio is determined with the input voltage V_{in} with a reasonable line voltage variation e and the minimum output voltage V_{out_min}.

$$N = \frac{V_{in} \cdot (1+e)}{V_{out\_min}} \tag{3-25}$$

(2) The gain requirement is determined by satisfying the min and max values given in Equations (3-26) and (3-27).

$$M_{min} = \frac{V_{out\_min} \cdot N}{V_{in}} \tag{3-26}$$

$$M_{max} = \frac{V_{out\_max} \cdot N}{V_{in}} \tag{3-27}$$

The battery voltages vary from 240 V to 403.2 V, and the voltage across the DC link (input of the DC-DC converter) is constant 380V, thus the DC gain range can be calculated as [1.04, 1.67] in the forward mode and [0.71, 0.95] in the reverse mode.

(3) The typical operating switching frequency region can be determined by the switching devices characteristics and the passive components requirement. A higher switching frequency benefits the resonant converter with smaller size of the passive components and lower resonant capacitors voltage stress [127]. However, higher switching frequency causes higher losses in the switching devices. For a DC-DC converter that employs high-frequency MOSFET devices, the operating frequency is usually chosen between 100 to 150 kHz, because the

EMI testing starts at 150 kHz [136-139]. The switching frequency used for design should be the series resonant frequency because the most of the fundamental energy is transferred in this frequency and thus makes it the most efficient point [140]. In this design, 130 kHz is used as the initial value of the series resonant frequency. This value will need adjustment during the design since it is related to the magnetic inductance design.

(4) If the CLLC design is based on an existed LLC resonant converter, the LLC resonant tank parameters can be obtained easily. Otherwise this step involves the building of a high-performance LLC resonant tank firstly. The procedure of designing a LLC resonant tank, as shown in Fig. 3-12, has been extensively described and presented in literature [70, 128-135] thus will not be detailed here, but will be summarized in four steps:

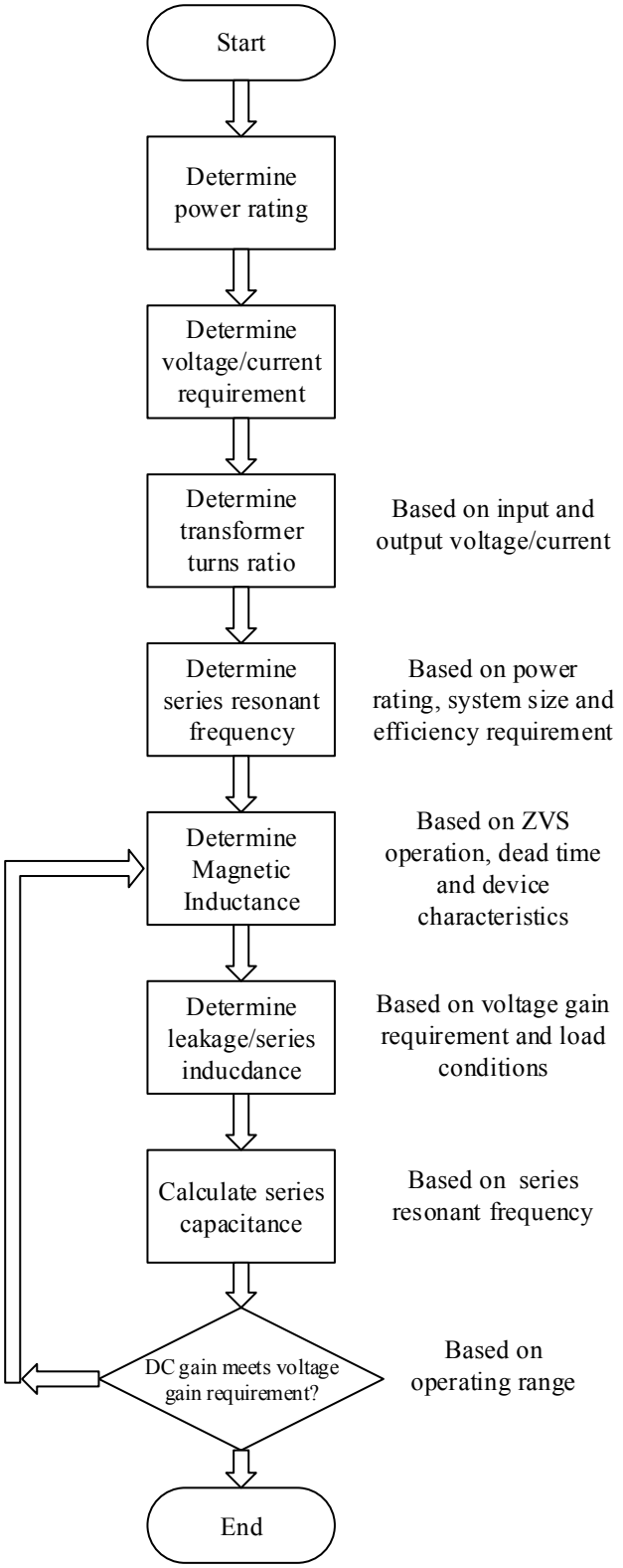

Fig. 3-12 Typical design procedure of LLC resonant converter

a) determine the magnetic inductance L_m based on the ZVS operation requirement, dead time t_{dead}, device dynamic characteristics and the MOSFET output capacitance C_{oss}.

$$L_m \leq \frac{t_{dead}}{16 \cdot f_{sr} C_{oss}} \tag{3-28}$$

b) determine the series inductance L_s based on Equation (3-29). A smaller value of L_n (small L_m) results in a larger voltage gain across a narrow frequency range. However, this leads to a smaller input impedance and thus increased circulating current resulting larger power losses. A large value of L_n will reduce the power losses, but the operating frequency needs to be adjusted in a wider region to meet the gain requirement. Thus there is a trade-off to tune L_n.

$$L_n = \frac{L_m}{L_s} \tag{3-29}$$

c) calculate the series capacitance according to the series resonant frequency. In this design, the series resonant frequency of the designed LLC resonant tank is 128 kHz.

$$f_{sr} = \frac{1}{2\pi\sqrt{L_s \cdot C_s}} \tag{3-30}$$

d) check whether the DC gain region meets the required maximum and minimum gain, if not, return to step a) and adjust the magnetic inductance L_m.

(5) With the designed LLC resonant tank, an extra series capacitor will be added in the secondary side. The selection is constrained with four factors: the series resonant frequency, the load independent point, capacitor size and the gain requirement.

a) In the 4-element CLLC resonant tank, load independent point does not equal to the series resonant frequency point. In order to ensure that the system can be operated in a wide input/output voltage varying range while regulating the switching frequency in a narrower range, C_{s2} can be selected carefully to make the load-independent point close to the series resonant frequency, which is usually the most efficient point [140]. A new factor L_d is defined as the ratio of the frequency at load independent point to the series resonant frequency as shown in Equation (3-31).

$$L_d = \frac{f_{load-independent}}{f_{sr}} \tag{3-31}$$

The variation of the load-independent point at nominal load condition versus C_{s2} is shown in Fig. 3-13. It can be observed that with increasing C_{s2}, the frequency of the load-independent point decreases, approaching the series resonant frequency. In addition, from the FHA analysis, larger C_{s2} leads to smaller magnetizing current which corresponds to smaller circulating current and reduced conduction losses. This implies that a larger C_{s2} is preferred.

To be specific in this design, when the value of C_{s2} increases from 50 nF to 500 nF, L_d decreases from 1.48 to 1.05 in the forward mode and from 1.56 to 1.07 in the reverse mode. Since the design switching range is 100 kHz to 150 kHz, to meet this maximum switching frequency, as shown in the curve, C_{s2} must be larger than 160 nF which sets the lower limit of L_d. Further increase of C_{s2} beyond 500 nf will not make a big change but only increase the size and cost, since the slope becomes flat after this region as shown in Fig. 3-13. Thus 1.05 and 1.07 can be set to be the high limit of L_d in the G2V forward mode and the V2G reverse mode, respectively.

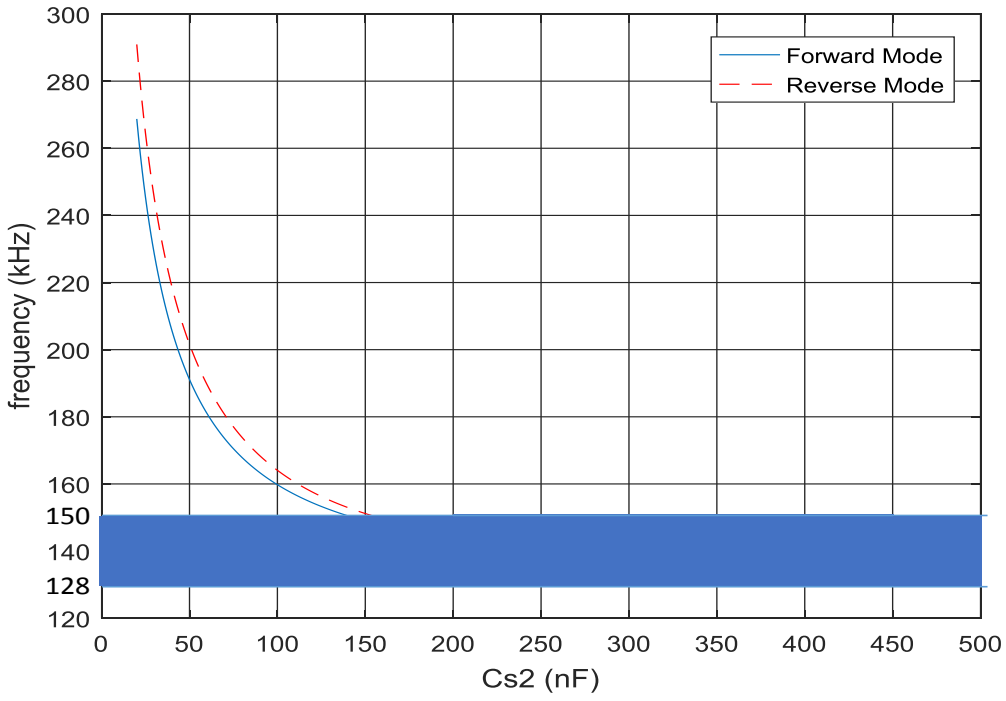

Fig. 3-13 Load independent points with sweeping of Cs2

b) Within this region, C_{s2} must be selected to satisfy both the required maximum and minimum gains in order to cope with the wide voltage variation of the battery pack, thus the value of the capacitance is restrained by the system gain requirement. Fig. 3-14 illustrates the gain at the heaviest load condition. In the forward mode, gain increases with the increase of C_{s2}, thus the peak gain must be above the minimum gain requirement, as shown with dash line in the figure. To be specific in this design, 250 nF is the minimum value for selecting of C_{s2}.

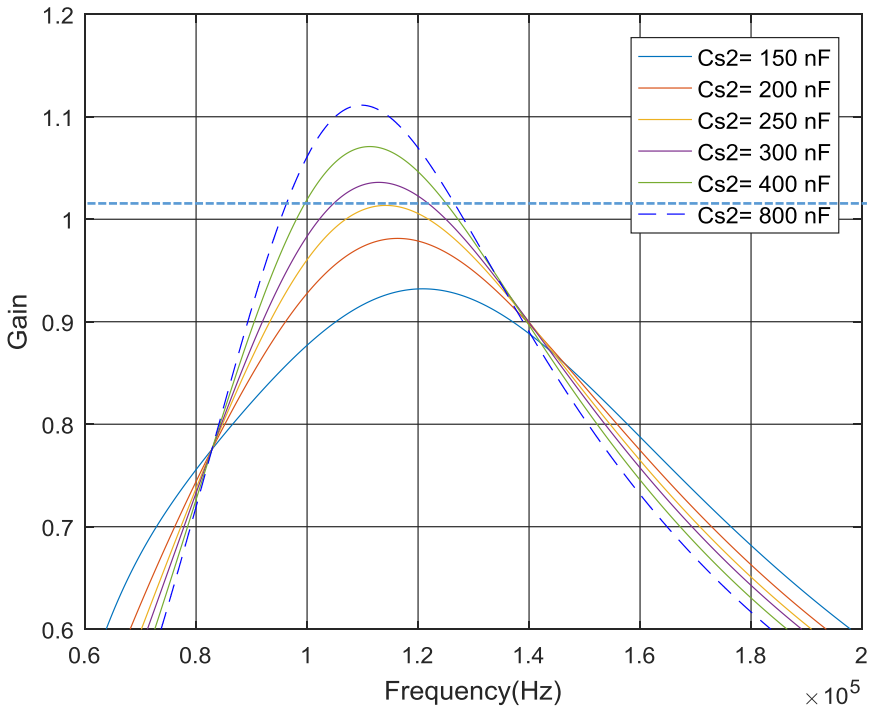

(a)

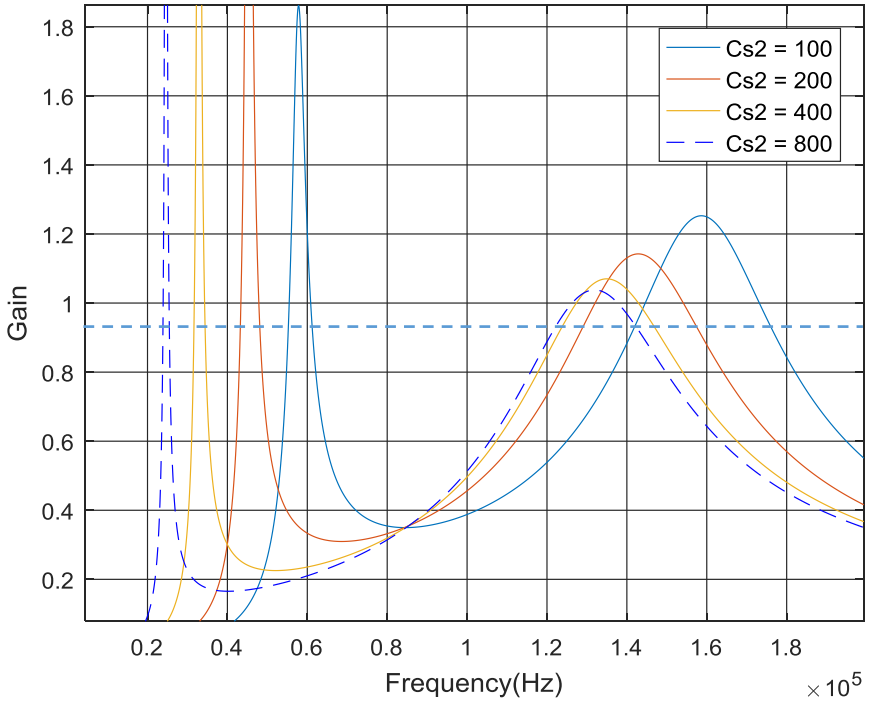

(b)

Fig. 3-14 Gain with sweeping Cs2 in (a) the forward mode and (b) the reverse mode

In reverse mode, the gain decrease when C_{s2} increases, therefore the gain must meet the maximum requirement. In this design, since the gain requirement in reverse mode is [0.71, 0.95], which can be met by most of the C_{s2} as shown in Fig. 3-14 (b). However, for the applications where require a wide variety of gain, C_{s2} need to be tuned carefully.

c) Finally, within this constraint range, C_{s2} should be further adjusted. A proper selection of C_{s2} depends on how similar the gain characteristics in the forward mode and the reverse mode, in terms of both the magnitude and shape.

(6) With the resultant 4-element CLLC resonant tank, the voltage gain should be checked whether it can meet the system requirement in both forward and reverse modes and cover both the required maximum and minimum gains in different load conditions to manage the wide variation of the battery voltage. If not, go back to C_{s2} design and tune it again.

In this design, after tuning the capacitance and comparing the gain curve features in the forward and reverse modes, C_{s2} is designed to be 427 *nF*. The gain curve with this parameter are shown in Fig. 3-15. As can be observed, the gain requirement is satisfied

in both the forward and reverse modes. The load independent point is around 130 kHz, with L_n around 1.05, which verified the design.

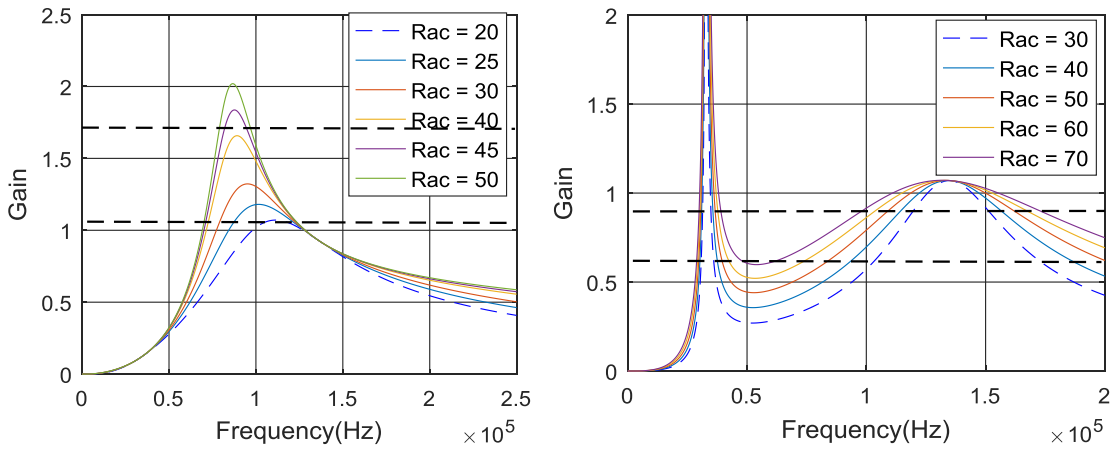

(a) (b)

Fig. 3-15 Gain curve with the designed parameters in (a) forward mode and (b) reverse mode

It should be noted that although this method has the advantage of alleviating the difficulties of optimizing the four elements resonant tank, this is not the fully optimized design. Firstly, the gain bound is limited because the gain range is already determined by the LLC resonant tank. Secondly, the magnetizing inductor, usually integrated in the transformer, cannot be changed to further reduce the magnetizing current for efficiency improvement. This design method is more suitable with an existed LLC resonant converter while requiring the conversion efficiency improvement.

3.5 Time-domain Simulation

The performance of the designed converter is assessed by extensive simulations over the wide operating range of the battery voltages and loads with a battery charging system based on the designed CLLC resonant converter with the specification shown in Table 3-4.

Table 3-4 The designed CLLC resonant converter specification

Parameters	Symbol	Value	Unit
Series inductor	L_s	97.0	μH
Parallel inductor	L_m	136.5	μH
Primary series capacitor	C_s	15.8	nF
Secondary series capacitor	C_{s2}	427	nF
Output filter capacitor	C_f	330	μF
DC link voltage	V_{dc}	380	V
Battery charging current	I_{bat}	9.0	A

Parameters	Symbol	Value	Unit
Battery internal resister	R_{bat}	0.1148	Ω
Battery rated capacity	$A \cdot h$	66.2	Ah
Battery fully charged voltage	V_{max}	403.2	V
Battery initial voltage	V_{min}	240	V

Simulation waveforms with fixed 380V DC link voltage, 9A battery charging current, 240V battery voltage at 100 kHz switching frequency in the forward mode are displayed in Fig. 3-16. It is clear that, the simulated series inductor current, magnetic inductor current and the diode current waveforms match the theoretical waveforms illustrated in Section 3.2.2, which verifies the accuracy of the simulated model.

More time-domain simulations have been performed and the simulation results will be used for power loss analysis in Section 3.6, while the simulation waveforms presented in Section 3.7 for comparison of simulation and test results.

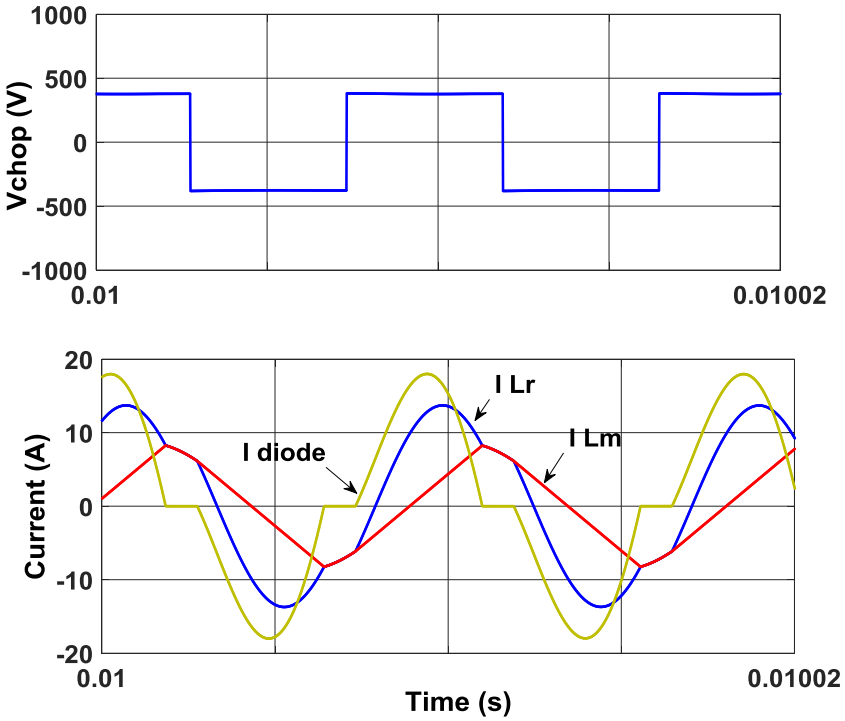

Fig. 3-16 Waveforms of the CLLC resonant converter at constant 380V DC link voltage in the time-domain model simulation in the forward mode

3.6 Power Loss Prediction

For evaluating the efficiency of the designed CLLC resonant converter, it is essential to characterize and quantify the power losses in the converter. A practical method for calculating the power loss in the converter is described in this section. It should be noticed that, although the RMS current and voltage are evaluated from the time-domain simulation, for the sake of accurate calculation, the specific parameters of the switching devices are updated with the experimental test prototype described in Section 3.7.

3.6.1 Power loss distribution in a DC-DC converter

In a DC-DC converter, the losses usually can be divided into semiconductor loss and magnetic loss [141-143]. Semiconductor loss includes the switching loss and the conduction loss in power devices [144]. Magnetic loss contains the core losses (iron loss) in the ferrite cores and the copper loss (winding loss) in the coil of the inductor and transformer [67].

(1) Device conduction losses

The conduction losses are caused by the current flowing through the on-state resistance of the switching device. The conduction loss in a MOSFET device and a rectifier diode can be estimated by:

$$P_{con\_MOS} = \frac{1}{T_{sw}} \int_0^{Tsw} R_{DS} \cdot i_D^2(t)dt = R_{DS} \cdot I_{D\_rms}^2 \tag{3-32}$$

$$\begin{aligned} P_{con\_D} &= \frac{1}{T_{sw}} \int_0^{Tsw} (u_{D0} \cdot i_F(t) + R_D \cdot i_F^2(t))dt \\ &= u_{D0} \cdot I_{F\_av} + R_D \cdot I_{F\_rms}^2 \end{aligned} \tag{3-33}$$

where T_{sw} is the switching period in one cycle, R_{DS} and R_D is the MOSFET drain-source on-state resister and diode on-state resistance, respectively, u_{D0} is the diode on-state zero-current voltage, I_{D_RMS}, I_{F_av}, and I_{F_rms} represent the RMS value of the MOSFET on-state current, averaged diode current and the RMS of the diode current, respectively. In the designed resonant converter, the switching device used in the bridges are ROHM SCH2080KE N-channel SiC power MOSFET. The rectifier diodes are the internal diode of the MOSFET. The parameter characteristics are shown in Table 3-4 below:

Table 3-4 Electrical characteristics of the MOSFET in datasheet

Parameter	Symbol	Value	Unit
Drain-source on-state resister	R_{DS}	80	mΩ
Diode on-state resistance	R_D	65	mΩ
Diode on-state zero-current voltage	u_{D0}	1.3	V

(2) Device switching losses

The switching loss is caused by the energy loss during the transient behavior of the switches. The losses during switching-on and switching-off in the MOSFET and diode are estimated by:

$$P_{sw\_MOS} = (E_{sw\_on\_MOS} + E_{sw\_off\_MOS}) \cdot f_{sw} \tag{3-34}$$

$$P_{sw\_D} = (E_{sw\_on\_D} + E_{sw\_off\_D}) \cdot f_{sw} \tag{3-35}$$

where f_{sw} is the switching frequency. $E_{sw\_on\_MOS}$, $E_{sw\_off\_MOS}$, $E_{sw\_on\_D}$, and $E_{sw\_off\_D}$ is the energy loss of MOSFET and diode when turning on and off, respectively, and can be calculated by:

$$\begin{aligned} E_{sw\_on\_MOS} &= \int_0^{tri+tfu} u_{DS}(t) \cdot i_D(t)dt \\ &= U_{DD} \cdot I_{Don} \cdot \frac{tri + tfu}{2} + Q_{rr} \cdot U_{DD} \end{aligned} \tag{3-36}$$

$$\begin{aligned} E_{sw\_off\_MOS} &= \int_0^{tru+tfi} u_{DS}(t) \cdot i_D(t)dt \\ &= U_{DD} \cdot I_{Doff} \cdot \frac{tru + tfi}{2} \end{aligned} \tag{3-37}$$

$$E_{sw\_on\_D} = \int_0^{tri+tfu} u_D(t) \cdot i_F(t)dt \approx E_{rr\_D} = \frac{1}{4} Q_{rr} \cdot U_{Drr} \tag{3-38}$$

$$E_{sw\_off\_D} \approx 0 \tag{3-39}$$

where U_{DD} is the chopped voltage in the input side, I_{Don} and I_{Doff} is the MOSFET turning on current and turning off current respectively. E_{rrD} is the energy loss of the diode during reverse recovery operation, U_{Drr} is the diode reverse recovery voltage, Q_{rr} is the charge during the reverse recovery of the diode. Since in the resonant converter the MOSFET is always operating at ZVS operation, the turning on loss $E_{sw\_on\_MOS}$ =0. *tri* and *tfi* is the current rising time and current falling time during the switching period, respectively, and can be read from MOSFET datasheet. MOSFET voltage falling time and voltage rising time, denoted by *tfu, tru,* cannot be read from the datasheet directly, but can be obtained by:

$$tfu = (U_{DD} - R_{DSon} \cdot I_{Don}) \cdot R_G \cdot \frac{C_{GD}}{U_{Dr} - U_{plateau}} \quad (3\text{-}40)$$

$$tru = (R_{DSon} \cdot I_{Doff} - U_{DD}) \cdot R_G \cdot \frac{C_{GD}}{U_{plateau}} \quad (3\text{-}41)$$

where R_G is the gate resistor, U_{Dr} is the voltage from driving circuit, $V_{plateau}$ is the gate plateau voltage. C_{GD} is the MOSFET gate-drain capacitance obtained from the datasheet as displayed in Fig. 3-17 (a). For the purpose of reasonable accuracy in the calculation of the *tfu* and *tru*, the non-linearity of C_{GD} should be taken into consideration. The polynomial function of C_{GD} against the drain—source voltage can be shown in Fig. 3-18 (b) and the function is shown as:

$$C_{GD} = 4319 \cdot e^{(-1.39V_{DS})} + 182 \cdot e^{(-0.02V_{DS})} \quad (3\text{-}42)$$

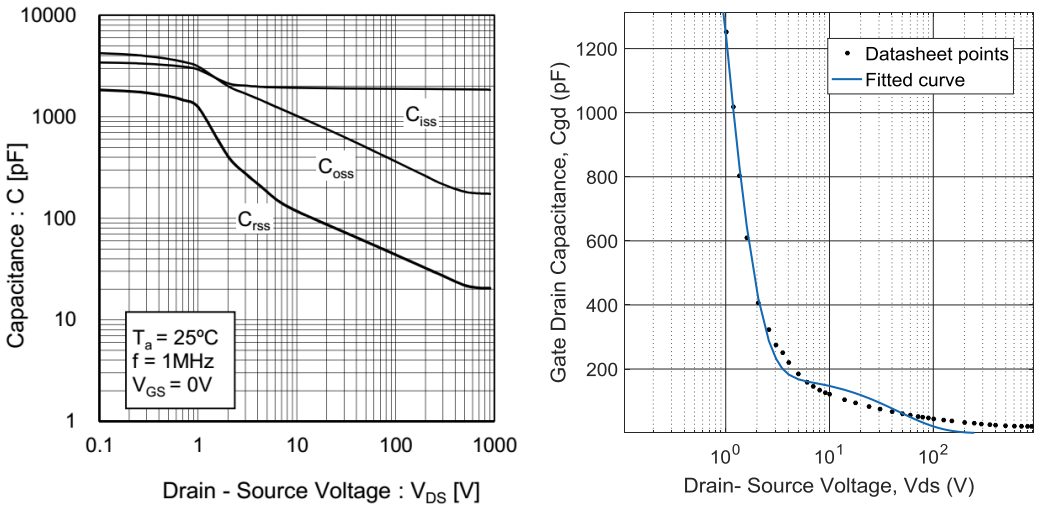

(a) (b)

Fig. 3-17 Gate-Drain Capacitance of the MOSFET (a) in datasheet, (b) fitting curve

Other parameters are determined by the system requirement and the ROHM SCH2080KE N-channel SiC power MOSFET datasheet, as shown in Table 3-5:

Table 3-5 The SiC MOSFET data at series resonant frequency

Parameter	Symbol	Value	Unit
Switching frequency	f_{sw}	134	kHz
Input voltage	U_{DD}	380	V
Diode reverse-recovery charge	Q_{rr}	60	nC
Current rising time	*tri*	33	ns
Current falling time	*tfi*	28	ns
Gate resistor	R_G	6.3	Ω
Driving voltage	U_{Dr}	12	V
Gate plateau voltage	$V_{plateau}$	9.7	V

(3) Ferrite core loss

The core loss in the magnetic components includes the hysteresis losses, which is associated with the magnetic domain align friction during the changing of the external magnetic field, and the eddy loss caused by eddy current induced perpendicular to the flux direction which has the potential to avoid the flux to penetrating into the core. Total core loss in the ferrite is related to the core material characteristics, and can be estimated with Steinmetz Equation, depending on frequency, flux density and temperature.

The core material used in this design is from FERROXCUBE, and the core loss with sweeping the flux density at different frequencies can be read in the datasheet as shown in Fig. 3-18. This implies that the core losses can be predicted by the peak flux density which is obtained by Equation (3-43).

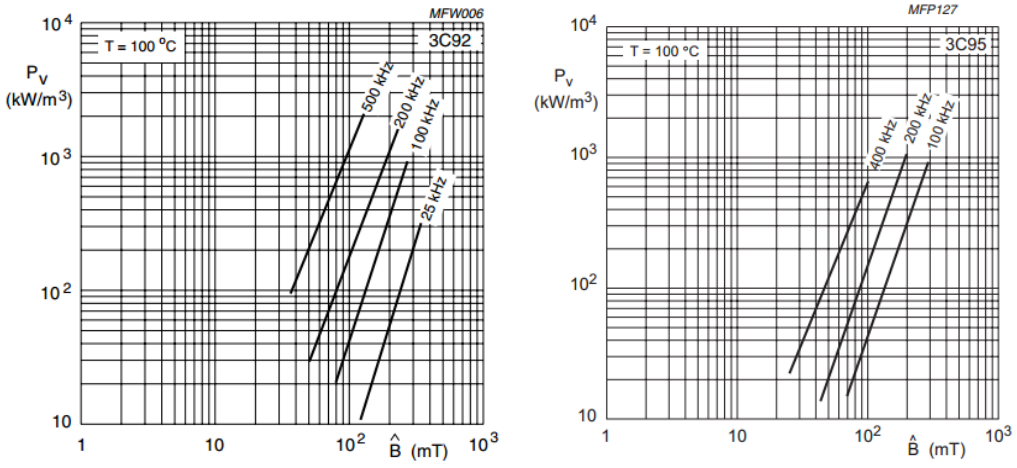

(a) (b)

Fig. 3-18 specific power loss estimation as a function of peak flux density at varying frequencies of (a) 3C92 material, (b) 3C95 material

$$\hat{B} = \frac{L \cdot I_{pk}}{A_{core} \cdot N} \tag{3-43}$$

where L and I_{pk} represent the inductance value and the peak current of the inductor, respectively. A_{core} is the effective crossing section area, and N is the turns number of the winding coil. The details of the inductor with the ferrite material are shown in Table 3-6 and the transformer is listed in Table 3-7 below:

Table 3-6 The material specific of 3c95 for the inductor

Parameters	Symbol	Value	Unit
Series inductor	L_s	97.0	μH
Core area	$A_{core,\ E65}$	540	mm^2
Volume	V_e	79000	mm^3
Number of turn	N_{Ls}	24	N/A
Number of coil layer	N_c	4	N/A

Table 3-7 The material specific of 3c92 in transformer

Parameters	Symbol	Value	Unit
Magnetizing inductor	L_m	136.5	μH
Core area	$A_{core,\ ETD59}$	363	mm^2
Volume	V_e	44000	mm^3
Number of turn in primary side	N_{Lm}	15	N/A
Number of turn in secondary side	NLm'	9	N/A

(4) Magnetic loss - copper loss

Copper loss is related to the current flowing in the copper wire of the magnetic components. Copper losses in the inductor and transformers can be calculated by:

$$P_{copper\_L} = (R_{ac\_L} + R_{dc\_L}) \cdot I_{Ls\_rms}^2 \tag{3-44}$$

$$P_{copper\_Tx} = (R_{ac_{pri}} + R_{dc_{pri}}) \cdot I_{pri\_rms}^2 + (R_{ac_{sec}} + R_{dc_{sec}}) \cdot I_{sec\_rms}^2 \tag{3-45}$$

where the RMS current through the series inductor (I_{Ls_rms}), primary side (I_{pri_rms}) and secondary side of transformer (I_{sec_rms}) can be measured in simulation/test or calculated in the theoretical circuit. In this design, the ac resistance at certain switching frequency can be measured with a LCR meter, as shown in Table 3-8 below. It should be noticed that the measurement of the ac resistance is implemented with the core, thus the ac resistance actually includes the core loss, and the resultant ac resistance is higher than the actual value.

Table 3-8 Specific of inductor and transformer at 130 kHz

Parameters	Symbol	Value	Unit
Inductor dc resistance	$R_{ac,L}$	11.45	mΩ
Inductor ac resistance	$R_{dc,L}$	138.79	mΩ
Primary side dc resistance	$R_{dc,\ pri}$	4.80	mΩ
Primary side ac resistance	$R_{ac,pri}$	346.12	mΩ
Secondary side dc resistance	$R_{dc,pri}$	3.80	mΩ
Secondary side ac resistance	$R_{ac,pri}$	99.9	mΩ

3.6.2 Power loss prediction with simulated voltage and current waveforms

The previous section indicates that, the parameters of switching devices and magnetic components are fixed with a certain converter prototype, and the power loss is related to the current and voltage in converter operation. To be specific, the device conduction losses are dependent on the MOSFET on-state RMS current (I_{D_RMS}), diode average current (I_{F_av}) and the diode RMS current (I_{F_rms}). The switching losses are functions of the switching-on current (I_{Don}) and switching-off current (I_{Doff}) in the MOSFET. The core loss is affected by the peak current through the inductor and transformer. RMS current through the series inductor (I_{Ls_rms}), primary side (I_{pri_rms}) and secondary side of transformer (I_{sec_rms}) determine the copper losses in the inductor and transformer.

This implies the power loss can be predicted and analysed with the converter currents and voltages at different operating conditions. Although first harmonic analysis can be utilized for loss prediction, it is expected to have significant errors specially in calculation of the switching-on current and the switching-off currents. Moreover, the switching-on and the switching-off currents also depend on the interaction of Cds with the resonant tank which is not easily modelled in FHA. Therefore, for purpose of loss estimation time domain simulation is utilized.

3.6.2.1 Power Loss Prediction in the forward mode

In the forward mode, simulation was performed at five different load conditions with constant 380V DC link voltage. The resultant current and voltages are shown in

Table 3-9 and Table 3-10 for CLLC and LLC converters, respectively, for the purpose of comparison.

Table 3-9 The simulation results of CLLC at different conditions in forward mode

Parameters	Symbol	Value	Value	Value	Value	Value	Unit
Switching frequency	f_{sw}	122.15	111.98	106	100.7	98.9	kHz
DC link voltage	V_{DC}	379.2342	379.0624	378.9140	378.7394	378.6963	V
DC link current	I_{DC}	6.0276	7.3741	8.5492	9.9240	10.2617	A
Battery voltage	V_{bat}	241.7154	289.2567	332.3322	381.0006	412.6826	V
Battery current	I_{bat}	9.0632	9.2800	9.3438	9.2147	8.9789	A
Primary current	$I_{Ls,\ rms}$	7.3665	8.6849	9.8373	11.1266	11.4728	A
Secondary current	$I_{sec,\ rms}$	10.6923	11.5897	12.1611	12.7185	12.3837	A
MOSFET turn off current	I_{off}	5.00	4.985	4.90	3.831	3.669	A
MOSFET peak current	$I_{pk,\ M}$	10.66	12.83	14.71	16.86	17.28	A
Diode peak current	$I_{pk,\ D}$	16.22	18.57	20.3	22	21.77	A

As detailed in

Table 3-9, the DC link voltage is kept at 380V. The battery voltage increases from 240V to 400V for delivering power from 2 kW to 4kW, in order to attain rated charging current (9 A), the switching frequency decreases from 122.15 kHz to 98.9 kHz for higher resonant gain, as explained previously. As a consequence, with the delivered power increasing, the DC link current I_{DC}, primary side resonant current I_{Ls} and secondary side resonant current I_{sec} increase correspondingly. However, the MOSFET turns off (I_{off}) current decrease especially in higher power ratings. This is because under higher power conditions, the operating frequency is below the resonant frequency, resulting in DCM operation, during which the current through the transformer drops to zero. This trend will be illustrated in the waveforms in next section.

Table 3-10 shows the simulation results from the LLC resonant converter at a constant DC link voltage (380V) are s. As can be seen, the simulation condition is the same as the those in the CLLC converter. When the power increases from 2 kW to 4kW, to attain rated 9 A charging current, the switching frequency decreases from 123.2 kHz to 98.9 kHz, in order to achieve higher resonant gain, as illustrated in the gain curve previously. Thus the DC link current, primary side current and secondary side increases accordingly. On the contrary, the MOSFET turns off (I_{off}) decrease, due to the DCM operation.

Table 3-10 The simulation results of LLC at different conditions in forward mode

Parameters	Symbol	Value	Value	Value	Value	Value	Unit
Switching frequency	f_{sw}	123.2	113	107.4	102.2	98.9	kHz
DC link voltage	V_{DC}	379.2600	379.0882	378.9511	378.7753	378.6051	V
DC link current	I_{DC}	5.8256	7.1731	8.2569	9.6374	10.9810	A
Battery voltage	V_{bat}	237.6981	285.4695	327.3212	381.2854	425.1389	V
Battery current	I_{bat}	8.9126	9.1585	9.2022	9.2168	9.2511	A
Primary current	$I_{Ls,\ rms}$	7.2919	8.6419	9.8067	11.1104	12.3841	A
Secondary current	$I_{sec,\ rms}$	10.1869	11.0965	11.6038	12.1051	12.6868	A
MOSFET turn off current	I_{off}	5.09	5.534	6.08	5.70	4.80	A
MOSFET peak current	$I_{pk,\ M}$	10.42	12.58	14.42	16.50	18.53	A
Diode peak current	$I_{pk,\ D}$	14.96	17.25	18.74	20.38	21.89	A

With the simulation data listed above, the power loss distributed in the converter can be quantified based on the calculation methods in Section 3.6.1. Fig. 3-19 shows the conduction loss *P_con* (in blue), the switching loss *P_sw* (in red), the core loss *P_core* (in gray) and the copper loss *P_copper* (in yellow) in both the CLLC resonant converter and LLC resonant converter.

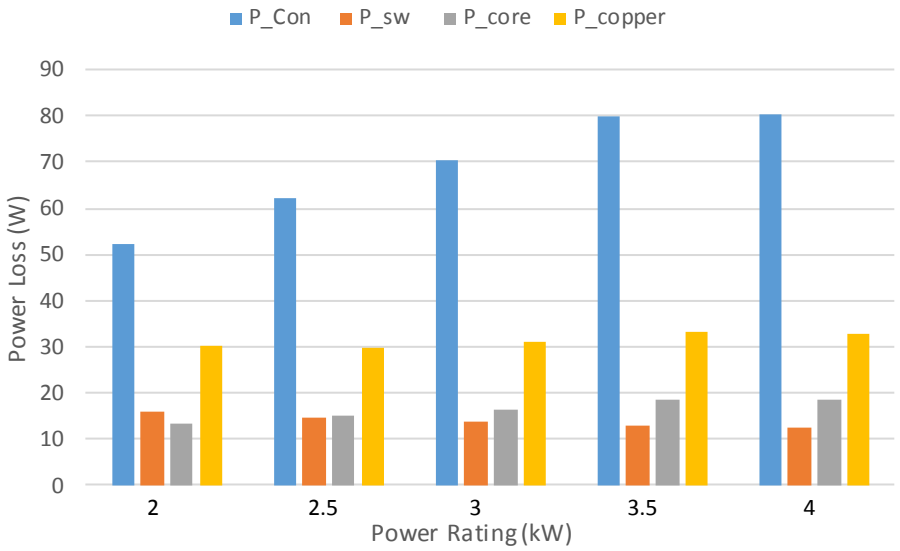

(a)

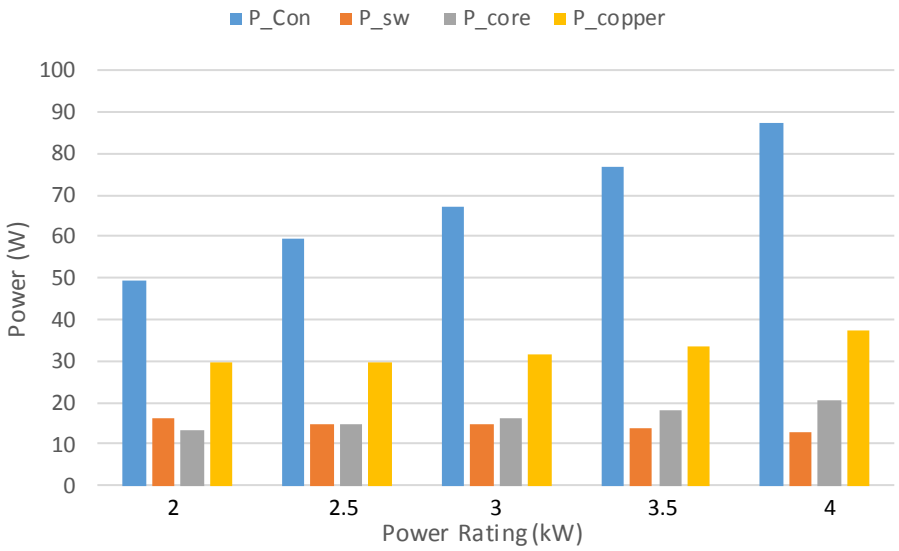

(b)

Fig. 3-19 Power loss distribution in the CLLC and LLC resonant converter in the forward mode. (a) CLLC, (b) LLC, the conduction loss *P_con* is in blue bar, switching loss *P_sw* is in red bar, core loss *P_core* is in gray bar and copper loss *P_copper* in yellow bar.

As evident from the figure, the CLLC and the LLC resonant converter exhibit similar power loss distribution characteristics. Under different operating conditions in both the two types of converters, the conduction loss dominates the power loss and increases when the power increases because the increased RMS device currents. This is expected since the primary side MOSFETS operate in ZVS while and secondary side diodes at ZCS operation which contributes to reduced switching loss. On the contrary, the core loss increases only slightly because with a certain core material and layout, the flux density varies in a small range even under different conditions. In addition, the copper loss does not increase dramatically even with large increase in the current through the coils, since the ac resistance decreases with reduced switching frequency at higher power rating, as explained previously. With the above breakdown, the total power loss of the CLLC and the LLC resonant converter are compared in Fig. 3-20 (a). As indicated, the power losses in the CLLC resonant converter are approximately similar to those in the LLC counterpart, the latter being slightly higher under higher power rating. This feature can be further illustrated in Fig. 3-20 (b), where the efficiency of the LLC varies from 95.07% to 96.20% while it goes from 95.10% to 96.29% in the CLLC counterpart.

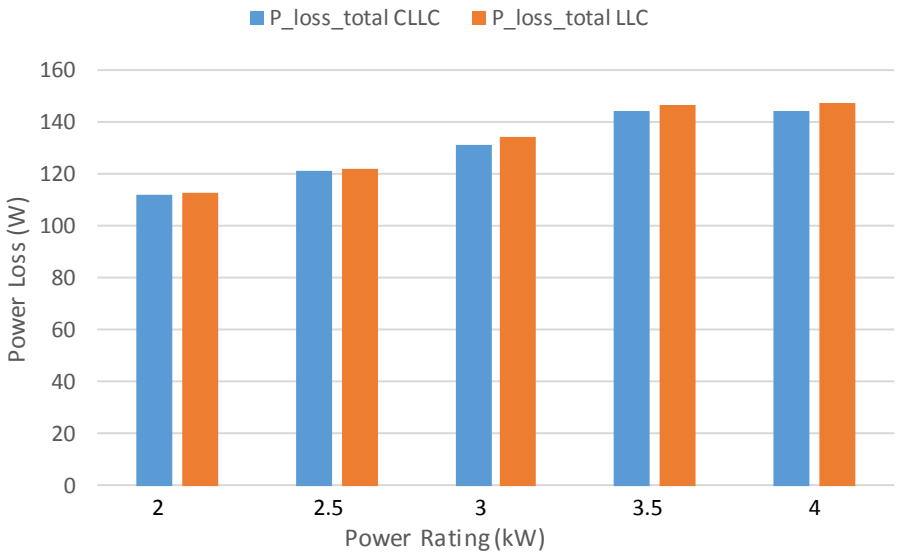

(a)

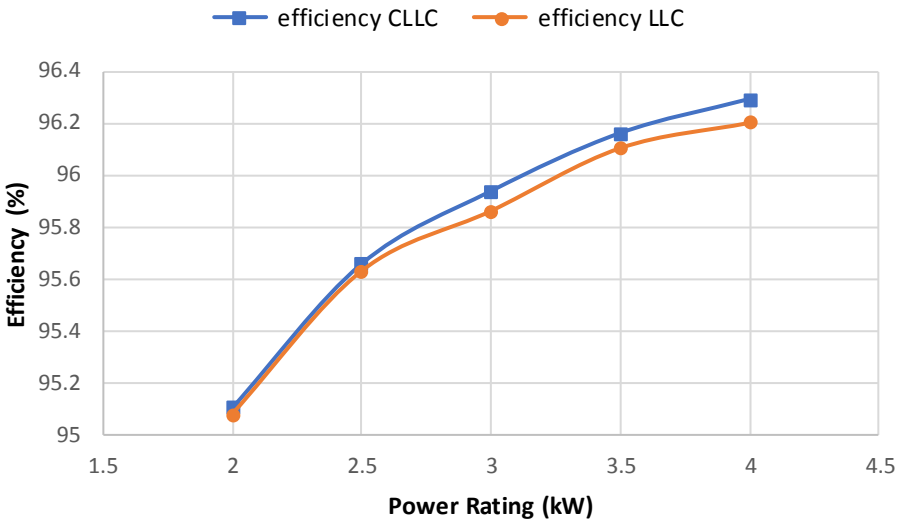

(b)

Fig. 3-20 Efficiency comparison of the CLLC resonant converter and LLC resonant converter in forward mode (a) total power loss comparison and (b) efficiency comparison

To conclude, in the forward charging mode, similar operation characteristics is seen in the CLLC and the LLC topologies, thus the power loss in the CLLC and the LLC converter are comparable with the CLLC converter having a slight efficiency advantage over LLC. This is consistent with the theoretical analysis in Section 3.2.

3.6.2.2 Efficiency comparison in the reverse mode

When the converter is operating in the reverse mode, battery delivers the power, with a constant discharging current of 9A. All the currents and voltages in both CLLC and LLC resonant converter under five different power rating (and different switching

frequency accordingly) can be derived for the power loss calculation from time domain simulations.

The performance data of the CLLC resonant converter in the reverse mode pertinent to power loss prediction is shown in Table 3-11. As analysed in the previous section, the CLLC in reverse mode operates as a conventional LLC resonant converter in the forward mode, thus its performance has similar trend to that in the forward mode. To be specific, when the battery voltage is increased from 240V to 400V, to attain constant DC link voltage and constant discharge current, switching frequency decreases from 125.94 kHz to 90 kHz for a higher resonant gain, as explained previously. All the currents in the circuit increase with the rise of power rating except the secondary side RMS current which is kept approximately constant since the discharge current is constant.

Table 3-11 The simulation results of CLLC at different conditions in the reverse mode

Parameters	Symbol	Value	Value	Value	Value	Value	Unit
Switching frequency	f_{sw}	125.94	105.82	100	95.8773	90.9090	kHz
Battery voltage	V_{bat}	234.9959	267.1525	302.1267	348.4944	397.0508	V
Battery current	I_{bat}	9.6137	9.7472	9.6567	9.5094	8.5059	A
DC link voltage	V_{DC}	396.3258	400.2520	394.1311	398.7220	385.3090	V
DC link current	I_{DC}	5.4779	6.1698	7.0418	7.8835	8.4201	A
Primary current	$I_{Ls,\ rms}$	6.2816	7.3840	8.3132	9.2388	9.6475	A
Secondary current	$I_{sec,\ rms}$	11.3479	11.5644	11.5748	11.6371	10.8137	A
MOSFET turn-off current	I_{off}	7.38	8.17	7.64	8.45	11.49	A
MOSFET peak current	$I_{pk,\ M}$	16.13	17.96	18.9	19.65	18.49	A
Diode peak current	$I_{pk,\ D}$	9.19	11.65	13.29	14.83	15.59	A

For the purpose of comparison, Table 3-12 shows the data of the LLC resonant converter pertinent to power loss prediction in the reverse mode. The operation is similar to SRC due to the magnetic inductor clamped by the voltage across the rectifier in the primary side. Thus the switching frequency increases from 132.80 kHz to higher frequencies far away from resonant frequency to maintain the ZVS operation, when the battery voltage increases. Thus, all the current through the circuit increases correspondingly.

Table 3-12 The simulation results of LLC at different conditions in the reverse mode

Parameters	Symbol	Value	Value	Value	Value	Value	Unit
Switching frequency	f_{sw}	132.80	149.93	160	166.11	168.07	kHz
Battery voltage	V_{bat}	241.3715	268.2811	306.9763	355.2441	387.9207	V
Battery current	I_{bat}	9.1917	9.8135	9.9782	10.2113	10.5710	A
DC link voltage	V_{DC}	392.9957	402.4656	399.9209	410.4023	414.0037	V
DC link current	I_{DC}	5.4319	6.2055	7.1459	8.1143	9.0239	A
Primary current	$I_{Ls,\ rms}$	6.0499	6.7770	7.9138	9.1233	10.1939	A
Secondary current	$I_{sec,\ rms}$	10.9580	14.0085	17.0140	19.9300	22.3805	A
MOSFET turn off current	I_{off}	7.7	17.85	22.39	28.76	34.41	A
MOSFET peak current	$I_{pk,\ M}$	14.06	19.62	22.71	28.94	34.30	A
Diode peak current	$I_{pk,\ D}$	8.439	8.994	10.52	12.28	13.88	A

As evident from the table, the RMS value of the secondary side current increases significantly with the increase of the power rating, which is different from that observed in the CLLC. This is because when the operating frequency is above the series resonant frequency, a large distortion in current waveform occurs in the LLC resonant tank, and a small increase of the discharging current will lead to a large RMS current in the resonant tank, causing more losses in the resonant circuit. The current waveforms will be further displayed in the next section for the comparison of the simulation and the tests.

With the simulation data listed above, the power loss distribution in the reverse mode can be quantified based on the calculation methods in Section 3.6.1, as illustrated in Fig. 3-21. The core loss *P_core,* the conduction loss *P_con*, the switching loss *P_sw*, and the copper loss *P_copper* are displayed both for the CLLC resonant converter and LLC resonant converter.

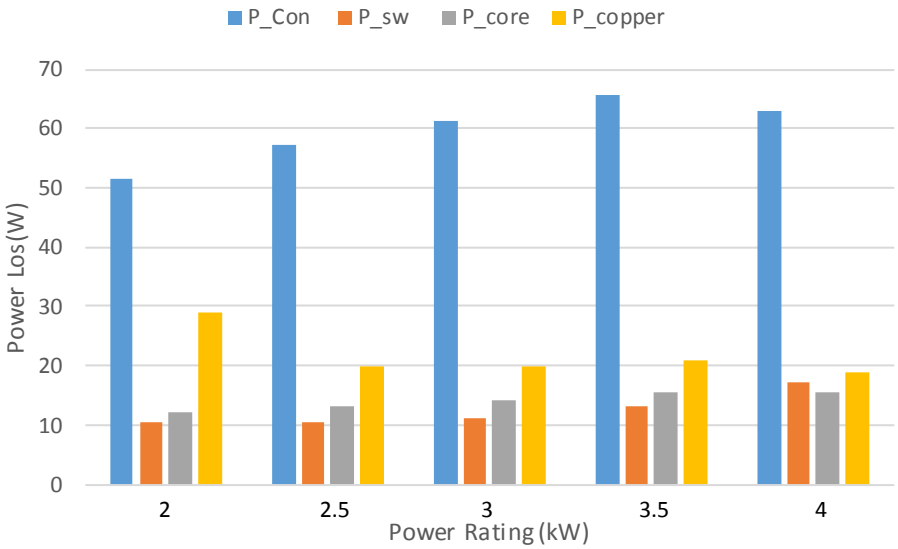

(a)

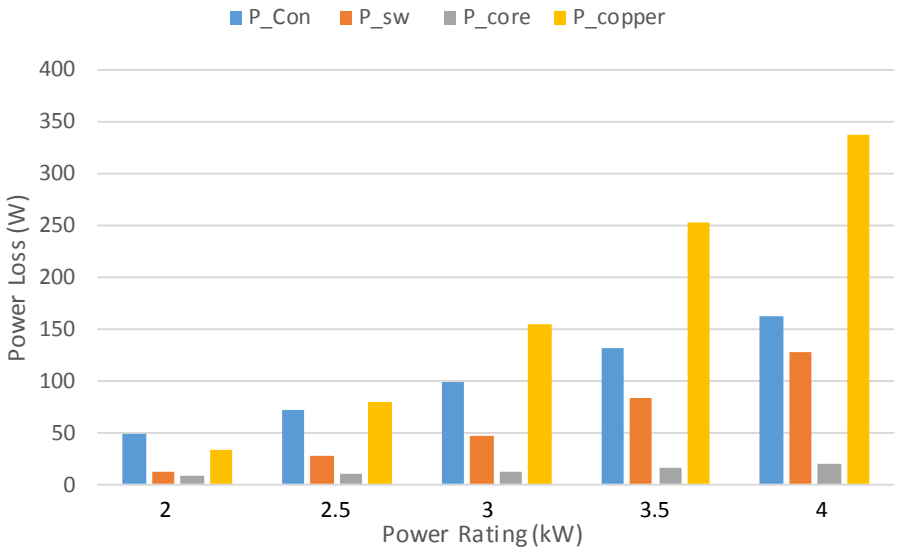

(b)

Fig. 3-21 Power loss distribution in the CLLC and LLC resonant converter in the reverse mode. (a) CLLC, (b) LLC. conduction loss *P_con* is in blue bar, switching loss *P_sw* is in red bar, core loss *P_core* is in gray bar and copper loss *P_copper* in yellow bar.

As observed in Fig. 3-21 (a), the loss distribution of the CLLC in the reverse mode has similar trend as in the forward mode. The conduction loss dominates the total power loss with the trend to increase with the increase of the power rating. In contrast, the copper loss decrease in higher power rating because the switching frequency is lower in order to attain higher resonant gain, as explained in the forward mode.

However, the LLC resonant converter operates as a SRC in the reverse mode. When the battery voltage decreases with constant discharge current, for the purpose of achieving constant DC link voltage while attaining ZVS operation, the resonant gain need to be reduced with increased switching frequency. In this simulation, the battery voltage

increases from 240 to 400V, and the switching frequency increases from 130 kHz to 170 kHz, causing much larger ac resistance in the magnetic components and therefore higher copper losses. In addition, switching losses in the devices is higher resulted from higher switching frequency. And large current waveform distortion increases the RMS current in the resonant tank and leads to high losses. As a consequence, much higher total power losses incur in the LLC resonant converter compared with the CLLC counterpart, as evident in Fig.-3-22 (a). This trend can be illustrated in Fig.-3-22 (b), where the efficiency of the CLLC varies from 95.42% to 96.60% and it drops from 95.41% to 84.29% in the LLC counterpart.

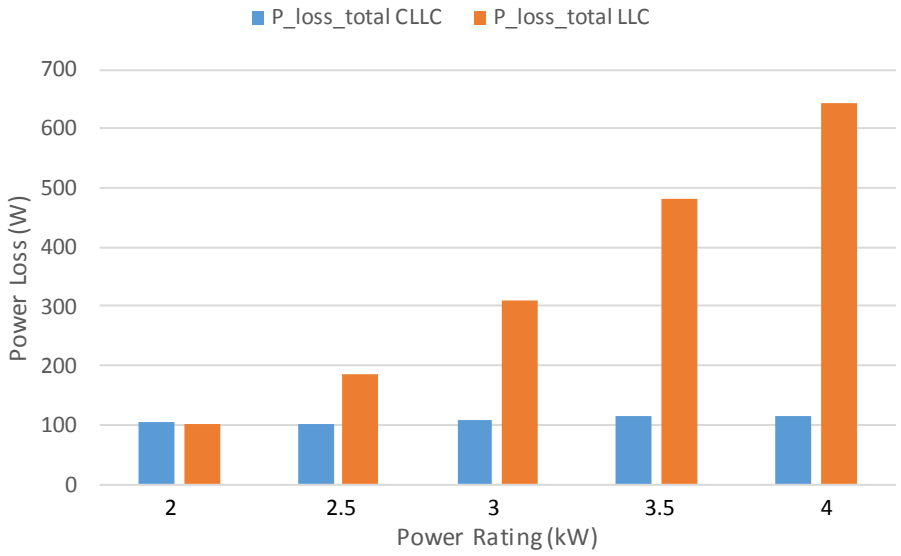

(a)

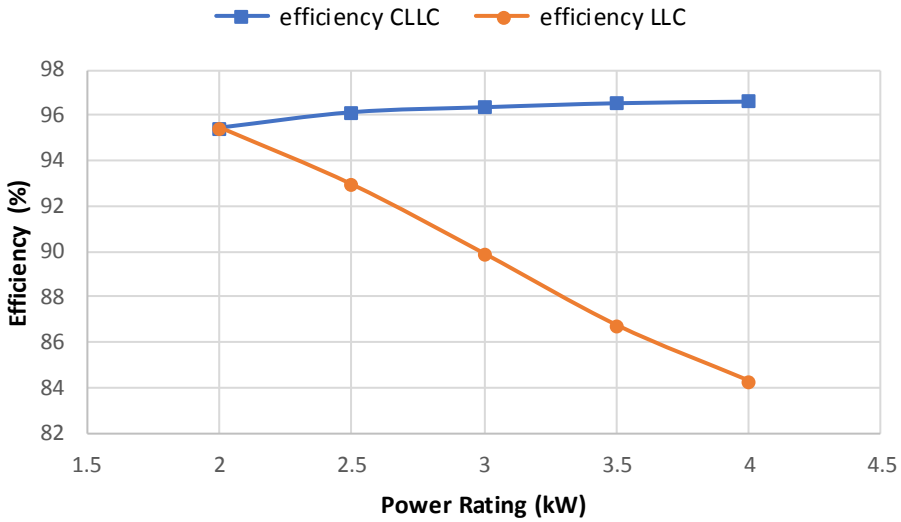

(b)

Fig.-3-22 Simulation efficiency comparison of the CLLC and LLC resonant converters

To conclude, to deliver similar power in the reverse mode, the CLLC and LLC have different operation conditions and the efficiency improvement offered by the CLLC topology is apparent especially in higher power ratings, where the CLLC works in a lower frequency while the LLC has to work in higher frequency to attain ZVS therefore causing higher power losses. This is in line with the theoretical analysis in Section 3.2, and will be further assessed with the experimental data from a prototype converter in the next section.

3.7 Experimental Test and Validation

To validate the designed CLLC resonant converter, experimental tests have been performed based on the test rig described in previous chapters. SCH2080KE N-channel Silicon Carbide (SiC) power MOSFETs are used for the full bridge devices in both sides.

In the forward mode, a variac is used to deliver an adjustable single-phase AC voltage to the charger for adjusting the input voltage. The test load is a "second life" Honda Civic NiMH battery pack [120]. In the reverse mode, a power supply unit is used to simulate the battery for fast discharging experiments.

The only difference between the CLLC and LLC resonant converter is the additional resonant capacitor C_{s2} in the transformer secondary side. The prototype bidirectional charger and the battery load are shown in Fig. 3-23.

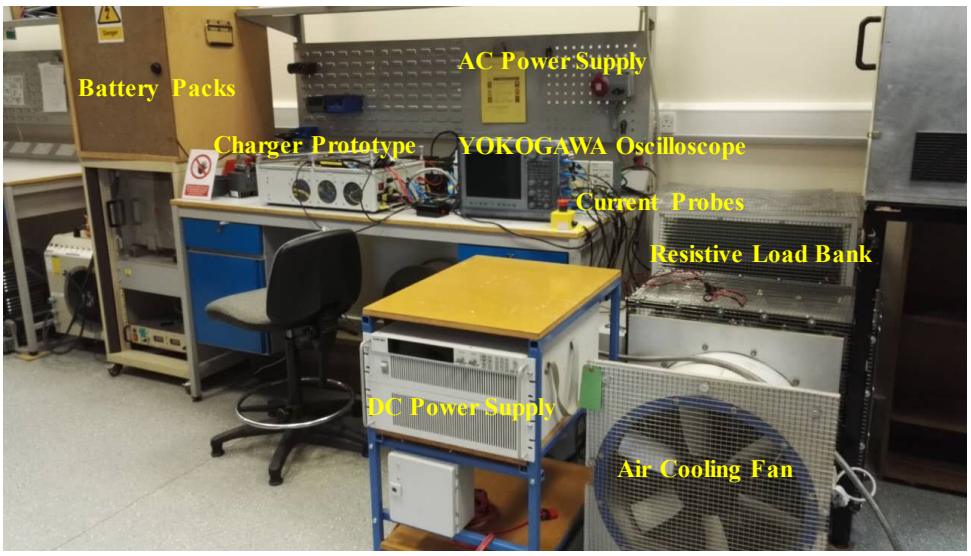

Fig. 3-23 The prototype testing system

All the parameters of the testing bench are listed in Table 3-13:

Table 3-13 The designed CLLC resonant converter specification

Parameters	Symbol	Value	Unit
Series inductor	L_s	97.0	μH
Parallel inductor	L_m	136.5	μH
Primary series capacitor	C_s	15.8	nF
Secondary series capacitor	C_{s2}	427	nF
Output filter capacitor	C_f	330	μF
DC link voltage	V_{dc}	380	V
Battery charging current	I_{bat}	9.0	A
Battery internal resister	R_{bat}	0.1148	Ω
Battery rated capacity	$A \cdot h$	66.2	Ah
Battery fully charged voltage	V_{max}	403.2	V
Battery initial voltage	V_{min}	240	V

3.7.1 Forward mode experimental tests

The performance of the proposed converter is assessed by extensive experimental tests over the wide operating range of the battery voltages and loads with the battery charging system. The switching frequency range is 90 – 130 kHz to cater for wide range of battery voltage.

3.7.1.1 Performance at 2 kW power rating

Fig. 3-24 and Fig. 3-25 illustrate the experimental waveforms from the prototype with the CLLC and LLC resonant tanks at constant 380 V DC link voltage in the forward mode at 2 kW power rating and 121 kHz operating switching frequency.

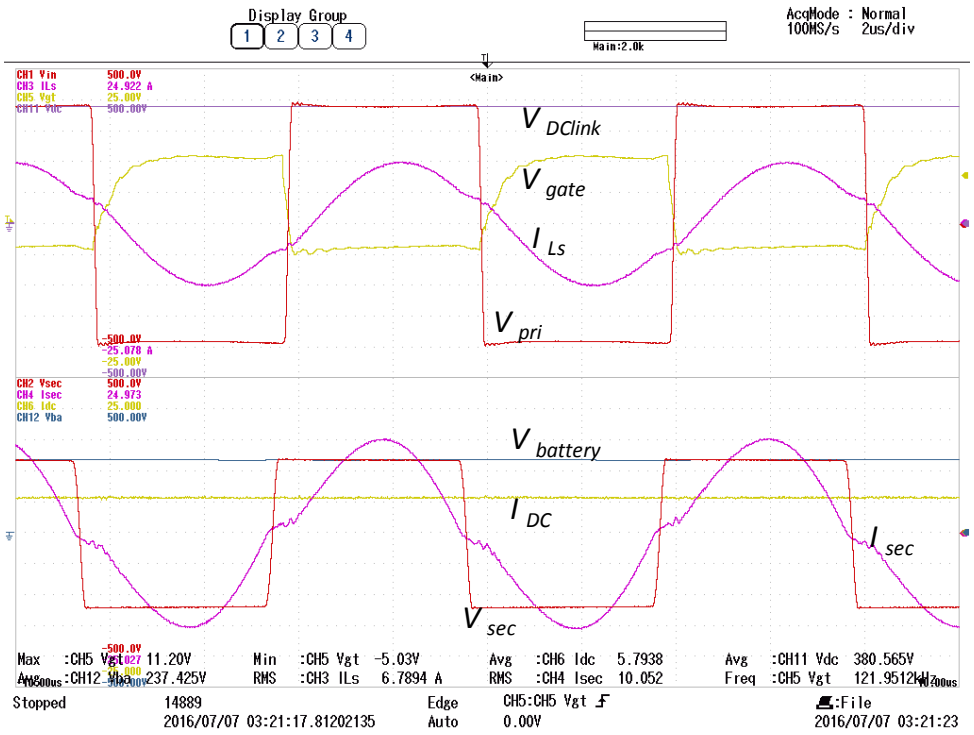

(a)

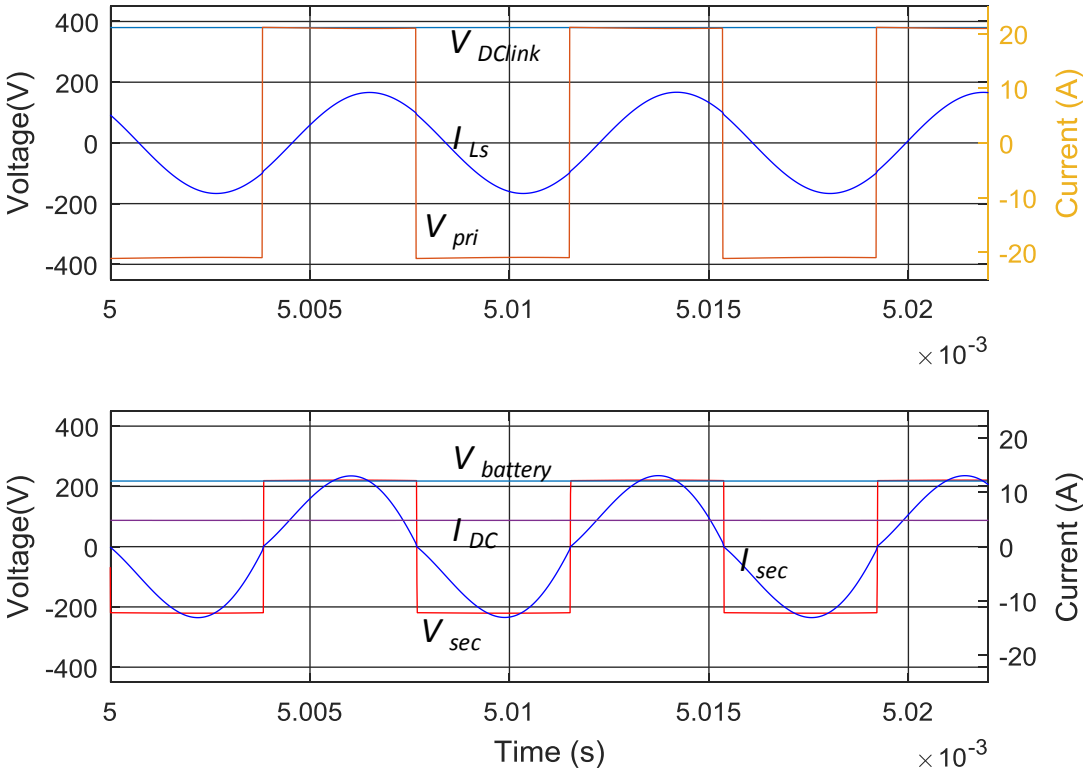

(b)

Fig. 3-24 Waveforms from the CLLC resonant converter in the forward mode at 2 kW power rating (V_{DClink} = 380V, I_{DC} =5.79A, $V_{battery}$ = 240V, $I_{battery}$ = 9A) at 121 kHz with (a) experimental test and (b) time-domain simulation model.

In this condition, V_{DClink} = 380V, I_{DC} =5.79A, $V_{battery}$ = 240V, $I_{battery}$ = 9A. From top to bottom, DC link voltage V_{DClink}, resonant tank current I_{Ls}, transformer primary side full bridge chopped voltage V_{pri}, battery side output voltage $V_{battery}$, DC link side input current I_{DC} secondary side voltage V_{sec}, and secondary side diode bridge current I_{sec} are illustrated. Gate drive voltage V_{gt} is also shown in the test waveforms. To verify the simulation model, simulation results from the time-domain models are also included. It can be observed that the simulation results are close to experimental results in terms of wave shape and peak currents

As indicated in Fig. 3-24 (a), the gate drive signal commands the switching devices operating with square waveform at the required frequency. The resonant tank current I_{Ls} is almost pure sinusoidal because it operates close to the series resonant frequency. I_{Ls} lags the chopped voltage in the transformer primary side. It is negative before positive voltage provided across the devices, which ensures that the Drain-Source voltage V_{DS} decrease to zero first and then the switch turns on. By this way, the ZVS operation can be achieved. Furthermore, ZCS is achieved in the turns-off of the diodes in the secondary side rectifier bridge, with a low *di/dt*.

The experimental waveforms match closely the time-domain simulation waveforms, as shown in Fig. 3-24 (b). Thus, the experimental waveforms validate the operation principles of the CLLC resonant converter described in the previous section.

The measured and simulated waveforms of the DC-DC converter with LLC resonant tank under the same condition are compared in Fig. 3-25. As evident in Fig. 3-25 (a), the gate drive signal commands the switching devices with square waveform at desired switching frequency. The resonant tank current I_{Ls} is almost pure sinusoidal because it operates close to the series resonant frequency. I_{Ls} lags the chopped voltage in the transformer primary side. It is negative before positive voltage provided across the devices, which ensures that the Drain-Source voltage V_{GS} decrease to zero first and then the switch turns on. By this way, the ZVS operation can be achieved. Furthermore, ZCS is achieved in the turns-off of the diodes in the secondary side rectifier bridge, with a low *di/dt*. The experimental waveforms match the simulation waveform from the time-domain simulation which is displayed in Fig. 3-25 (b).

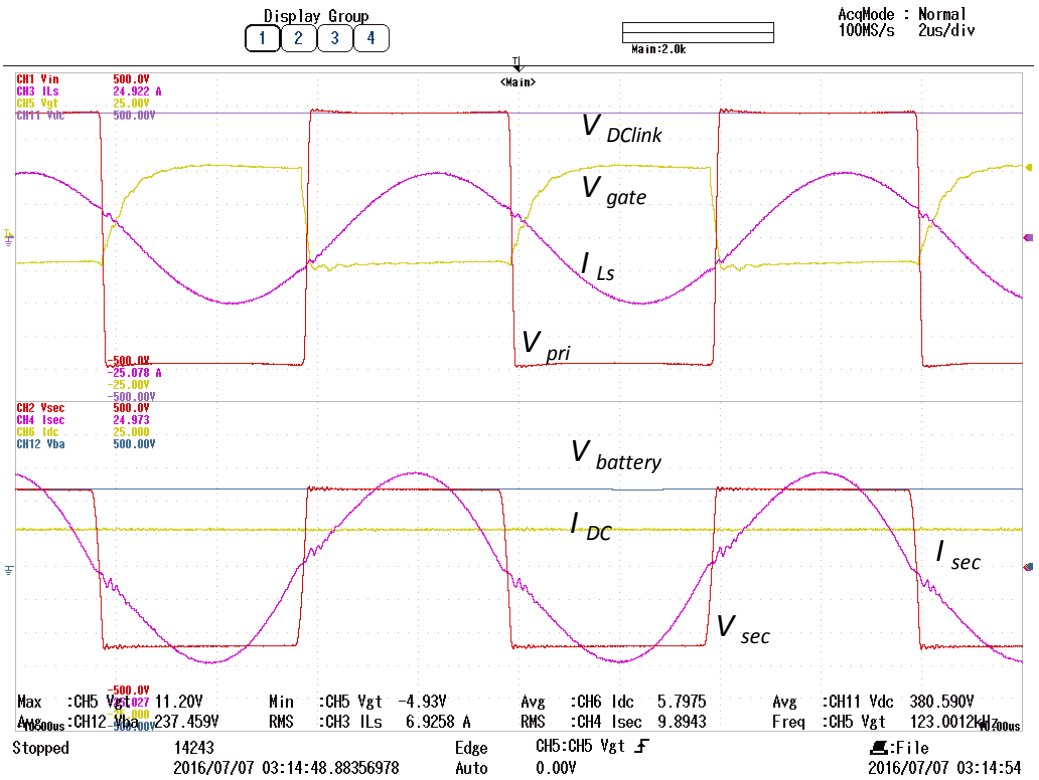

(a)

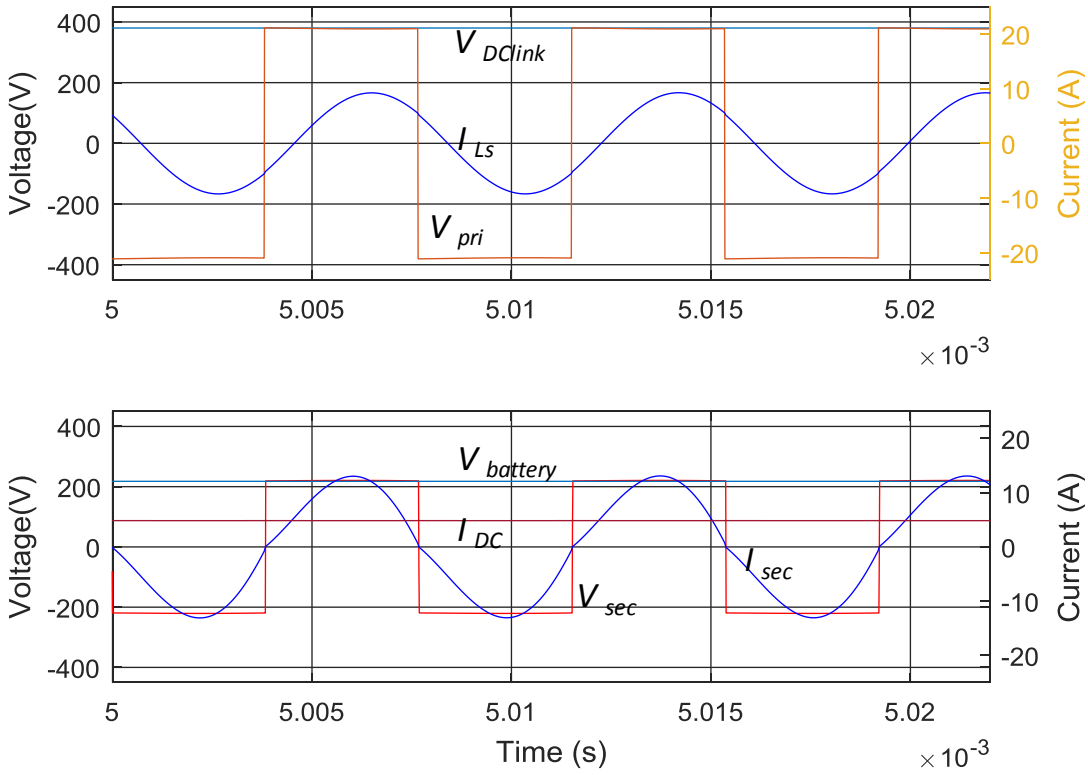

(b)

Fig. 3-25 Waveforms of the LLC resonant converter in the forward mode at 2 kW power rating (*VDClink* = 380V, *IDC* =5.79A, *Vbattery* = 240V, *I battery* = 9A) at 123 kHz with(a) experimental test and (b) time-domain simulation model.

As can be seen, the LLC converter operation is very similar to that of the CLLC converter in the forward model. The experimental waveforms in the forward mode at 2kW verify the operation principles described previously.

3.7.1.2 Performance at 4 kW power rating

Fig. 3-26 and Fig. 3-27 show the waveforms from the prototype with the CLLC resonant tank and the LLC resonant tank, respectively, at 4 kW power rating (V_{DClink} = 380V, I_{DC} =9.5 ~ 10A, $V_{battery}$ = 400 ~ 410V, $I_{battery}$ = 9A) at 99 kHz switching frequency. From top to bottom, DC link voltage V_{DClink}, resonant tank current I_{Ls}, transformer primary side full bridge chopped voltage V_{pri}, battery side output voltage $V_{battery}$, DC link side input current I_{DC} secondary side voltage V_{sec}, and secondary side diode bridge current I_{sec} are illustrated. Gate drive voltage V_{gt} is also shown in the test waveforms. To verify the simulation model and predict the converter waveforms, time-domain simulation results are also illustrated.

As indicated in Fig. 3-26 (a), the resonant circuit current I_{Ls} lags the chopped voltage. Consequently, the Drain-Sourcevoltage V_{DS} decrease to zero before the switch turns on, leading to ZVS operation.

However, the current waveforms are quite different with the 2 kW condition. I_{Ls} is not pure sinusoidal because it operates much below the series resonant frequency. After I_{Ls} reaches to the peak, it decreases until reaches the same value of the magnetizing current I_{Lm}. This happens before the positive voltage duration finishes, so the power transfer is ceased to the load although I_{Lm} is still continuous. During this period, the reflected output voltage to the transformer is higher than the transformer primary side, thus the secondary diode is not able to conduct. So the diode current is zero, and not continuous any more. This discontinuous current mode (DCM) period can be clearly observed from the simulation waveform in Fig. 3-26 (b). When sufficient voltage across the transformer primary side (and consequently the secondary side) diodes to forward-biased, the DCM mode ends and the output diodes begin to conduct.

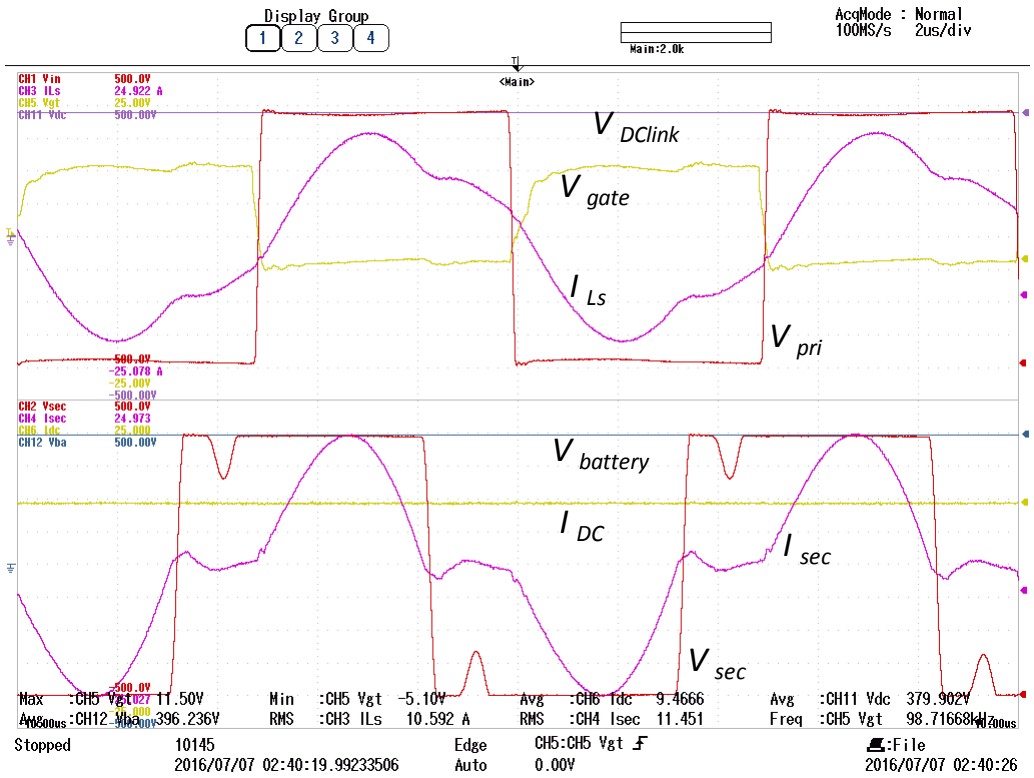

(a)

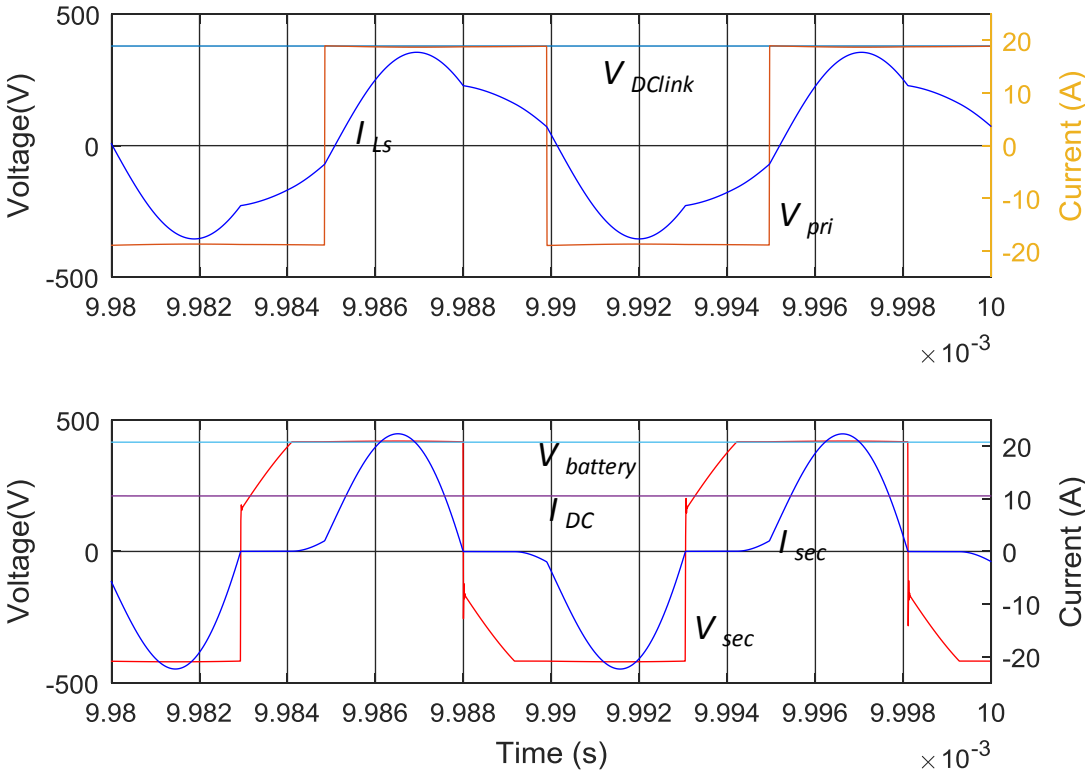

(b)

Fig. 3-26 Waveforms of the CLLC resonant converter in the forward mode at 4 kW power rating (V_{DClink} = 380V, I_{DC} =9.5A, $V_{battery}$ = 400V, $I_{battery}$ = 9A) at 98.9 kHz with (a) experimental test and (b) time-domain simulation model.

In the simulation, the diode characteristic is closed to ideal, and no reverse recovery is observed in the current and voltage waveforms. However, in experimental waveforms as illustrated in Fig. 3-26 (a), the body diode presents reverse recovery current in the turn-off period under the heavy load. This reverse recovery gives rise to a delay of the DCM, corresponding to the voltage dip on the secondary side voltage, compared to the simulation waveforms. Further improvement could be made by applying better SiC MOSFETs with fast reverse recovery characteristics. It will however increase the total cost, so a trade-off must be considered. For this prototype, the SiC MOSFET SCH2080KE shows acceptable capabilities. Although the reverse recovery current is clearly visible, it can hardly degrade the power conversion efficiency due to the small current magnitude.

The performance of the DC-DC converter with the LLC resonant tank, as seen in Fig. 3-27 is similar to the performance of the CLLC resonant tank in Fig. 3-26, including the ZVS in the primary side bridge, ZCS in the secondary side bridge and the DCM operation.

In summary, in the forward mode, both the LLC and CLLC converters exhibit similar performance. In particular, at 2 kW power rating, since the switching frequency is close to the series resonant frequency, the resonant current waveform is nearly sinusoidal both in the LLC and CLLC converters. However, at 4 kW power rating, both the LLC and CLLC converter have more pronounced DCM with current distortion, in order to deliver more power. Despite this, as observed in the waveforms in both the LLC and CLLC converters, the resonant current is lagging the chopped bridge voltage, which implies the inductive characteristics and ZVS operation in the primary side. In addition, the ZCS operation in the secondary side can be achieved with low di/dt. It can be concluded that the experimental waveforms confirmed the operation principle described previously.

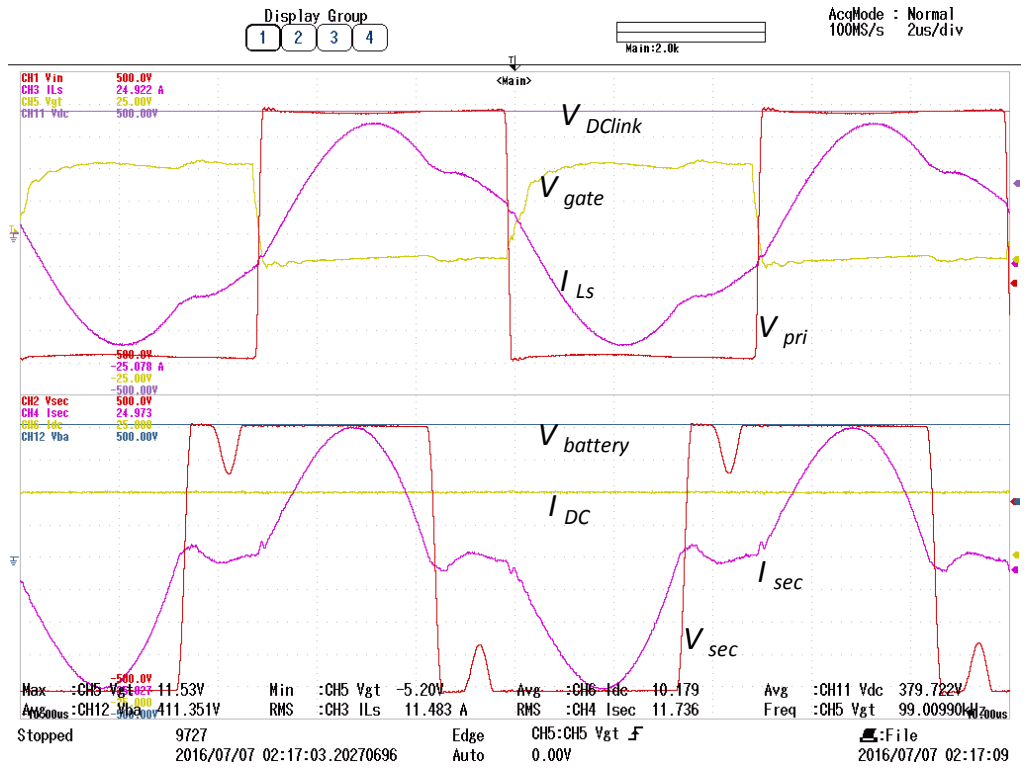

(a)

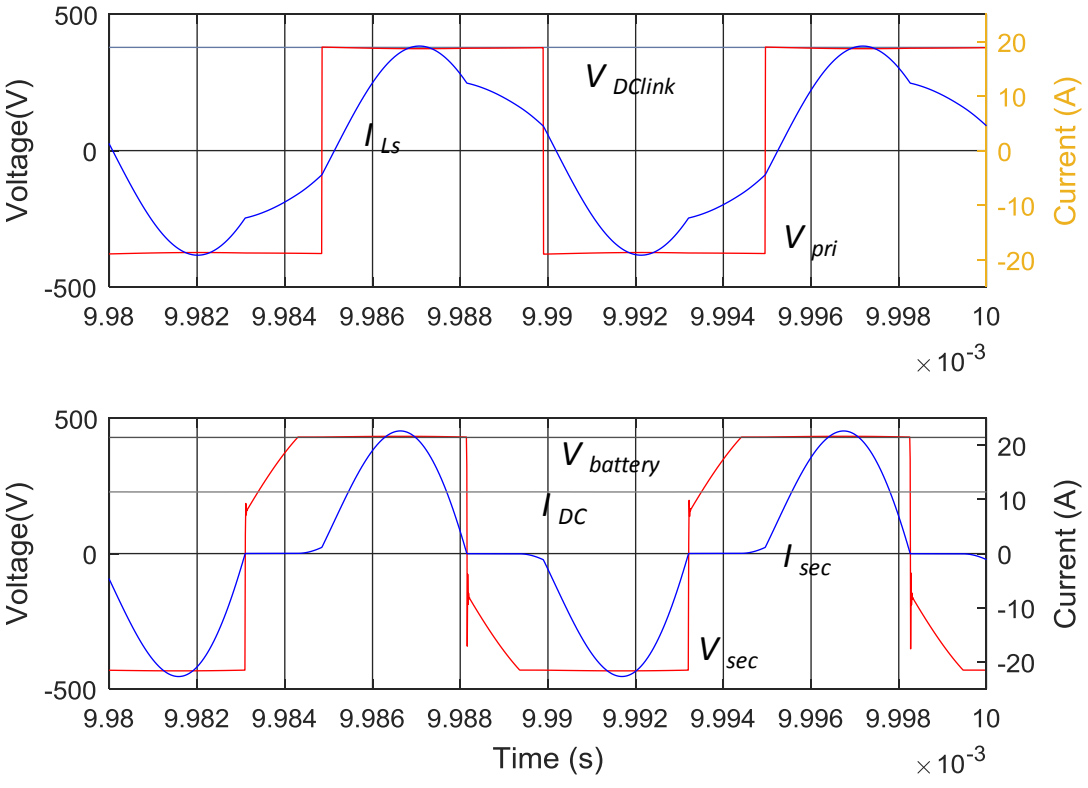

(b)

Fig. 3-27 Waveforms of the LLC resonant converter in the forward mode at 4 kW power rating (V_{DClink} = 380V, I_{DC} =10A, $V_{battery}$ = 400V, $I_{battery}$ = 9A) at 99 kHz with (a) experimental test and (b) time-domain simulation model.

3.7.2 Reverse mode experimental tests

In the reverse mode, a power supply unit is used to simulate the battery for fast discharging experiments. The waveforms obtained from the experimental tests and time-domain simulations in the reverse mode are shown in this section.

3.7.2.1 Performance at 2 kW power rating

Fig. 3-28 and Fig. 3-29 illustrate the operation at 2 kW power rating (V_{DClink} = 380V, I_{DC} =5.3A, $V_{battery}$ = 240V, $I_{battery}$ =9A) at 125 kHz switching frequency. From top to bottom, DC link voltage V_{DClink}, battery current I_{bat}, series inductor current I_{Ls}, primary side voltage V_{pri}, battery side input voltage $V_{battery}$, secondary side current I_{sec} and secondary side chopped voltage V_{sec} are displayed. It should be noted that in the reverse mode, since the MOSFETs in the secondary side H-bridge act as the active devices, the secondary side current I_{sec} flows through the MOSFET. And the inductor current I_{Ls} flows through the diode bridge current because the primary side MOSFETs are turned off with only the body diode acting as the rectifying bridge.

As observed in Fig. 3-28 (a), the gate drive signal commands the switching devices in the transformer secondary side with square wave at required switching frequency. The MOSFET current I_{sec} is almost pure sinusoidal since it operated near the series resonant frequency. I_{sec} lags the chopped voltage in the transformer primary side. It is negative before the positive voltage is applied to resonant tank by the gate drive signal. This ensures the Drain-Source voltage V_{GDS} decreases to zero before the switches turns on and hence, facilitating ZVS operation. Furthermore, the diode turns off under ZCS with a low *di/dt*.

The experimental waveforms match the time domain simulation waveforms, as shown in Fig. 3-28 (b). As a conclusion, the experimental waveforms verify the operation principles of the CLLC resonant tank in the reverse mode described previously.

Fig. 3-29 (a) shows the measured waveforms from the LLC resonant converter under the same condition as that of the CLLC converter. As is seen, The MOSFET current I_{sec} and diode current are similar to those observed in the CLLC converter, and hence the performance of the LLC converter at 2kW is very closed to that of CLLC converter. The experimental waveforms match the simulation waveform from the time-domain simulation, as displayed in Fig. 3-29 (b).

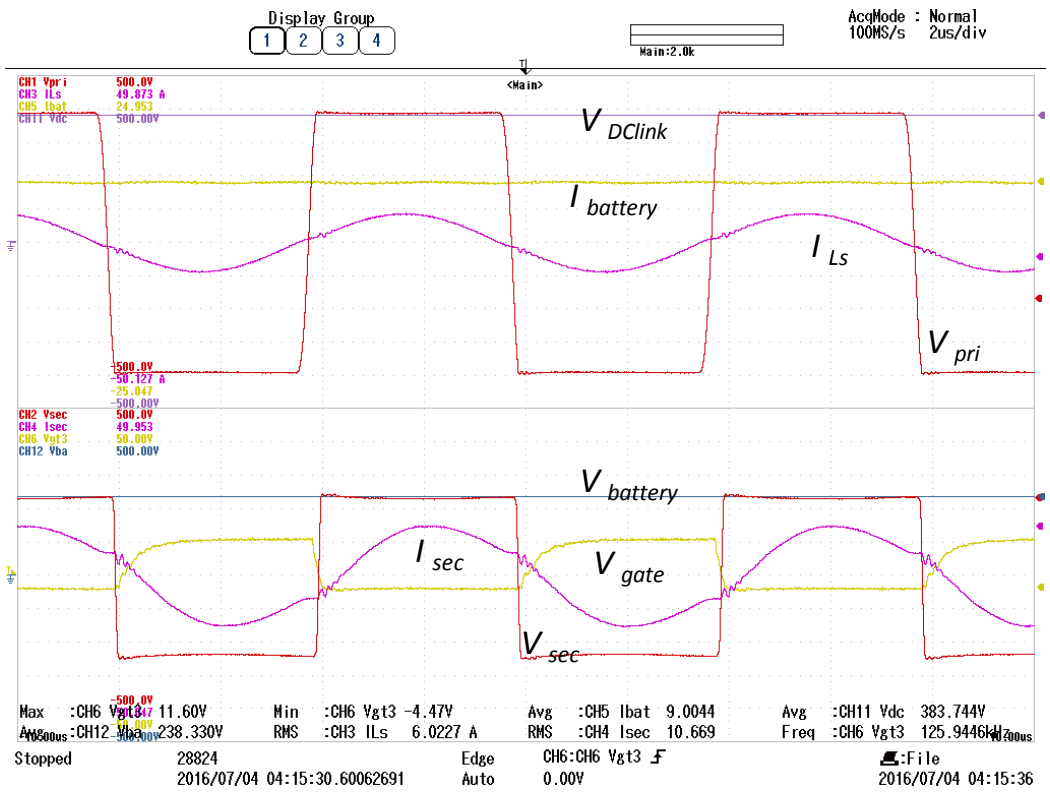

(a)

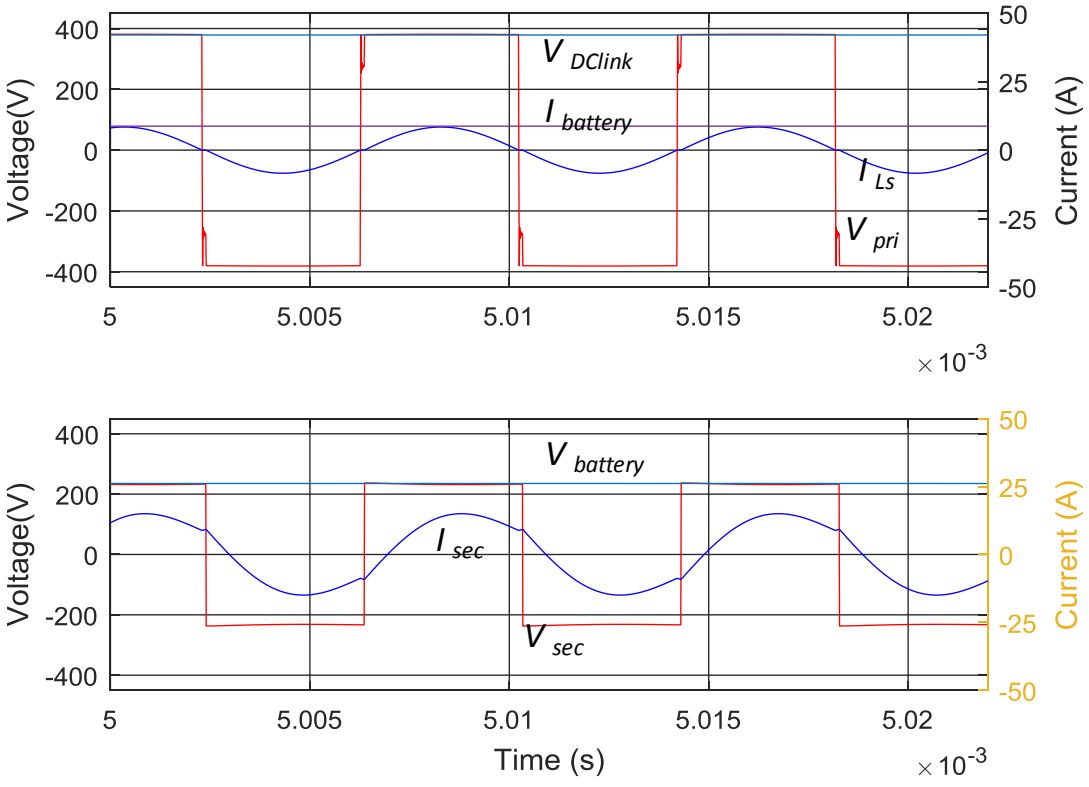

(b)

Fig. 3-28 Waveforms of the DC-DC converter with CLLC resonant tank in the reverse mode at 2 kW power rating (V_{DClink} = 380V, I_{DC} =5.3A, $V_{battery}$ = 240V, $I_{battery}$ = 9A) at 125kHz with (a) experimental test and (b) time-domain simulation.

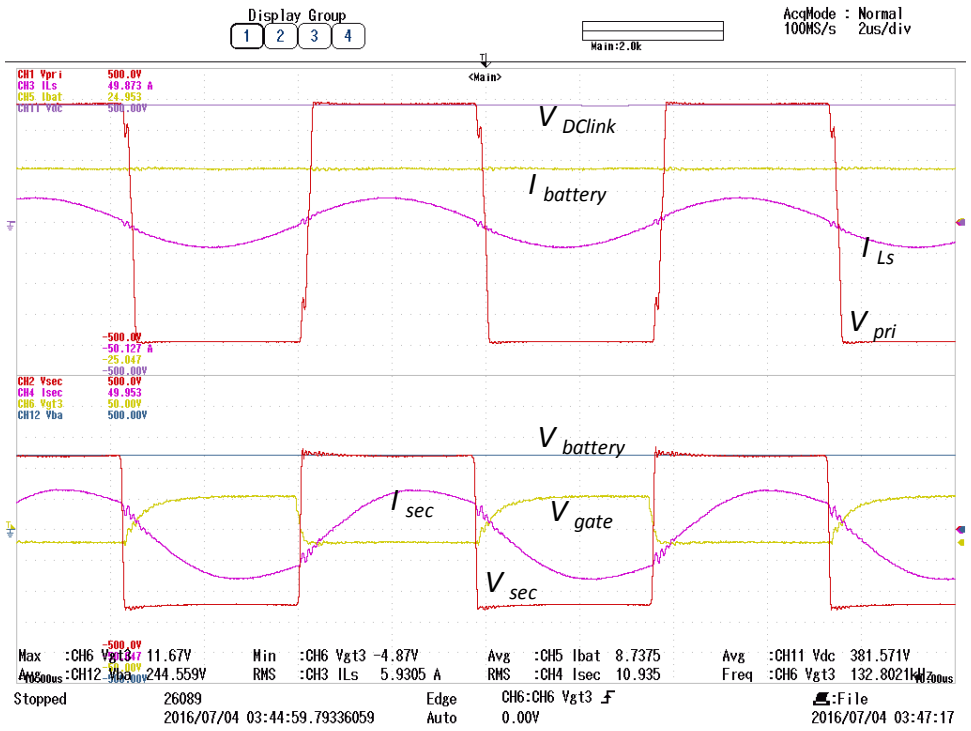

(a)

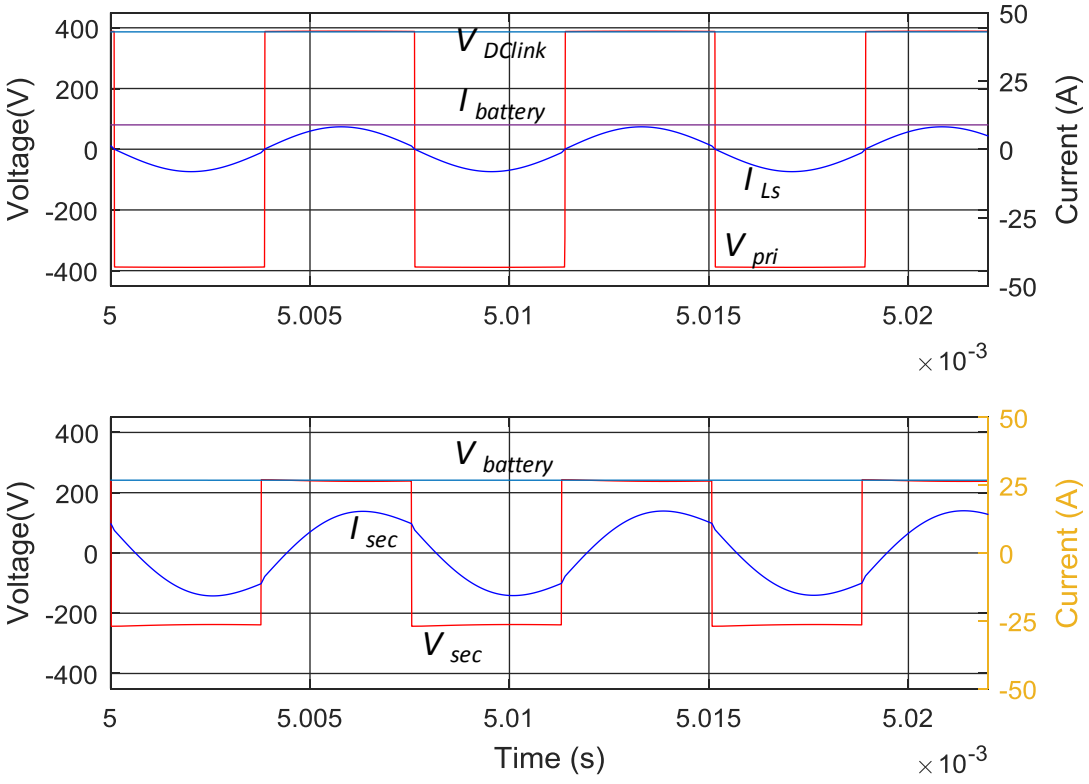

(b)

Fig. 3-29 Waveforms of the LLC resonant converter in the reverse mode at 2 kW power rating (V_{DClink} = 380V, I_{DC} =5.27A, $V_{battery}$ = 240V, $I_{battery}$ = 9A) at 132 kHz with (a) experimental test and (b) time-domain simulation model.

To conclude, the experimental waveforms in the reverse mode have validated the predictions of both the CLLC and the LLC converters described previously.

3.7.2.2 Performance at 4 kW power rating

Fig. 3-30 and Fig. 3-31 demonstrate the waveforms at 4 kW power rating (V_{DClink} = 380V, I_{DC} =8.2A, $V_{battery}$ = 390V, $I_{battery}$ = 9A) at 90 kHz switching frequency for the CLLC resonant converter and at 168 kHz for the LLC resonant converter. From top to bottom, DC link voltage V_{DClink}, battery current I_{bat}, series inductor current I_{Ls}, primary side voltage V_{pri}, battery side input voltage $V_{battery}$, secondary side current I_{sec} and secondary side chopped voltage V_{sec} are displayed. Similar to the waveforms at 2 kW, since the MOSFETs in the secondary side H-bridge act as the active devices, the secondary side current I_{sec} flows through the MOSFET. And the inductor current I_{Ls} flows through the diode bridge current because the primary side MOSFETs are turned off with only the body diode acting as the rectifying bridge.

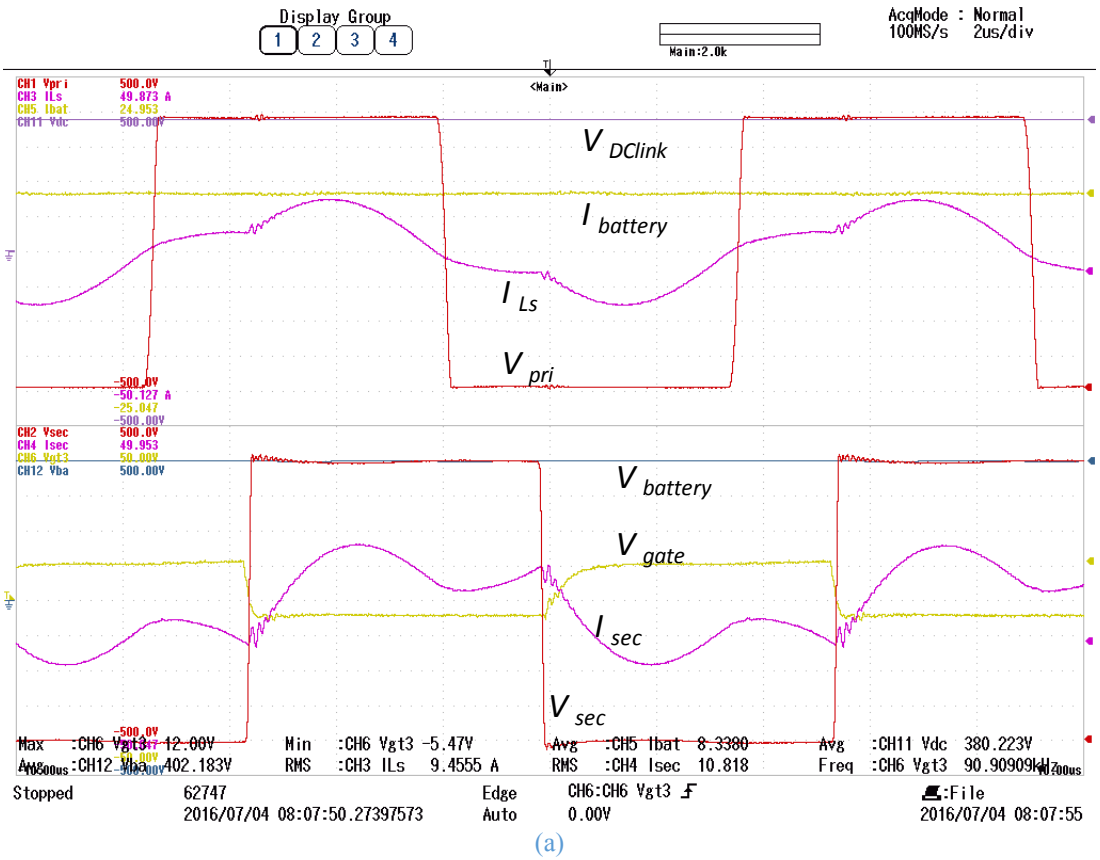

(a)

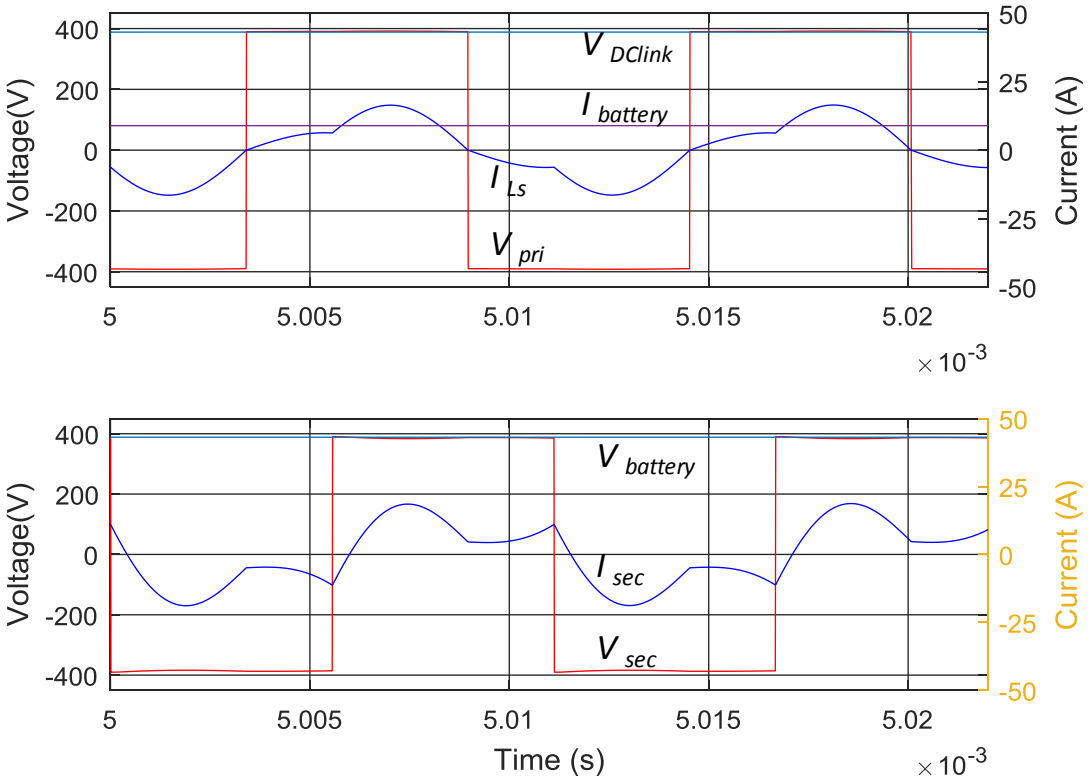

(b)

Fig. 3-30 Waveforms of the CLLC resonant converter in the reverse mode at 4 kW power rating (V_{DClink} = 380V, I_{DC} =8.3A, $V_{battery}$ = 400V, $I_{battery}$ = 9A) at 90 kHz with (a) experimental test and (b) time-domain simulation model.

As shown in Fig. 3-30 (a), the MOSFET current I_{sec} lags the chopped voltage in the transformer secondary side, which implies the ZVS operation. However, compared to the 2 kW condition, I_{sec} is not pure sinusoidal since the operating frequency of 90 kHz is much lower than the series resonant frequency. As a result, severe DCM operation similar to the forward mode can be observed in the waveforms.

The measured and simulated waveforms from the LLC DC-DC converter at 4 kW are compared in Fig. 3-31. It is evident that they are totally different from those in the CLLC resonant topology. Although the ZVS operation in the transformer secondary side bridge and the ZCS operation in the primary side bridge are achieved in both the test and simulation conditions, the MOSFET current in the secondary side exhibits large distortion, while high *di/dt* is seen in the primary side diode current, because its operation region is much higher than the series resonant frequency.

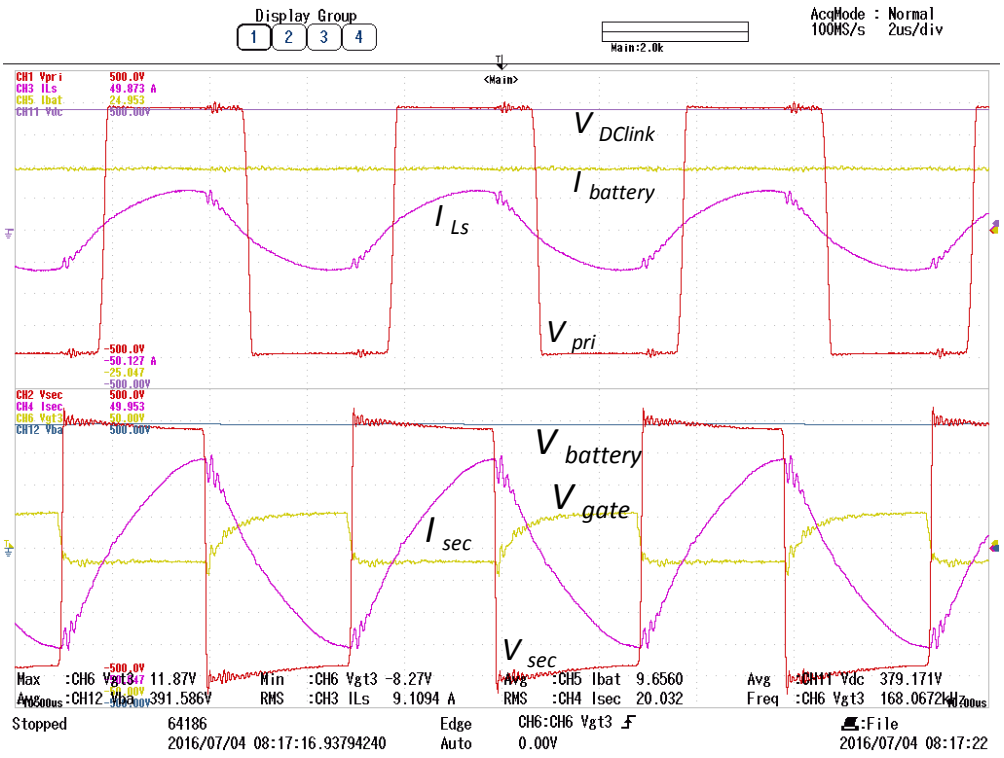

(a)

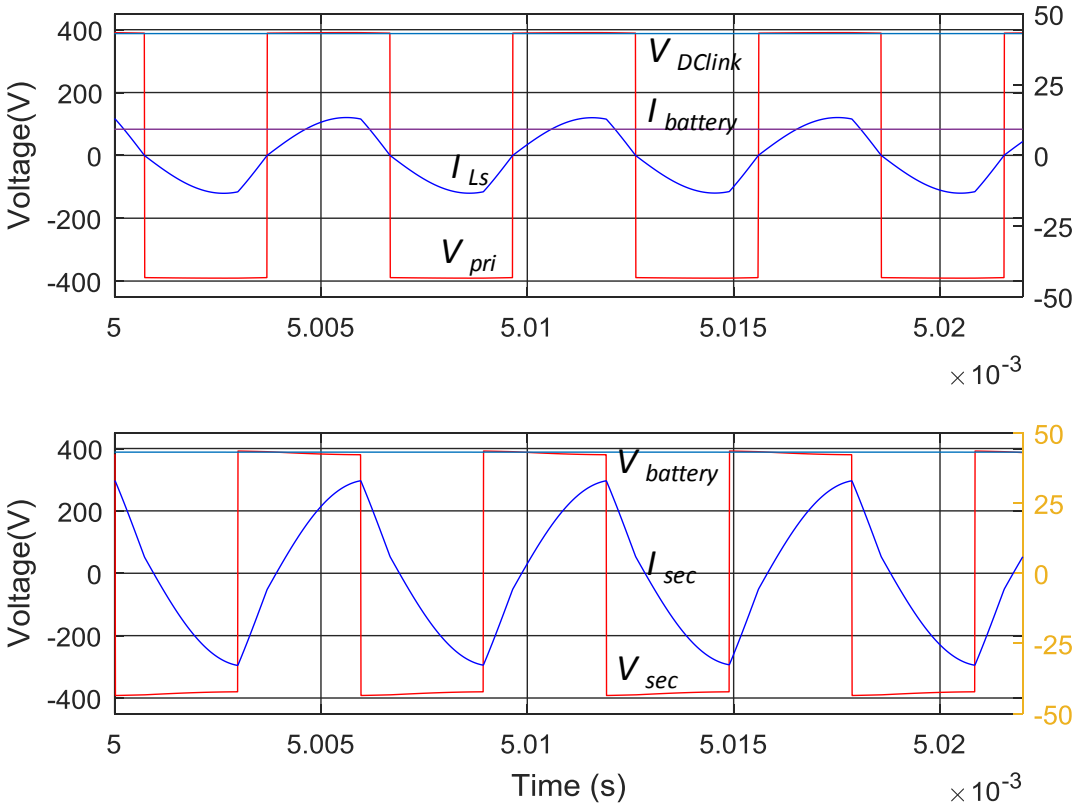

(b)

Fig. 3-31 Waveforms of the LLC resonant converter in the reverse mode at 4 kW power rating (V_{DClink} = 380V, I_{DC} =8.27A, $V_{battery}$ = 400V, $I_{battery}$ = 9A) at 168 kHz with (a) experimental test and (b) time-domain simulation model

In summary, in the reverse mode, at 2 kW power rating, the switching frequency is close to the series resonant point in both the LLC and CLLC circuit, similar current waveforms are seen in LLC and CLLC. However, at the high power, significant difference can be observed. The LLC converter operates in the region much above the series resonant frequency for the purpose of delivering high power, causing serious current distortion. On the contrary, lower switching frequency can be seen in the waveforms of the CLLC converter, corresponding to the DCM operation.

3.8 Efficiency Measurements and Comparison

In order to evaluate the converter efficiency, the actual power delivery efficiency in the experimental prototype under different conditions are measured and compared in this section.

3.8.1 Measured efficiency comparison

In the experimental tests, the DC link voltage and battery voltage are measured with a YOKOGAWA oscilloscope using 1200V probes. The DC link current and battery current are measured by the Tektronix current probes and displayed in the YOKOGAWA oscilloscope. Once all the data are obtained from YOKOGAWA oscilloscope, the averaged values of the DC link voltage/current and the battery voltage/current are calculated easily. After that, input power and output power can be calculated with which the power conversion efficiency can be analysed. Measured efficiency comparison of the LLC and CLLC converters in the forward and reverse mode is illustrated in Fig. 3-32.

As can be observed, in both forward and reverse modes, the efficiency of CLLC is higher than LLC at all power ratings. The efficiency of CLLC and LLC converter is comparable in the forward mode. For example, the efficiency of the LLC and CLLC converters in the forward mode are equivalent around 95% at 2 kW, and 96% at 4kW. The difference in efficiency between the two converters is insignificant.

However, in the reverse mode, the benefit of CLLC topology is clearly demonstrated. It is evident that in the CLLC topology the efficiency varies between 95% and 96% over 2kW to 4kW range, while the efficiency of LLC topology decreases from 95% at 2kW to as low as 86% at 4kW. The CLLC has a 10.22% improvement on the efficiency over the LLC counterpart at 4kW. The measured efficiencies in the prototype converters are

consistent with the analysis in Section 3.2.2, and the power loss prediction in Section 3.6.2.

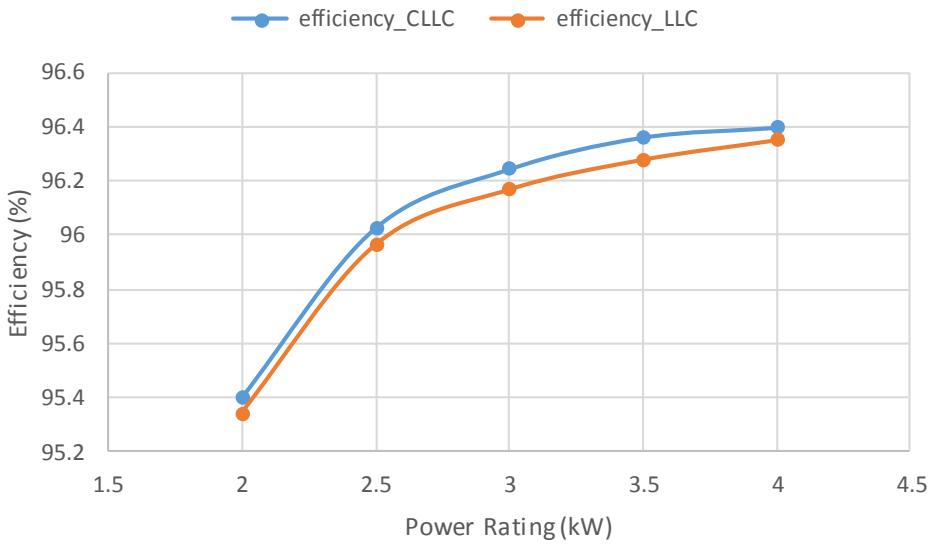

(a)

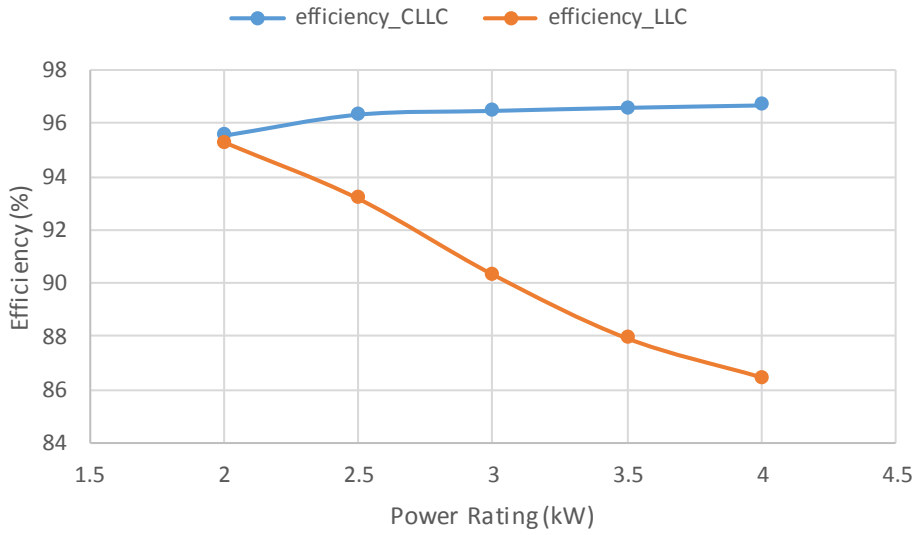

(b)

Fig. 3-32 Comparison of measured efficiency variations of CLLC and LLC converters with output power in (a) the forward mode and (b) the reverse mode

The low efficiency of LLC converter is expected since the circuit actually operates as a series resonant converter (SRC) in the reverse mode, which has to operate in a wider frequency range to accommodate wide voltage variation in the battery and therefore causes more losses. Also, the operation region of the SRC converter can be above the series resonant frequency to insure the inductive operation which further cause higher switching frequency and thus higher switching losses. This is the reason why the LLC converter is not usually preferred for the revere mode operation.

On the other hand, the CLLC topology in reverse mode operates as a normal LLC, which has wider ZVS range, and the boundary of the ZVS is the system resonant peak point rather than the series resonant frequency. So the system can operate below the series resonant frequency (while must be above the system resonant frequency to obtain the inductive operation range).This is further illustrated in Fig. 3-33 which compares the switching frequency as a function of load for both LLC and CLLC topologies. As can be observed, in the forward mode, the switching frequencies of the CLLC and LLC topologies are close to each other with the same trend of reduction as the power rating increases. However, in the reverse mode, in order to deliver more power, the CLLC operates at lower frequency as the power increases, while the LLC needs to increase the switching frequency from 130 kHz to 170 kHz.

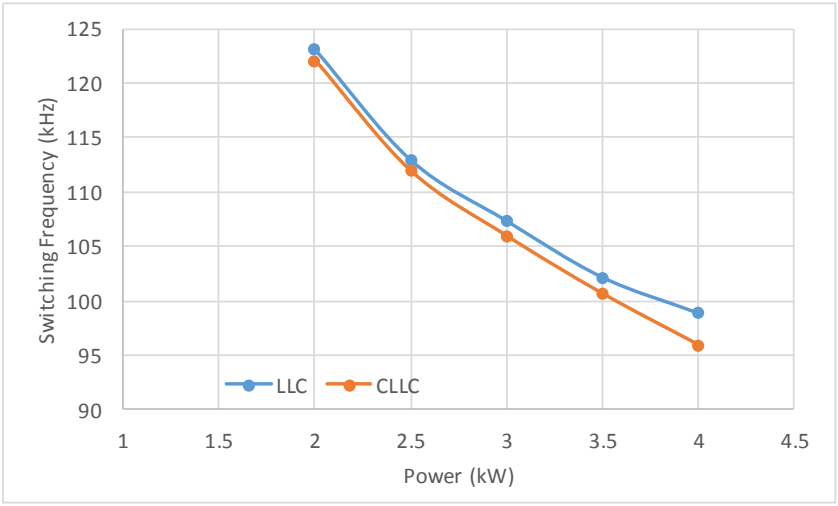

(a)

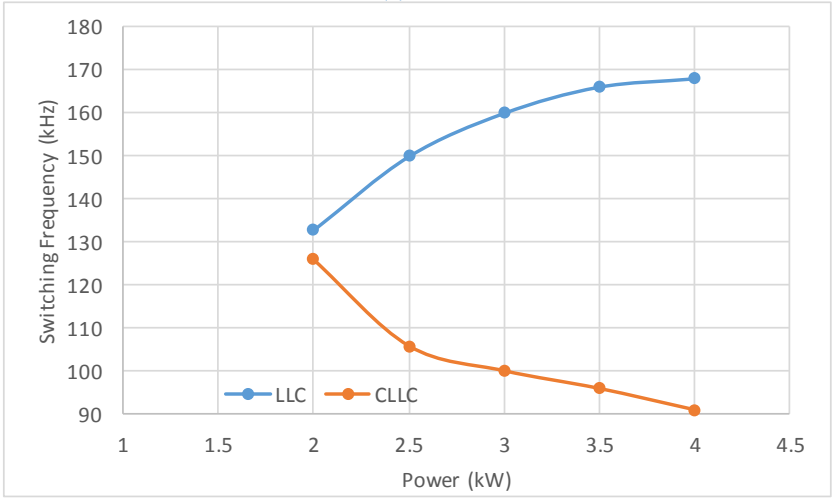

(b)

Fig. 3-33 Switching frequency required at different power in (a) the forward mode and (b) the reverse mode

3.8.2 Measured and predicted efficiency comparison

The comparison of the measured efficiency from the prototype bench and the predicted efficiency from the simulation is shown in Fig. 3-34.

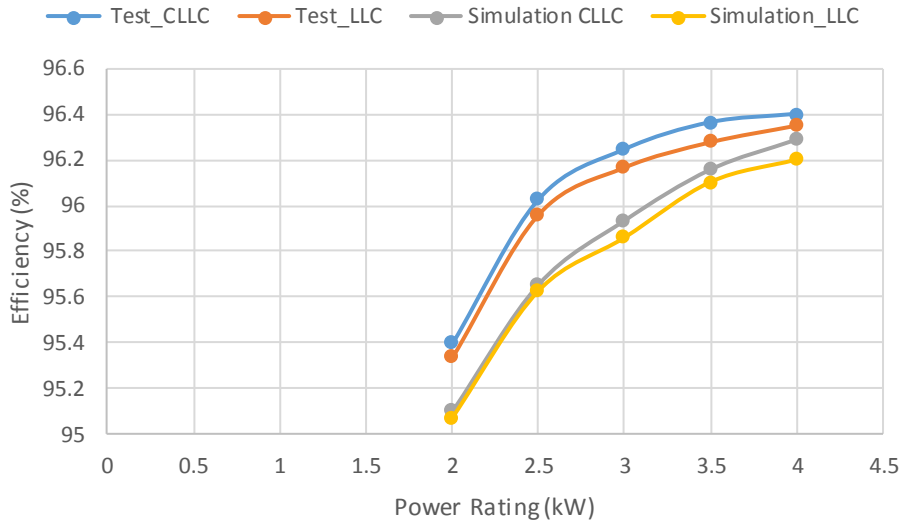

(a)

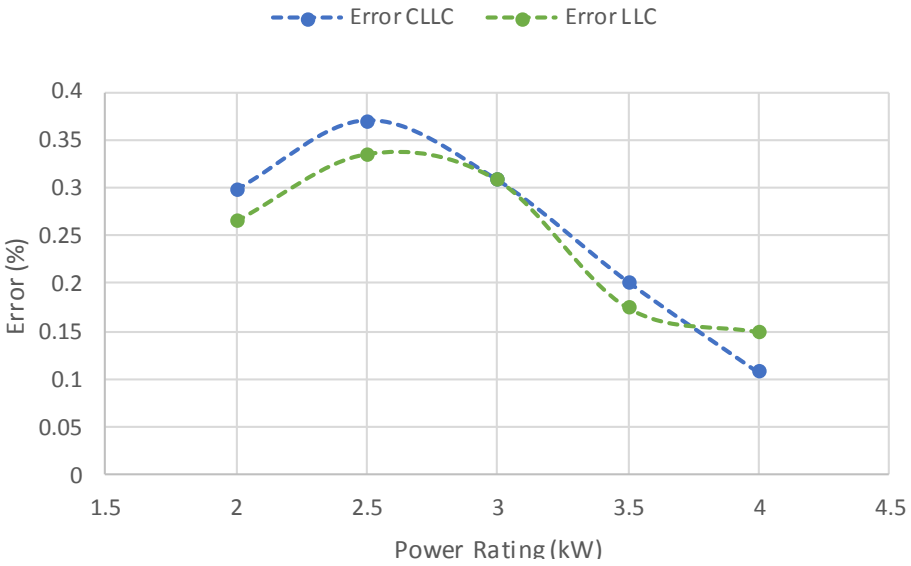

(b)

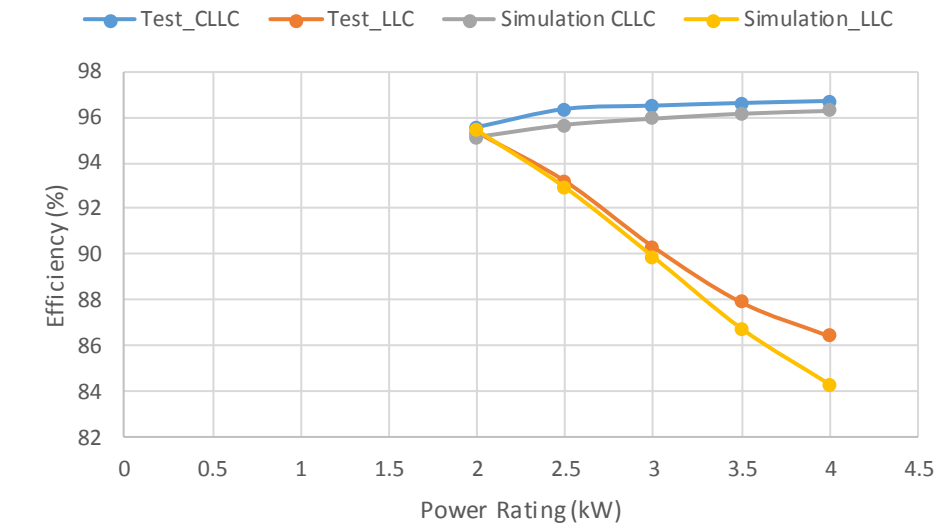

(c)

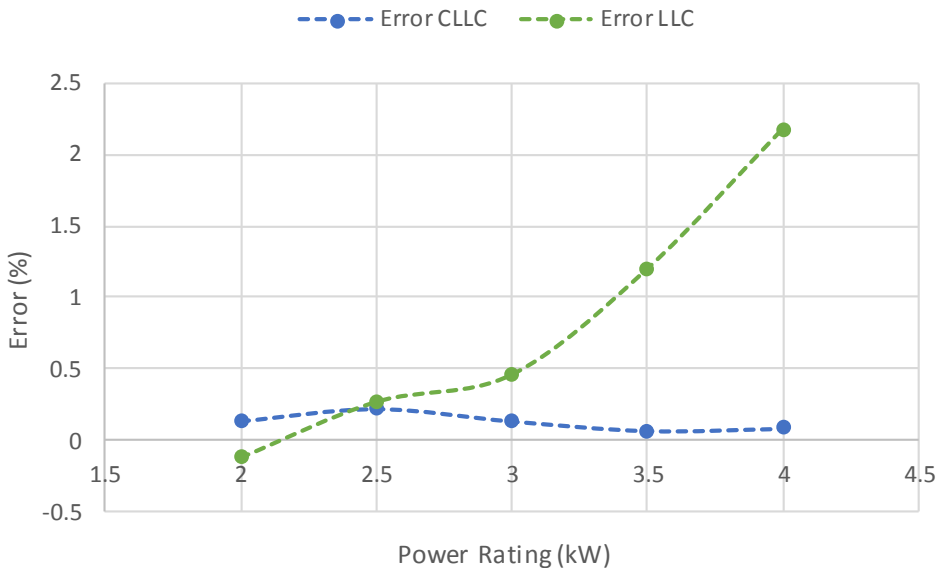

(d)

Fig. 3-34 Comparison of the measured and predicted efficiencies. (a) efficiency comparison in the forward mode, (b) error in the forward mode, (c) efficiency comparison in the reverse mode and (d) error in the reverse mode.

As can be seen, in general, it is apparent that under all the conditions, the measured efficiencies of both the CLLC and LLC converters agree with the predictions in both the forward and the reverse modes. As detailed in Fig. 3-34 (a) and (b), in the forward mode, the measured efficiency follows similar trend to the prediction. The errors are in a fairly reasonable range and may be attributed to a number of factors, such as the deviation of the devices characteristics from their datasheet values, and measurement errors due to limited accuracy of the current and voltage probes.

Reasonable results are also observed in the reverse mode as illustrated in Fig. 3-34 (c) and (d). It is clear that measured efficiency matches the predicted trend in all the power ratings. ~~It should, however, be noted that in the LLC topology when the power rating increases, the error increases significantly and reaches 2.2% at 4 kW. While in the CLLC converter, the error is only 0.08%.~~

The large difference in measured and predicated efficiencies of the LLC converter at 4kW may be due to errors in switching loss prediction. As has been indicated in the previous analysis, the main difference between the CLLC and LLC in the reverse mode is the switching frequency, which will affect the device switching losses and the copper losses (due to the variation of ac resistance at different switching frequency). Since the conduction loss dominant at heavy load, it is possible that the overestimation of the predicted power loss of the LLC converter at 4kW could be explained by the inaccuracy of the component datasheet, such as the overestimated MOSFET on-resistance and the turn-off energy (again the drain-source voltage and drain current), due to the lack of values in different temperatures. Thus, further power loss analysis and comparison should be implemented, especially with the LLC resonant converter in the reverse mode.

3.8.3 Power loss distribution in the test system

It is difficult to measure the power loss in all the devices and components directly, since most of the devices are not accessible in the testing rig. Nevertheless, it can be estimated with all the measured currents and voltages, based on the power loss calculation method in Section 3.6.1.

In the experimental tests, DC link voltage and battery voltage are measured with a YOKOGAWA oscilloscope using 1200V probes. DC link current and battery current are measured by the Tektronix current probes and displayed in the YOKOGAWA oscilloscope. Once all the data are obtained from YOKOGAWA oscilloscope, the averaged values of the DC link voltage/current and the battery voltage/current are calculated accordingly. The MOSFET turn-off current, MOSFET peak current, diode peak current is observed and obtained from the waveforms captured with YOKOGAWA oscilloscope.

3.8.3.1 Power Loss distribution in the forward mode

The experimental measured currents and voltages in the prototype are detailed in Table 3-14 and Table 3-15 below. As the data have similar trend to the simulation data in Section 3.6.2, they will not be presented in detail here.

Table 3-14 The test results of CLLC at different conditions in forward mode

Parameters	Symbol	Value	Value	Value	Value	Value	Unit
Switching frequency	f_{sw}	122.15	111.98	106	100.7	96	kHz
DC link voltage	V_{DC}	380.565	380.386	380.27	379.929	379.732	V
DC link current	I_{DC}	5.7938	6.824	7.8511	9.1213	10.227	A
Battery voltage	V_{bat}	237.425	278.197	317.691	370.019	410.188	V
Battery current	I_{bat}	8.9934	9.0031	8.9998	9.0029	8.975667	A
Primary current	$I_{Ls,\ rms}$	6.7894	7.6963	8.8009	10.24	11.57	A
Secondary current	$I_{sec,\ rms}$	10.052	10.302	10.85	11.544	12.113	A
MOSFET turn off current	I_{off}	3.8	4.2	4.1	3.6	1.2	A
MOSFET peak current	$I_{pk,\ M}$	9.8	11.6	13.3	15.1	17.2	A
Diode peak current	$I_{pk,\ D}$	15	16.8	18.2	19.8	21.2	A

Table 3-15 The test results of LLC at different conditions in forward mode

Parameters	Symbol	Value	Value	Value	Value	Value	Unit
Switching frequency	f_{sw}	123.2	113	107.4	102.2	98.9	kHz
DC link voltage	V_{DC}	380.59	380.429	380.249	379.981	379.72	V
DC link current	I_{DC}	5.7975	6.8321	7.838	9.1548	10.179	A
Battery voltage	V_{bat}	237.459	278.177	317.407	370.485	411.351	V
Battery current	I_{bat}	8.9947	9.0025	8.9917	9.0142	9.0011	A
Primary current	$I_{Ls,\ rms}$	6.9258	7.9071	9.0075	10.455	11.483	A
Secondary current	$I_{sec,\ rms}$	9.8943	10.074	10.572	11.342	11.736	A
MOSFET turn off current	I_{off}	4	5	5.2	5.2	4	A
MOSFET peak current	$I_{pk,\ M}$	10	11.8	13.5	15.5	17.8	A
Diode peak current	$I_{pk,\ D}$	14.3	16.2	17.8	19	19.8	A

With the measured data listed above, the power loss distributed in the converters can be quantified based on the calculation methods in Section 3.6.1, as illustrated in Fig. 3-35. The the core loss *P_core,* the copper loss *P_copper*, conduction loss *P_con* and the switching loss *P_sw* are displayed both in the CLLC resonant converter and LLC resonant converter.

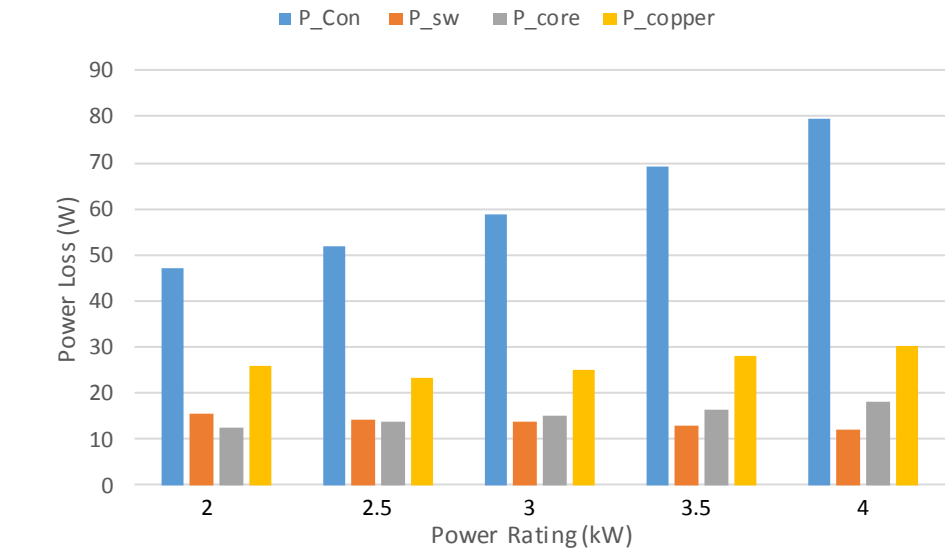

(a)

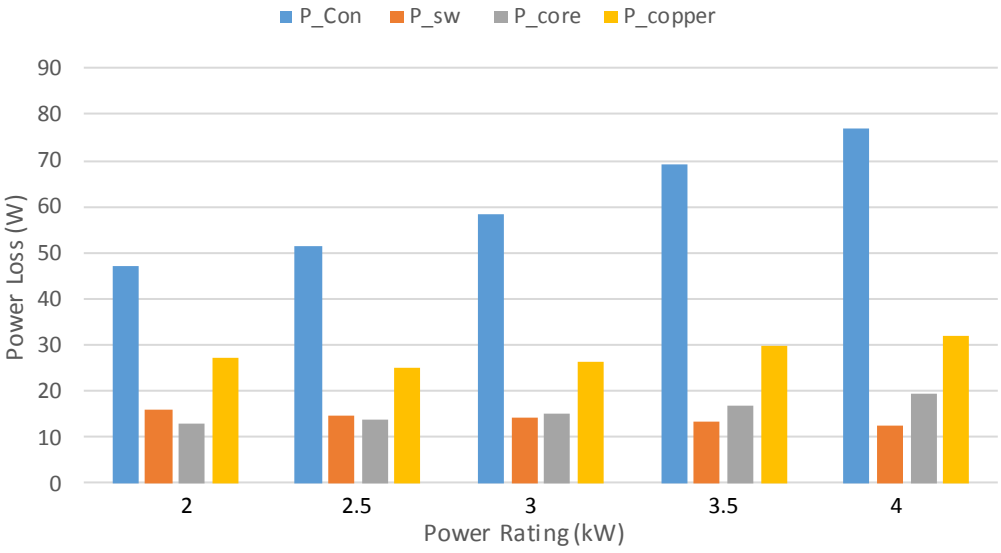

(b)

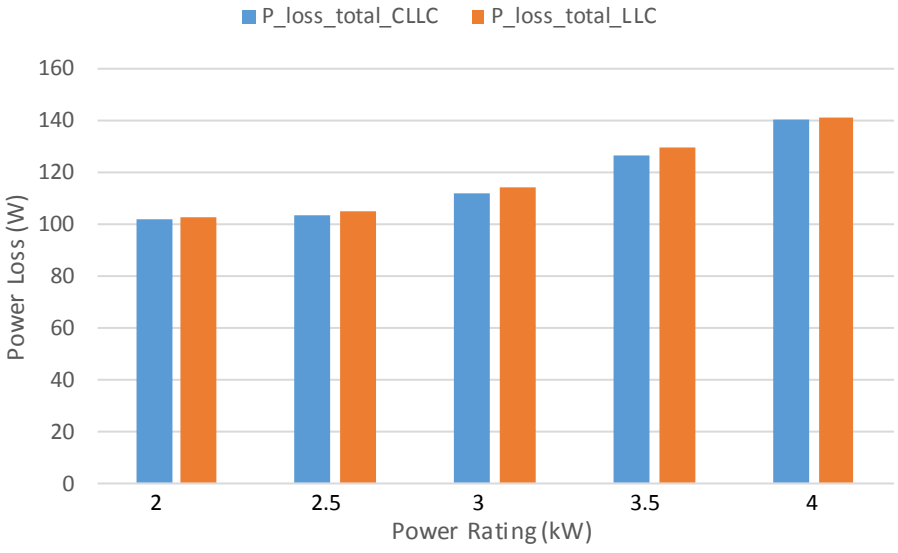

(c)

Fig. 3-35 Power loss distribution of the experimental tests in the forward mode. (a) CLLC, (b) LLC and (c) total loss comparison.

Similar to the predicted power loss distributions in Section 3.6.2, it can be illustrated that the CLLC and the LLC resonant topology exhibit similar power loss breakdown features. To be specific, due to the ZVS operation in the MOSFETs and ZCS operation in the secondary side rectifier, the switching losses are minimized. At different power ratings in both the CLLC and LLC resonant converter, the conduction loss dominates the power loss and increases when the power rating increases because the increasing RMS device currents. On the contrary, the core loss only increases slightly because the small variation of the flux density. The switching loss even decrease at 4 kW because of the decease of switching frequency. Moreover, the copper loss does not increase significantly even with large increase in the current, because the ac resistance decreases with switching frequency. With the above power loss distribution, the entire power losses in the CLLC and LLC resonant converters are compared as detailed in Fig. 3-35 (c). As indicated, the power losses in the CLLC resonant converter are approximately the same as the power loss in the LLC resonant converter, while higher loss occurs in the LLC resonant converter at higher power rating.

In summary, when the two resonant converters operate in the forward charging mode, as illustrated in the theoretical analysis in Section 3.2 and predicted in Section 3.6.2, the CLLC and the LLC topologies have similar characteristics. Thus the power loss in the CLLC and the LLC converters are comparable with the CLLC converter having a slight efficiency advantage over the LLC. This is in line with the predicted and the measured efficiency.

3.8.3.2 Power Loss distribution in the reverse mode

Similarly, the measured currents and voltages of the prototypes in the reverse mode are listed in Table 3-16 and Table 3-17 below:

Table 3-16 The test results of CLLC at different conditions in the reverse mode

Parameters	Symbol	Value	Value	Value	Value	Value	Unit
Switching frequency	f_{sw}	125.94	105.82	100	95.8773	90.9090	kHz
Battery voltage	V_{bat}	238.33	270.539	305.475	351.791	402.183	V
Battery current	I_{bat}	9.0044	8.9378	9.0055	8.9845	8.338	A
DC link voltage	V_{DC}	383.74	384.219	380.487	387.635	380.223	V
DC link current	I_{DC}	5.3077	5.9293	6.8066	7.6759	8.2788	A
Primary current	$I_{Ls,\ rms}$	6.0227	6.7372	7.7878	8.7966	9.4555	A
Secondary current	$I_{sec,\ rms}$	10.669	10.41	10.844	11.182	10.818	A
MOSFET turn off current	I_{off}	6.8	7	7.75	8	10	A
MOSFET peak current	$I_{pk,\ M}$	14.2	16	16.8	18	16	A
Diode peak current	$I_{pk,\ D}$	8.5	12	11.8	13.8	14.5	A

Table 3-17 The test results of LLC at different conditions in the reverse mode

Parameters	Symbol	Value	Value	Value	Value	Value	Unit
Switching frequency	f_{sw}	132.80	149.93	160	166.11	168.07	kHz
Battery voltage	V_{bat}	244.56	271.69	310.44	358.79	391.59	V
Battery current	I_{bat}	8.7375	9.0587	9.0885	9.2755	9.656	A
DC link voltage	V_{DC}	381.57	383.39	375.83	380.49	379.17	V
DC link current	I_{DC}	5.2776	5.9166	6.7232	7.5346	8.3018	A
Primary current	$I_{Ls,\ rms}$	5.9305	6.4116	7.2853	8.2632	9.1094	A
Secondary current	$I_{sec,\ rms}$	10.935	13.28	16.081	18.544	20.232	A
MOSFET turn off current	I_{off}	8.1	15.5	19.8	23.8	28	A
MOSFET peak current	$I_{pk,\ M}$	12.5	16	19.8	23.8	28	A
Diode peak current	$I_{pk,\ D}$	8	8.3	9.8	10.5	12	A

With the data listed above, the power loss distributions in the converter can be quantified based on the calculation methods in Section 3.6.1, as shown in Fig. 3-36. As illustrated in Fig. 3-36 (a), the CLLC has similar loss distributions in the reverse mode as the forward mode. The conduction loss dominates the power loss with the trend to rise with the increase of the power rating. In contrary, the copper loss decrease in higher power rating because the switching frequency is lower in order to attain higher resonant gain. However, as indicated in Fig. 3-36 (b), the LLC resonant converter operates as a SRC in the reverse mode. When the battery voltage increases from 240 to 400V, and the switching frequency needs to increase from 130 kHz to 170 kHz in order to reduce the resonant gain while attaining ZVS operation, ac loss in the magnetic components is significantly increased. In addition, higher operating frequency leads to higher switching losses in the devices. As a consequence, much higher total power losses are seen in the LLC resonant topology compared with the CLLC resonant topology, as shown in Fig. 3-36 (c).

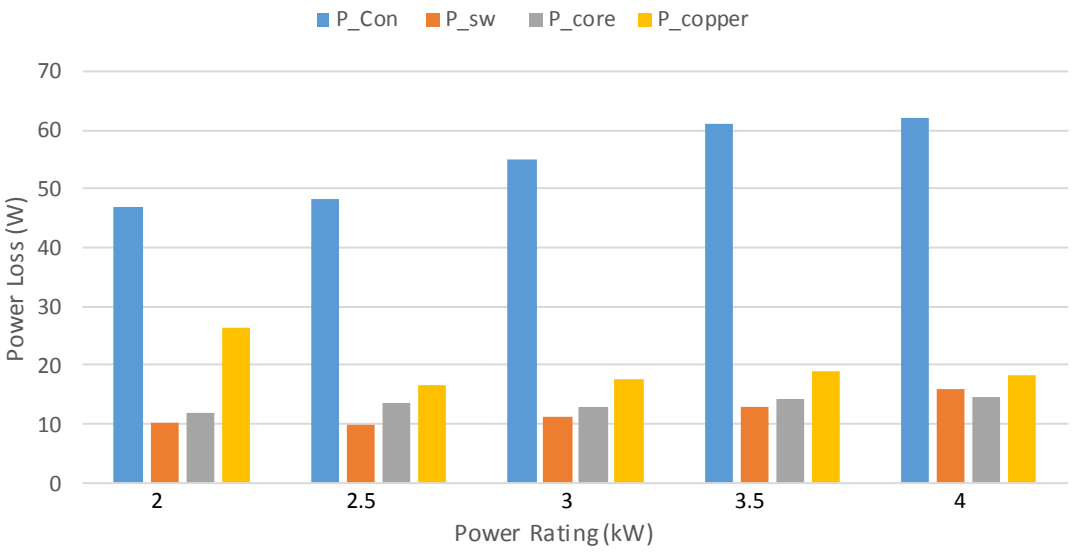

(a)

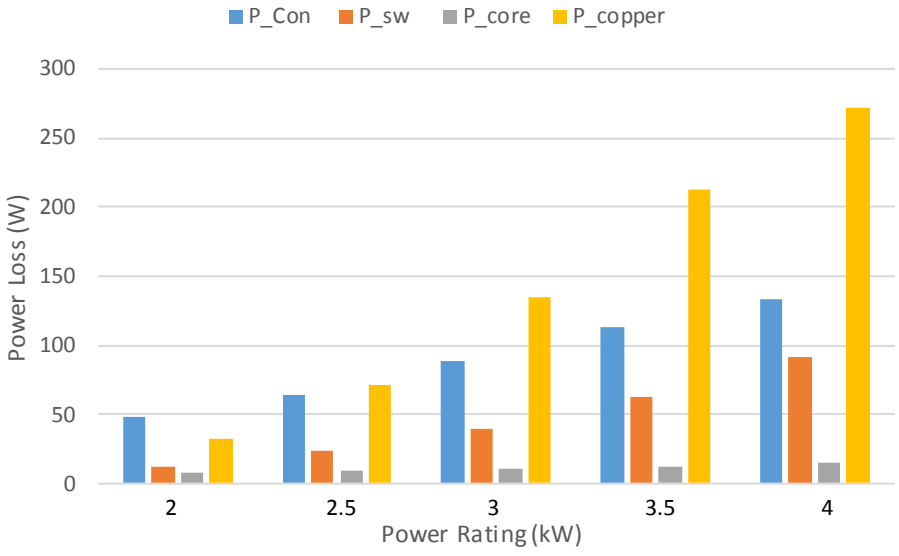

(b)

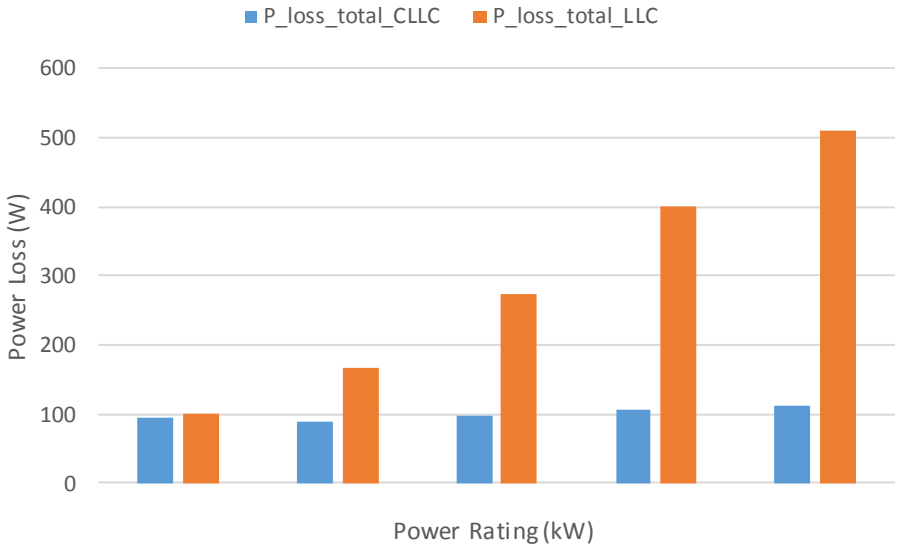

(c)

Fig. 3-36 Power loss distribution of the experimental tests in the reverse mode. (a) CLLC, (b) LLC and (c) total loss comparison.

To conclude, in order to deliver similar power in the reverse mode, the CLLC and LLC have different operation characteristics and the benefit of CLLC topology is evident especially in higher power rating, where the CLLC works at a lower frequency while the LLC has to work in higher frequency to attain ZVS therefore causing higher power losses. This is in line with the theoretical analysis and the predicted power loss in Section 3.6.2.

3.9 Summary

Based on the understanding of the operation principle, a bidirectional CLLC resonant converter is designed and optimized using fundamental harmonic approximation (FHA) analysis on the CLLC network in both G2V and V2G modes. The design process is summarized for general use. With the CLLC resonant tank, the converter achieves ZVS+ZCS features in both forward and reverse modes. Power loss prediction of the converter is implemented with the simulation results, and verified with the experimental tests. Power loss analysis shows that the efficiency of CLLC improves from 1% to 10.02 % in the whole operating range compared to the LLC alternative. The time-domain simulation and the experimental tests validates that the CLLC converter has high power conversion efficiency and high power density (with reduced heat-sink), and it is a suitable candidate for a bi-directional on-board battery charger.

From the above analysis, CLLC topology can increase the efficiency especially in the reverse mode. However, the current still exhibits a large distortion at heavy loads, which will cause more power loss. To solve this problem, variable DC link control will be developed for the CLLC converter, which will be described in the next chapter. In addition, the copper loss of the converter may not be predicted with a good accuracy, and this issue will be investigated in chapter 5.

CHAPTER 4
Optimum Resonant Frequency Tracking with Variable DC link Voltage Control for the CLLC Resonant Converter

This chapter presents an optimum-resonant-frequency-tracking scheme to further enhance the efficiency of the CLLC DC-DC converter proposed in Chapter 3. The operation of the CLLC resonant tank is analysed to identify the optimal operating frequency for this converter. In order to maintain the operating frequency close to the optimum resonant frequency corresponding to the maximum efficiency point in a wide battery voltage range, the DC link voltage is adjusted accordingly when the battery voltage varies. Thus, the resonant converter is always operating with less circulating current in the resonant tank and transformer, less turn-off current in the primary side MOSFETs and less di/dt in the secondary side diodes. Simulation and comparison with the conventional fixed DC link voltage are presented to verify the effectiveness of the proposed control scheme.

Part of the contents in this chapter has been published in [121] by the author.

4.1 Introduction

It is well known that the terminal voltage of automotive batteries varies as a function of its state-of-charge (SoC) [23, 145, 146]. Therefore, if a traditional frequency controller is employed for the LLC or CLLC resonant converter with a constant DC link voltage, the switching frequency deviates from the series resonant frequency when battery voltage or state-of-charge (SoC) changes in order to maintain constant charging or discharging current. In the reverse V2G mode this can lead to operation at much higher frequencies and increased converter losses due to waveform distortions and larger circulating current in the resonant tank [147]. However, constant DC link voltage is not absolutely necessary to maintain operation of the converter. Power flow can still be guaranteed with variable DC link. One of the solutions to alleviate the problem and therefore increase efficiency for unidirectional forward mode LLC battery charger is the maximum efficiency tracking method [140, 148-150] where the input voltage across the DC link is varied proportional to the battery voltage. By doing so, the converter always operates close to its series resonant frequency over a wide battery voltage range. However, this technique has not been analysed, evaluated and applied to bi-directional power flow converters with the CLLC topology. One of the key challenges is to identify the optimal operating frequency and resonant gain at which to operate the CLLC resonant converter, since compared with the LLC resonant converter featuring three-element resonant tank, the CLLC has different

resonant gain characteristics and different resonant frequency features with four-element resonant tank.

To further improve the power conversion efficiency, in this chapter, the maximum efficiency tracking method employing variable DC link control strategy is designed and implemented for the bidirectional charger. Section 4.2 analyses the operation of resonant converter over different switching frequency ranges in both forward and reverse modes in order to identify the optimized operating frequency. Section 4.3 describes control design for maintaining the optimal operating frequency by varying DC link voltage and evaluates the performance. Simulation studies based on the time-domain model are performed in Section 4.4. Section 4.5 describe the experimental tests and efficiency comparisons of the proposed control with conventional techniques.

4.2 Optimum Frequency Selection

The power loss analysis in Chapter 3 has shown that, the power loss is related to the current and voltage in the circuit. To be specific, the device conduction losses are dependent on the MOSFET on-state RMS current (I_{D_RMS}), diode average current (I_{F_av}) and the diode RMS current (I_{F_rms}). The switching losses are functions of the turn-on and turn-off current denoted by I_{Don} and I_{Doff} respectively. The core loses is affected by the peak current through the inductor and transformer. RMS currents through the series inductor (I_{Ls_rms}), primary side (I_{pri_rms}) and secondary side of transformer (I_{sec_rms}) determine the copper losses in the inductor and transformer.

This implies that with less current distortion, lower di/dt, lower turn-on turn-off current, the power loss is minimized and power conversion efficiency can be improved. Thus, the operating waveforms in both forward (G2V) and reverse (V2G) modes at different conditions are analysed in this section to identify the optimized operation frequency for minimized power loss.

4.2.1 CLLC forward mode

The gain curve of the typical CLLC resonant converter, is shown in Fig. 4-1.

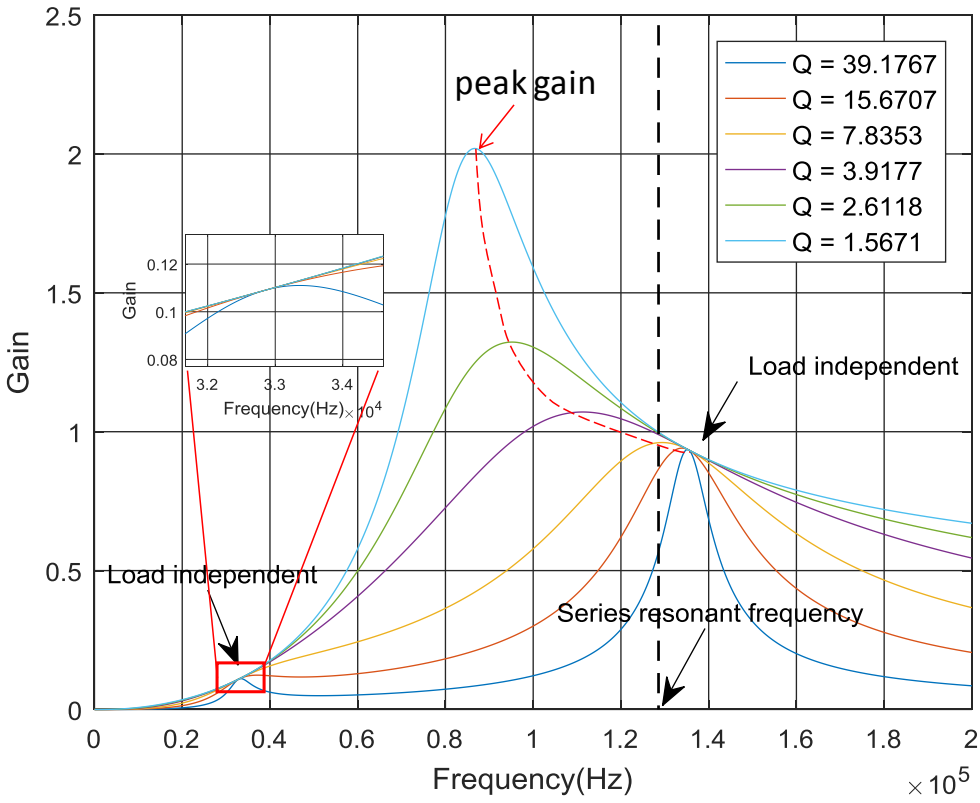

Fig. 4-1 Voltage gain characteristics of a typical CLLC resonant converter in the forward mode

As analysed in the previous chapter, the resonant tank has inductive characteristic and ZVS operation in the region above the peak series frequency which corresponds to the peak gain for a given load. While in the region below the system resonant frequency, the converter operates at ZCS condition with capacitive feature which should be avoided. Therefore, although the two load-independent points can be observed in the gain curve, the one in higher frequency (which is close to the series resonant frequency) is preferred for the purpose of coping with the battery voltage variation. Since series resonant frequency is the favorable operation frequency in the LLC converter[140, 151], operations of the CLLC resonant converter when the switching frequency is below, above and at the series resonant frequency in the forward mode is analysed in this section.

Fig. 4-2 shows the typical voltage and current waveforms of the CLLC resonant converter in ZVS operation zone when the switching frequency is below, above and at the series resonant frequency. As the detailed operation of CLLC has been analysed and presented in Chapter 3, only the series inductor current, parallel inductor (magnetizing inductor) current and secondary side rectifying diode current are illustrated, from the top to the bottom in each set of waveforms.

As can be seen in Fig. 4-2 (a), the converter operates in the region where the operating frequency is below the series resonant frequency. As already shown in Chapter 3, during this discontinuous current mode (DCM). When the secondary diode current is zero or discontinuous, there is no current going through the transformer and the transformer secondary is separated with the primary. The parallel magnetizing inductor participates in the resonance and the resonant current is circulating only in the primary side without delivering any power to the load side. This operating mode causes more circulating current and more loss for a given amount of power transfer. Hence, compared with continuous current mode, to deliver the same power to the output, more RMS current is needed in the resonant tank, which will cause more conduction loss in the devices, and more losses in the resonant tank.

When the switching frequency is over the series resonant frequency, as shown in Fig. 4-2(b), the primary side devices have high turn-off current while the secondary side diodes turns off rapidly at high *di/dt*, both of which lead to high switching losses. In addition, higher operating frequency away from the series resonant frequency is not preferred in the CLLC resonant converter because this will result in smaller gain which makes it not easy to meet the output requirement especially with wider output voltage variation conditions. When the switching frequency is close to the series resonant frequency, as can be seen in Fig. 4-2 (c), the resonant current is almost pure sinusoidal without large distortion. The circulating current is much less which corresponds to minimum circulating energy and low conduction losses. As illustrated in the previous chapter, the conduction loss dominates the total power loss in the forward mode. The circulating energy of the resonant tank is minimized, which will lead to lower conduction loss and the increased conversion efficiency. Moreover, the primary side switches turn on at ZVS with less turn-off current and the secondary side diodes turn off at ZCS with low *di/dt* which implies low switching losses. The reverse recovery losses in the rectifying diode are eliminated. This is consistent with the power loss analysis in Chapter 3.

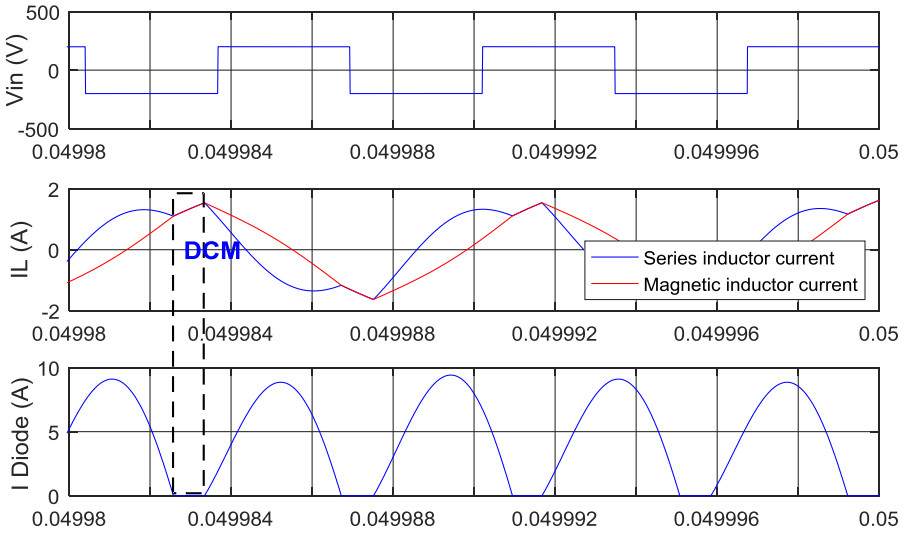

(a)

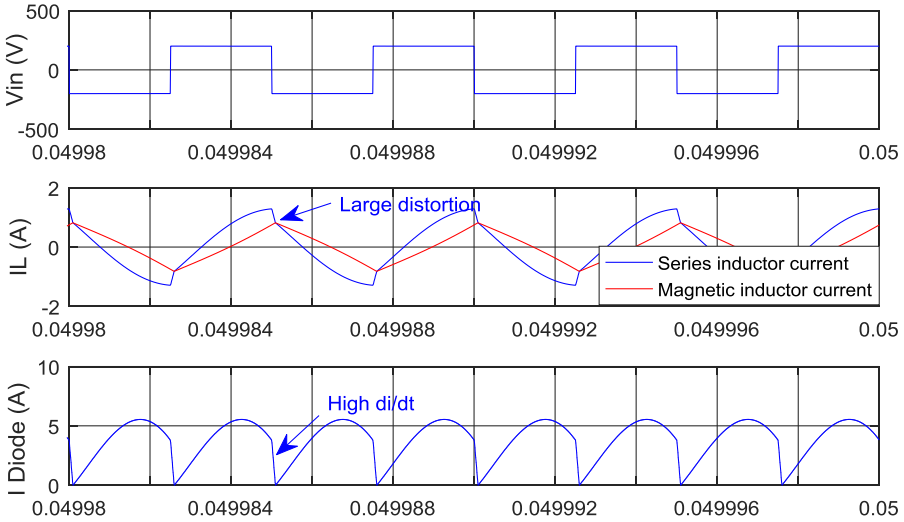

(b)

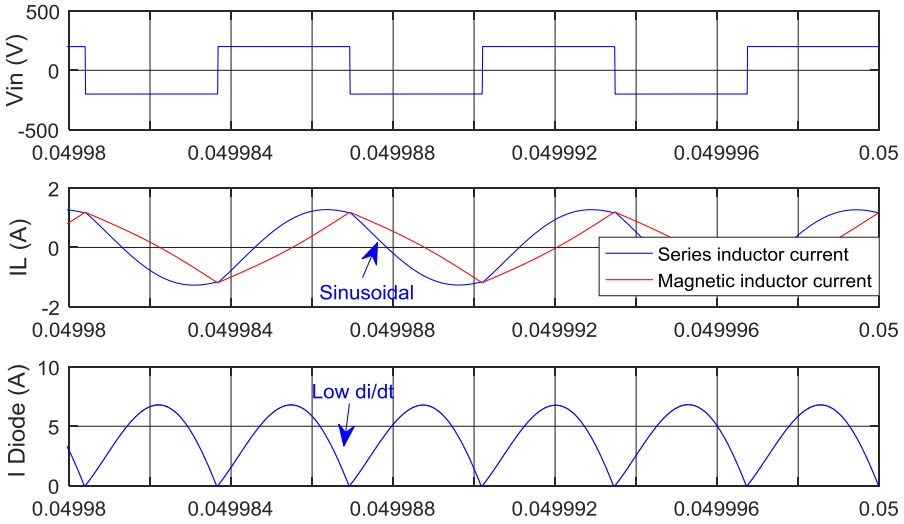

(c)

Fig. 4-2 Typical CLLC resonant converter operation when the switching frequency (a) below, (b) above and (c) at series resonant frequency

Thus, operating at the series resonant frequency is beneficial for minimized losses and maximum conversion efficiency. This frequency operating point is the optimized point to be maintained in the whole operating range.

4.2.2 CLLC reverse mode

Similarly, Fig. 4-3 shows the voltage gain characteristic of the CLLC resonant converter in the reverse mode. The typical waveforms of the CLLC resonant converter in reverse mode when the switching frequency is above, equal to and below the series resonant frequency are illustrated in Fig. 4-4.

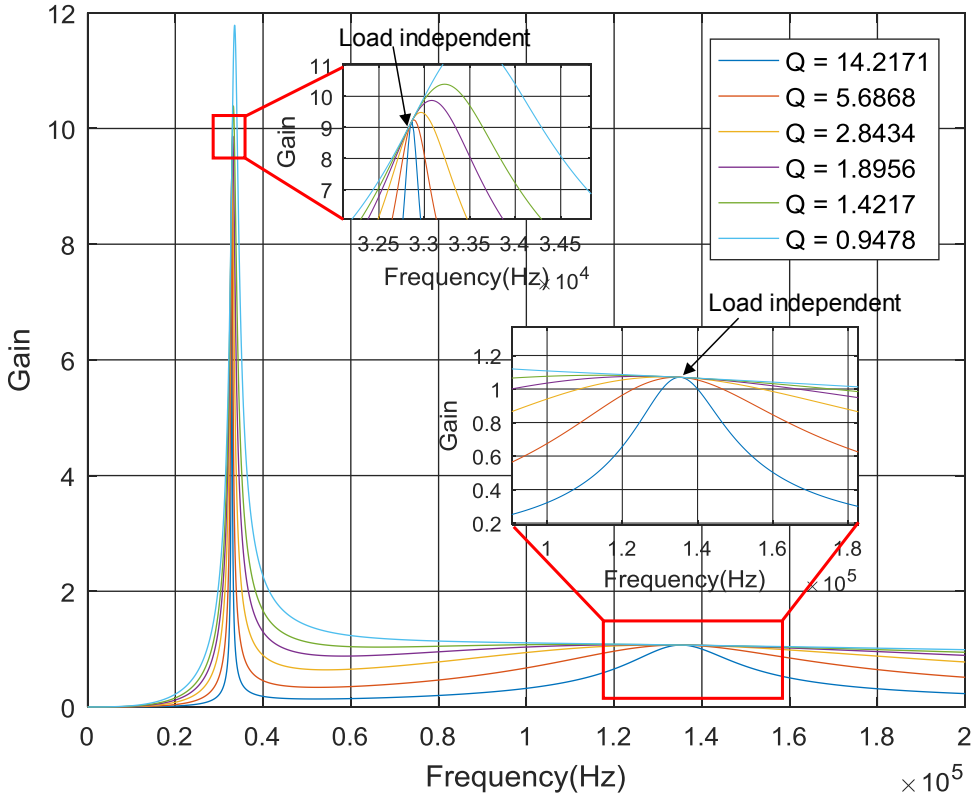

Fig. 4-3 Voltage gain characteristics of the CLLC resonant converter in the reverse mode

Differing from the conventional LLC resonant circuit, the CLLC topology has advantages of similar operational characteristics in both the forward mode and reverse mode.

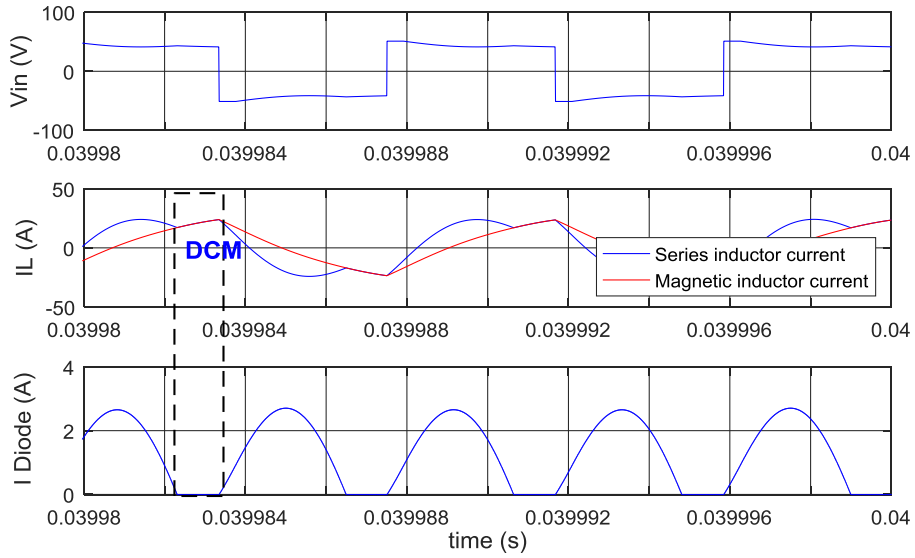

(a)

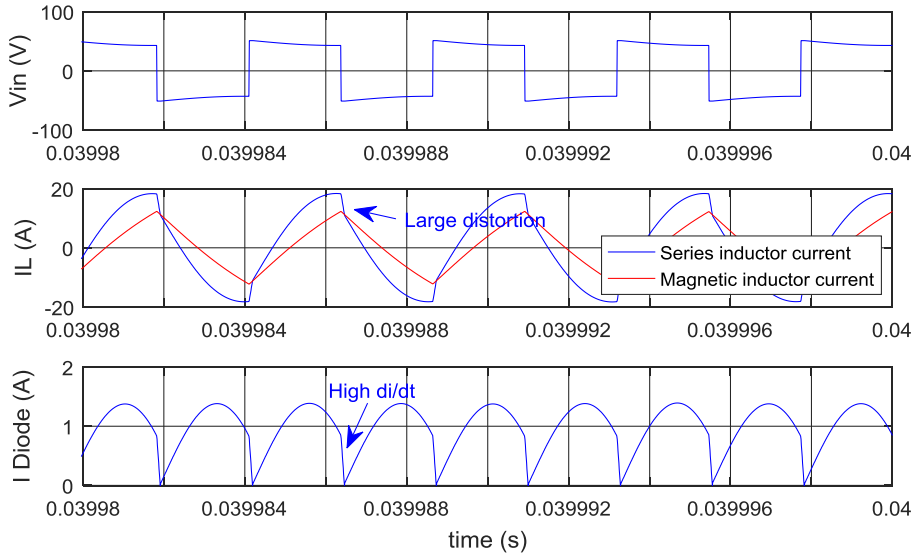

(b)

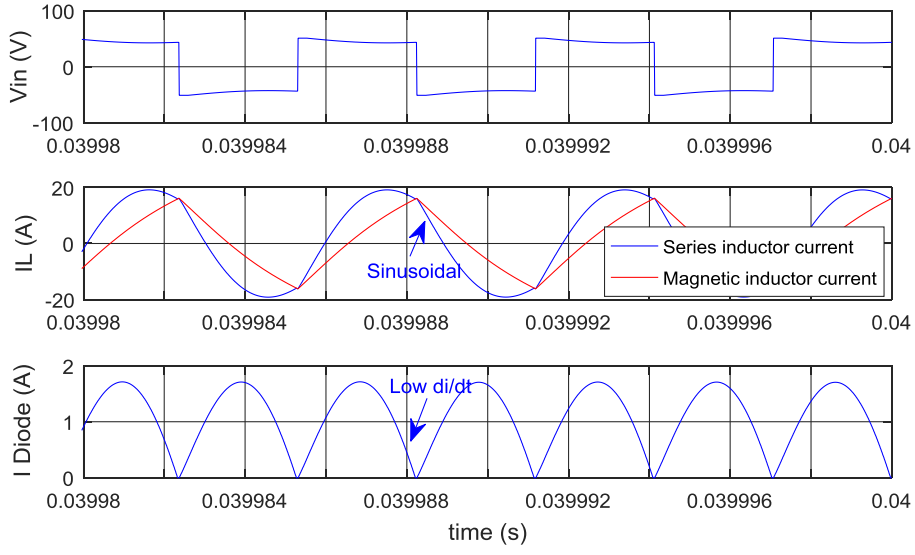

(c)

Fig. 4-4 Typical CLLC resonant converter operation in reverse mode when the switching frequency is (a) below, (b) over and (c) at the series resonant frequency

When the switching frequency is below the series resonant frequency, as can be seen in Fig. 4-4 (a), the converter operates at the discontinuous current mode. The current in the transformer primary becomes zero and the resonant current is circulating only in the secondary side without delivering any power to the DC link side. Consequently, more circulating current and more losses in the devices and resonant tank occur. More RMS current is required to deliver the same power with more losses.

As observed in Fig. 4-4 (b), high turn-off current and high diode *di/dt* can be seen in the region over the series resonant frequency, which results in high switching losses.

Similar to the operation in the forward mode, when the switching frequency is close to the series resonant frequency, as can be seen in Fig. 4-4 (c), the resonant current in the reverse mode is almost pure sinusoidal with lower current distortion, smaller circulating current and less peak current, corresponding to lower conduction loss, lower switching loss and lower loss in the resonant tank. The ZVS operation with less turn-off current in the secondary side switches and ZCS operation with low *di/dt* in the primary side diodes can be maintained, leading to lower switching losses.

It follows that for the reverse mode, operation at (or close to) the series resonant frequency is beneficial for minimizing the losses and maximising the conversion efficiency. This frequency operating point is the optimized resonant frequency to be maintained in the whole operating range.

4.3 Optimal Resonant Point Tracking

4.3.1 Variable DC link control scheme

As explained in the previous section, when the CLLC resonant converter operates at the optimized resonant frequency in both forward mode and reverse modes, the power loss will be minimised. However, the conventional control method for the CLLC resonant converters is to adjust the switching frequency in order to regulate the output current. To cater for a wide variation of battery voltage resulted from the change in battery SoC, the switching frequency needs to be regulated widely and deviate significantly from the series resonant frequency especially in higher power rating or under light load conditions.

To keep the switching frequency close to the optimized resonant frequency that corresponds to the maximum efficiency point, the DC link voltage of the front end converter may be varied. By adjusting the DC link voltage through the front end controller

based on the battery voltage variation, the switching frequency can be regulated at the optimized resonant frequency and the resonant current is always close to a pure sinusoidal shape, with minimum circulating current and low *di/dt*. By doing so, the power loss can be minimized across a wide operating range and thus the power conversion efficiency can be optimized without adding any additional circuit or employing complicated control strategy.

It is of note that the PFC power loss linearly increases with higher DC link voltage. However, since in high power raging, the switching loss dominates the power losses and the DC-DC converter loss dominates the total power loss, the increase of DC link voltage will not decrease the total power efficiency greatly.

Fig. 4-5 shows the overall control structure for the battery charger which includes a front end AC-DC converter for active power factor correction (PFC) and a DC-DC converter to regulate the battery current. The controller consists of an inner current control loop to regulate the battery current by adjusting the switching frequency and an outer voltage control loop to adjust the DC link voltage. The voltage controller is integrated into the front end converter.

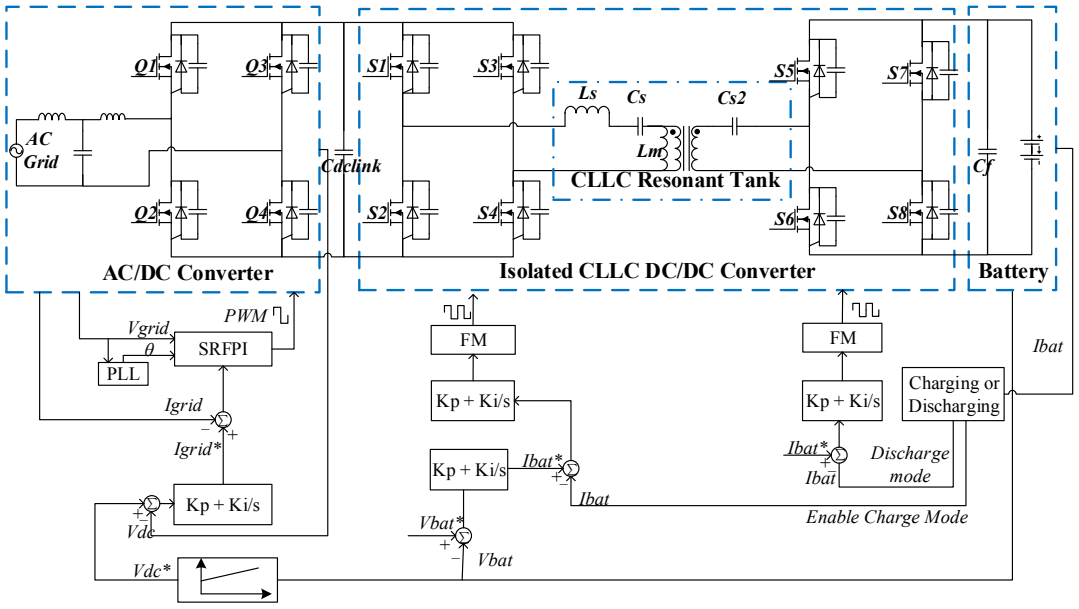

Fig. 4-5 Variable DC link voltage control diagram

The real-time voltage and current of the battery are detected with the voltage transducer and current transducer. The charging mode and discharging mode can be set in the code and be verified by detecting the current direction. At each control loop

calculation step, the DC link voltage reference for the front end voltage controller is computed based on Equation (4-1), where G is the gain of the resonant tank at the optimized resonant frequency , N is the transformer turns ratio and V_D is the voltage drop across each rectifying MOSFET body-diode. Thus, the DC link voltage increases in proportion to the battery voltage in the forward mode (charging increases battery voltage) and vice-versa in the reverse mode.

$$V_{DC}^{*} = \begin{cases} \left(1/G\right) \cdot N \cdot (V_{BAT} + 2V_D), & Forward\ mode \\ G \cdot N \cdot (V_{BAT} + 2V_D), & Reverse\ mode \end{cases} \quad (4\text{-}1)$$

For example, in the constant current charging mode, the battery is charged with constant current, and the voltage increases gradually during this period. In the conventional frequency control approach, the switching frequency is adjusted to regulate the resonant gain for maintaining the constant charging current. While in this proposed control strategy, the battery current and voltage are sensed and fed to the compensation based on Equation (4-1) to generate reference DC link voltage command (*VDC*),* for generating the demand reference of the grid current (I_{grid}*) through the front-end controller. I_{grid}* is then tracked by the synchronous rotating frame PI (SRFPI) controller which generates the PWM signals to drive the H-bridge in the front-end and eventually track the DC link voltage. With the variable DC link voltage, the current controller is able to track any current demand by varying the switching frequency in a much reduced range close to the optimized resonant frequency. In the reverse discharging mode, the DC link voltage is varied according to the battery voltage and the controller is operated in the similar manner.

With this control approach, the switching frequency is tuned to be close to the optimal resonant frequency automatically, while the DC link voltage varied according to the battery voltage, through the multi-control loops. Thus the maximum efficiency point can be tracked continuously across the wide battery voltage variation and the conversion efficiency of the converter is optimized over the wide operation range.

4.3.2 DC link voltage variation range

Since the DC link voltage reference for the front end voltage controller is calculated in relation to the variation of the battery voltage it is necessary to constrain its range in order to ensure power delivery and safe circuit operation. Fig. 4-6 shows the flowchart to determine the battery voltage range between $V_{battery\_low}$ and $V_{battery\_high}$. First the lower and

upper limit of the voltage across the resonant tank, denoted by V_{tank_low} and V_{tank_high}, respectively, can be calculated by $V_{battery\_low} * N$ and $V_{battery\_high} * N$. As the bidirectional charger is connected to the grid converter, the minimum value of the DC link voltage should meet the minimum requirement of the front end converter, which is the peak voltage of the AC grid (with +/-10% variation). The maximum value of the DC link voltage is constrained by the drain-source voltage of the switching devices (MOSFETs in most applications) and maximum voltage of the DC link capacitors.

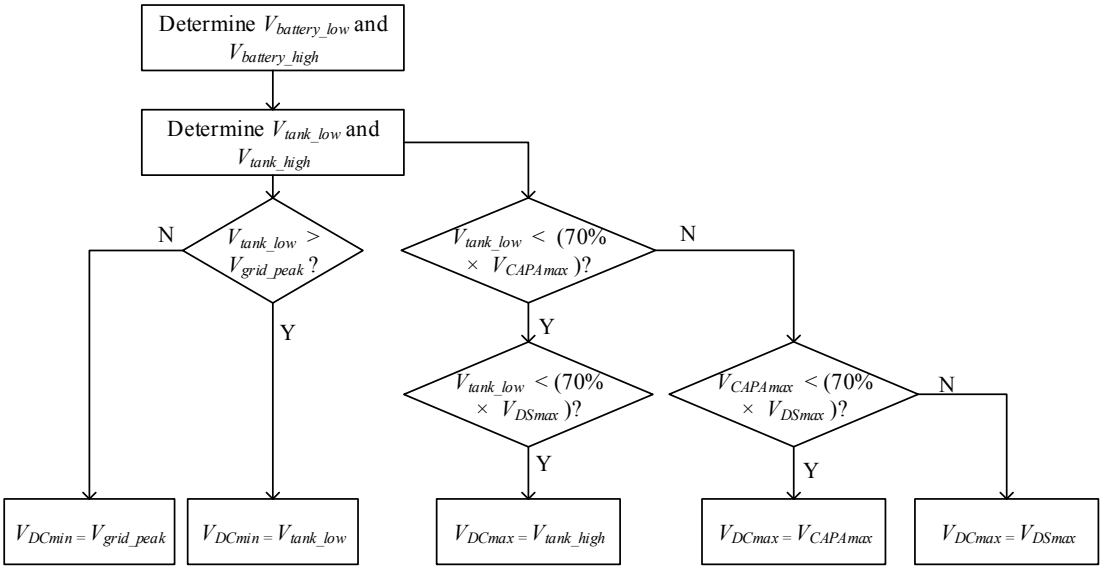

Fig. 4-6 Determine the DC link voltage variation range

Table 4-1 shows the constraint specification of the charging system designed in Chapter 3. The grid AC voltage is 230V rms (peak value 325V) with +/-10% variation, implying a minimum DC voltage range of [357V 292V] below which power flow will not occur. The battery voltage varies between 240V to 400V. The transformer turn ratio is set to 1.66 in this design. The SiC MOSFET has 1200V maximum drain-source voltage.

Table 4-1 The Constraint specification of the DC link voltage range

Parameters	Symbol	Value	Unit
Minimum Battery voltage	$V_{battery\_low}$	240	V
Maximum Battery voltage	$V_{battery\_high}$	400	V
Transformer turns ratio	N	1.66	-
MOSFET maximum drain-source voltage	V_{DSmax}	1200	V
DC link capacitor break down voltage	V_{Cf}	550	V
Grid rms voltage	V_{grid_rms}	230	V
Grid peak voltage	V_{grid_peak}	339	V
Grid peak voltage with variation	V_{grid_peak}	357	V

With the designed resonant tank, the subsequent DC link voltage varies between 370V and 609V, which can be accommodated by commonly available switching devices. However, in the experimental prototype presented in the previous chapter, the DC link capacitor has a maximum voltage rating of 550V, because this capacitor was selected based on the constant 380V DC link. Thus the DC link variation range is adjusted between [370V, 480V]. It should be noted that this compromised narrow voltage range is just for the experimental work to validate the control performance using the existing hardware setup. It is possible to improve the performance. A possible solution is to replace the DC link capacitor to achieve a higher breakdown voltage. However, it will increase the cost and size. Thus a trade-off must be taken into account.

4.4 Simulation Study

The performance of the proposed converter is assessed by simulations over the wide operating range of the battery voltages and loads with a battery charging system based on a front end AC-DC converter and the CLLC resonant converter with the specification shown in Table 4-2.

Table 4-2 The designed CLLC resonant converter specification

Parameters	Symbol	Value	Unit
Series inductor	L_s	97.0	μH
Parallel inductor	L_m	136.5	μH
Primary series capacitor	C_s	15.8	nF
Secondary series capacitor	C_{s2}	427	nF
Output filter capacitor	C_f	330	μF
AC Grid Voltage	V_{grid}	230	Vrms
AC Grid Voltage frequency	f	50	Hz
DC link voltage	V_{dc}	380	V
Battery charging current	I_{bat}	9.0	A
Battery internal resister	R_{bat}	0.1148	Ω
Battery rated capacity	$A \cdot h$	66.2	Ah
Battery fully charged voltage	V_{max}	403.2	V
Battery initial voltage	V_{min}	240	V

Fig. 4-7 shows the waveform in charging and discharging process. As illustrated, the battery voltage increases from 300V to 400V for delivering power from 2.5 kW to 4 kW during the charging operation and decreases from 400V to 300V in the reverse (discharging) operation. The DC link voltage is varied in proportion to the battery voltage variation (between 500V to 610V) and the charging/discharging current is kept constant at designed 9A. In both the forward and reverse modes the switching frequency is

regulated around the optimized resonant frequency of 134 kHz (determined in Chapter 3). Thus the maximum efficiency operation is tracked across the wide battery voltage range.

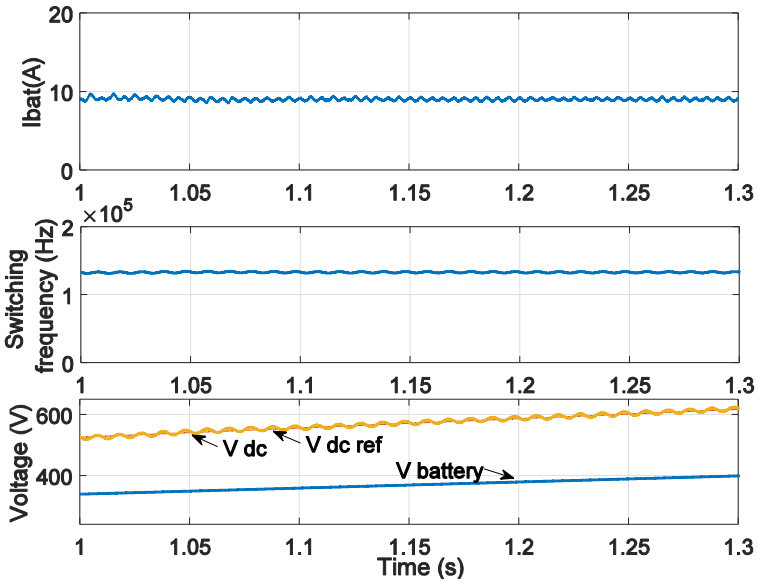

(a)

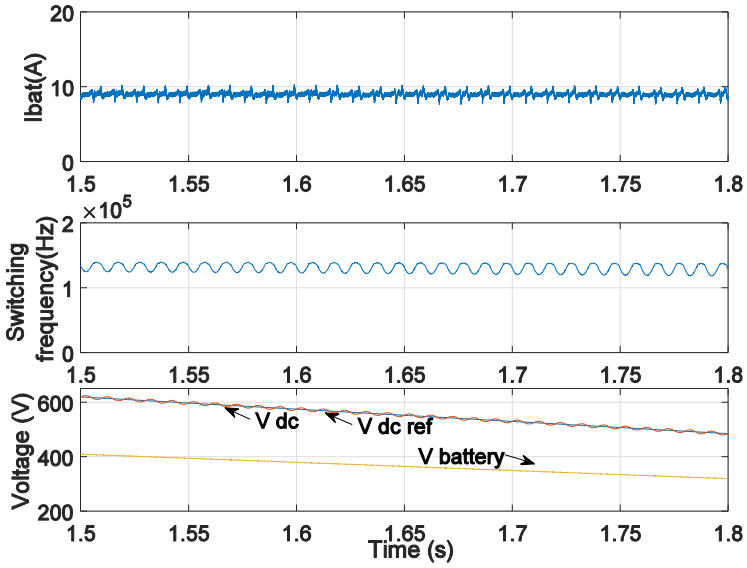

(b)

Fig. 4-7 Battery current and voltage in (a) forward charging mode and (b) reverse discharging mode

Fig. 4-8 shows the waveforms in both the forward and reverse modes at 4 kW when the DC link voltage is 600V. As can be seen, the current in the resonant tank is close to sinusoidal with low harmonic distortion and low circulating current in the resonant tank. The resonant current can be seen to lag the converter voltage, implying that the primary switching devices are operating in ZVS mode. The diode current in the rectifier side shows ZCS operation. Thus wide-range soft-switching operation is achieved from light-load to full-load conditions without using any additional switching circuits.

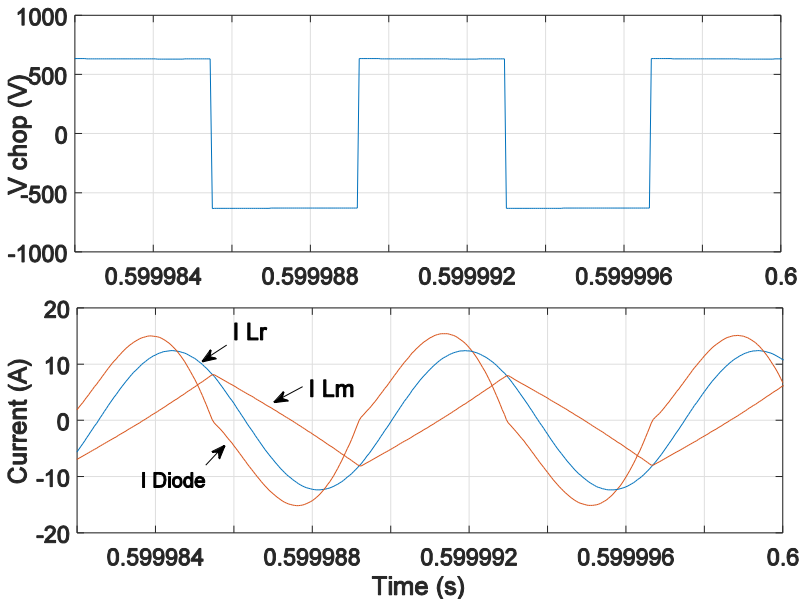

(a)

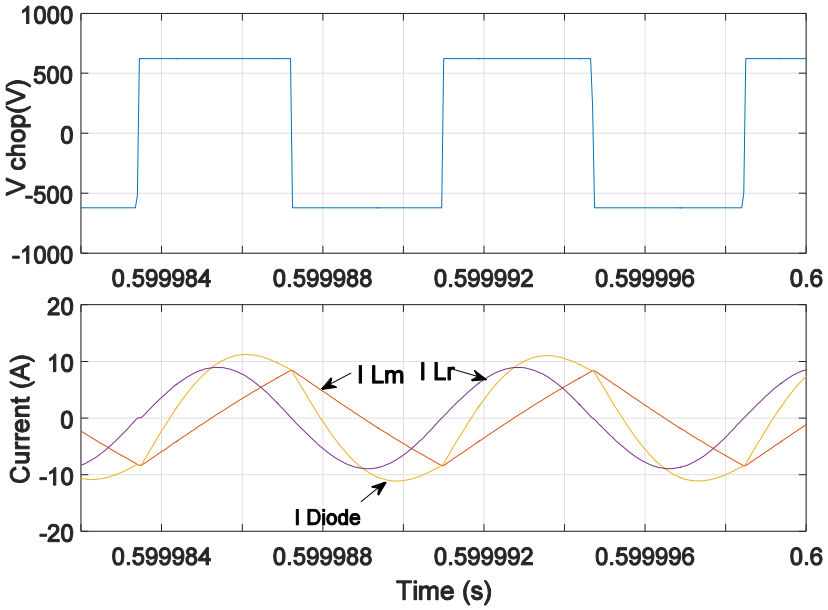

(b)

Fig. 4-8 Resonant tank and diode currents with CLLC resonant converter in (a) forward and (b) reverse mode when the DC link voltage is 600V at 4 KW.

Compared with the simulation waveforms of the conventional CLLC converter with fixed DC link voltage (380V) at 4 kW presented in previous chapter, it can be seen that in both the forward mode and the reverse mode, the proposed variable dc link voltage control results in much lower circulating current and turn-off current, which means that the switching losses are significantly reduced. In contrast, the constant DC link voltage CLLC converter is operating at DCM for the charging power, while with the proposed control the diode current is continuous, therefore the circulating current is minimized.

4.5 Experimental Tests and Validation

The CLLC resonant converter based bidirectional charger prototype has been designed and described in Chapter 3. To further improve the efficiency performance, variable DC link control is implemented on the existing prototype and compared with the converter operating at the constant DC link voltage. The target is to maintain the switching frequency close to series resonant point and attain the sinewave resonant current, while keeping the same power delivered. The prototype of the bidirectional charger and the battery load have been presented and discussed in Chapter 3.

4.5.1 Digital controller implementation

The structure of the prototype and control platform is shown in Fig. 4-9, in which the hardware is represented in blue blocks while the software coding is shown in yellow blocks. National Instrument Compact RIO 9082 Controller with 1.33 GHz Dual-Core CPU and LX150 FPGA is used as the processor. National Instrument 9215 four channel 16Bit Simultaneous Analog Input Module is used for sampling the voltage and current signals from LEM voltage sensor LV 25-p and LEM current sensor LA 25-p. National Instrument 9401 eight channel 100 ns high-speed bidirectional Digital I/O Module is used to output switching signals for the gate driving board of the H-bridges.

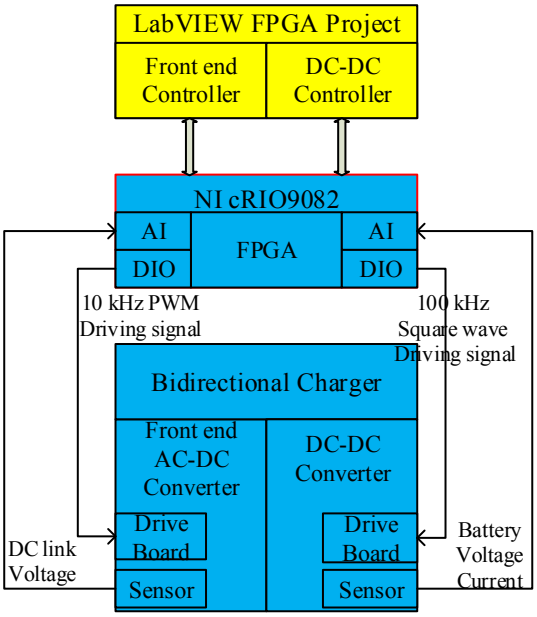

Fig. 4-9 Diagram of the Controller Implementation

The Compact RIO 9082 shown in Fig. 4-10 processes the front end controller and the DC-DC converter controller simultaneously. The I/O blocks, also shown in Fig.

4-10 have multiple differential channels which are shared between the Front end and the DC-DC resonant converter. The FPGA coding is implemented using the NI LabVIEW FPGA, which enables programming graphically digital circuits within an FPGA chip, as shown in Fig. 4-11.

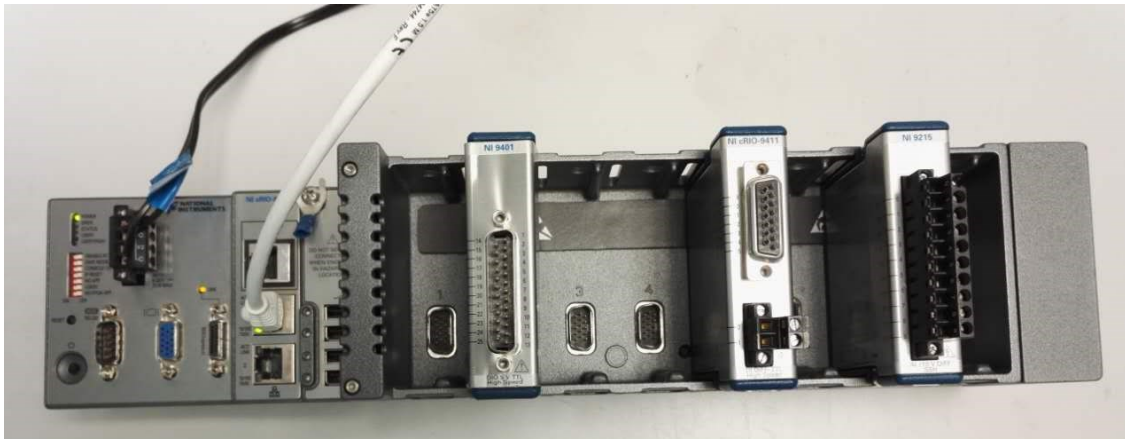

Fig. 4-10 Processor Compact-RIO 9082 and the I/O blocks

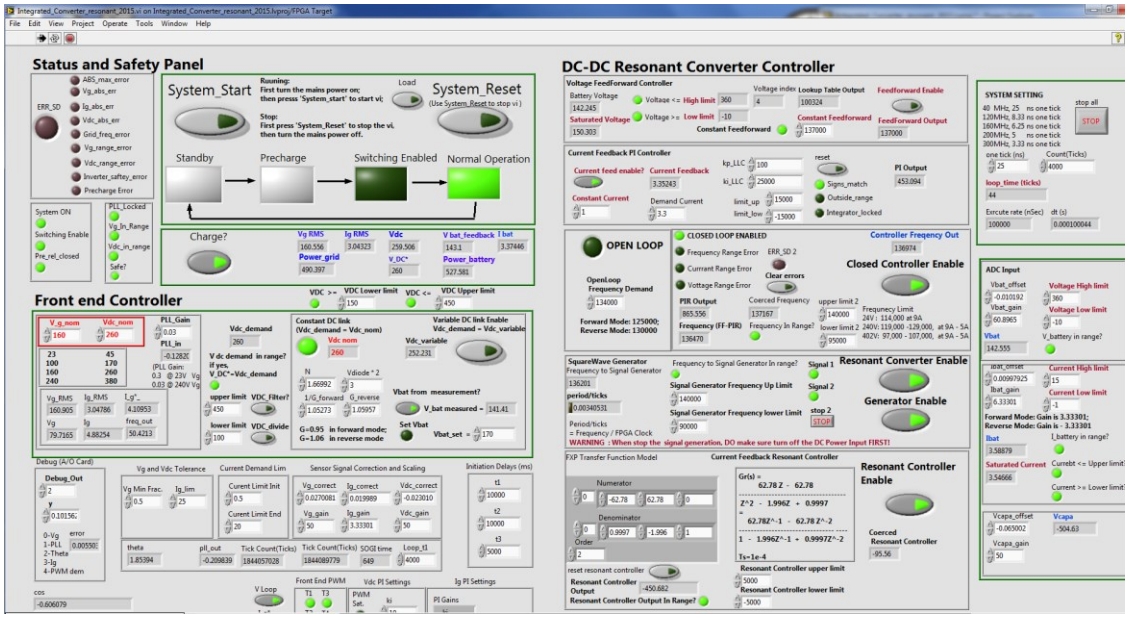

Fig. 4-11 The control coding using the NI LabVIEW FPGA programing tool

A LabVIEW FPGA project is built and the front panel contains three main parts: the Status and Safety Panel, the Front end Controller, and the DC-DC Resonant Converter Controller. The Status displays the system operation procedure, current condition, health monitoring and error indicator. The Front End Controller communicates with the DC-DC Resonant Converter Controller and they share real-time information with each other. The detailed programing code is presented in the Appendix.

As described in Section 4.3.2, the reference demand of the DC link voltage, *VDC**, is calculated and updated based on the real-time battery voltage. It should be noted that *VDC** should be constrained within the maximum and maximum range defined by Table 4-1. The error between the reference and the real-time value is compensated through a PI controller which outputs the demand reference (I_{grid}*) of the grid current controller (SRFPI) to generate the PWM signal for the front-end converter switches. In this way, the DC link voltage is tracked by voltage control loop to achieve optimal operation close to the optimal resonant frequency. The programing flowchart of one single control loop is further illustrated in Fig. 4-12.

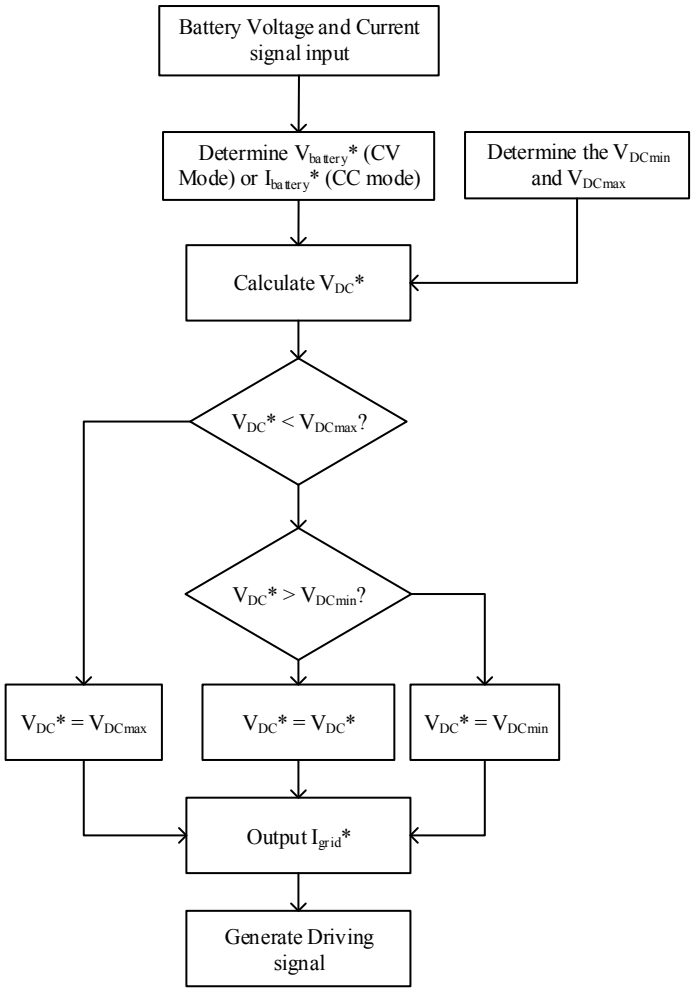

Fig. 4-12 Programming flowchart of the control algorithm

4.5.2 DC link voltage tracking operation

With the Compact-RIO processor and the programing in NI LabVIEW FPGA described above, experimental tests were performed based on the existing test rig, which has been described in Chapter 2 and Chapter 3. The measured DC-link and battery voltage

waveforms during the forward mode charging and the reverse mode discharging procedure are illustrated in Fig. 4-13.

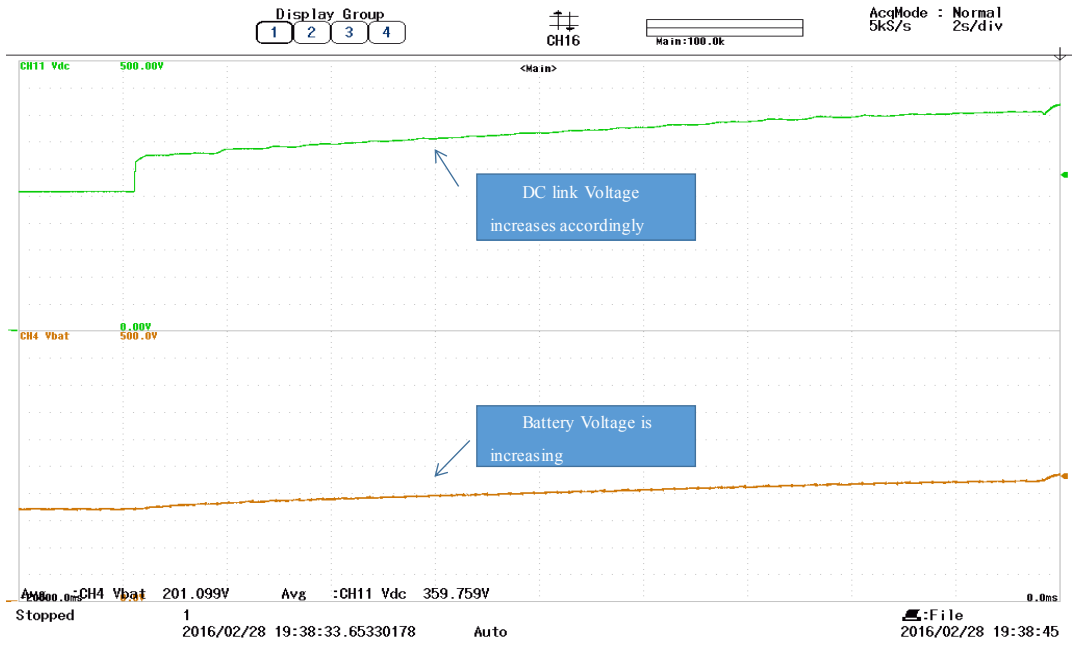

(a)

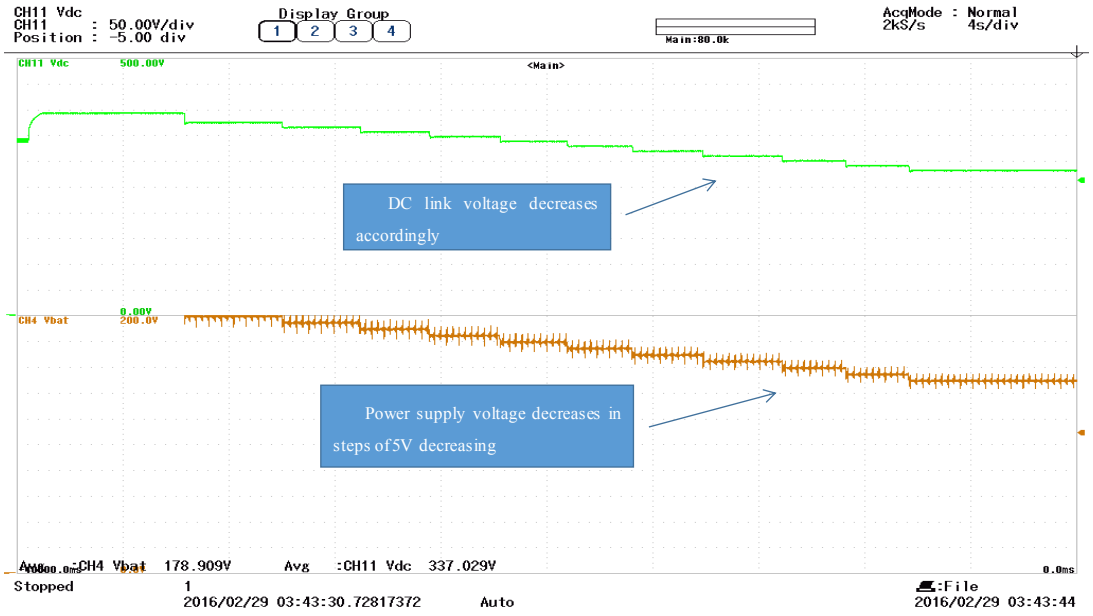

(b)

Fig. 4-13 Variable DC link voltage tracking in (a) the forward mode and (b) the reverse mode

As can be observed from Fig. 4-13 (a), when battery voltage rises from 150V to 200V at 9A constant current during charging, the DC link voltage is varied in proportion to the battery voltage variation and increases from 260V to 350V accordingly. During the tests of the reverse mode of operation, the battery is replaced by a DC power supply so that the input voltage can be varied quickly. Fig. 4-13 (b) shows the resultant DC link voltage

variation from 340V to 260V when the DC power supply (representing as the battery) decreases from 210V to 150V (in 5V step) at 9A discharging current. It can be concluded that the controller is able to track the DC link voltage effectively.

To further examine the control performance, the measured voltage and current waveforms with variable DC link controller in both forward and reverse modes at 2 kW (battery voltage 240V, battery current 10A) are shown in Fig. 4-14. From top to bottom, DC link voltage V_{DClink}, resonant tank current I_{Ls}, transformer primary side full bridge chopped voltage V_{pri}, battery side output voltage $V_{battery}$, DC link side input current I_{DC} secondary side voltage V_{sec}, and secondary side diode bridge current I_{sec} are illustrated. As can be seen, the resonant tank current is close to sinusoidal with low harmonic distortion and low circulating current while the switching frequency is regulated around the resonant frequency (134 kHz), the optimized point. The resonant current can be seen to lag the converter voltage, implying that the primary switching devices are operating in ZVS mode. The diode current in the rectifier side shows ZCS operation.

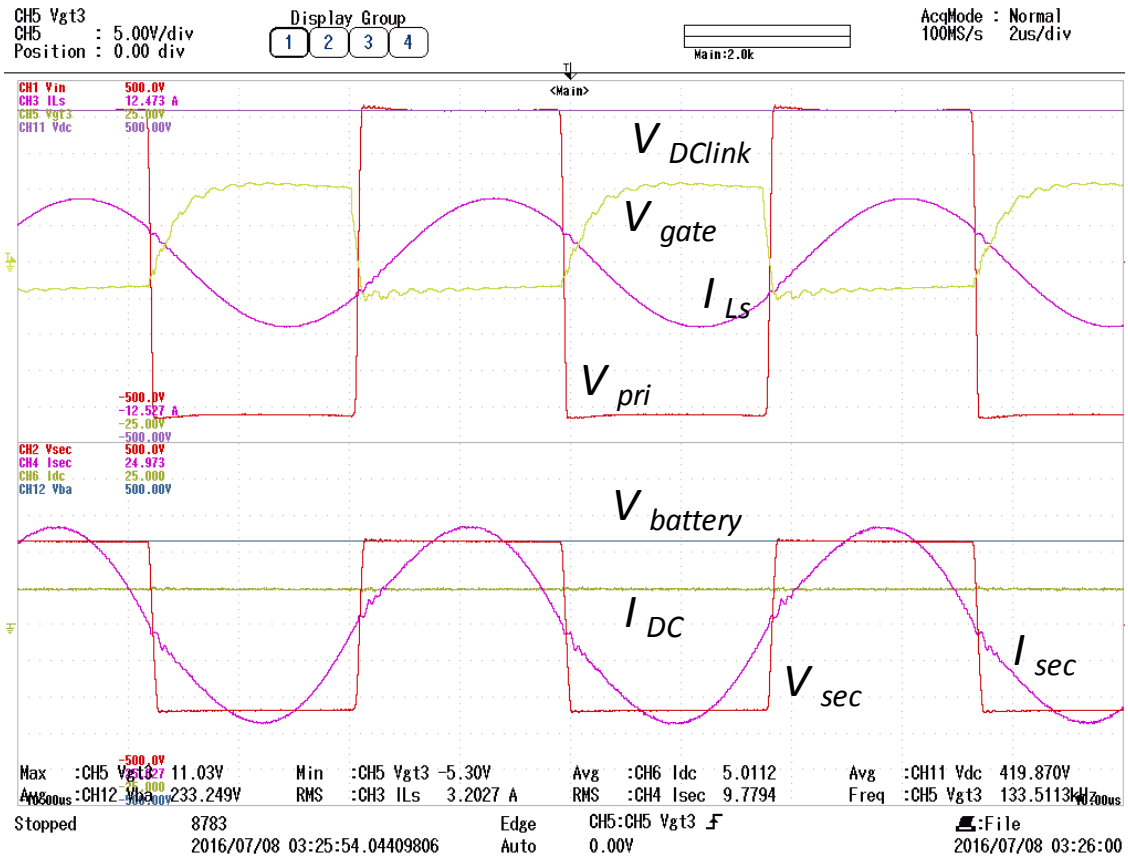

(a)

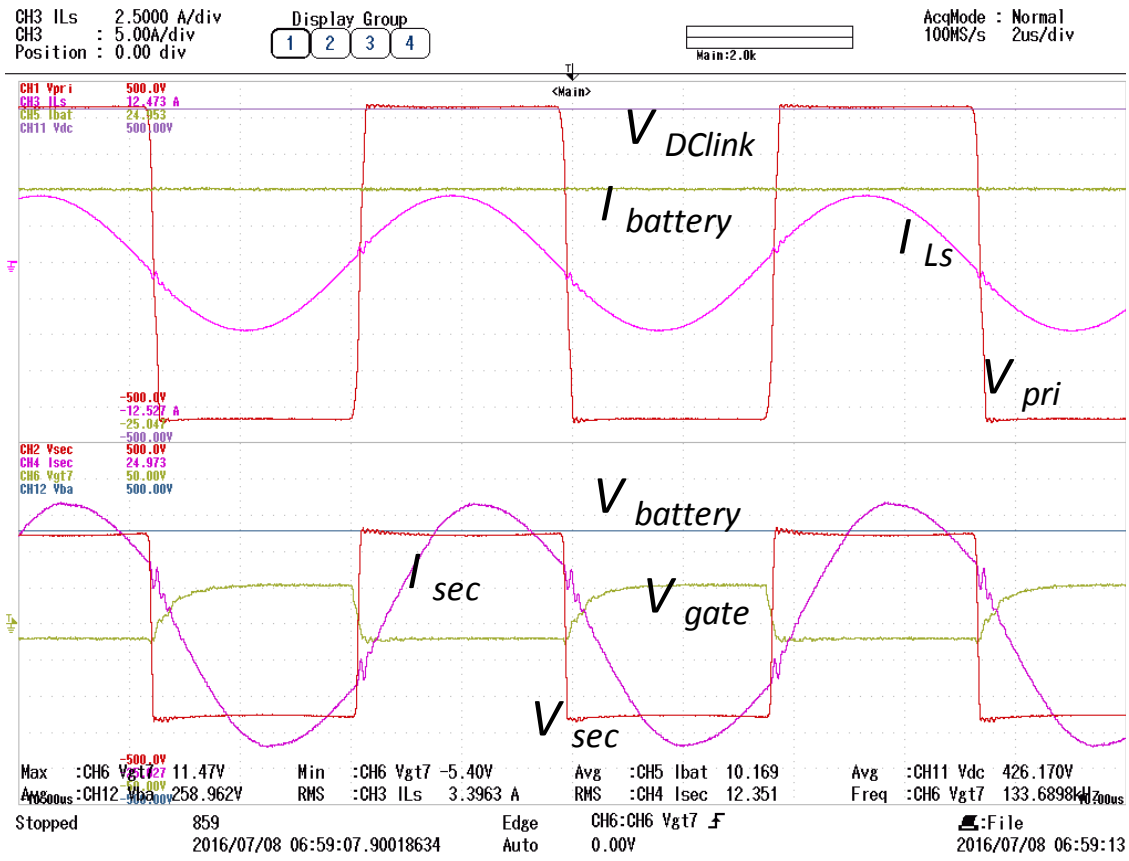

(b)

Fig. 4-14 Operation at 2kW with variable dc link in (a) forward mode; (b) reverse mode

4.5.3 Operation at different power rating

To evaluate the performance at the whole operation conditions, further tests have been implemented in both forward and reverse modes at other power ratings, and the waveforms are illustrated in Fig. 4-15 and Fig. 4-16.

As can be observed, in the forward mode, at 2.5 kW, 3 kW and 4 kW power rating, the switching frequency is kept close to 134 kHz (slightly higher than the series resonant frequency). The current waveform in the resonant tank is almost pure sinusoidal. The MOSFET turn-off current, resonant rms current, diode peak current and diode turn off *di/dt* are smaller compared the constant DC link control in Chapter 4, in which the big current distortion and high *di/dt* correspond to more circulating energy, higher conduction loss and higher switching losses. This will be further proved in the efficiency comparison later in this section. In the reverse mode, at 2.5 kW, 3 kW and 4 kW power rating, the switching frequency is also kept near 134 kHz, which is designed in Chapter 3. Also, as can be observed in both modes, the primary side devices operate at ZVS while the secondary side diodes at ZCS. It should be noticed that, as stated in Section 4.3.2, due to

the voltage limit on the capacitors used in the testing prototype, the DC link voltage is not able to be increased higher than 480V. Therefore, in order to implement the high power rating tests at 3 kW and 4 kW, the battery current is regulated with higher demands than the nominal 9A (12 A at 3 kW and 13.53A at 4kW). In this way, for delivering the same amount of power, a higher battery current results in a lower battery voltage. Therefore, the DC link voltage can be regulated accordingly within a narrower range below 480V. Although the charging/discharging current changes, the controller is still running with variable DC link voltage scheme thus this compromise will not influence the converter performance and the controller operation.

Thus, from the test waveforms, it follows that in both the forward and reverse modes, the DC link voltage is varied in proportion to the battery voltage variation across all the operating ranges. The switching frequency is regulated around the optimized resonant frequency. Thus the optimized resonant point is tracked across the wide battery voltage range.

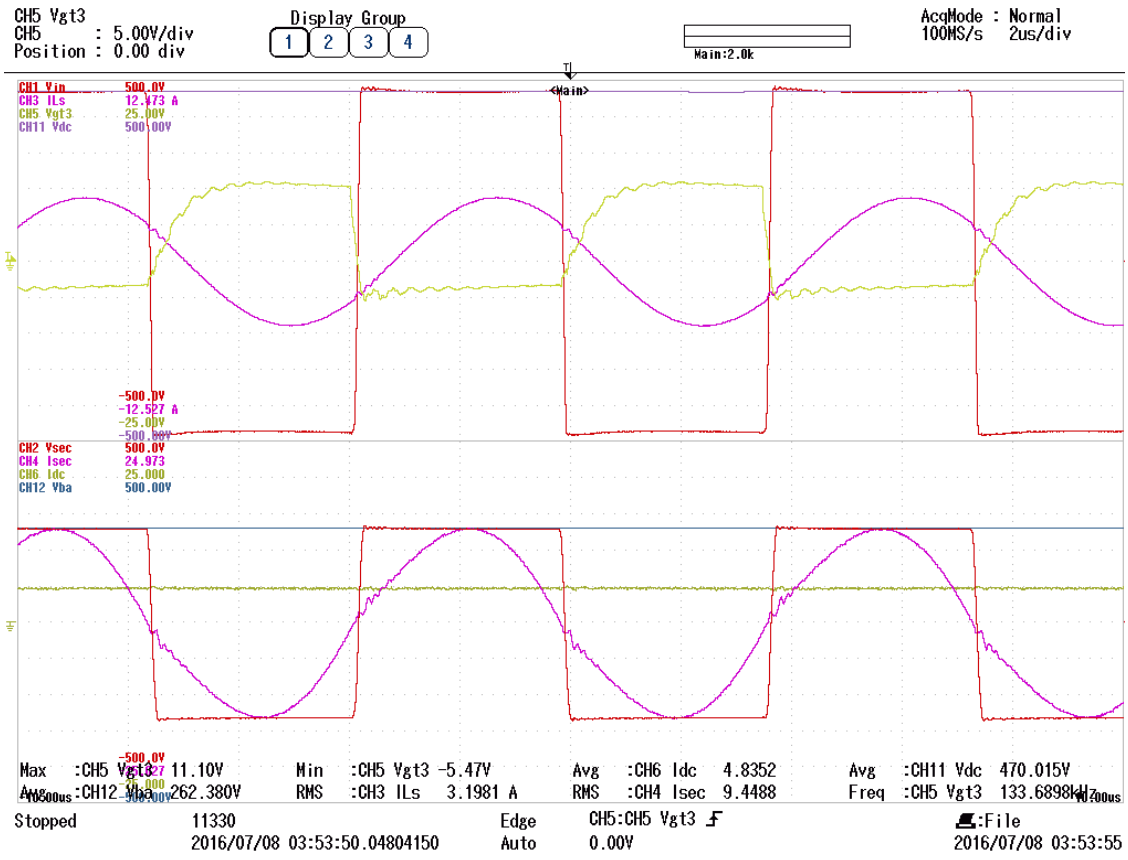

(a)

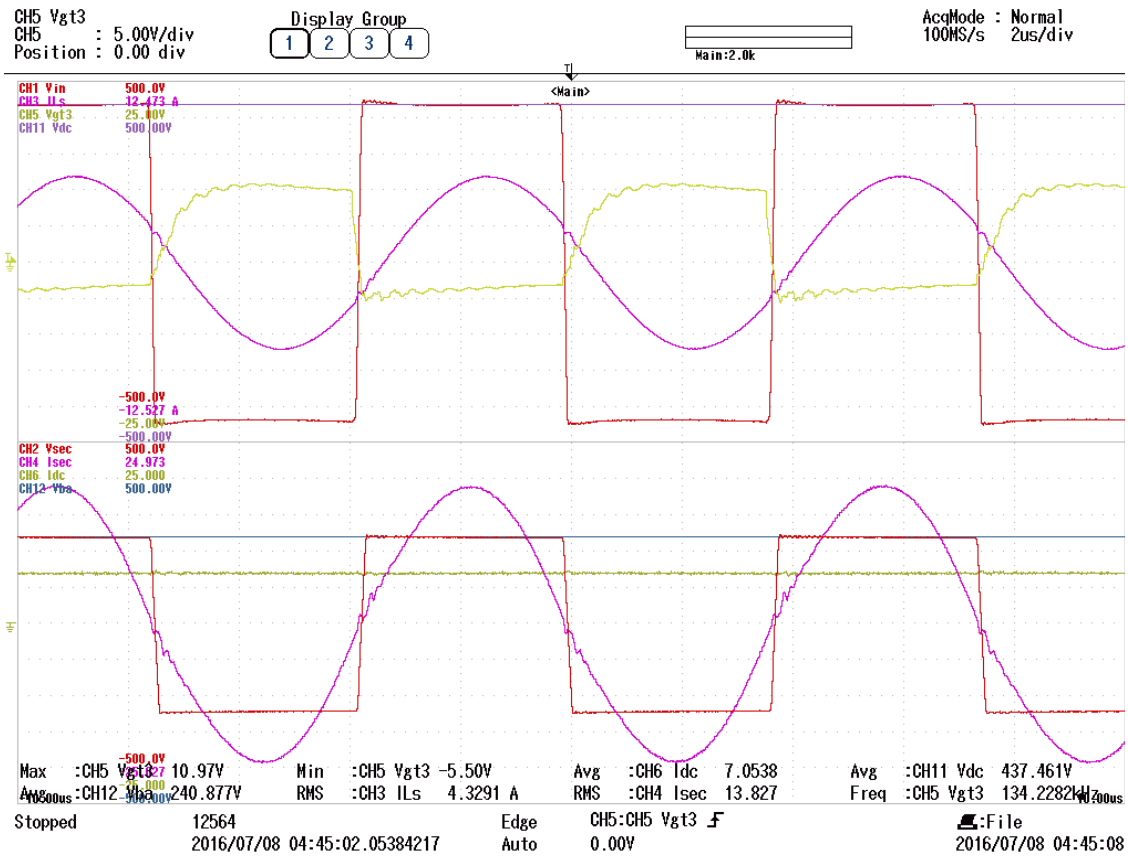

(b)

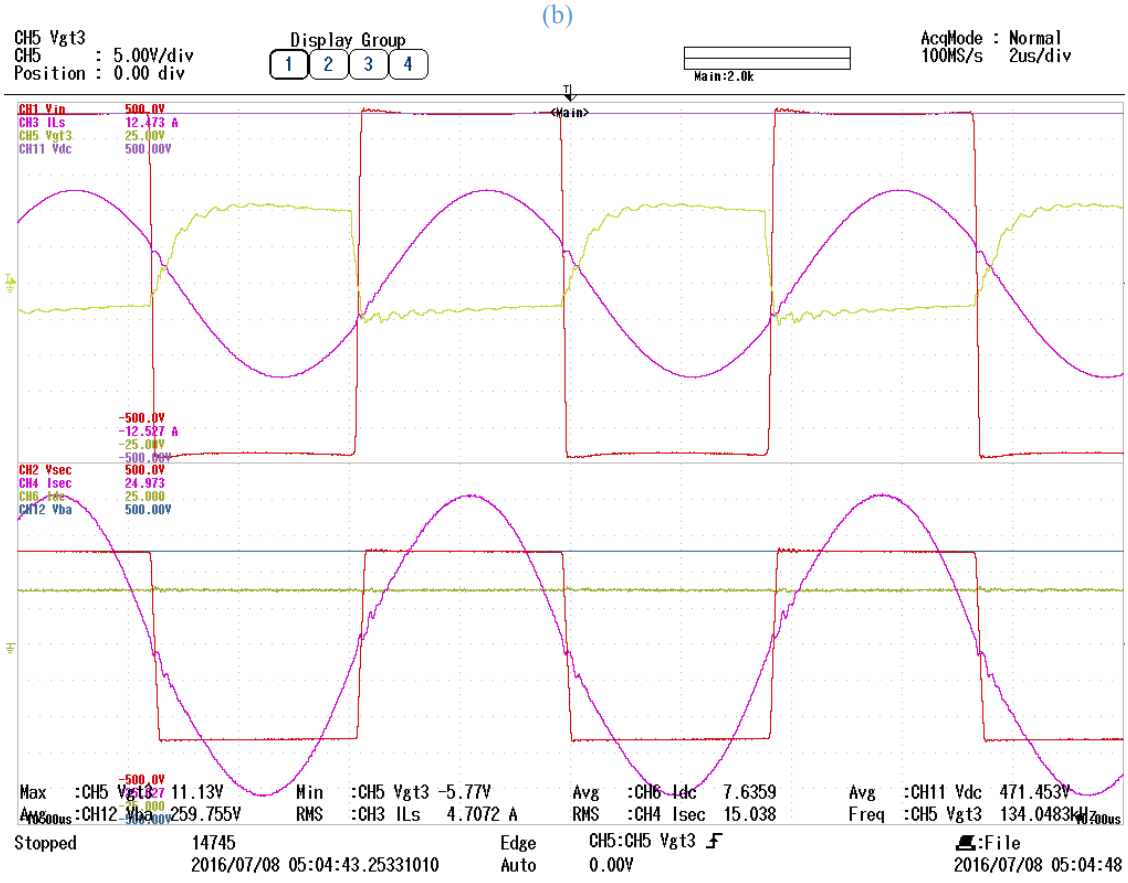

(c)

Fig. 4-15 Waveforms in the forward mode at different power rating (a) 2.5 kW, (b) 3kW and (c) 4 kW

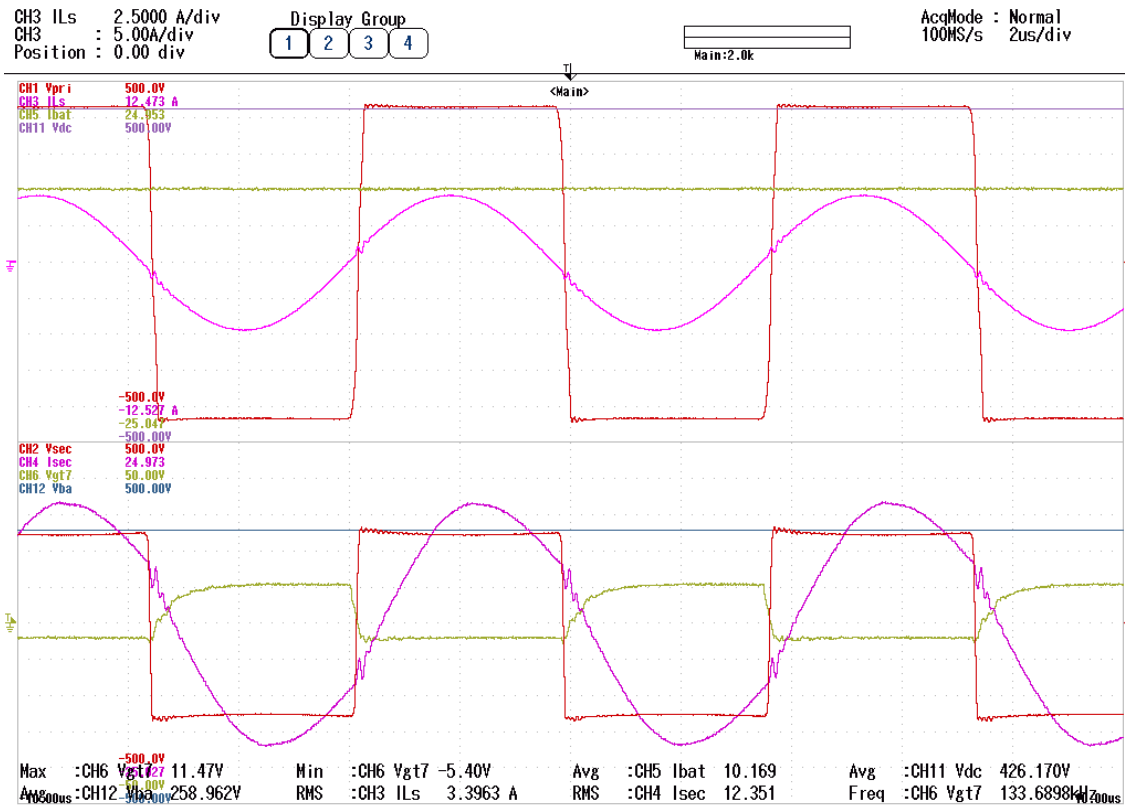
CH3 ILs 2.5000 A/div
CH3 : 5.00A/div
Position : 0.00 div
Display Group
1 2 3 4
Main:2.0k
AcqMode : Normal
100MS/s 2us/div
<Main>
CH1 Vpri 500.0V
CH3 ILs 12.473 A
CH5 Ibat 24.953
CH11 Vdc 500.00V
-500.0V
-12.527 A
-25.047
-500.00V
CH2 Vsec 500.0V
CH4 Isec 24.973
CH6 Vgt7 50.00V
CH12 Vba 500.00V
-500.0V
Max :CH6 Vgt7 11.47V
Min :CH6 Vgt7 -5.40V
Avg :CH5 Ibat 10.169
Avg :CH11 Vdc 426.170V
Avg :CH12 Vba 258.962V
RMS :CH3 ILs 3.3963 A
RMS :CH4 Isec 12.351
Freq :CH6 Vgt7 133.6898kHz
Stopped
859
2016/07/08 06:59:07.90018634
Edge
Auto
CH6:CH6 Vgt7
0.00V
:File
2016/07/08 06:59:13

(a)

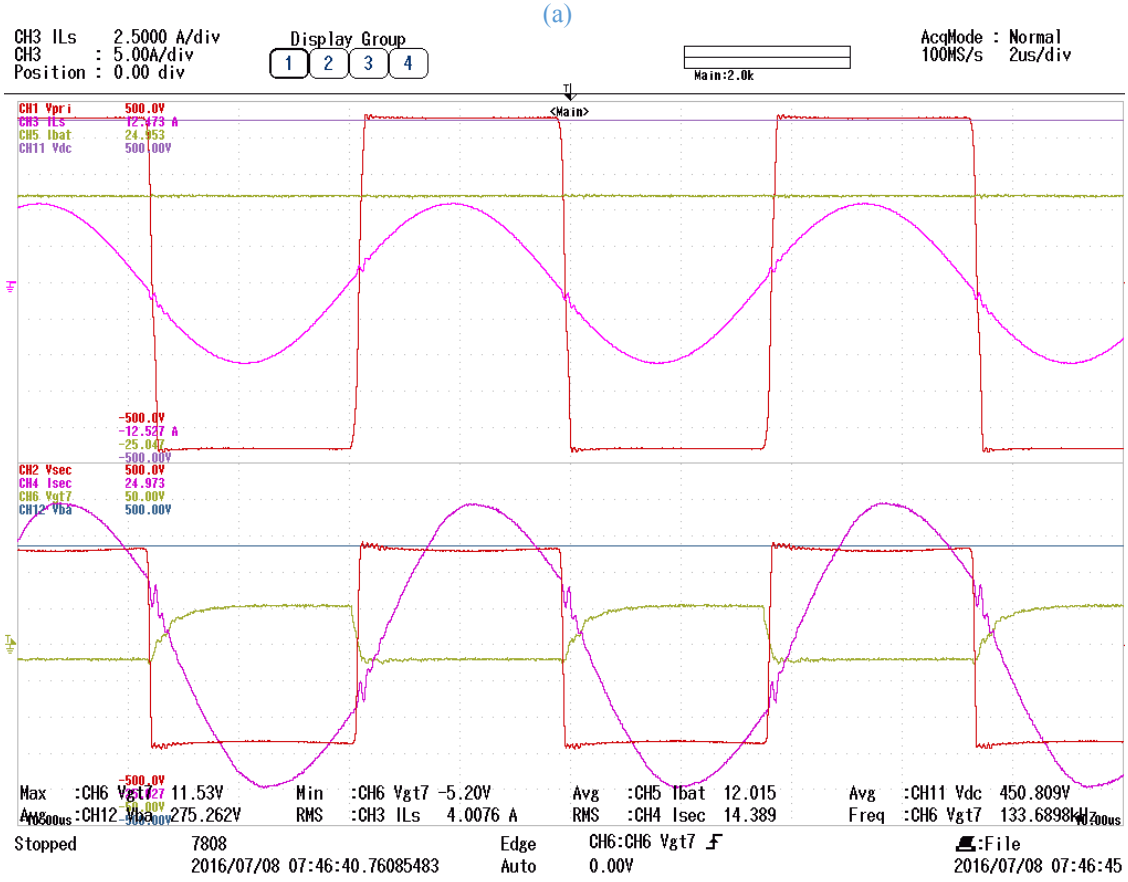
CH3 ILs 2.5000 A/div
CH3 : 5.00A/div
Position : 0.00 div
Display Group
1 2 3 4
Main:2.0k
AcqMode : Normal
100MS/s 2us/div
<Main>
CH1 Vpri 500.0V
CH3 ILs 12.473 A
CH5 Ibat 24.953
CH11 Vdc 500.00V
-500.0V
-12.527 A
-25.047
-500.00V
CH2 Vsec 500.0V
CH4 Isec 24.973
CH6 Vgt7 50.00V
CH12 Vba 500.00V
-500.0V
Max :CH6 Vgt7 11.53V
Min :CH6 Vgt7 -5.20V
Avg :CH5 Ibat 12.015
Avg :CH11 Vdc 450.809V
Avg :CH12 Vba 275.262V
RMS :CH3 ILs 4.0076 A
RMS :CH4 Isec 14.389
Freq :CH6 Vgt7 133.6898kHz
Stopped
7808
2016/07/08 07:46:40.76085483
Edge
Auto
CH6:CH6 Vgt7
0.00V
:File
2016/07/08 07:46:45

(b)

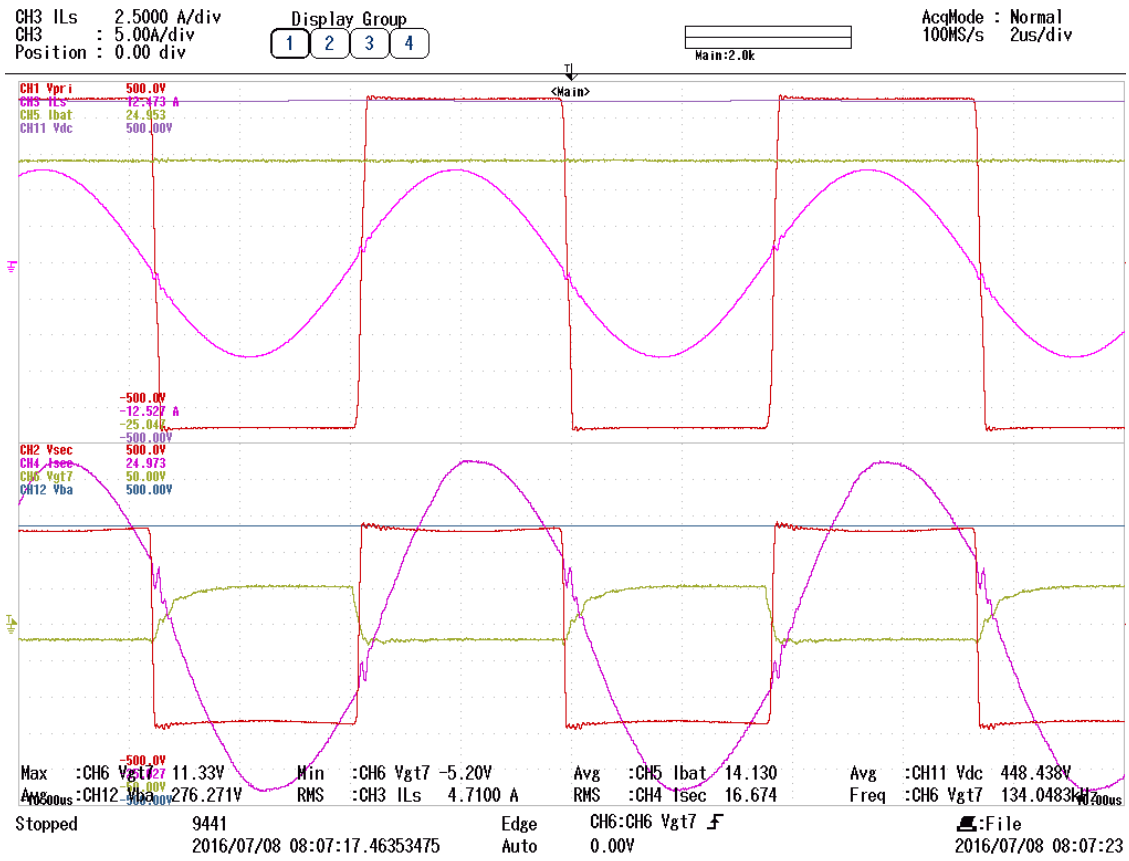

(c)

Fig. 4-16 Waveforms in the reverse mode at different power rating (a) 2.5 kW, (b) 3 kW and (c) 4 kW

Fig. 4-17 shows the variations of switching frequency for different load conditions compared to constant DC link voltage control. It is clear that the frequency range is reduced by 29% (134 kHz versus 95 kHz) in the forward mode and 32% (134 kHz versus 90 kHz) in the reverse mode, by adopting the variable DC link control optimized resonant frequency.

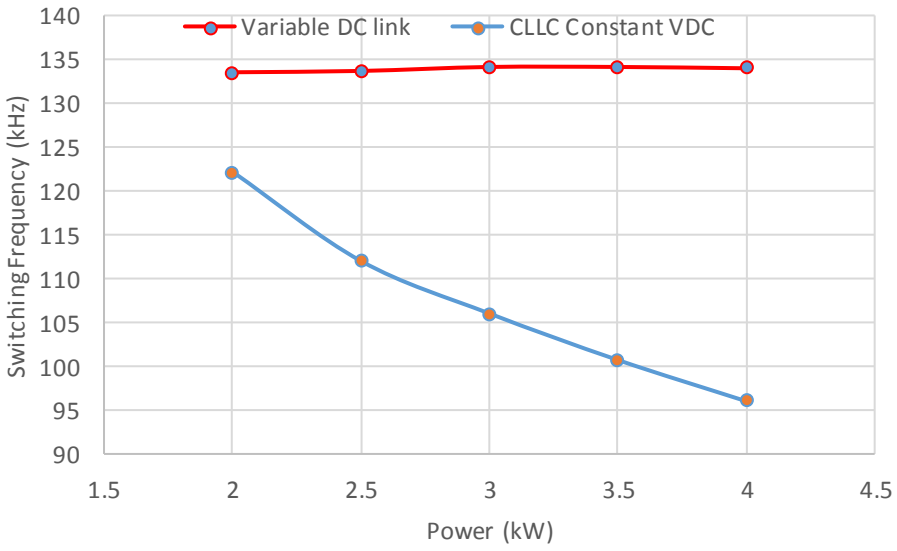

(a)

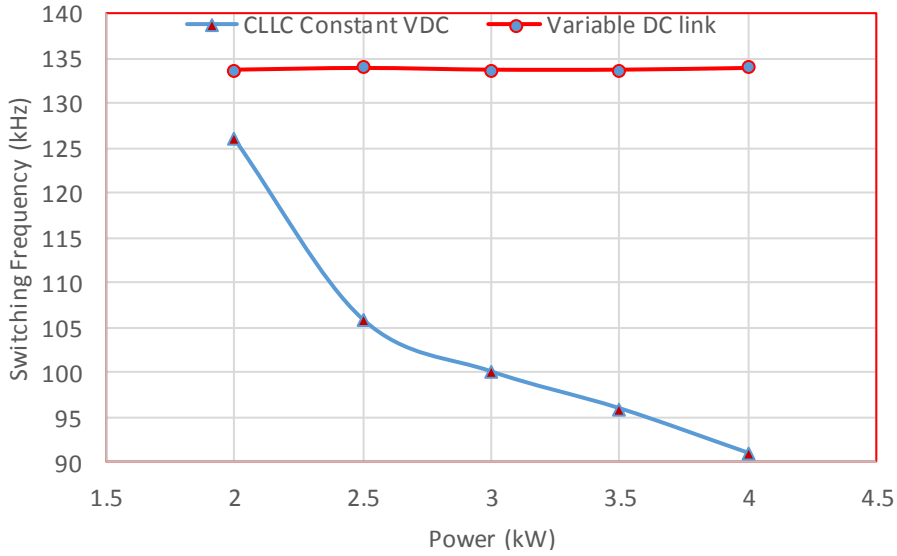

(b)

Fig. 4-17 Switching frequency variations with output power (a) in the forward mode and (b) in the reverse mode

With similar measurement set up, the efficiency at all the conditions is measured and shown in Fig. 4-18. The efficiencies of the converter under the constant DC link voltage are also displayed for comparison.

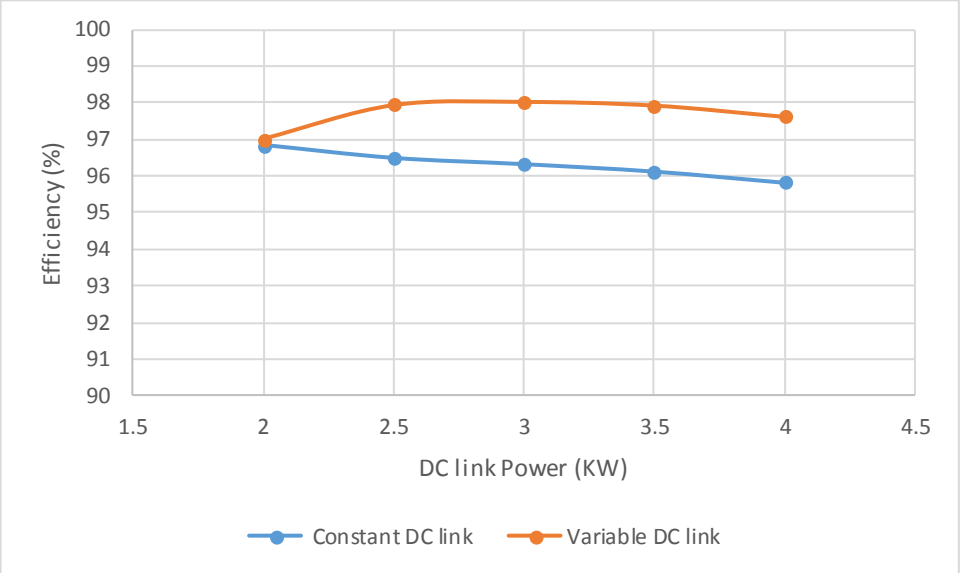

(a)

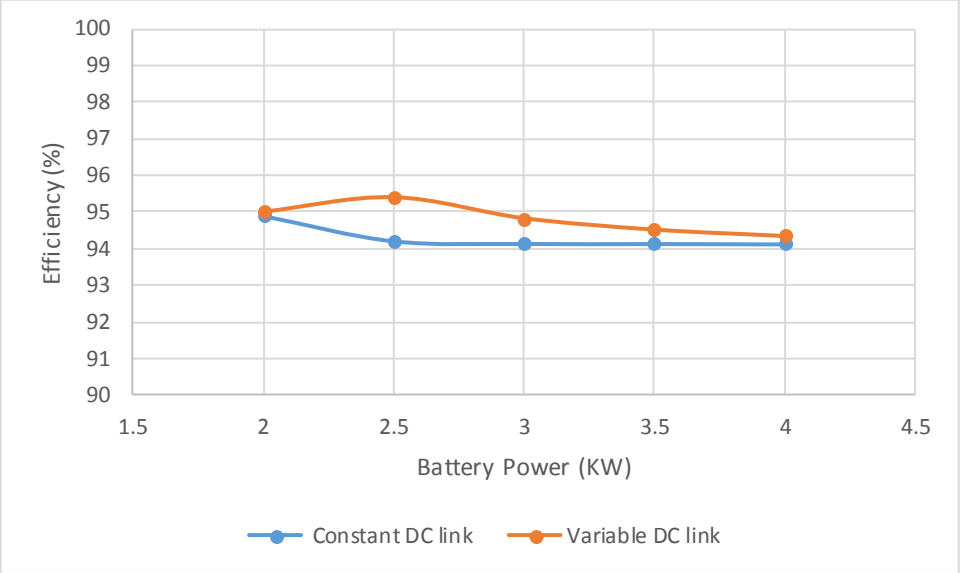

(b)

Fig. 4-18 Efficiency performance with constant DC link (in blue) and variable DC link control (in red) in (a) the forward mode and (b) the reverse mode

It can be shown that with the proposed controller, the efficiency is higher than the constant dc link voltage in both forward and reverse modes. The best efficiency improvement is 2%. However, it should be noticed that, either with constant or variable DC link voltage, the reverse mode efficiency is comparatively lower than the forward mode. This is because the transformer is designed to be step-down with N = 1.66 and the current in secondary side is always higher than the primary side. When the MOSFETs in secondary side are used as the active switches, more circulating current exists in the circuit which accordingly cause more losses.

4.6 Summary

In this chapter, the optimal resonant point tracking is employed in the CLLC resonant converter designed in Chapter 3. A variable DC link voltage control method is developed for the front end converter controller to adjust the DC link voltage when the battery voltage changes. Thus in both G2V and V2G modes, the resonant converter is always operating close to its optimal frequency, allowing tracking of the optimal efficiency point over full battery ranges and load conditions with less circulating current in the resonant tank and transformer, less turn-off current in the primary side MOSFETs and less *di/dt* in the rectifying diodes. Therefore, with these features of high power conversion efficiency and simply control structure, it can boost the efficiency of the CLLC resonant converter based bi-directional on-board battery charger. The experimental test shows that the efficiency is improved by 1~2%.

CHAPTER 5
Magnetic Components Power Loss Evaluation Using Finite Element Analysis (FEA)

This chapter describes a 2D and 3D finite element (FE) method to calculate the power losses for magnetic components in the DC-DC converter operating at high frequency. The characteristics of litz wire winding are taken into consideration. The FE model is built based on the definitions of the geometries, meshes, materials, mechanical motion, electric circuits, boundary conditions and load conditions. The flux density is calculated via finite element analysis (FEA) at the given load condition. Then, the power loss of each element is calculated using the obtained nodal flux densities and power loss density function. Finally, the total loss is the sum of the power losses of all the elements. Compared to the conventional method described in Chapter 4, the FEA approach can predict the flux density more accurately, owing to a detailed model with all the geometric parameters and thus the flux leakage and end-winding effects can be considered. In addition, the nonlinear effect of the core material can be considered in the B-H curve definition in FEA. Experimental tests have been implemented to validate the calculation method.

5.1 Introduction

Magnetic components, inductor and transformer employed in LLC and CLLC resonant converters, operate at high frequency and litz wires are widely used in these components to mitigate high eddy current loss and proximity loss due to the fringing fields in the windings (coils) [152, 153]. It is usually constructed from small insulated strands, woven or twisted to distribute the current density over the entire cross-sectional area of the wire [154-156]. Thus, improvement of the power converter efficiency can be achieved as the skin effect can be reduced and homogeneous distribution of the conducted current is expected [152, 157]. On the other hand, although the proximity effect can be reduced owing to the twisted structure, the proximity loss is still considerable owing to the high external magnetic fields generated by adjacent strands [158-160]. Moreover, the use of litz wire in the magnetic components makes it more difficult to evaluate the power loss since the litz wire strings are not easy to model [161-166]. The power loss calculation method described in Chapter 3 is capable of evaluating the core loss and copper loss in the magnetic components. However, the accuracy of quantifying the achievable losses is challenged since the ac resistance cannot be obtained directly but can only be estimated as illustrated previously.

Several methods have been proposed to characterise the losses in litz wires. In [154] a computational procedure was proposed to predict the losses in the realistic litz wire constructions by computing the equivalent ac resistance of a straight litz wire. However,

the wire is only considered in the free air and the influence of the core winding effect in the actual inductor or transformer has not been considered. In [167], the squared-field-derivative method is proposed to calculate the proximity loss in round-wire or litz wire. A frequency-independent matrix is derived to describe the transformer and inductor, by the use of a numerical magneto-static field calculation. However, it is still challenging to obtain the flux density since the geometries, structure and materials need to be taken into account.

As the eddy current loss is reduced in the litz wire with minimised skin effect and the bundle level eddy current loss is eliminated by transposition (twist) of strands, the proximity loss is the main concern which causes ac losses in the winding. Since the proximity loss is caused by the external magnetic fields generated by adjacent strands if the magnetic field can be modelled with a reasonable accuracy, the proximity loss can be evaluated. This chapter is organised as follows. Section 5.2 presents the 2D FEA method employed to characterize the inductor core loss. In Section 5.3 and Section 5.4, the inductor copper loss and transformer copper loss are evaluated with 3D FEA, respectively. All the results have been verified with experimental measurements.

5.2 Inductor Core Losses

5.2.1 Inductor core loss calculation with 2D FEA

This section presents the calculation of the inductor core loss with 2D FEA. Compared to the conventional method described in Chapter 3, the FEA approach can predict the flux density in the core more accurately. This is because (a) FEA allows a detailed model with all the geometric parameters and thus the flux leakage effects can be considered; (b) the nonlinear effect of the core material can be considered in the B-H curve definition in FEA. Therefore, the core loss can be predicted more accurately using FEA.

The flow chart of the core loss calculation with FEA is shown in Fig. 5-1. First, the FE model is built with the definitions of its geometries, meshes, materials, mechanical motion, electric circuits, boundary conditions and load conditions. Subsequently, the flux density of each node in the core can be calculated via FEA at the given load condition. Then, the power loss density function with respect to the flux density and frequency needs to be established according to the material power loss curve given by its supplier. Thereafter, the core loss of each element can be calculated using the obtained nodal flux

densities and power loss density function. Finally, the entire core loss can be obtained by summing all the core losses in all the elements.

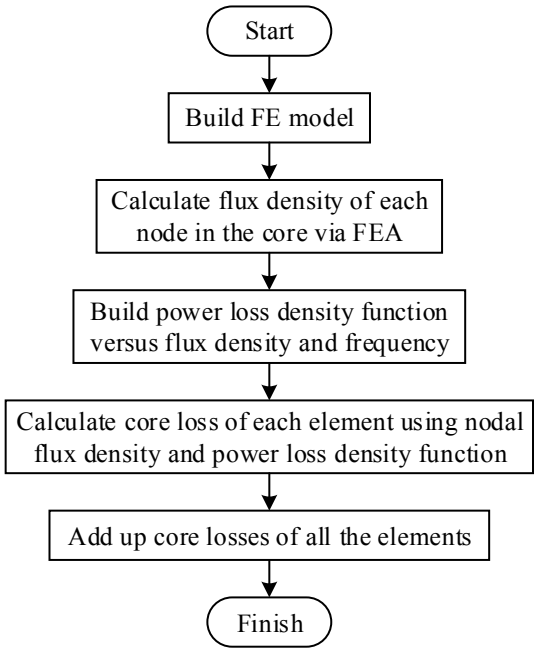

Fig. 5-1 Flow chart of the core loss calculation with FEA.

5.2.2 FE model

The FE tool FLUX 2D developed by CEDRAT [168] is employed to build the inductor FE model and thereafter perform the core loss calculation. Fig. 5-2 is the photo of the inductor.

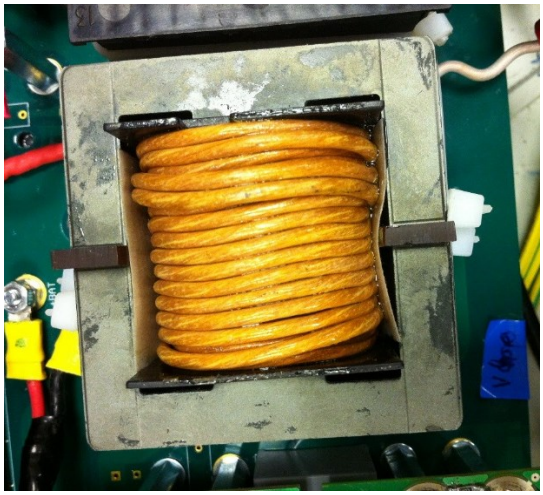

Fig. 5-2 Photo of the inductor in the experimental test rig

Fig. 5-3 (a) illustrates the inductor model in FLUX 2D, consisting of the core, winding, airgap, air and infinite box. Given that the magnetic field in the full model satisfies the even symmetry condition along the *y*-axis, the full model can be simplified and represented by half of the model as illustrated in Fig. 5-3 (b). The boundary condition

along *y*-axis is with tangent magnetic field and normal electric field. Fig. 5-3 (c) shows the electric circuit model in which the winding current is determined by the current defined in the current source.

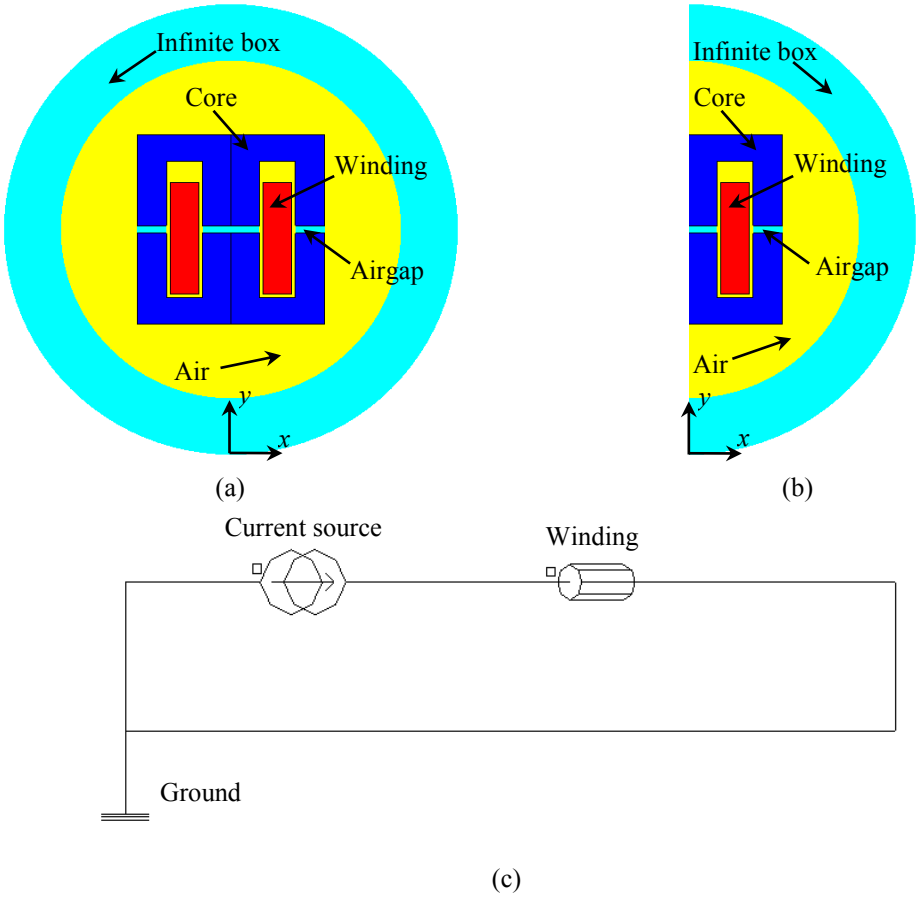

Fig. 5-3 2D FE model of the inductor. (a) Full model. (b) Simplified model considering symmetries. (c) Circuit model.

Subsequently, the geometry model built above is meshed with second order meshes in which each triangle element consists of six nodes, as shown in Fig. 5-4 (a). The mesh density of the inductor model excluding the air surrounding and infinite box can be found in Fig. 5-4 (b). It can be observed that high-density mesh is employed to minimise the computation error.

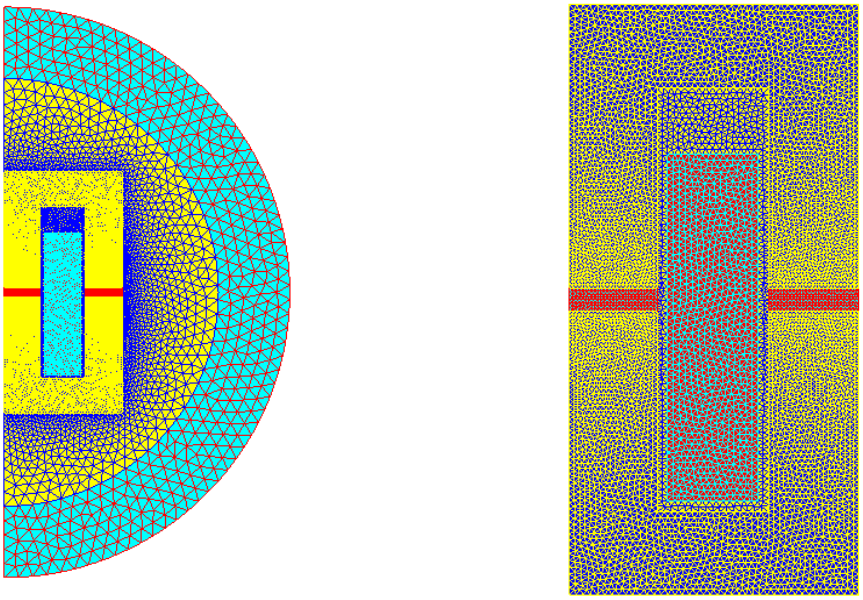

(a) (b)

Fig. 5-4 2D Mesh of the inductor FE model. (a) Inductor model. (b) Inductor model excluding air surrounding and infinite box.

The core material used in this application is 3C95 whose datasheet B-H curve is illustrated in Fig. 5-5(a). Its B-H curve with uniform scale at 100°C is presented in Fig. 5-5 (b).

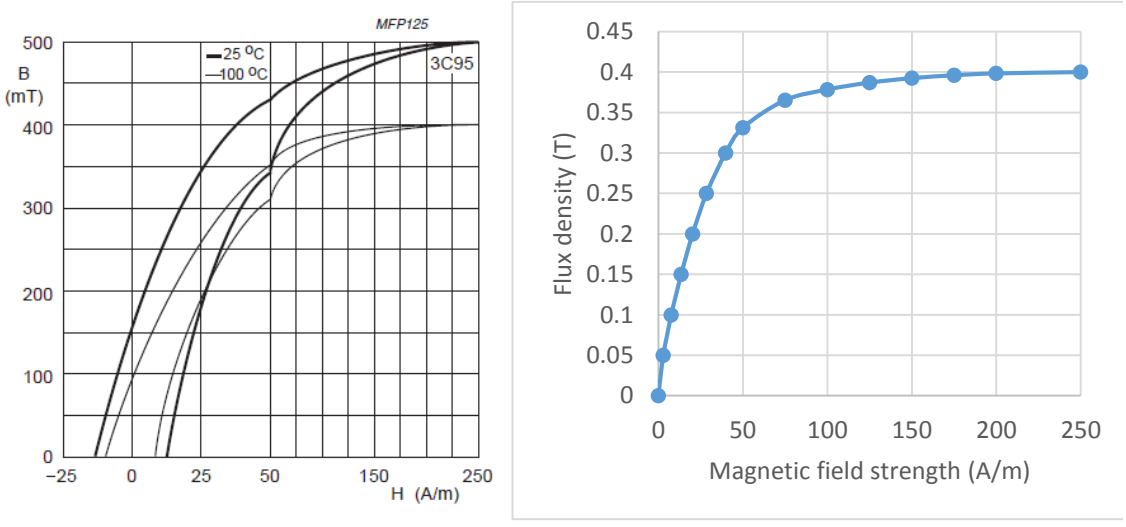

(a) (b)

Fig. 5-5 B-H curve of the core material 3C95. (a) Datasheet. (b) Rebuild with uniform scale.

5.2.3 Nodal flux density

The FE model built in Section 5.2.2 is run at 8.5 RMS (the nominal current measured in Chapter 3 and Chapter 4, assumed as sinusoidal waveforms for the sake of analysis) load condition with the static analysis. Subsequently, the resultant flux density

distribution of the full model is shown in Fig. 5-6 to demonstrate the magnetic field symmetry. Fig. 5-7 illustrates the flux density contour of the inductor at the same load condition. As can be seen, the flux densities over the core are non-uniform, particularly at its geometrical corners in which the localised effects are considerable. These localised effects cannot be captured by the conventional magnetic circuit based method.

Then, the flux density at each node is exported before the core loss calculation which will be discussed in the next section.

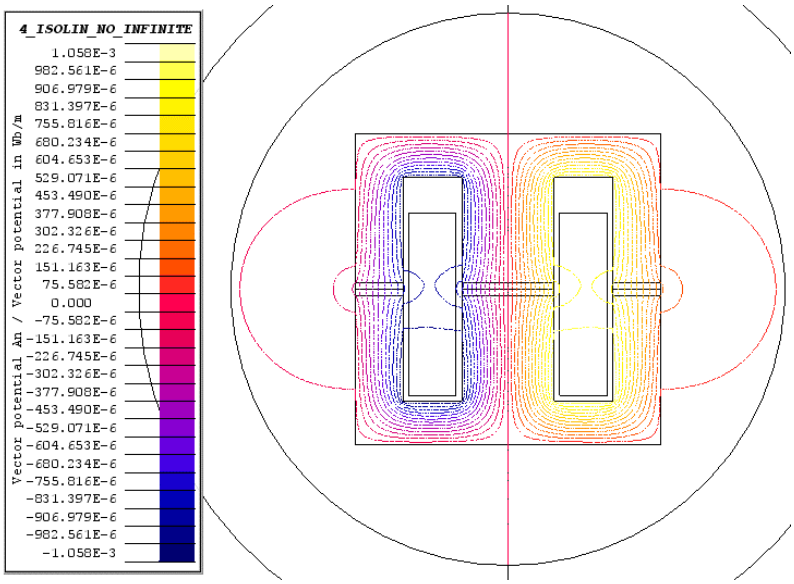

Fig. 5-6 Flux isolines of the inductor FE model at 8.5A(RMS).

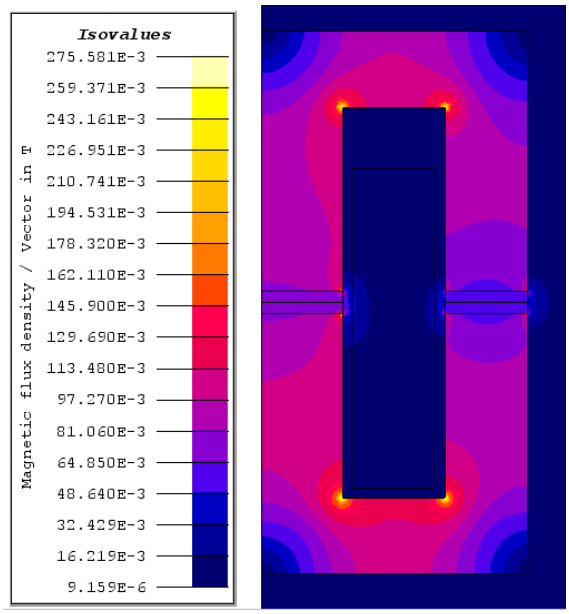

Fig. 5-7 Flux density contour of the inductor FE model at 8.5A(RMS).

5.2.4 Core loss calculation

The power loss density function of the core used in this application needs to be built before performing the core loss calculation. This power loss density is a function of core flux density and frequency, as shown in Fig. 5-8 which is from 3C95 datasheet.

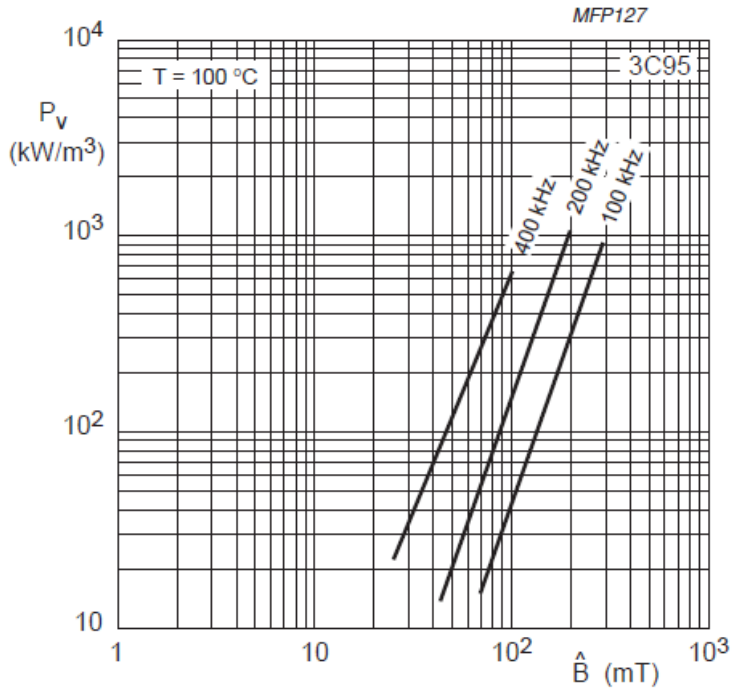

Fig. 5-8 Power loss density characteristics of the core material 3C95 from its datasheet.

Given that the dominated core loss is resulted from the eddy current, the power loss density function can be written as Equation (5-1).

$$P_{loss}(B,f) = a \cdot B^b \cdot f^c \tag{5-1}$$

where $P_{loss}(B,f)$ is the power loss density in kW/m^3, B represents the flux density in the unit of T, f represents the electric frequency in the unit of kHz, and a, b and c are the constant coefficients which are affected by the curve fitting based on the power loss density characteristics of the core material. Table 5-1 lists the values of these constant coefficients a, b and c. It should be noted that those values in Table 5-1 are only valid for the core material 3C95.

Table 5-1 Coefficients determined by curve fitting of power loss density

Coefficient	Unit	Value
a	-	7.862
b	-	2.384
c	-	1.652

Fig. 5-9 compares the power loss densities using curve fitting with those from manufacture's datasheet. A good correlation can be observed. Note that the *x*- and *y*-axes in Fig. 5-8 are in logarithmic scales while those in Fig. 5-9 are normal.

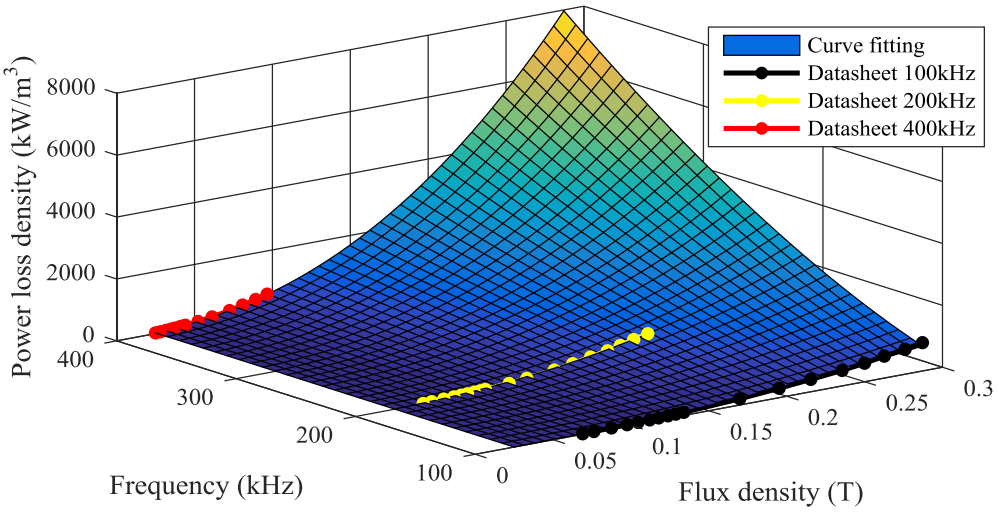

Fig. 5-9 Curve fitting of the power loss density function $P_{loss}(B, f)$.

On the other hand, the average flux density at each element can be calculated by the flux densities of the nodes which belongs to the given element. The element-nodes relationships can be obtained by the mesh information. The volume of each element can also be calculated using the element-nodes relationships and node coordinates.

Further, the power loss density at each element is calculated by substituting the average flux density and the electric frequency into Equation (5-1). Subsequently, the core loss at each element is obtained by the product of the power loss density and the element volume. Finally, the total core loss can be obtained by summing all the element losses. It should be noted that the symmetry and/or periodicity factors also need to be considered in the core loss calculation.

The above FEA method is applied in the CLLC resonant converter in the reverse mode to validate the accuracy. In the test, the battery voltage is 238.33 V, the DC link voltage is 383.7 V, discharging current is 9.0A, and the switching frequency is approximately 125.94 kHz. In this condition, the average peak flux density B of the inductor core is 0.06 T, and the core loss is 2.40W. The flux density in the core is clearly quite low, and the reason is (a) the design of the inductor was based on as low as 0.137 T at 20A current, in order to reach lower power losses. And the loading in this calculation is even lower since the RMS current through the inductor is approximately 6A. (b) As can be observed in Fig.

5-7, the flux density in the corner of the core is between 0.0162T and 0.0486 T, which makes the averaged flux density in the whole core small.

In the calculation with the conventional method in Chapter 3, the average flux density is 0.0638T, with which the calculated core loss is 2.5916W. As can be seen, the averaged flux density in conventional analytical method is slightly higher (7% error) than that in the FEA. This is because in the conventional method, the fringing effect is not considered while in the FE model, the flux leakage can be predicted.

5.3 Inductor Copper Losses

5.3.1 Inductor copper loss calculation with 3D FEA

This section describes the calculation of the inductor copper loss with 3D FEA. Compared to the conventional method described in Chapter 3, the 3D FEA approach can predict more accurate winding flux density and thus more accurate proximity loss. The reason is the same as that in Section 5.2.1. It should be noted that the 3D FEA rather than 2D FEA is employed in the proximity loss calculation. The reason is that the end-winding cannot be neglected and this can only be modelled in 3D FEA.

The flow chart of the inductor copper loss calculation with 3D FEA is shown in Fig. 5-10.

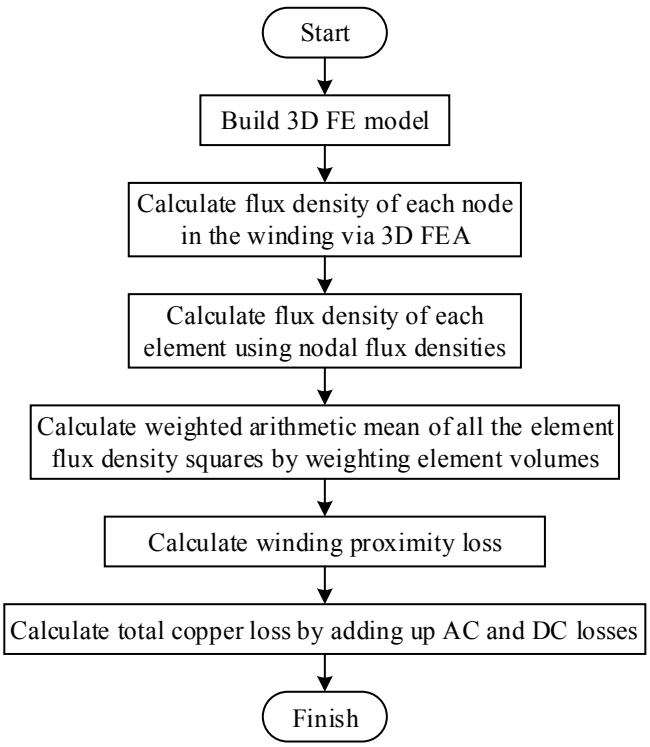

Fig. 5-10 Flow chart of the inductor copper loss calculation with 3D FEA.

First, the 3D FE model is built with the definitions of its geometries, meshes, materials, mechanical motion, electric circuits, boundary conditions and load conditions. Subsequently, the flux density of each node in the core can be calculated via 3D FEA at the given load condition. Then, the flux density of each element is obtained using the nodal flux densities and the element-nodes relationships. Thereafter, calculate the weighted arithmetic mean of all the element flux density squares by weighting element volumes. After this, the winding proximity loss is calculated using the weighted arithmetic mean of all the element flux densities. Finally, the winding copper loss can be obtained by summing the DC loss and ac loss which is the proximity loss because the skin effect is negligible in the litz wire used in the inductor and transformer.

5.3.2 FE model

The FE tool FLUX 3D developed by CEDRAT [168] is employed to build the 3D FE model of the inductor and subsequently perform the proximity loss calculation. Fig. 5-2 is the photo of the inductor while Fig. 5-11 shows the inductor geometries built in the 3D FE model. It can be seen that the end-winding part is also modelled.

Given that the magnetic field in the full model satisfies the symmetry conditions along the *XOY*, *YOZ* and *ZOX* planes, the full model can be simplified and represented by one eighth of the model as illustrated in Fig. 5-12 (a). The definitions of *XOY*, *YOZ* and *ZOX* planes can also be found in Fig. 5-12 (a). The boundary conditions along *XOY* and *YOZ* planes are with tangent magnetic field and normal electric field while that along *ZOX* plane is with normal magnetic field and tangent electric field. The electric circuit model is the same as that in Fig. 5-3 in which the winding current is determined by the current defined in the current source.

Subsequently, the geometry built in Fig. 5-12 (a) is meshed and Fig. 5-13 illustrates the mesh densities on the core and winding. It should be noted that the mesh in the 3D FE model cannot be as dense as that in the 2D model shown in Fig. 5-4 due to a much more computation needed in 3D FEA.

The core material used in this 3D FE model 3C95 is the same as that in Section 5.2.1. The datasheet B-H curve is shown in Fig. 5-5.

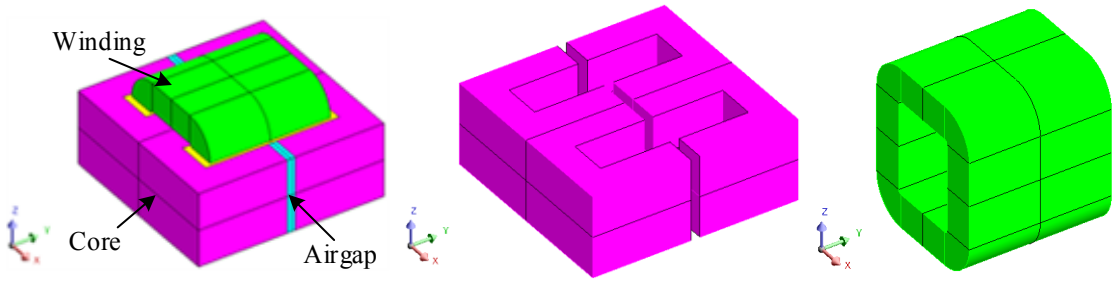

(a) (b) (c)

Fig. 5-11 Inductor geometries in the 3D FE model. (a) Winding and core. (b) Core. (c) Winding.

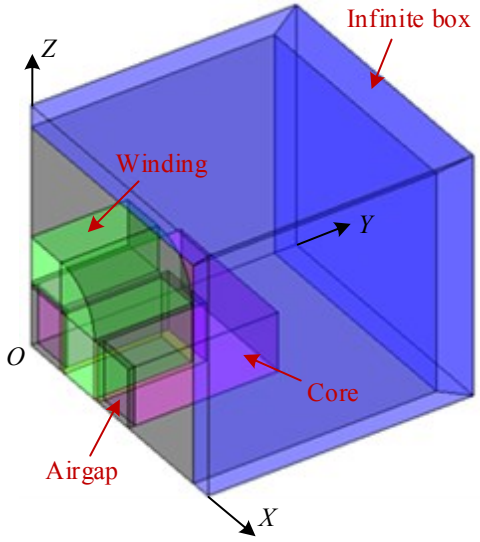

(a)

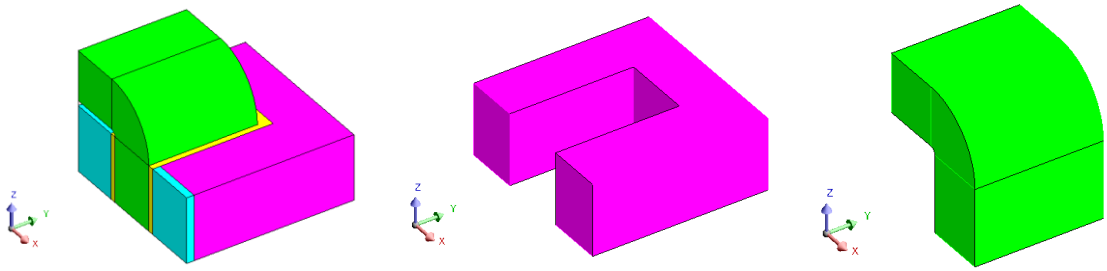

(b) (c) (d)

Fig. 5-12 Inductor 3D FE models considering symmetries. (a) Full model. (b) Core, winding and airgap. (c) Core. (d) Winding.

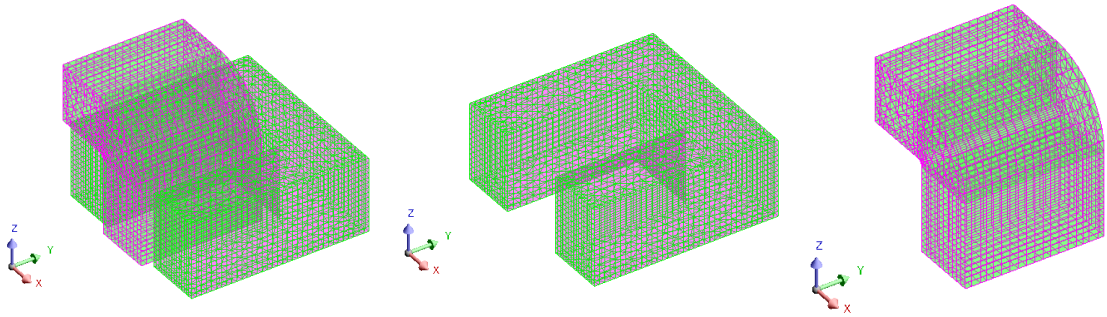

(a) (b) (c)

Fig. 5-13 3D mesh of the inductor FE model. (a) Core and winding. (b) Core. (c) Winding.

5.3.3 Nodal flux density

The 3D FE model built in Section 5.3.2 is run at 6A(RMS) load condition (the minimum battery charging current) with the static analysis. Fig. 5-14 illustrates the flux density contours of the inductor core and winding.

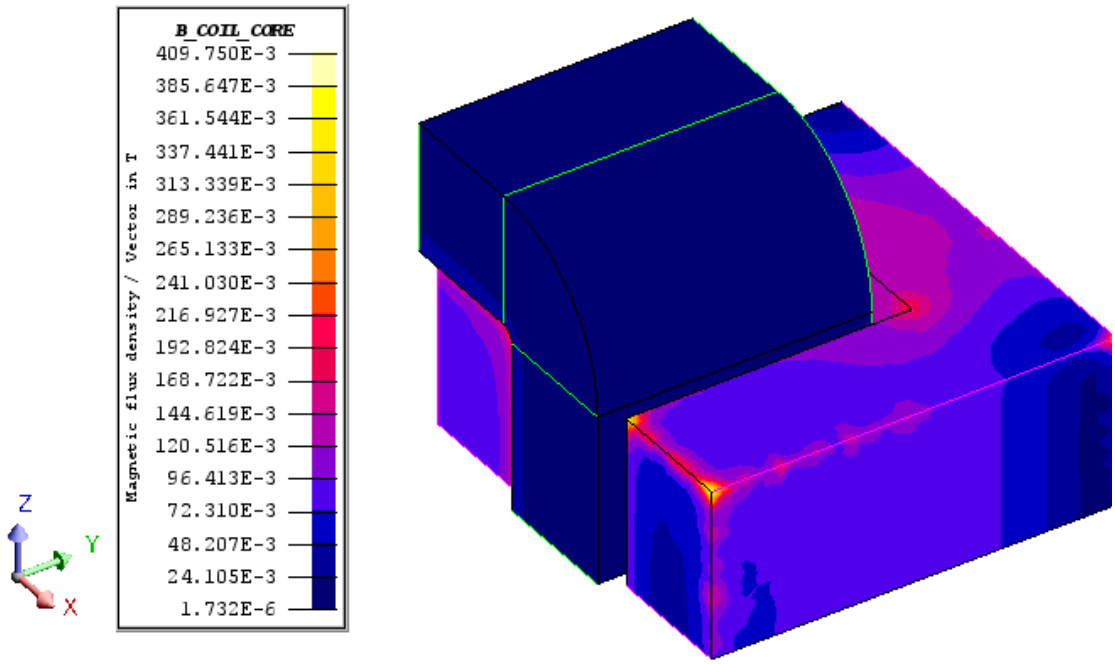

(a)

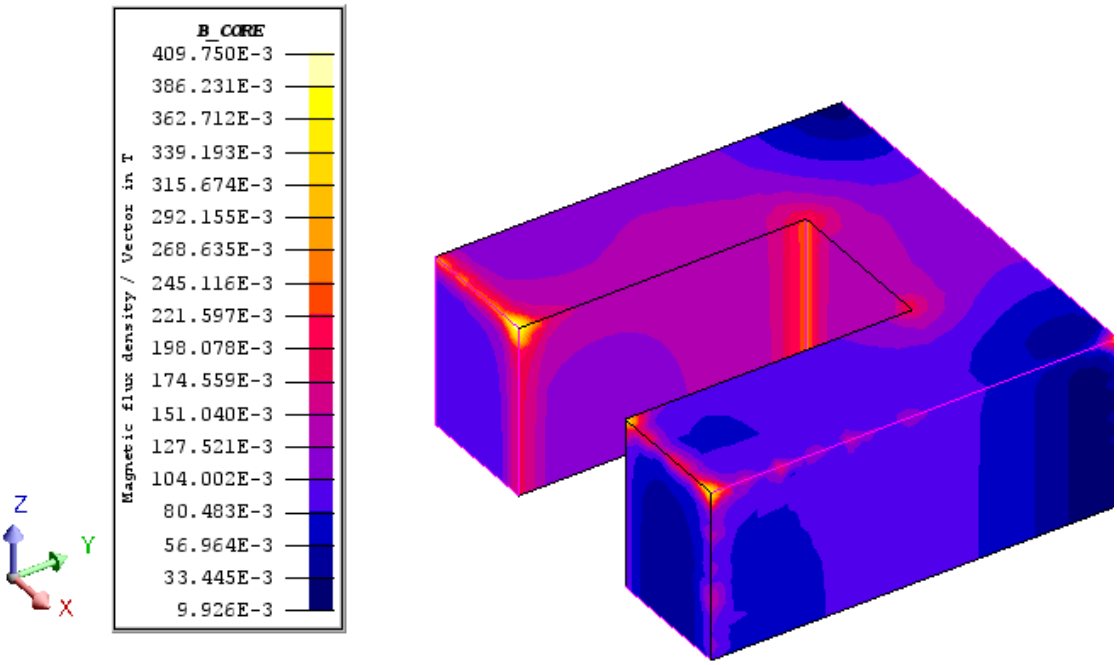

(b)

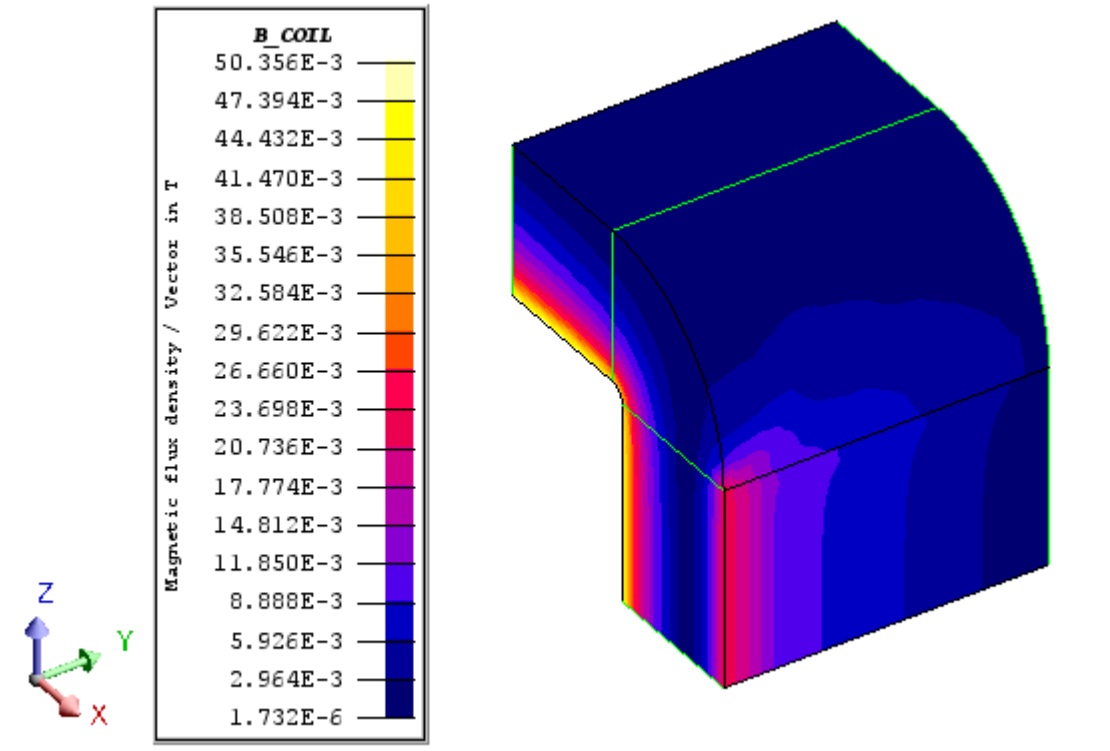

(c)

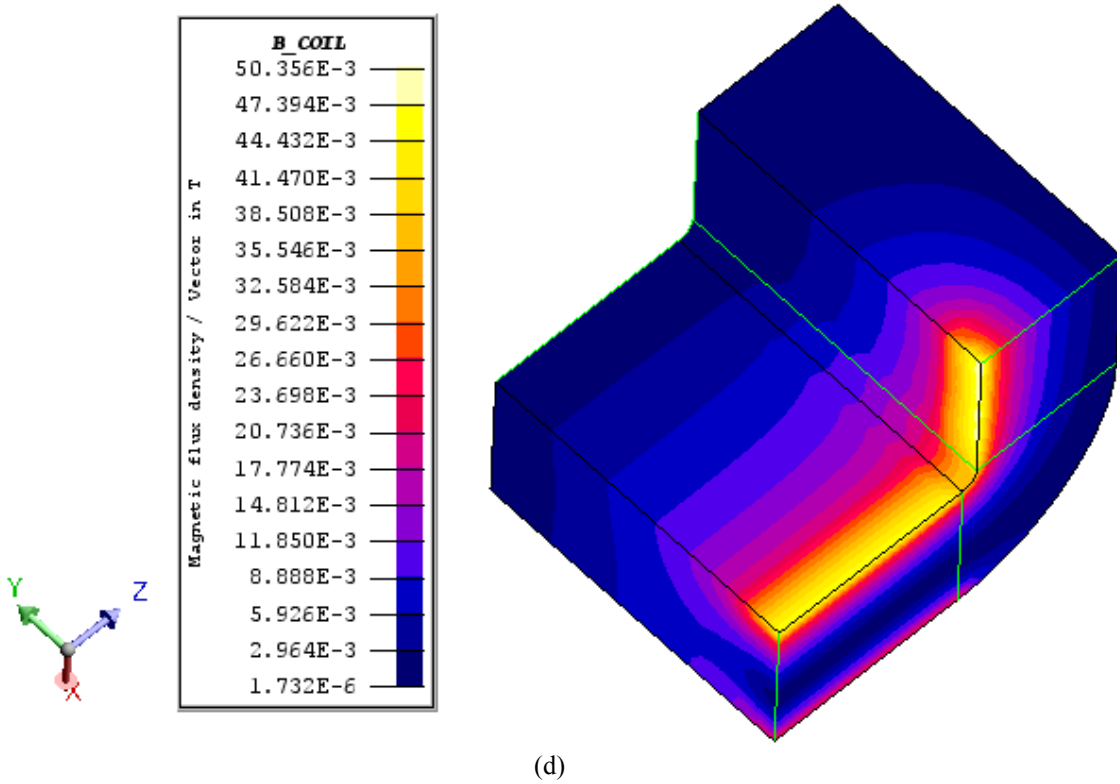

(d)

Fig. 5-14 Flux density contours of the inductor core and winding at 6A(RMS). (a) Core and winding. (b) Core. (c) Winding. (d) Winding.

From Fig. 5-14 (c) and (d), it is clear that the flux densities at the winding corners close to the airgap, particularly the inner layer, are relatively higher than those in the other parts. This is because most of the flux leakage occurs in this area due to the presence of

the airgap. Subsequently, the flux density at each node of the winding is exported before the winding copper loss calculation which will be discussed in section 5.3.4.

5.3.4 Copper loss calculation

The proximity loss in the litz wire of the inductor can be calculated using Equation (5-2) derived in [167].

$$P_{px\_ind} = \frac{\pi L_t N_{ts} {d_c}^4}{64\rho_c} \langle \overline{\left(\frac{dB_k}{dt}\right)^2} \rangle \tag{5-2}$$

where P_{px_ind} is the inductor proximity loss, $L_t$represents the average length of one turn, N_{ts} is the product of the turn number per coil and the strand number per turn, d_c is the strand diameter, ρ_c is the wire resistivity, dB_k/dt is the time derivative of average flux density in k^{th} element of the winding, $\langle \cdot \rangle$ is the spatial average operator and $\bar{\cdot}$ is the time average operator.

The current fed into the winding can be expressed as Equation (5-3), neglecting the current harmonics.

$$i = I_m \sin(2\pi f t + \varphi) \tag{5-3}$$

where i is the winding transient current, I_m is the current amplitude, f represents the frequency, and φ represents the current initial phase angle.

Given that winding permeability is constant, the flux density B_k in the winding obtained at a given current with I_m amplitude can be calculated by linearly scaling the flux density B_{0k} at the reference current with I_{0m} amplitude, as described by Equation (5-4). Therefore, only one 3D FEA with the reference current I_{0m} is needed to generate the nodal flux densities and thereafter the element flux densities.

$$B_k = \frac{I_m}{I_{0m}} B_{0k} \tag{5-4}$$

The flux density B_{0k} at the reference current with I_{0m} amplitude can be expressed as Equation (5-5).

$$B_{0k} = B_{0km}\sin(2\pi ft + \varphi) \tag{5-5}$$

where B_{0km} is the average flux density amplitude in k^{th} element at the reference current I_{0m}.

Based on Equation (5-3), (5-4) and (5-5), the derivative of B_k against time is derived to be Equation (5-6).

$$\frac{dB_k}{dt} = \frac{B_{0km}}{I_{0m}} \cdot \frac{di}{dt} \tag{5-6}$$

Substituting Equation (5-6) into Equation (5-2), the proximity loss in the inductor can be expressed as Equation (5-7).

$$P_{px\_ind} = \frac{\pi L_t N_{ts} {d_c}^4}{64\rho_c {I_{0m}}^2} \langle {B_{0km}}^2 \rangle \overline{\left(\frac{di}{dt}\right)^2} \tag{5-7}$$

Therefore, the average flux density square over all the elements $\langle {B_{0km}}^2 \rangle$ at the reference current I_{0m} needs to be obtained. However, since the mesh sizes of the winding elements may be non-uniform, the average flux density square over all the elements $\langle {B_{0km}}^2 \rangle$ may not represent the true spatial average flux density square. Therefore, the weighted arithmetic mean of all the element flux density squares by weighting element volumes are employed to calculate the spatial average flux density square, as described in Equation (5-8).

$$P_{px\_ind} = \frac{\pi L_t N_{ts} {d_c}^4}{64\rho_c {I_{0m}}^2 V_{ol}} \langle {B_{0km}}^2 V_k \rangle \overline{\left(\frac{di}{dt}\right)^2} \tag{5-8}$$

where V_k is the volume of the k^{th} element in the winding and V_{ol} is the total winding volume. The above equation implies that 3D computation of magnetic field and the resultant mean flux density over the winding volume only needs to be performed once with excitation of the reference current. Proximity loss at any current waveforms can be scaled accordingly as long as the conditions stated in [167] are satisfied.

Based on Equation (5-8), Table 5-2 lists the winding proximity losses in the inductor at 6.22A and 6.50A at 134 kHz.

The winding DC loss P_{DC} in the inductor can be calculated with the conventional equation shown in Equation (5-9).

$$P_{DC} = \frac{1}{2} {I_m}^2 R_{DC} \tag{5-9}$$

where R_{DC} is the winding DC resistance which can be calculated with Equation (5-10).

$$R_{DC} = \frac{4\rho_c L_t N_{ts}}{\pi {d_c}^2} \tag{5-10}$$

Thus, the inductor copper loss is obtained by summing the proximity loss P_{px_ind} and the DC loss P_{DC}.

Table 5-2 Summary of proximity losses in the inductor at 134 kHz

Resonant current	SIMULATION		Unit
	6.22A	6.50A	
Copper loss	13.77	15.04	W
Proximity loss	13.35	14.58	W
DC loss	0.42	0.46	W

5.3.5 Experimental verification

To validate the calculation method, experimental tests are performed in the test rig. And the series inductor current and voltage are obtained with the YOKOGAWA oscilloscope, with which the power loss can be calculated.

5.3.5.1 Measurement with LCR meter

In order to validate the FEA method, the inductor ac resistance R_s is measured at the same excitation frequency of 134kHz as in the FE model. The predicted method in [154] is also implemented for comparison.

The HIOKO LCR meter, as shown in Fig. 5-15, is used to measure the R_s and R_{dc} of the inductor coil. When the inductor has the core on, the measured R_s is 138.79 mΩ. In contrast, when the core is removed, only the coil is wound around the bobbin, and then the measured R_s is 69.20 mΩ.

Fig. 5-15 The measurement using LCR meter.

By changing the core area to air, the FE model can be employed to estimate the copper loss in the coil without the influence of the core and then the corresponding ac resistance. In this case, the resultant ac resistance at 6.50A is 71.09 mΩ and agrees well with the measured value of 69.20 mΩ in the air-cored inductor.

From the resultant ac resistance above, it is clearly that the FE model has good accuracy with the measured resistance.

5.3.5.2 Sinusoidal current in low power

To further verify the FE method for ac loss prediction, experimental tests have been implemented in the CLLC resonant converter in the reverse mode. In the test, the battery voltage is 238.33 V, the DC link voltage is 383.70 V, the discharging current is 9.00A, and the operating frequency is approximately 125.94 kHz. With the measurement of the inductor voltage and current, the actual losses in the inductor can be calculated and compared with the FEA result in the same condition.

The measured voltage and current of the series inductor are obtained from the waveform data from the oscilloscope and plotted in Fig. 5-16.

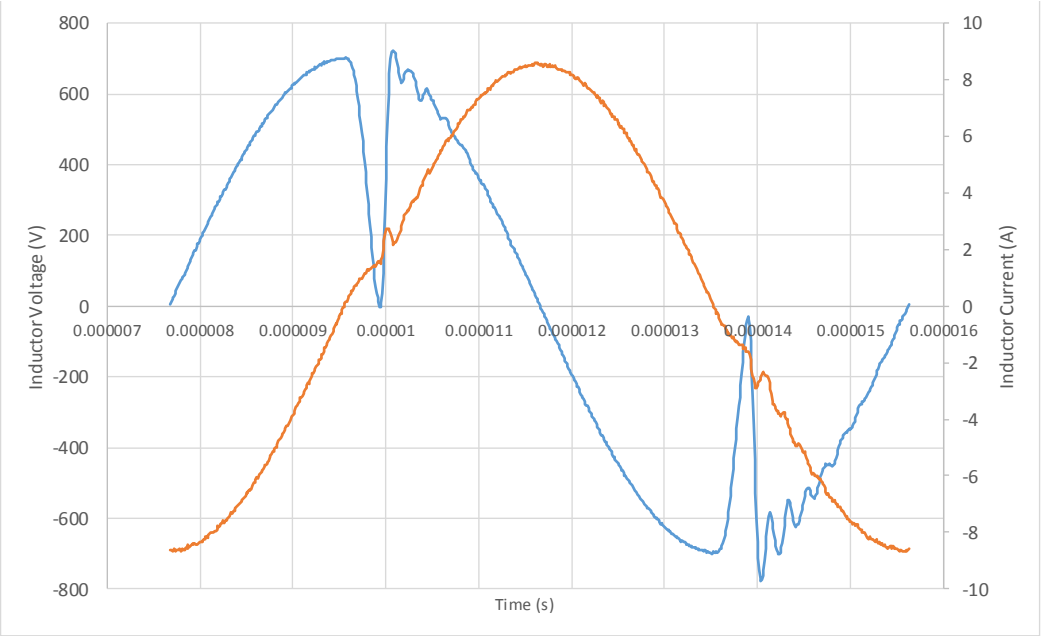

Fig. 5-16 Measured inductor voltage (in blue) and current (in red) waveforms

As can be see, the inductor current is lagging the inductor voltage with ~90-degree phase shift. The inductor current waveform is close to sinusoidal, despite of a small distortion in the period immediate after the zero-crossing in the DCM, because the operating frequency is near (slightly below) the series resonant frequency. In this period, the inductor voltage drops to zero since the *di/dt* is zero.

The sampling rate of the oscilloscope is 100MS/s (corresponding resolution 1E-8). The switching frequency is 125.94 kHz, and thus 800 sampling is recorded in one switching cycle. The instantaneous power loss at each sampling time is calculated with the instantaneous voltage and current, and then the averaged power loss in one switching cycle is calculated. In this condition, the entire power losses of the inductor is 10.02W.

Then, the FEA method is also applied with the same condition, and the copper loss is calculated to be 11.5394 W. If 2.3946 W core loss (calculated in Section 5.2.4) is added up, then the total loss of the inductor is 13.934 W. The results of FEA is slightly higher than the actual test results. This error may be caused by the measurement inaccuracy and phase delay between the inductor voltage and current. Since the switching frequency is quite high, only 800 samples are recorded in one switching cycle, thus even a small phase delay in the inductor voltage and current will cause big error. With regard to possible phase measurement error margins in voltage and current waveforms, as 800 samples per cycle will give rise to 0.45 degree's phase error in one waveform, thus the maximum total error caused by the voltage and current waveforms could reach 0.9 degree.

The conventional prediction method described in Chapter 3 is also applied to calculate the power loss. The measured R_s (no core in the inductor but only the coil winding in the bobbin) is 60 mΩ, the copper loss is 2.176W, core loss is 2.592W (calculated in Section 5.2.4) and the total loss is 4.768W. This result is consistent with the prediction in Chapter 3.

The comparison of the three methods is shown in the table below:

Table 5-3 Comparison with different methods

Methods	Measured	FEA	Conventional	Unit
Total loss	10.02	13.93	4.768	W
Error percentage	-	39.0%	52.4%	-
Core loss	2.395	2.395	2.592	W
Copper loss	7.625	11.54	2.176	W

As can be observed from the table, the resultant power loss from FEA model is 13.93W, 39% more than the test results 10.02W. However, the loss predicted by the conventional method is 4.768W with 52.4% less than the measured results. The large error could be explained by the inaccuracy of the component datasheet, such as the ac resistance from the curve fitting, due to the lack of values in different temperatures. Overall, the FEA is clearly more accurate than the conventional prediction methodology, despite of the inaccuracy caused by the phase delay between the inductor voltage and current.

5.3.5.3 Non-sinusoidal current in high power

The analysis above can be used in the applications where the current waveform is close to sinusoidal. However, when the converter operates in high power, the operating frequency deviates from the series resonant frequency and large distortion occurs in the current. In this case, the current used in the FEA method is not the RMS of the current anymore. Thus FFT needs to be applied in the current, and all the current distortions at each frequency are used to calculate the power loss with the magnetic field and then add up to get the total power loss.

In the experimental test system, the YOKOGAWA scope probe can be used to measure maximum 1 kV voltage. However, when the resonant converter is running at 4 kW, the peak voltage across the inductor is 1.5 kV. Thus for the sake of safety, the measurement in higher power is run at 3.5 kW power rating at 95.69 kHz. In this case,

the battery voltage is 351.791 V, the DC link voltage is 387.835 V, and the discharging current is 8.984 A. The current in the inductor, ILs RMS, is 7.443 A. With the measured voltage and current from the experimental inductor, the actual power loss in the inductor can be calculated and compared with the FEA result in the same condition.

The measured voltage and current of the series inductor is obtained from the waveform data from the oscilloscope and plotted in Fig. 5-17.

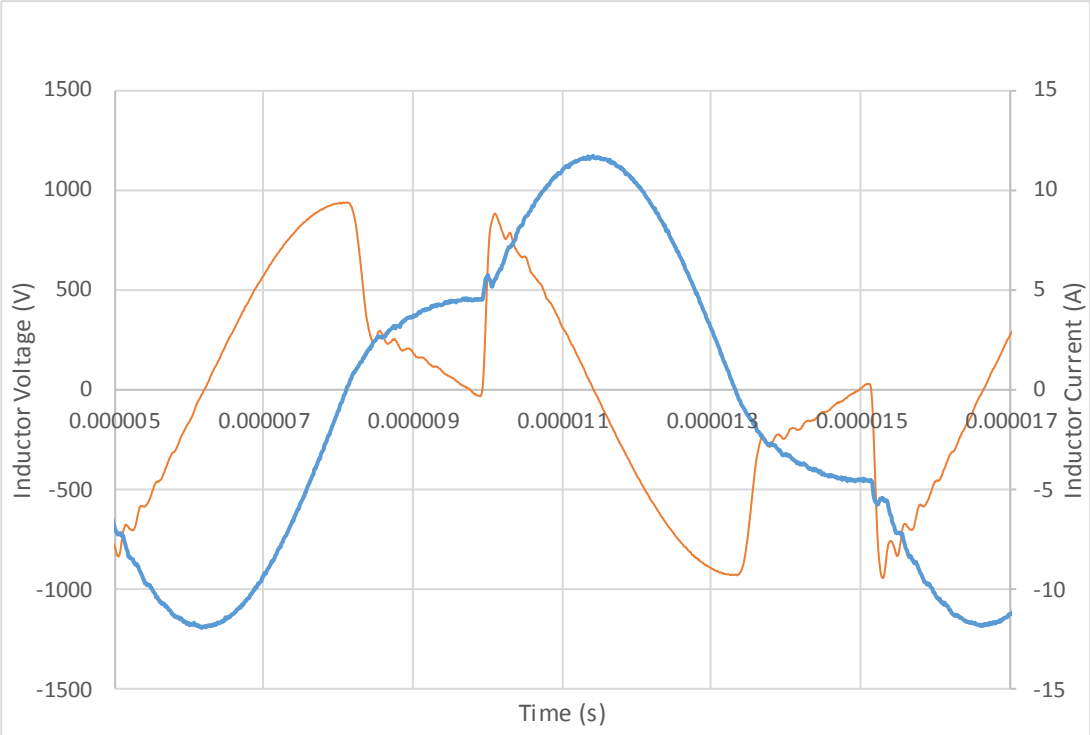

Fig. 5-17 Measured inductor voltage (in red) and current (in blue) at 3.5 kW

As can be seen, the current of inductor is lagging the voltage. The inductor current waveform is not close to sinusoidal, but has large distortion with flat area during DCM. During this flat area of the current, the inductor voltage drops close to zero since the *di/dt* is zero.

The sampling rate of the oscilloscope is 100MS/s (corresponding resolution 1E-8). The switching frequency is 95.69 kHz, and thus 1045 sample points are recorded in one switching cycle. The instantaneous power loss at each sampling time is calculated with the instantaneous voltage and current, and then the averaged power loss in one switching cycle is calculated. In this condition, the total power loss is 26.06 W.

Then, the FEA method is also applied with the same condition. First the FFT analysis is carried out to find out the harmonic current values, as shown in Fig. 5-18. With the magnetic field predicted by 3D FEA, the ac copper loss in each frequency can be calculated and then the total ac copper loss can be obtained by summing the loss associated with each frequency. The resultant copper loss, including DC copper loss, is 14.22 W. With core loss 6.225 W, the total loss in the inductor is 6.225 + 14.22 = 20.44 W.

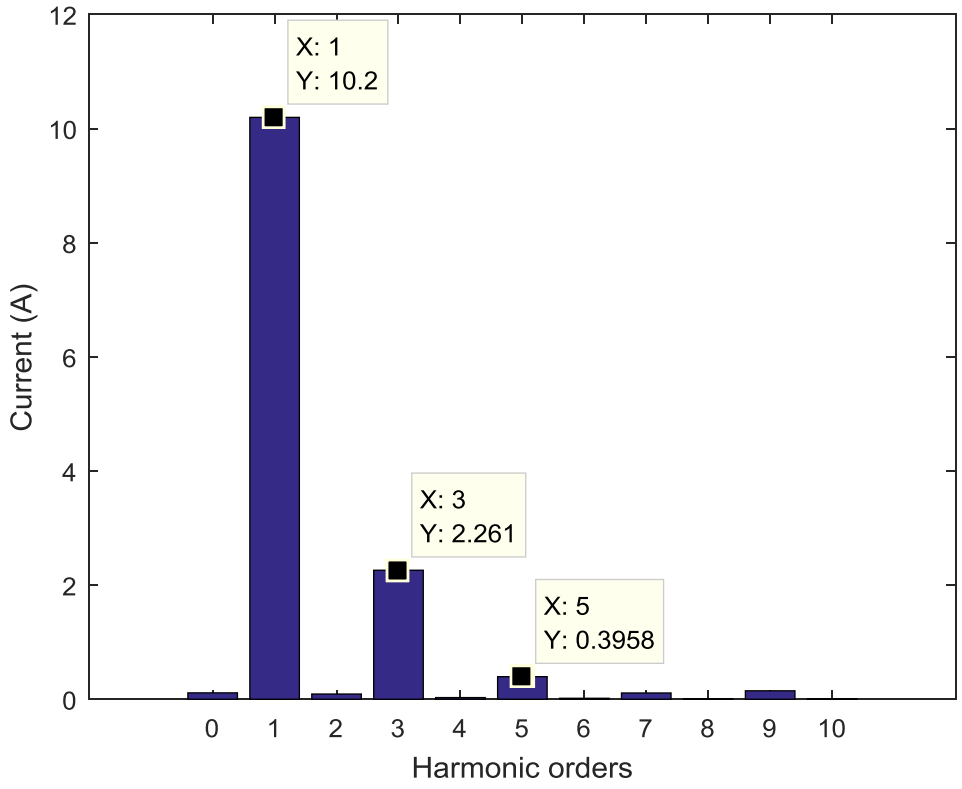

Fig. 5-18 Harmonics of the current with curent disrotion at 3.5 kW

The conventional prediction method described in Chapter 3 is also applied to calculate the power loss. The copper loss predicted by the conventional method is 4.994W, and the total loss in the prediction is 6.225 + 4.994= 11.22 W. This results are in line with the prediction in Chapter 3 in the case that the operating frequency goes far below the series resonant frequency.

The comparison of these three methods is listed in Table 5-4:

Table 5-4 Comparison of three power loss calaulction methods

Methods	Measured	FEA	Conventional	Unit
Total loss	26.06	20.44	11.22	W
Error percentage	-	21.55%	56.95%	-
Core loss	6.225	6.225	6.225	W
Copper loss	19.83	14.21	4.994	W

As can be observed, compared with the measured copper loss 26.06W, the resultant power loss from FEA model is 20.44W, 21.55% less than the test results. An error is seen between the FEA results and the actual test results. This error may be caused by the inaccuracy in the phase measurement of the inductor voltage and current. Since the switching frequency is quite high, only 1045 samples are recorded in one switching cycle (although this is more than the 800 samples in precious section), thus even a small phase delay in the inductor voltage and current will cause big error. However, despite of the inaccuracy in the phase measurement, the FEA method is clearly more accurate than the conventional method which is 11.22W with 56.95% less than the test results.

5.4 Transformer Copper Loss Calculation with 3D FEA

The FEA method described previously for the inductor can also be used to calculate the power loss in a transformer. This section presents the calculation of the transformer copper loss with 3D FEA. The calculation principle and procedure are similar to those for the inductor presented in Section 5.3.1. However, the main difference is that the transformer has windings in both primary and secondary sides. Therefore, it is essential to calculate the proximity loss in the primary winding due to the current in the secondary winding and vice versa. This will be described in Section 5.4.3.

5.4.1 FE model

The FE tool FLUX 3D developed by CEDRAT [168] is employed to build the 3D FE model of the transformer and subsequently perform the proximity loss calculation. Fig. 5-19 shows the transformer geometries built in the 3D FE model.

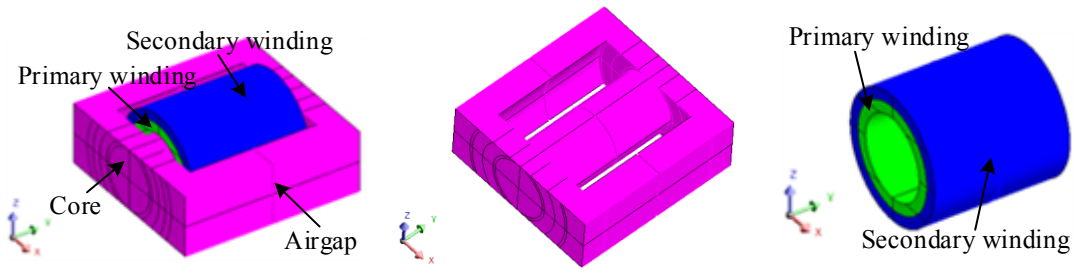

Fig. 5-19 Inductor geometries in the 3D FE model. (a) Winding and core. (b) Core. (c) Winding.

Given that the magnetic field in the full model satisfies the symmetry conditions along the *XOY* and *YOZ* planes, the model can be simplified to the one fourth of the whole model as illustrated in Fig. 5-20. The definitions of *XOY* and *YOZ* planes can also be found in Fig. 5-20 (a). The boundary conditions along *XOY* and *YOZ* planes are with tangent magnetic field and normal electric field. It should be noted that the model is built via the extrusion of the 2D geometry shown in the *ZOX* plane. The 2D geometry contains all the intersection points and lines in the projection of the 3D model against *ZOX* plane. Therefore, the 2D geometry shown in the *ZOX* plane is divided into many areas, as shown in Fig. 5-20 (a). The objective to employ this model strategy is to address the issue that the mesh cannot be easily generated in a complex 3D geometry with both arcs and very narrow airgaps. Subsequently, the geometry built in Fig. 5-20 (a) is meshed and Fig. 5-21 illustrates the mesh densities on the core and winding.

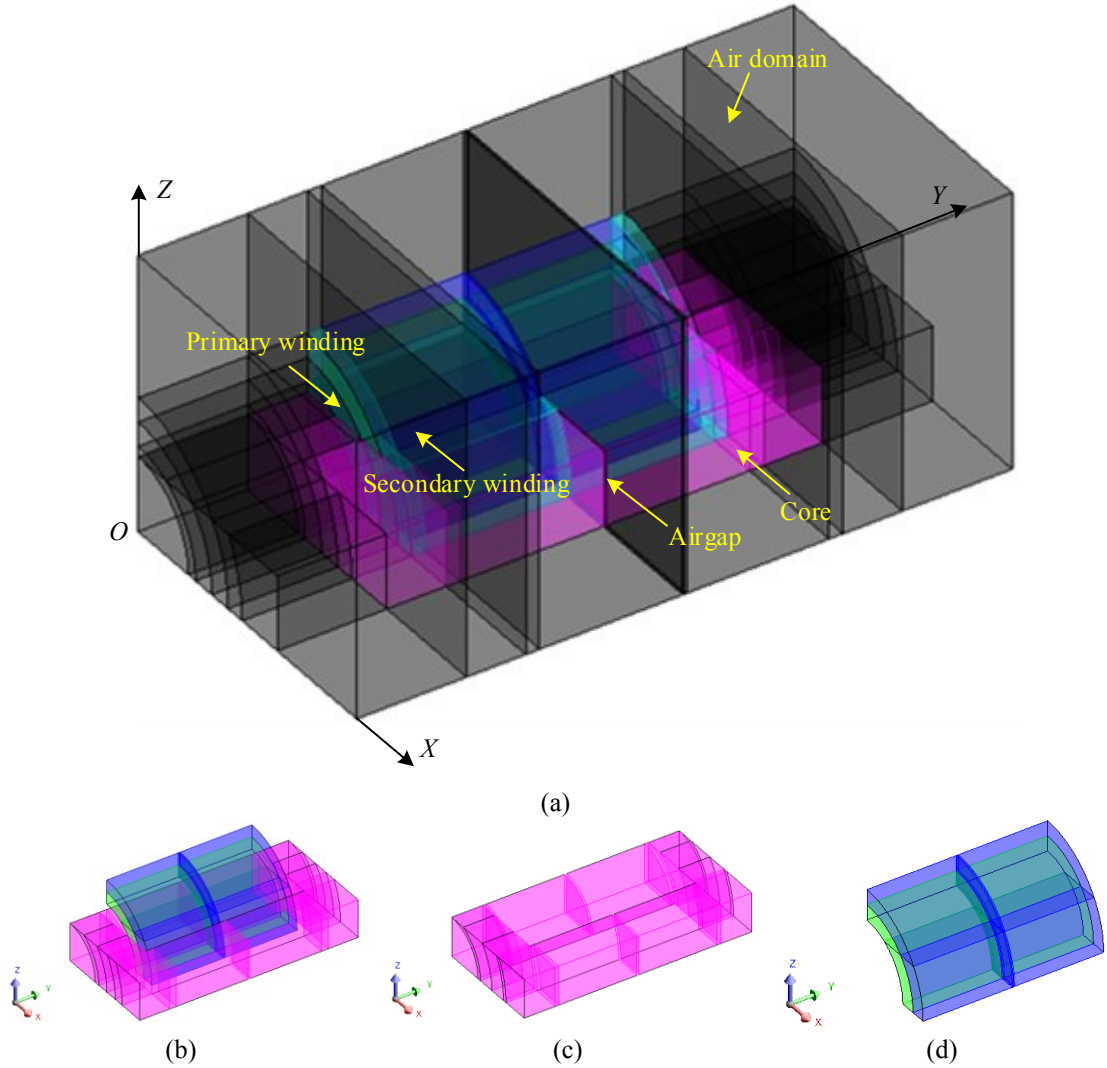

Fig. 5-20 Transformer 3D FE models considering symmetries. (a) Full model. (b) Core, winding and airgap. (c) Core. (d) Winding.

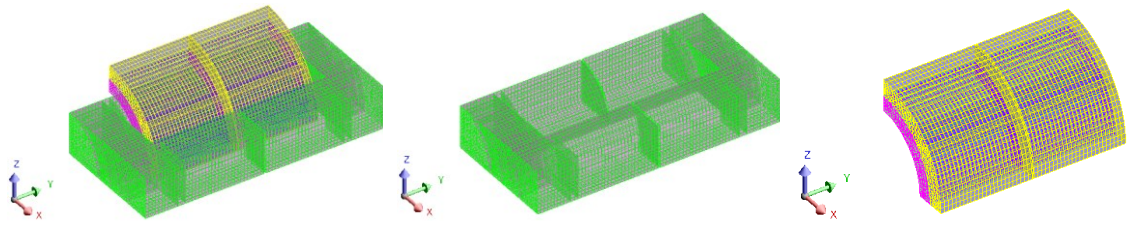

(a) (b) (c)

Fig. 5-21 3D mesh of the transformer FE model. (a) Core and winding. (b) Core. (c) Winding.

It can be seen that the mesh on all the surfaces parallel to *ZOX* plane are identical due to the 3D model is extruded from the 2D model on *ZOX* plane and thus the extrusion mesh generator is used in the mesh generation process.

The material used in this 3D FE model is 3C92 (which is different with the core material 3C95 used in the inductor) whose datasheet B-H curve is displayed in Fig. 5-22 (a). To be specific, Fig. 5-22 (b) presents its B-H curve with uniform scale at 100°C.

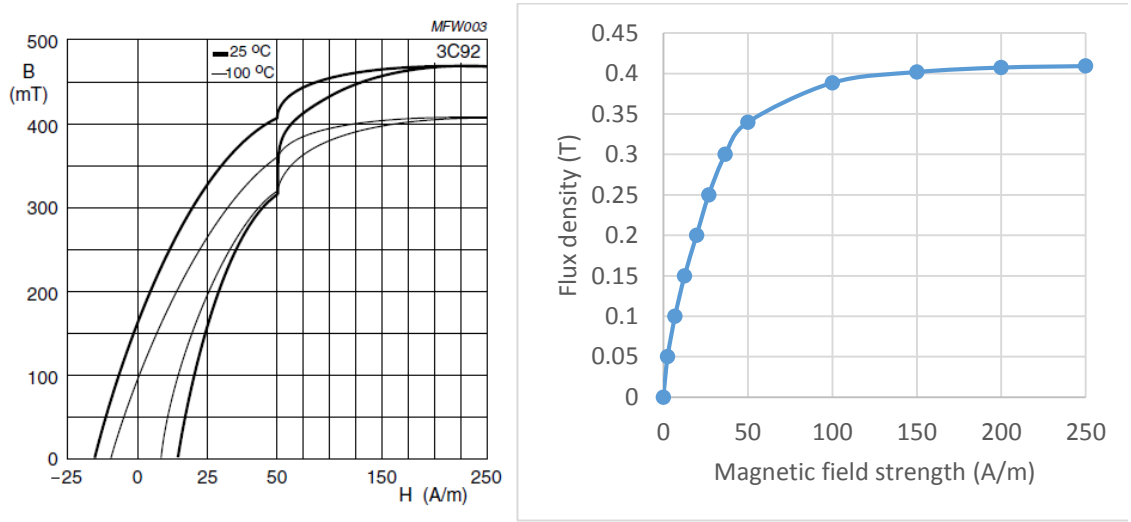

(a) (b)

Fig. 5-22 B-H curve of the core material 3C92. (a) Datasheet. (b) Rebuild with uniform scale.

5.4.2 Nodal flux density

To consider the proximity effects in the primary winding due to both primary and secondary currents and those in the secondary winding due to both secondary and primary currents, the 3D FE model built in Section 5.4.1 is run with the combination of primary and secondary currents at (6A, 0A), (0A, 6A) and (6A, 6A) to generate the flux densities. Fig. 5-23 - Fig. 5-25 illustrates the contours. It should be noted that, ideally the Ampere-turns in the primary and secondary should be kept the same, however the influence of the current amplitude on the normalised flux density is negligible.

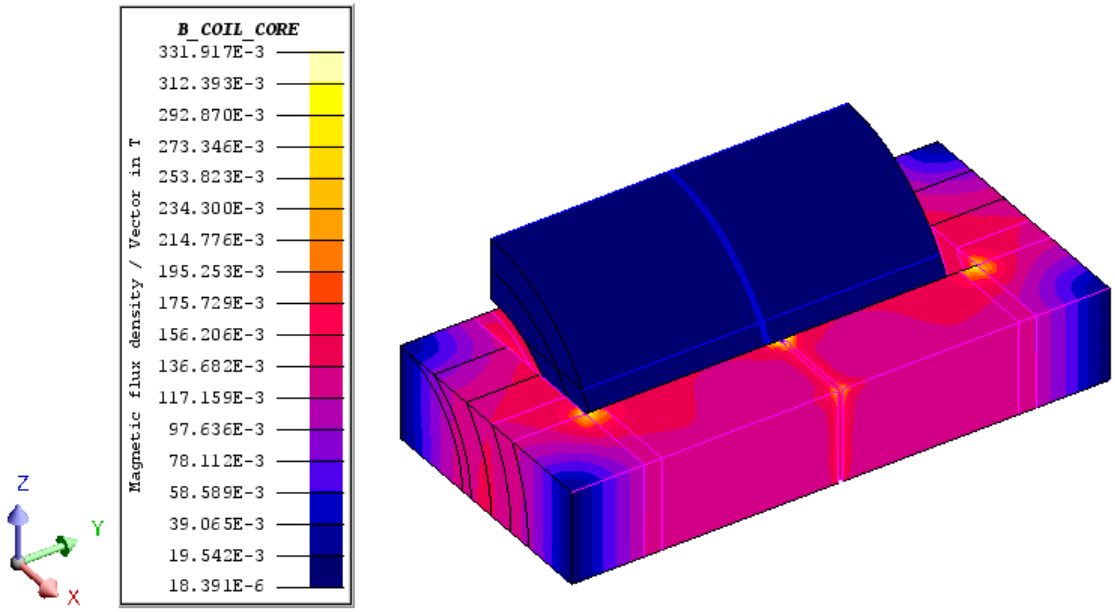
B_COIL_CORE
331.917E-3
312.393E-3
292.870E-3
273.346E-3
253.823E-3
234.300E-3
214.776E-3
195.253E-3
175.729E-3
156.206E-3
136.682E-3
117.159E-3
97.636E-3
78.112E-3
58.589E-3
39.065E-3
19.542E-3
18.391E-6
Magnetic flux density / Vector in T
Z
Y
X

(a)

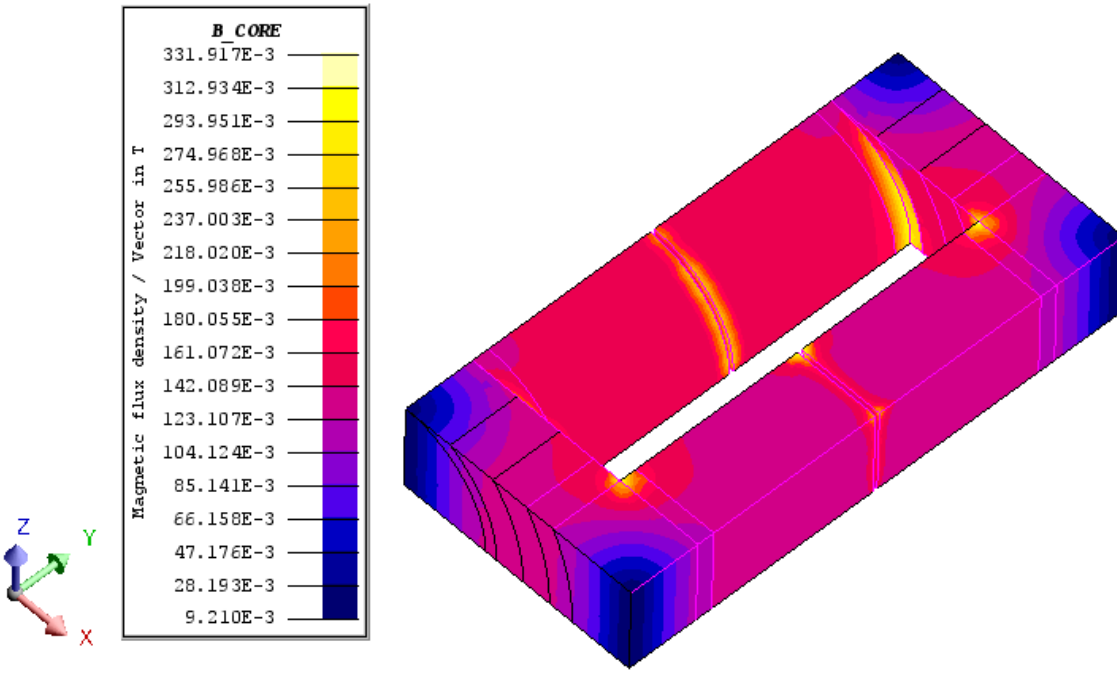
B_CORE
331.917E-3
312.934E-3
293.951E-3
274.968E-3
255.986E-3
237.003E-3
218.020E-3
199.038E-3
180.055E-3
161.072E-3
142.089E-3
123.107E-3
104.124E-3
85.141E-3
66.158E-3
47.176E-3
28.193E-3
9.210E-3
Magnetic flux density / Vector in T
Z
Y
X

(b)

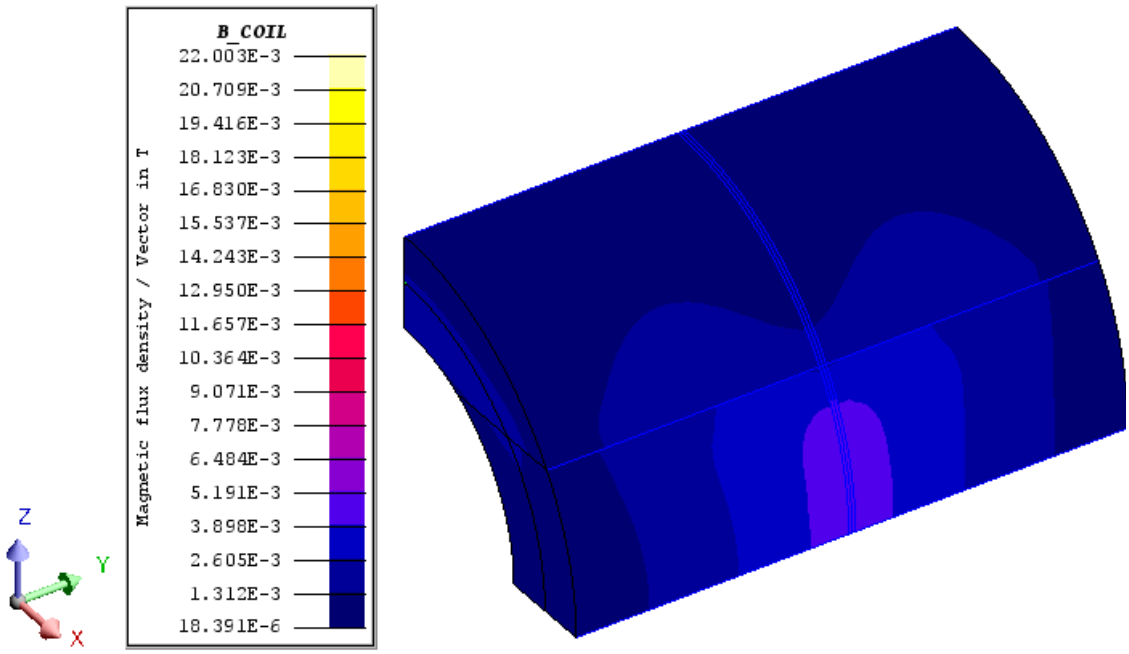

(c)

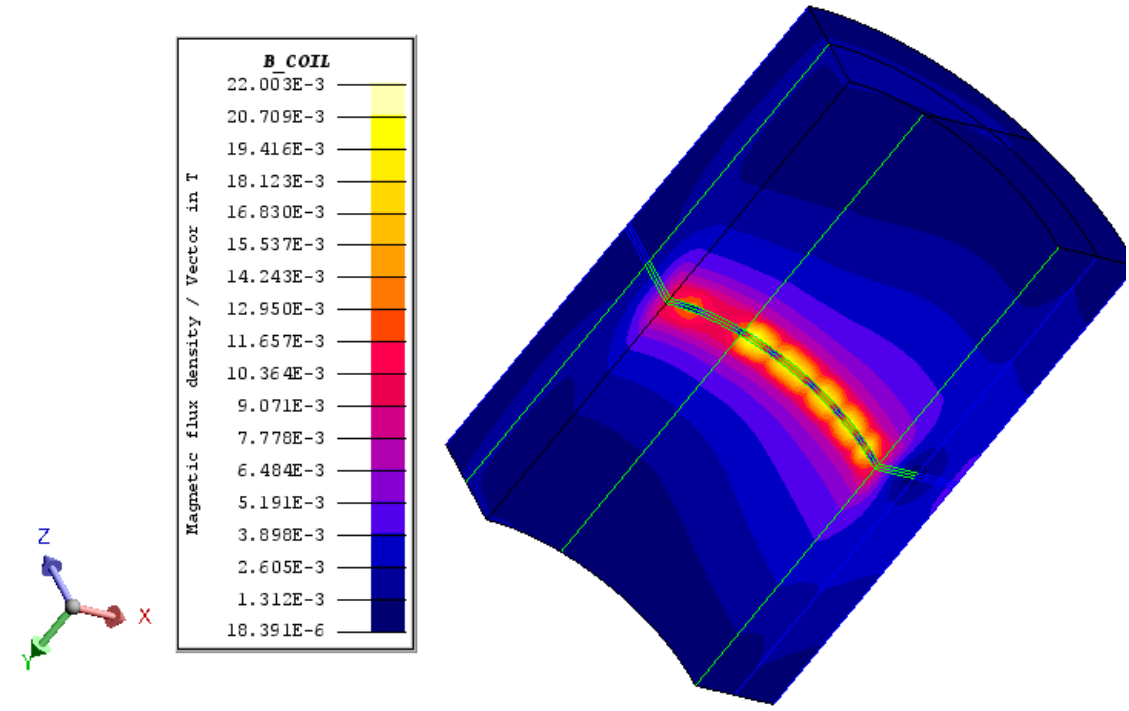

(d)

Fig. 5-23 Flux density contours of the transformer core and winding at 6A current in the primary and 0A current in the secondary. (a) Core and winding. (b) Core. (c) Winding. (d) Winding.

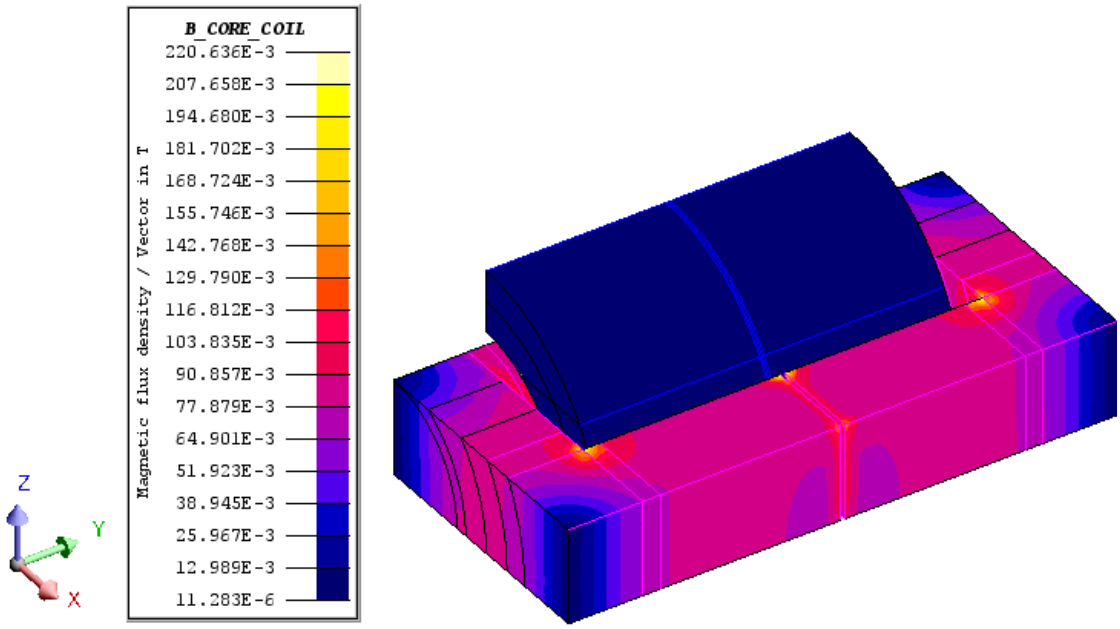
B_CORE_COIL
220.636E-3
207.658E-3
194.680E-3
181.702E-3
168.724E-3
155.746E-3
142.768E-3
129.790E-3
116.812E-3
103.835E-3
90.857E-3
77.879E-3
64.901E-3
51.923E-3
38.945E-3
25.967E-3
12.989E-3
11.283E-6
Magnetic flux density / Vector in T
Z
Y
X

(a)

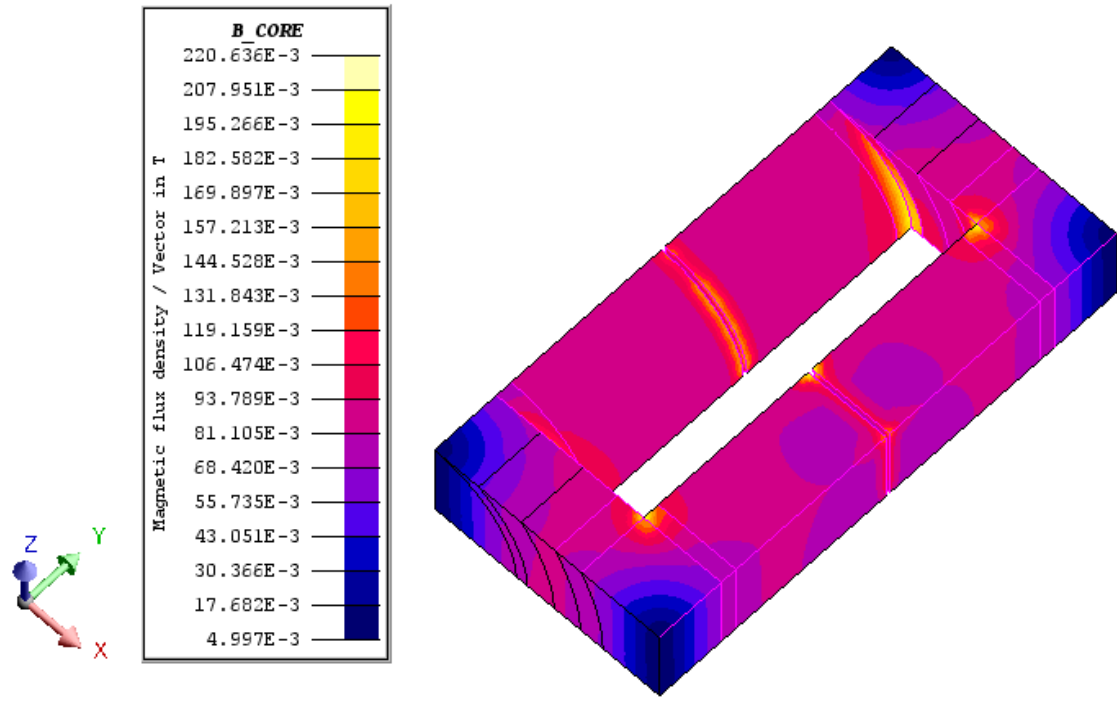
B_CORE
220.636E-3
207.951E-3
195.266E-3
182.582E-3
169.897E-3
157.213E-3
144.528E-3
131.843E-3
119.159E-3
106.474E-3
93.789E-3
81.105E-3
68.420E-3
55.735E-3
43.051E-3
30.366E-3
17.682E-3
4.997E-3
Magnetic flux density / Vector in T
Z
Y
X

(b)

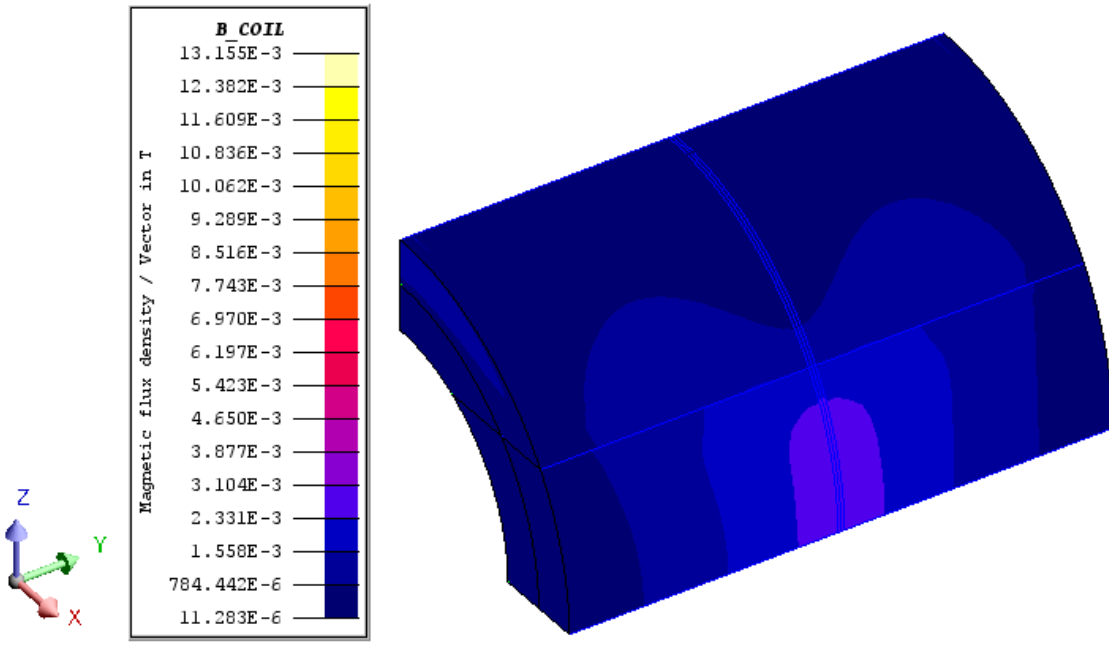

(c)

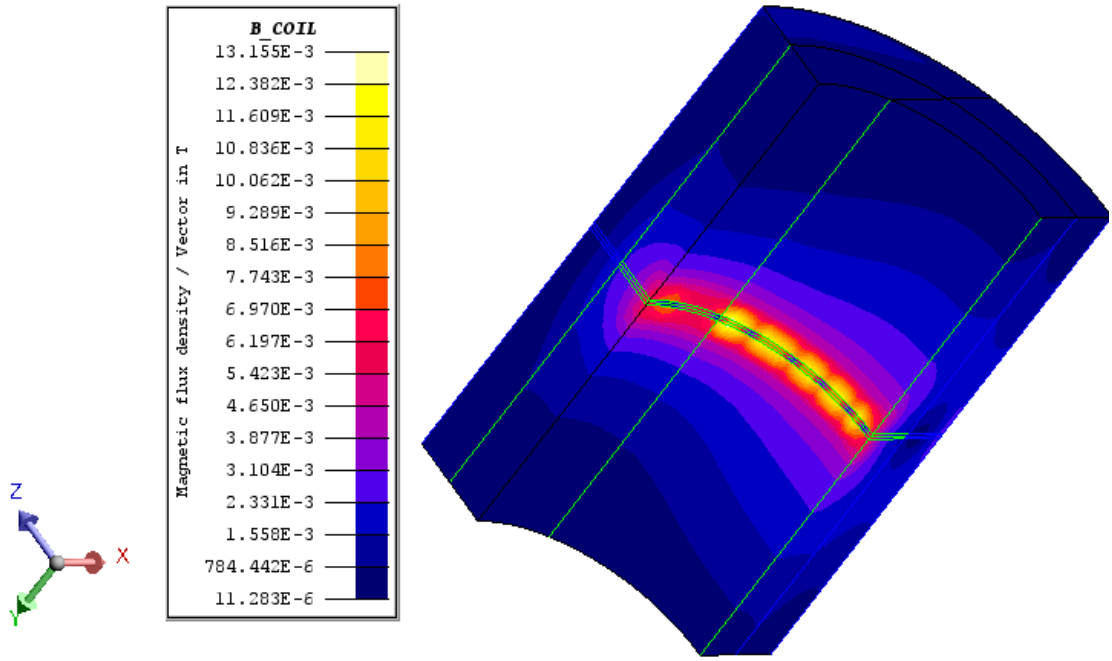

(d)

Fig. 5-24 Flux density contours of the transformer core and winding at 0A current in the primary and 6A current in the secondary. (a) Core and winding. (b) Core. (c) Winding. (d) Winding.

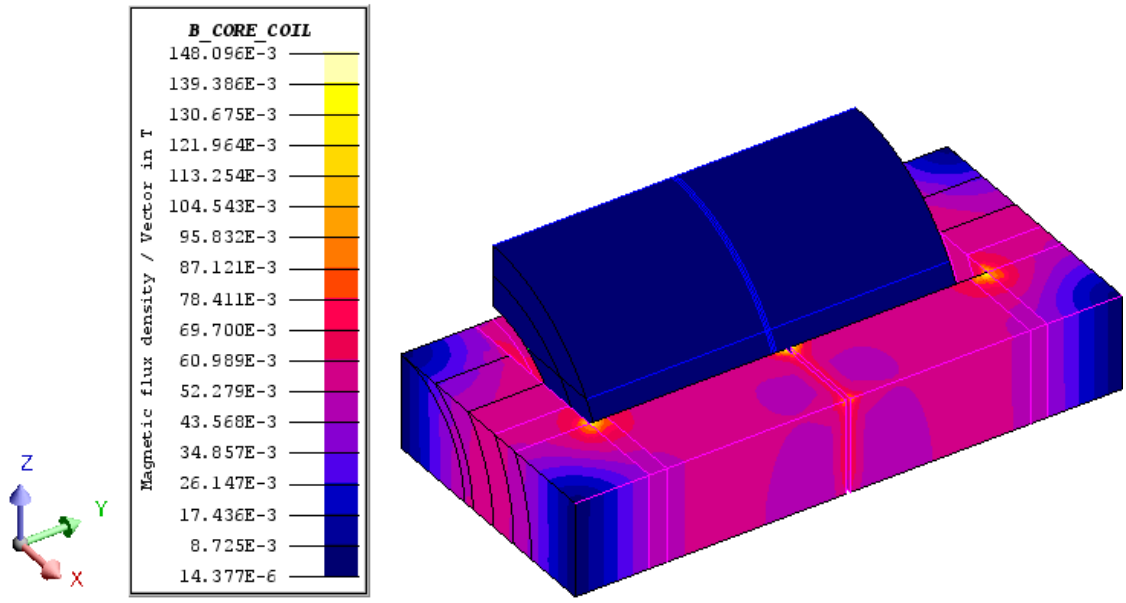
B_CORE_COIL
148.096E-3
139.386E-3
130.675E-3
121.964E-3
113.254E-3
104.543E-3
95.832E-3
87.121E-3
78.411E-3
69.700E-3
60.989E-3
52.279E-3
43.568E-3
34.857E-3
26.147E-3
17.436E-3
8.725E-3
14.377E-6
Magnetic flux density / Vector in T
Z
Y
X

(a)

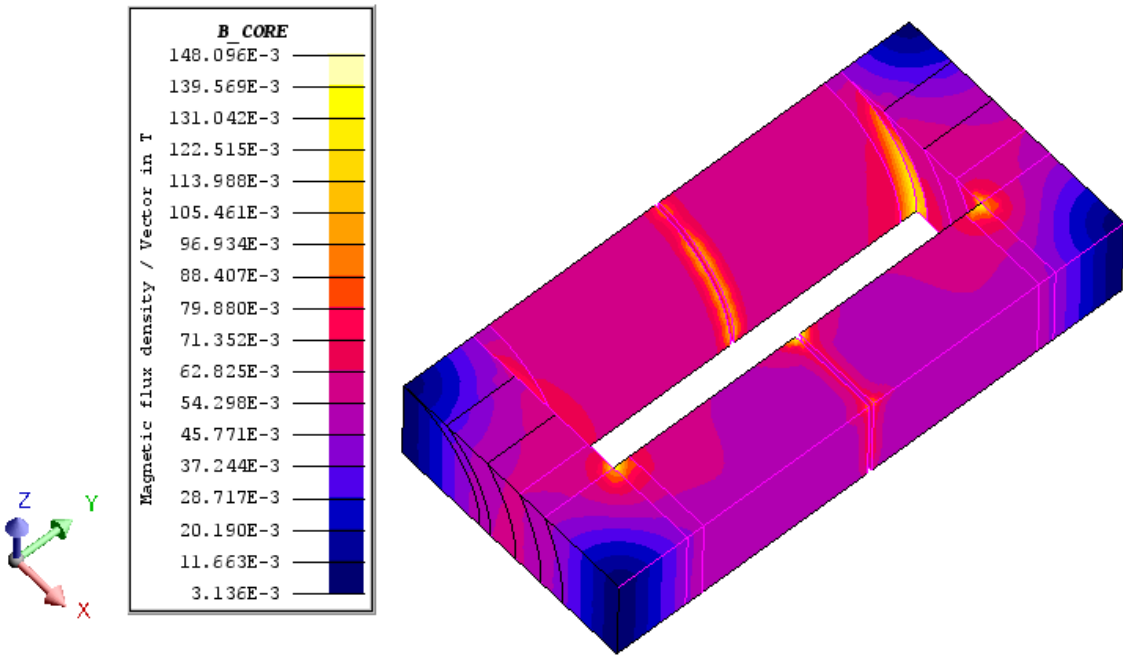
B_CORE
148.096E-3
139.569E-3
131.042E-3
122.515E-3
113.988E-3
105.461E-3
96.934E-3
88.407E-3
79.880E-3
71.352E-3
62.825E-3
54.298E-3
45.771E-3
37.244E-3
28.717E-3
20.190E-3
11.663E-3
3.136E-3
Magnetic flux density / Vector in T
Z
Y
X

(b)

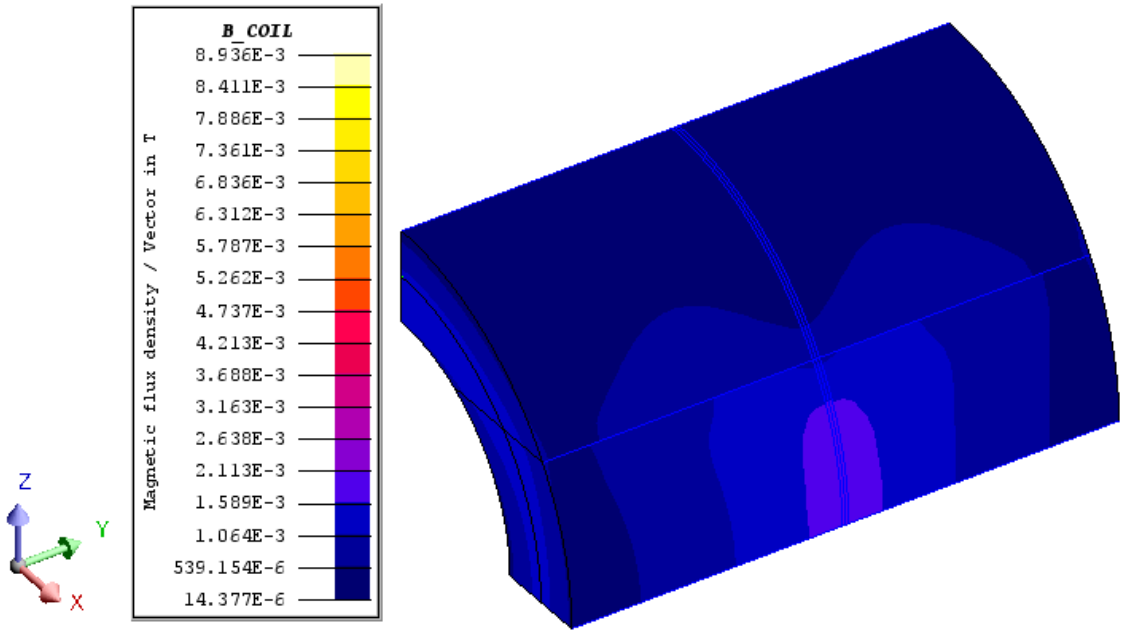

(c)

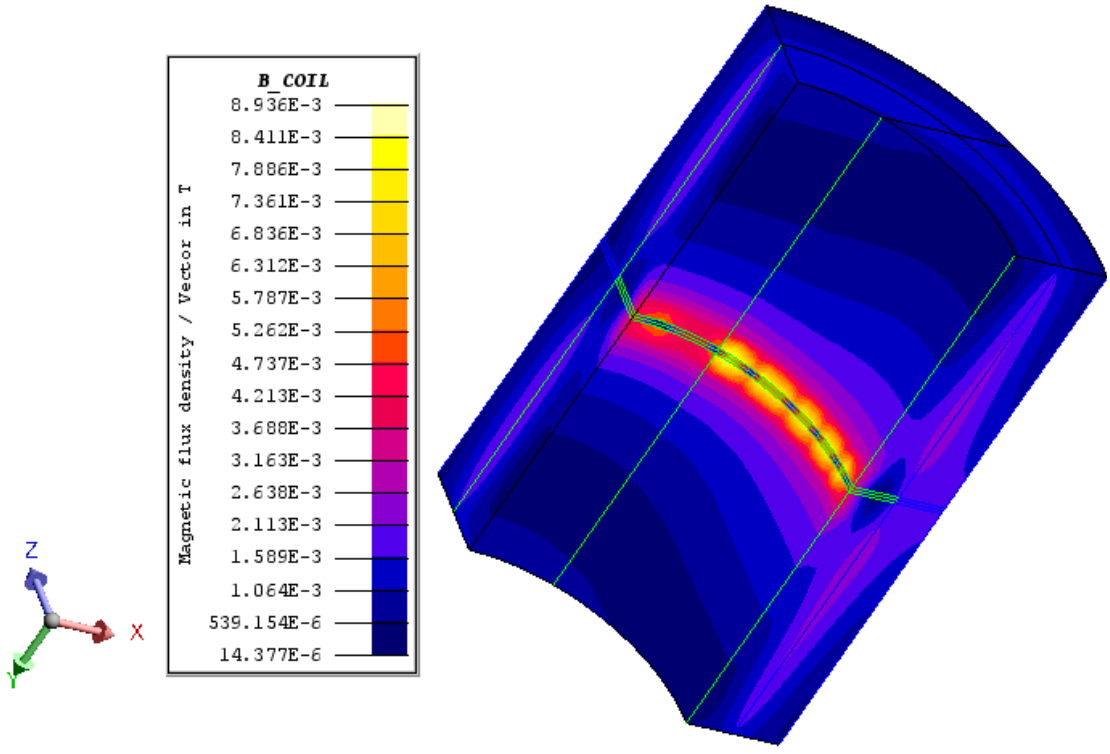

(d)

Fig. 5-25 Flux density contours of the transformer core and winding at 6A current in the primary and 6A current in the secondary. (a) Core and winding. (b) Core. (c) Winding. (d) Winding.

Similar to the inductor flux density distribution shown in Fig. 5-14, the flux densities at the winding corners close to the airgap, particularly the inner layer, are relatively higher than those in the other parts, as illustrated in Fig. 5-23 (c) and (d), Fig. 5-24 (c) and (d)

and Fig. 5-25 (c) and (d). This is also because most of the flux leakage occurs there due to the presence of the airgap.

It can also be observed that the peak flux density at (6A, 0A) is higher than that at (0A, 6A). This is because the primary winding has 15 turns coils, higher than the 9 turns in the secondary winding. Moreover, the peak flux density at (6A, 6A) is the lower than those at (6A, 0A) and (0A, 6A) due to the flux cancellation effects of the primary and secondary windings.

Subsequently, the flux density at each node at these three load conditions is exported before the winding copper loss calculation which will be discussed Section 5.4.3.

5.4.3 Copper loss calculation

As stated Section 5.1, the domination of the copper loss is the proximity loss. The transformer proximity loss can be calculated from Equation (5-11) derived in [167].

$$P_{px\_trs} = \frac{\pi L_{tp} N_{tsp} {d_{cp}}^4}{64\rho_c} \langle \overline{\left(\frac{d\vec{B}_k}{dt}\right)^2} \rangle_p + \frac{\pi L_{ts} N_{tss} {d_{cs}}^4}{64\rho_c} \langle \overline{\left(\frac{d\vec{B}_n}{dt}\right)^2} \rangle_s \tag{5-11}$$

where P_{px_trs} is the transformer proximity loss, L_{tp} and L_{ts} are the average length of a turn in the primary and secondary windings respectively, N_{tp} and N_{ts} are the product of the turns per coil times the strand number in each turn, in the primary and secondary sides respectively, d_{cp} and d_{cs} are the strand diameters of the windings in the primary and secondary side respectively, $\vec{B}_k$ is flux density vector in the k^{th} element of the primary winding, $\vec{B}_n$ is the flux density vector in the n^{th} element of the secondary winding, $\langle \cdot \rangle_p$ and $\langle \cdot \rangle_s$ are the spatial average operators over the primary and secondary windings respectively. It should be noted that the flux densities shown in Equation (5-11) is in vector format since the magnetic fields in the windings due to the primary and secondary currents will be three-dimensional.

Assuming that the leakage magnetic field in the winding regions is linearly proportional to current excitation, $\vec{B}_k$ in Equation (5-11) can be attributed to the superposition of the magnetic fields due to the primary and secondary currents, as described in Equation (5-12). Similarly, $\vec{B}_n$ can be expressed as Equation (5-13).

$$\vec{B}_k = \vec{B}_{pk} + \vec{B}_{sk} \tag{5-12}$$

$$\vec{B}_n = \vec{B}_{pn} + \vec{B}_{sn} \tag{5-13}$$

where $\vec{B}_{pk}$ and $\vec{B}_{sk}$ are the flux density vectors in the k^{th} element of the primary winding due to the primary and secondary currents, respectively, and $\vec{B}_{pn}$ and $\vec{B}_{sn}$ are the flux density vectors in the n^{th} element of the secondary winding due to the primary and secondary currents, respectively.

Based on Equation (5-12) and Equation (5-13), the time averages of the squared derivative of the flux densities in the primary and secondary windings can be derived and they are given in Equation (5-14) and Equation (5-15).

$$\langle \overline{\left(\frac{d\vec{B}_k}{dt}\right)^2} \rangle_p = \langle \overline{\left|\frac{d\vec{B}_{pk}}{dt}\right|^2} + \overline{\frac{d\vec{B}_{pk}}{dt} \cdot \frac{d\vec{B}_{sk}}{dt}} + \overline{\frac{d\vec{B}_{sk}}{dt} \cdot \frac{d\vec{B}_{pk}}{dt}} + \overline{\left|\frac{d\vec{B}_{sk}}{dt}\right|^2} \rangle_p \tag{5-14}$$

$$\langle \overline{\left(\frac{d\vec{B}_n}{dt}\right)^2} \rangle_s = \langle \overline{\left|\frac{d\vec{B}_{pn}}{dt}\right|^2} + \overline{\frac{d\vec{B}_{pn}}{dt} \cdot \frac{d\vec{B}_{sn}}{dt}} + \overline{\frac{d\vec{B}_{sn}}{dt} \cdot \frac{d\vec{B}_{pn}}{dt}} + \overline{\left|\frac{d\vec{B}_{sn}}{dt}\right|^2} \rangle_s \tag{5-15}$$

The currents fed into the primary and secondary windings can be expressed as Equation (5-16) and Equation (5-17) respectively, for a given frequency of f.

$$i_p = I_{pm}\sin\left(2\pi f t + \varphi_p\right) \tag{5-16}$$

$$i_s = I_{sm}sin(2\pi f t + \varphi_s) \tag{5-17}$$

where i_p and i_s are the primary and secondary winding instantaneous currents respectively, I_{pm} and I_{sm} are their amplitudes, and φ_p and φ_s are the initial phase angles between the primary winding and the secondary winding.

Given that the magnetic field in winding region can be considered as approximately linear, the flux density obtained at a given current can be calculated by linearly scaling the flux density obtained at the reference current, as described by Equation (5-18) to Equation (5-21)

$$\vec{B}_{pk} = \frac{I_{pm}}{I_{0pm}} \vec{B}_{0pk} \tag{5-18}$$

$$\vec{B}_{sk} = \frac{I_{sm}}{I_{0sm}} \vec{B}_{0sk} \tag{5-19}$$

$$\vec{B}_{pn} = \frac{I_{pm}}{I_{0pm}} \vec{B}_{0pn} \tag{5-20}$$

$$\vec{B}_{sn} = \frac{I_{sm}}{I_{0sm}} \vec{B}_{0sn} \tag{5-21}$$

where I_{0pm} and I_{0sm} are the amplitudes of the reference primary and secondary currents, $\vec{B}_{0pk}$ and $\vec{B}_{0sk}$ are the flux density vectors in the k^{th} element of the primary winding due to the reference primary and secondary currents with amplitudes I_{0pm} and I_{0sm} respectively, and $\vec{B}_{0pn}$ and $\vec{B}_{0sn}$ are the flux density vectors in the n^{th} element of the secondary winding due to the reference primary and secondary currents with amplitudes I_{0pm} and I_{0sm} respectively.

The flux density vectors $\vec{B}_{0pk}$, $\vec{B}_{0sk}$, $\vec{B}_{0pn}$ and $\vec{B}_{0sn}$ at the reference currents can be expressed as Equation (5-22) to Equation (5-25).

$$\vec{B}_{0pk} = \vec{B}_{0pkm} \sin\left(2\pi f t + \varphi_p\right) \tag{5-22}$$

$$\vec{B}_{0sk} = \vec{B}_{0skm} \sin(2\pi f t + \varphi_s) \tag{5-23}$$

$$\vec{B}_{0pn} = \vec{B}_{0pnm} \sin\left(2\pi f t + \varphi_p\right) \tag{5-24}$$

$$\vec{B}_{0sn} = \vec{B}_{0snm} \sin(2\pi f t + \varphi_s) \tag{5-25}$$

where $\vec{B}_{0pkm}$ and $\vec{B}_{0skm}$ are the flux density magnitude (magnitude over the time) vectors in the k^{th} element of the primary winding due to reference primary and secondary currents with amplitudes I_{0pm} and I_{0sm} respectively. $\vec{B}_{0pnm}$ and $\vec{B}_{0snm}$ are the flux density magnitude vectors in the n^{th} element of the secondary winding due to reference primary and secondary currents with amplitudes I_{0pm} and I_{0sm} respectively.

Based on Equation (5-15) to Equation (5-25), the derivative of $\vec{B}_{pk}$, $\vec{B}_{sk}$, $\vec{B}_{pn}$ and $\vec{B}_{sn}$ against time are derived in Equation (5-26) to Equation (5-29).

$$\frac{d\vec{B}_{pk}}{dt} = \frac{\vec{B}_{0pkm}}{I_{0pm}} \cdot \frac{di_p}{dt} \tag{5-26}$$

$$\frac{d\vec{B}_{sk}}{dt} = \frac{\vec{B}_{0skm}}{I_{0sm}} \cdot \frac{di_s}{dt} \tag{5-27}$$

$$\frac{d\vec{B}_{pn}}{dt} = \frac{\vec{B}_{0pnm}}{I_{0pm}} \cdot \frac{di_p}{dt} \tag{5-28}$$

$$\frac{d\vec{B}_{sn}}{dt} = \frac{\vec{B}_{0snm}}{I_{0sm}} \cdot \frac{di_s}{dt} \tag{5-29}$$

Substituting Equation (5-14), Equation (5-15) and Equation (5-26) to Equation (5-29) into Equation (5-11), the proximity loss in the transformer can be expressed as Equation (5-30).

$$\begin{aligned} P_{px\_trs} = \frac{\pi L_{tp} N_{tsp} {d_{cp}}^4}{64\rho_c} \Bigg[& \left\langle \frac{\left|\vec{B}_{0pkm}\right|^2}{{I_{0pm}}^2} \right\rangle_p \overline{\left(\frac{di_p}{dt}\right)^2} + \left\langle \frac{\vec{B}_{0pkm} \cdot \vec{B}_{0skm}}{I_{0pm} I_{0sm}} \right\rangle_p \overline{\frac{di_p}{dt} \cdot \frac{di_s}{dt}} \\ & + \left\langle \frac{\vec{B}_{0skm} \cdot \vec{B}_{0pkm}}{I_{0sm} I_{0pm}} \right\rangle_p \overline{\frac{di_s}{dt} \cdot \frac{di_p}{dt}} + \left\langle \frac{\left|\vec{B}_{0skm}\right|^2}{{I_{0sm}}^2} \right\rangle_p \overline{\left(\frac{di_s}{dt}\right)^2} \Bigg] \\ & + \frac{\pi L_{ts} N_{tss} {d_{cs}}^4}{64\rho_c} \Bigg[\left\langle \frac{\left|\vec{B}_{0pnm}\right|^2}{{I_{0pm}}^2} \right\rangle_s \overline{\left(\frac{di_p}{dt}\right)^2} \\ & + \left\langle \frac{\vec{B}_{0pnm} \cdot \vec{B}_{0snm}}{I_{0pm} I_{0sm}} \right\rangle_s \overline{\frac{di_p}{dt} \cdot \frac{di_s}{dt}} + \left\langle \frac{\vec{B}_{0snm} \cdot \vec{B}_{0pnm}}{I_{0sm} I_{0pm}} \right\rangle_s \overline{\frac{di_s}{dt} \cdot \frac{di_p}{dt}} \\ & + \left\langle \frac{\left|\vec{B}_{0snm}\right|^2}{{I_{0sm}}^2} \right\rangle_s \overline{\left(\frac{di_s}{dt}\right)^2} \Bigg] \end{aligned} \tag{5-30}$$

Therefore, the quantities needs to be obtained via FEA include the average flux density square over all the elements in the primary winding with the reference primary

current injected $\langle|\vec{B}_{0pkm}|^2\rangle_p$, the average flux density square over all the elements in the primary winding with the reference secondary current injected $\langle|\vec{B}_{0skm}|^2\rangle_p$, the average flux density square over all the elements in the secondary winding with the reference primary current injected $\langle|\vec{B}_{0pnm}|^2\rangle_s$, the average flux density square over all the elements in the secondary winding with the reference secondary current injected $\langle|\vec{B}_{0snm}|^2\rangle_s$, the average flux density product over all the elements in the primary winding with both the reference primary and secondary currents injected $\langle\vec{B}_{0pkm}\cdot\vec{B}_{0skm}\rangle_p$ and the average flux density product over all the elements in the secondary winding with both the reference primary and secondary currents injected $\langle\vec{B}_{0pnm}\cdot\vec{B}_{0snm}\rangle_s$.

However, given that the mesh sizes of the winding elements could be non-uniform, the average flux density squares and products $\langle|\vec{B}_{0pkm}|^2\rangle_p$, $\langle|\vec{B}_{0skm}|^2\rangle_p$, $\langle|\vec{B}_{0pnm}|^2\rangle_s$, $\langle|\vec{B}_{0snm}|^2\rangle_s$, $\langle\vec{B}_{0pkm}\cdot\vec{B}_{0skm}\rangle_p$ and $\langle\vec{B}_{0pnm}\cdot\vec{B}_{0snm}\rangle_s$ over the winding elements may not represent the true spatial average flux density squares and products. Therefore, the weighted arithmetic mean of all the element flux density squares and products by weighting element volumes are employed to calculate the spatial average flux density squares and products, as described in Equation (5-31).

$$
\begin{aligned}
P_{px\_trs} = {} & \frac{\pi L_{tp} N_{tsp} {d_{cp}}^4}{64 \rho_c V_{olp}} \left[\left\langle \frac{\left|\vec{B}_{0pkm}\right|^2}{{I_{0pm}}^2} V_k \right\rangle_p \overline{\left(\frac{d\imath_p}{dt}\right)^2} \right. \\
& + \left\langle \frac{\vec{B}_{0pkm} \cdot \vec{B}_{0skm}}{I_{0pm} I_{0sm}} V_k \right\rangle_p \overline{\frac{d\imath_p}{dt} \cdot \frac{d\imath_s}{dt}} \\
& \left. + \left\langle \frac{\vec{B}_{0skm} \cdot \vec{B}_{0pkm}}{I_{0sm} I_{0pm}} V_k \right\rangle_p \overline{\frac{d\imath_s}{dt} \cdot \frac{d\imath_p}{dt}} + \left\langle \frac{\left|\vec{B}_{0skm}\right|^2}{{I_{0sm}}^2} V_k \right\rangle_p \overline{\left(\frac{d\imath_s}{dt}\right)^2} \right] \\
& + \frac{\pi L_{ts} N_{tss} {d_{cs}}^4}{64 \rho_c V_{ols}} \left[\left\langle \frac{\left|\vec{B}_{0pnm}\right|^2}{{I_{0pm}}^2} V_n \right\rangle_s \overline{\left(\frac{d\imath_p}{dt}\right)^2} \right. \\
& + \left\langle \frac{\vec{B}_{0pnm} \cdot \vec{B}_{0snm}}{I_{0pm} I_{0sm}} V_n \right\rangle_s \overline{\frac{d\imath_p}{dt} \cdot \frac{d\imath_s}{dt}} \\
& \left. + \left\langle \frac{\vec{B}_{0snm} \cdot \vec{B}_{0pnm}}{I_{0sm} I_{0pm}} V_n \right\rangle_s \overline{\frac{d\imath_s}{dt} \cdot \frac{d\imath_p}{dt}} + \left\langle \frac{\left|\vec{B}_{0snm}\right|^2}{{I_{0sm}}^2} V_n \right\rangle_s \overline{\left(\frac{d\imath_s}{dt}\right)^2} \right]
\end{aligned}
\tag{5-31}
$$

where V_k is the volume of the k^{th} element in the primary winding, V_n is the volume of the n^{th} element in the secondary winding, and V_{olp} and V_{ols} is the volume of the primary winding and the secondary winding, respectively.

Equation (5-31) can also be written into the products of matrices format, as shown in Equation (5-32).

$$
P_{px\_trs} = \overline{\begin{bmatrix} \frac{d\imath_p}{dt} & \frac{d\imath_s}{dt} \end{bmatrix}} \mathbf{D} \overline{\begin{bmatrix} \frac{d\imath_p}{dt} \\ \frac{d\imath_s}{dt} \end{bmatrix}} \tag{5-32}
$$

where **D** matrix is expressed as Equation (5-33).

$$\mathbf{D} = \gamma_p \left\langle \begin{bmatrix} \frac{\left|\vec{B}_{0pkm}\right|^2}{I_{0pm}{}^2} V_k & \frac{\vec{B}_{0pkm} \cdot \vec{B}_{0skm}}{I_{0pm} I_{0sm}} V_k \\ \frac{\vec{B}_{0skm} \cdot \vec{B}_{0pkm}}{I_{0sm} I_{0pm}} V_k & \frac{\left|\vec{B}_{0skm}\right|^2}{I_{0sm}{}^2} V_k \end{bmatrix} \right\rangle_p + \gamma_s \left\langle \begin{bmatrix} \frac{\left|\vec{B}_{0pnm}\right|^2}{I_{0pm}{}^2} V_n & \frac{\vec{B}_{0pnm} \cdot \vec{B}_{0snm}}{I_{0pm} I_{0sm}} V_n \\ \frac{\vec{B}_{0snm} \cdot \vec{B}_{0pnm}}{I_{0sm} I_{0pm}} V_n & \frac{\left|\vec{B}_{0snm}\right|^2}{I_{0sm}{}^2} V_n \end{bmatrix} \right\rangle_s \tag{5-33}$$

where coefficients γ_p and γ_s can be calculated by Equation (5-34) and Equation (5-35) respectively.

$$\gamma_p = \frac{\pi L_{tp} N_{tsp} {d_{cp}}^4}{64 \rho_c V_{olp}} \tag{5-34}$$

$$\gamma_s = \frac{\pi L_{ts} N_{tss} {d_{cs}}^4}{64 \rho_c V_{ols}} \tag{5-35}$$

Based on Equation (5-32) to Equation (5-35), Table 5-5 lists the winding proximity losses in the transformer at 6.22A and 6.5A RMS currents.

The winding DC loss P_{DC} in the transformer can be calculated with the conventional equation shown in Equation (5-36)

$$P_{DC} = \frac{1}{2} {I_{pm}}^2 R_{pDC} + \frac{1}{2} {I_{sm}}^2 R_{sDC} \tag{5-36}$$

where R_{pDC} and R_{sDC} are the primary and secondary winding DC resistances which can be calculated with Equation (5-37) and Equation (5-38) respectively.

$$R_{pDC} = \frac{4 \rho_c L_{tp} N_{tsp}}{\pi {d_{cp}}^2} \tag{5-37}$$

$$R_{sDC} = \frac{4 \rho_c L_{ts} N_{tss}}{\pi {d_{cs}}^2} \tag{5-38}$$

Thus, the inductor copper loss can be obtained by summing the proximity loss P_{px_trs} and the DC loss P_{DC}.

Table 5-5 Summary of proximity losses in the transformer

Resonant current	SIMULATION		Unit
	6.22A	6.5A	
Total Loss	24.65	26.92	W
Proximity loss total	24.05	26.27	W
Proximity loss primary	13.39	14.62	W
Proximity loss secondary	10.66	11.65	W
DC loss total	0.60	0.65	W
DC loss primary	0.19	0.20	W
DC loss secondary	0.41	0.45	W

5.4.4 Experimental verification

Similarity, the measurement of the transformer voltages and currents performance is performed in the same CLLC resonant converter operating in the V2G reverse mode, under the same conditions: the battery voltage is 238.33 V, the DC link voltage is 383.7 V, the discharging current is 9.0A, and the switching frequency is approximately 125.94 kHz.

The measured voltages and currents of the transformer are obtained from the waveform data of the oscilloscope and plotted in Fig. 5-26. Then the power loss in the transformer can be calculated using the secondary side power subtracting the primary side power in the V2G reverse mode and vice versa in the G2V forward mode.

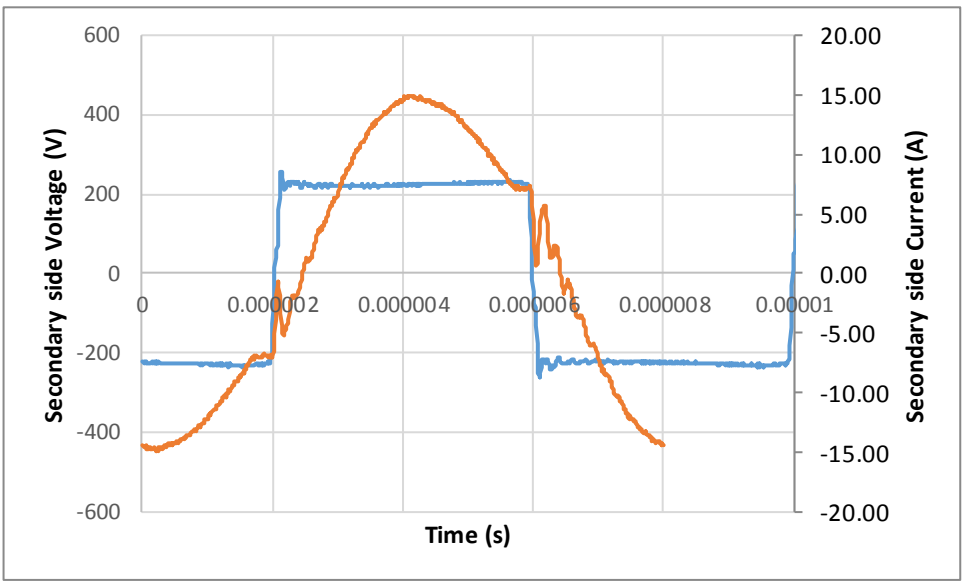

(a)

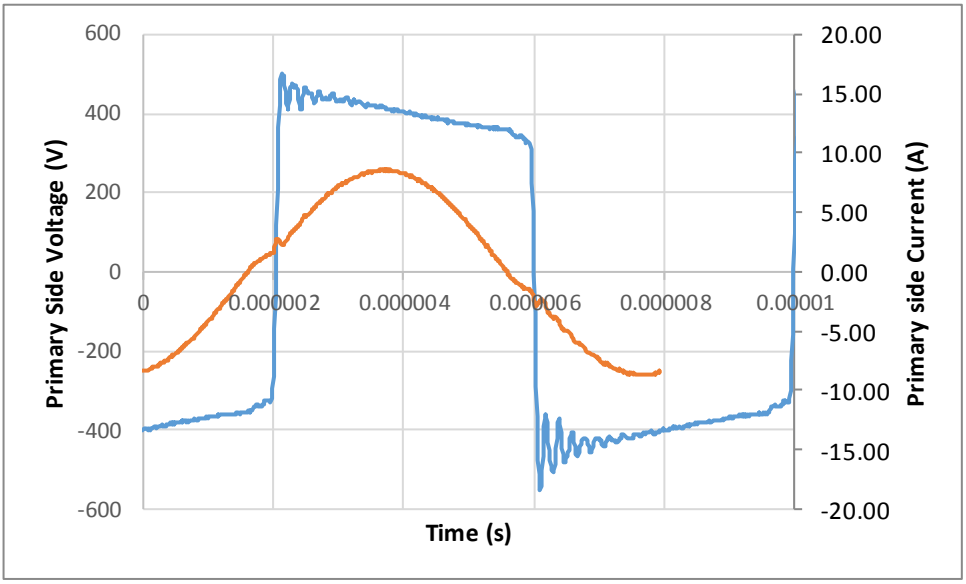

(b)

Fig. 5-26 The transformer voltage (in blue) and current (in red) in the (a) secondary side and (b) primary side

As observed in the figure, the secondary side current is lagging the chopped voltage due to the ZVS operation. The inductor current waveform is close to sinusoidal, despite of a small flat area in the DCM, because of the operating frequency close to (slightly below) the series resonant frequency. The primary side current (the current through the rectifier diodes) shows the rectifier diodes turned off at ZCS operation with low di/dt. The primary side voltage is not pure square wave but has a voltage drop owing to the leakage inductance, resonant tank and equivalent winding resistance.

The sampling rate of the oscilloscope is 100MS/s (corresponding resolution 1E-8). The switching frequency is 125.94 kHz, and thus 800 sample points are recorded in one switching cycle. The instantaneous secondary and primary side power at each sampling time is calculated with the instantaneous voltage and current, and then the averaged transformer power loss in one switching cycle is calculated as the subtraction of the power in the two sides of the transformer.

In this test, the power through the transformer can be calculated to be $P_{sec} - P_{pri}$ = 2092.28 - 2066.65 = 25.63 W.

Then, the FEA method is also applied with the same condition. The DC loss is 0.5614W, the proximity loss in the primary is 11.18W, and the proximity loss in the secondary side is 8.901 W, so the total copper loss in the transformer is 20.64W. The core loss is 9.169 W (Calculated in Chapter 3 in the same condition), thus the total power loss in the transformer is 29.81 W. As expected, there is a small error between the FEA result and the actual test results. As indicated previously, this error may be caused by the measurement inaccuracy. Since the switching frequency is quite high, only 800 samples are recorded in one switching cycle, thus even a small phase delay in the inductor voltage and current will cause big error.

For comparison, the conventional prediction method described in Chapter 3 is also applied to estimate the transformer power loss. The resultant copper loss is 29.80 W, core loss is 9.169W and the total loss is 34.80W. This result is in consistent with the prediction in Chapter 3. The reason why the power loss is higher than the test result and the FEA results is that in the predicted method, the ac resistance of the transformer is curve fitted from several measured data and the relationship is not accurate compared with the FEA method.

The comparison of the three methods is shown in Table 5-6.

Table 5-6 Comparison with different methods

Methods	Measured	FEA	Prediction	Unit
Total loss	25.63	29.80	34.80	W
Core loss	9.169	9.169	9.169	W
Copper loss	16.46	20.64	29.80	W
Error percentage	-	25.38%	81.08%	-

As can be observed from the table, the resultant power loss from FEA model is 20.64 W, 25.38% more than the test results 16.46 W. However, the conventional method is 29.80 W with 81.08% more than the test results. The FEA method is clearly more accurate than the prediction method.

5.5 Summary

A calculation method employing FLUX 2D and FLUX 3D is proposed in this chapter to calculate the power losses for magnetic components in the DC-DC converter. FE models are built based on the definitions of the geometries, meshes, materials, electric circuits, boundary conditions and load conditions. The number of strands and strand diameter of litz wire winding is taken into consideration. The flux density is calculated via FEA at a reference load condition. Then, the power loss of each element is calculated using the obtained nodal flux densities and power loss density function. Finally, the total loss is the sum of the power losses of all the elements. Compared to the conventional method described in Chapter 4, the FEA approach can predict the flux density more accurately, owing to a detailed model with all the geometric parameters and thus the flux leakage effects can be considered. In addition, the nonlinear effect of the core material can be considered in the B-H curve definition in FEA. The 3D FEA approach can predict more accurate winding flux density and thus more accurate proximity loss. Measurement results are compared to assess the accuracy of the proposed calculation method.

CHAPTER 6
Conclusion and Future Work

This chapter summarises the research work the author has undertaken over the PhD studies. Future work based on this thesis is also discussed.

6.1 Work Summary

A typical on-board EV battery charging system includes a front end AC-DC converter for active power factor correction (PFC) and a DC-DC converter to regulate the output voltage and current [9] [61]. In the DC-DC stage, full-bridge DC-DC converters that employ isolated transformer and active power switches are often used as the interface between the front end converter and the EV battery, to provide galvanic isolation, charging/discharging control and flexibility of installation on the EVs [89].

In the typical EV battery constant-current charging operation, the charging current is controlled at a desirable value for optimal battery performance. However, when the single-phase grid side AC voltage (50 or 60 Hz) is rectified, a second order mains frequency harmonic (100 or 120 Hz) will be present in the DC link voltage. This voltage harmonic in turn results in a low frequency current ripple during battery charging. The ripple current can be relatively high, due to low internal impedance of the battery.

This low frequency current ripple is not desired as it causes additional losses, resulting in an increase in battery temperature, which in turn reduce the battery lifetime and EV driving range. **Chapter 2** describes an effective approach to suppression of the battery harmonic current in a 4 kW EV battery charger. A feedforward-proportional-integral-resonant (FF-PIR) controller is employed to suppress the low-frequency current ripple in the LLC resonant converter. A small-signal model has been established from time-domain simulations by injecting a small perturbation signal to the converter operating frequency. An FF-PIR controller is subsequently designed. The proposed resonant controller for suppressing the harmonic current is verified by simulations and experimental tests. Therefore, this control strategy can be used in single phase grid-connected EV onboard charger to improve charger performance and hence enhancing battery performance, efficiency and lifetime. The advances over the current state-of-the art are: 1) the influence of battery SoC on dynamic behavior is taken into consideration in both the modelling and

control design of the battery charger; 2) control robustness to the grid frequency variations is addressed.

The LLC resonant converter, which exhibits high efficiency due to zero-voltage switching (ZVS) in the primary side and zero-current switching (ZCS) in the secondary side, and hence is a promising candidate topology for charging applications. However, LLC resonant converters lose its soft switching features in reverse (V2G) mode, thereby compromising the efficiency and limiting the capabilities of bidirectional power transfer. This limitation may be overcome by a bidirectional CLLC resonant converter which has an extra series capacitor to form a four-element resonant tank. In **Chapter 3**, the topology and the operation of the CLLC resonant converter in both forward mode and reverse mode at different operation conditions is described. The operational characteristics of the CLLC resonant network is analyzed using fundamental harmonic approximation (FHA) method in both G2V and V2G modes, based on which a design procedure for the CLLC resonant converter is discussed, presented and validated in the time-domain simulation and the experimental tests. Furthermore, power loss evaluation is presented and validated in the measurement and comparison. It has been shown that with the CLLC resonant tank, the converter achieves ZVS+ZCS features in both forward and revered modes, allowing less circulating current in the resonant tank and transformer, less turn off current in the primary side MOSFETs and low di/dt in the secondary side diodes. Power loss analysis shows that the efficiency of CLLC improves between 1% and 10.02 % in the whole operating range. All the time-domain simulation and the experimental tests show that with the features of high power conversion efficiency and high power density, it is a suitable candidate for a bi-directional on-board battery charger.

It is well known that terminal voltage of automotive batteries varies as a function of its SoC. With conventional frequency control, the switching frequency of the converter deviates from the series resonant frequency when battery voltage or SoC changes in order to maintain constant charging or discharging current. In the reverse V2G mode this can lead to operation at much higher frequencies and increased converter losses due to waveform distortions and larger circulating current in the resonant tank. Therefore, although power conversion efficiency is improved by employing the CLLC resonant converter in Chapter 3, to further improve the power conversion efficiency, in **Chapter 4**, the maximum efficiency tracking method employing variable DC link control strategy is designed and implemented for the bidirectional charger. This chapter first analyses the

operation of resonant converter over different switching frequency ranges in both the G2V forward and the V2G reverse modes in order to identify the optimal operating frequency. Then the controller is designed for maintaining the optimal operating frequency by varying DC link voltage and performance evaluated. Simulation studies based on the time-domain models and the experimental tests are performed. The efficiency comparisons of the proposed control with conventional techniques based on the experimental tests show that with the new control scheme the efficiency is further improved by 2%.

For evaluating the efficiency of the designed CLLC resonant converter, it is essential to characterize and quantify the power losses in the converter. Litz wire is generally used in the magnetic components of high frequency converters to reduce AC losses caused by skin and proximity effect. It is usually constructed from small insulated strands, woven or twisted to distribute the current density over the entire cross-sectional area. However, the use of litz wire in the magnetic components make it difficult to evaluate the power loss since the magnetic field and current distribution in litz wire due to its complex 3-D geometry is not easy to model. **Chapter 5** describes a novel method which employs 2D and 3D FEA to predict the power losses for magnetic components and AC winding proximity losses. The characteristics of litz wire winding is taken into consideration. The FE model is built with the definitions of the geometries, meshes, materials, electric circuits, boundary conditions and load conditions. The flux density is calculated via FEA at the given load condition. Then, the power loss of each element is calculated using the obtained nodal flux densities and power loss density function. Finally, the total loss is the sum of the power losses of all the elements. Compared to the conventional method for loss prediction described in Chapter 4, the FEA approach can predict the flux density more accurately, owning to a detailed model with all the geometric parameters and thus the flux leakage effects can be considered. In addition, the nonlinear effect of the core material can be considered in the B-H curve definition in FEA. The 3D FEA approach can predict more accurate winding flux density and thus more accurate proximity loss. Measurement results from experimental tests have verified the accuracy of this calculation method.

6.2 List of Publications

The publications as a result of PhD studies include:

- C. Liu, J. Wang, K. Colombage, C. Gould and B. Sen, "A CLLC Resonant Converter Based Bidirectional EV Charger with Maximum Efficiency Tracking," in the 8th IET International Conference on Power Electronics, Machines and Drives (PEMD), 2016, pp. 162-168.
- K. Colombage, J. Wang, C. Gould, and C. Liu, "PWM Harmonic Signature Based Islanding Detection for a Single-Phase Inverter with PWM Frequency Hopping," IEEE Transactions on Industry Applications, vol. 99, pp. 1-1, 2016.
- C. Liu, J. Wang, K. Colombage, C. Gould, B. Sen, and D. Stone, "Current ripple reduction in 4kW LLC resonant converter based battery charger for electric vehicles," in 2015 IEEE Energy Conversion Congress and Exposition (ECCE), 2015, pp. 6014-6021.
- K. Colombage, J. Wang, C. Gould, and C. Liu, "PWM harmonic signature based islanding detection for a single-phase inverter with PWM frequency hopping," in 2015 IEEE Energy Conversion Congress and Exposition (ECCE), 2015, pp. 2294-2301.

There are several publications under preparation to be submitted:

- C. Liu, J. Wang, K. Colombage, C. Gould, B. Sen, and D. Stone, " Modelling and Control of Electric Vehicle On-board Battery Charger with Current Ripple Reduction," to be submitted to IEEE Transactions on Vehicular Technology.
- C. Liu, J. Wang, B. Sen, K. Colombage, and C. Gould, " Design and Power Loss Analysis of CLLC Resonant Converter Based Bidirectional EV Charger with Optimum Resonant-Frequency-Tracking Control," to be submitted to IEEE Transactions on Power Electronics.
- C. Liu, X Chen, J. Wang, B. Sen, K. Colombage, and C. Gould, " Power Loss Analysis of the Magnetic Components in a CLLC Resonant Converter using Finite Element Analysis," to be submitted to IEEE Transactions on Power Electronics.

6.3 Future Work

The CLLC design in Chapter 3 is based on an existed LLC resonant tank. And the design procedure starts from the design of a conventional LLC resonant tank followed by the seizing of the secondary side capacitor. Although this method has the advantage of alleviating the difficulties of optimizing the four elements resonant tank, it can be further optimized. The gain bound is limited because the gain range is already determined by the resonant tank. In addition, the magnetizing inductor is integrated in the transformer, and cannot be modified to further reduce the magnetizing current for efficiency improvement. This design method is more suitable for the applications with an existed system while requiring the conversion efficiency improvement. Thus, the design procedure can be further improved by designing the four-element CLLC resonant tank directly through a more rigorous optimisation process.

The resonant point tracking controller in chapter 4 can be further analyzed. Since less current distortion, lower di/dt, lower turn-on turn-off current will minimize the power loss in the converter and thus increase the converter efficiency, the operating waveforms in both forward G2V forward and the V2G reverse modes at different conditions have been analyzed in order to identify the optimal operation frequency for minimum power loss. However, the analytical model maybe established to further prove the optimal frequency for maximum efficiency operation.

The FLUX 2D and FLUX 3D models can be used for the low power rating where the current waveform is close to sinusoidal. However, when the converter operates in high power, the operating frequency deviates from the series resonant frequency and large distortion occurs in the current. In this case, the current is not sinusoidal anymore. Thus FFT needs to be applied in the current, and all the current harmonics at each frequency should be used to calculate the power loss associated with the magnetic field distribution in the core and within the Litz wire windings. The losses associated with each harmonic should be summed up to obtain the total power loss. This has been implemented for the inductor and should be implemented for the transformer as well.

APPENDIX A
Simulink Models of the Converters

This research has implemented extensive simulation studies employing the software tool of MATLAB/SIMULINK. The Simulink models are listed as follows:

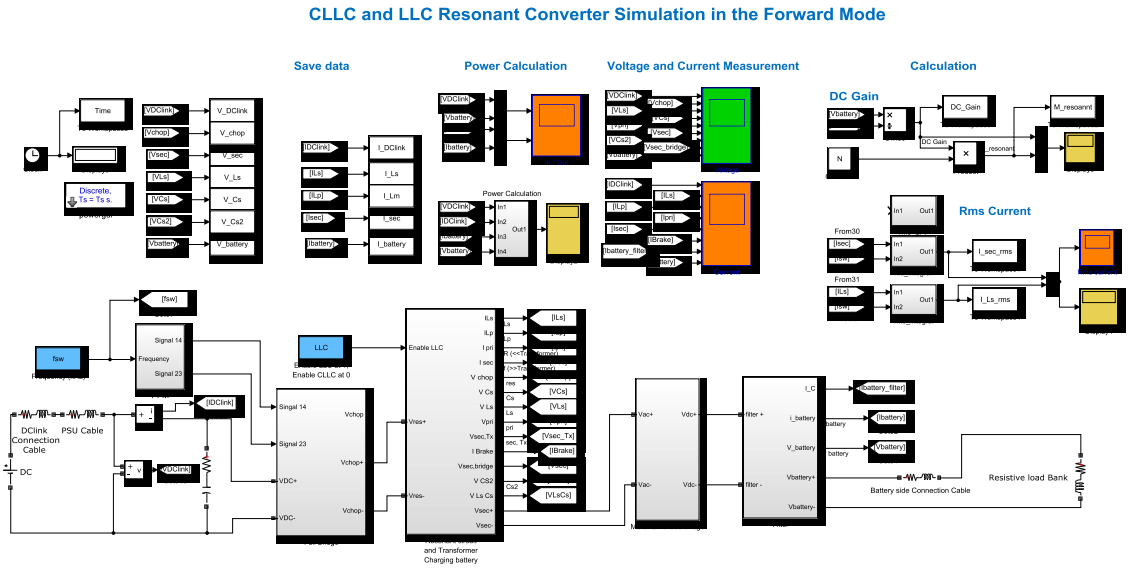

Fig. A-1. The DC-DC resonant converter Simulink model in the forward mode

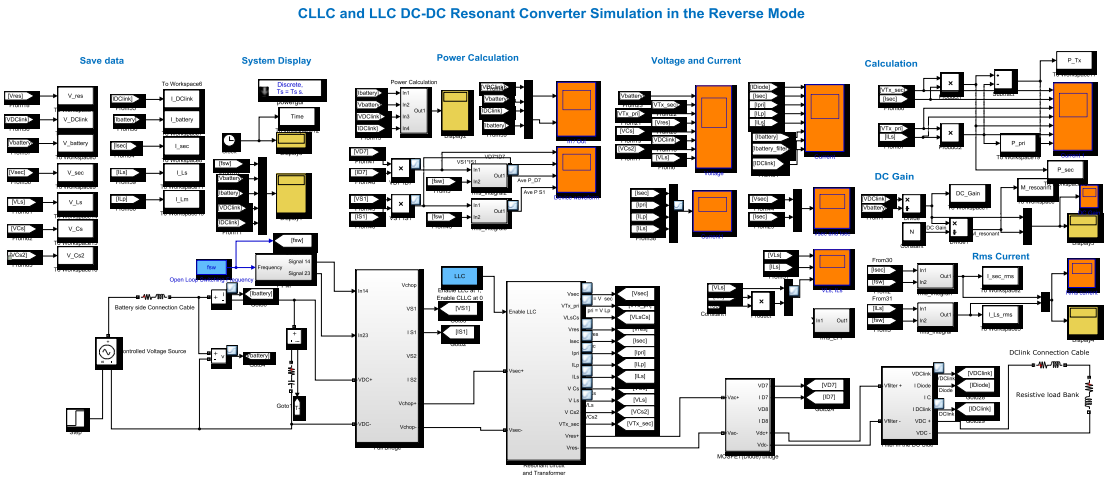

Fig. A-2. The DC-DC resonant converter Simulink model in the reverse mode

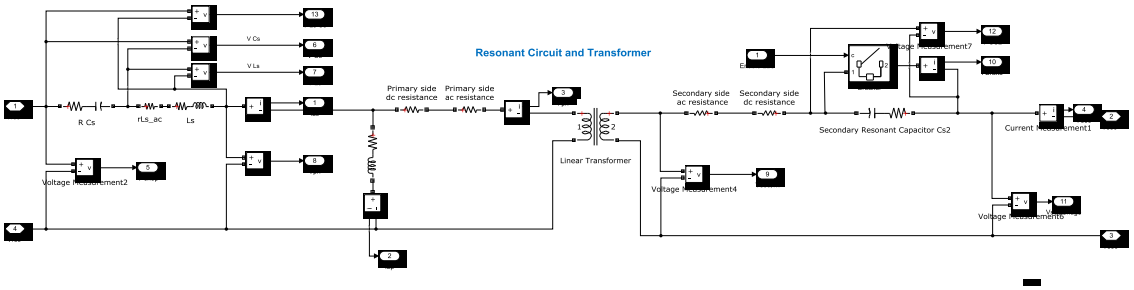

Fig. A-3. The sub-system of the resonant tank

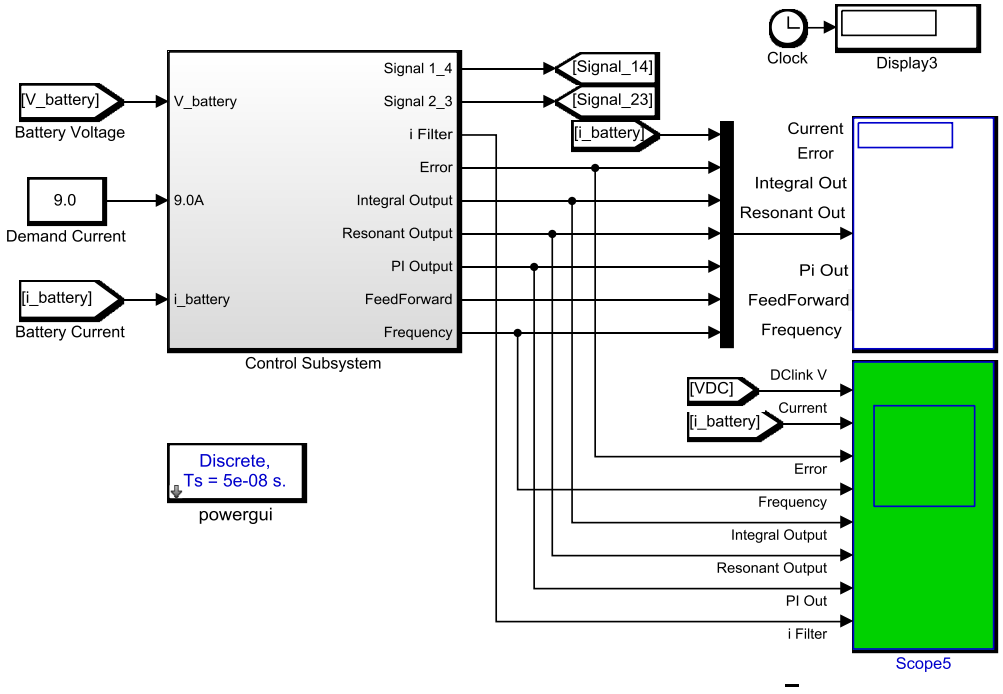

Fig. A-4. The control block of the DC-DC resonant converter

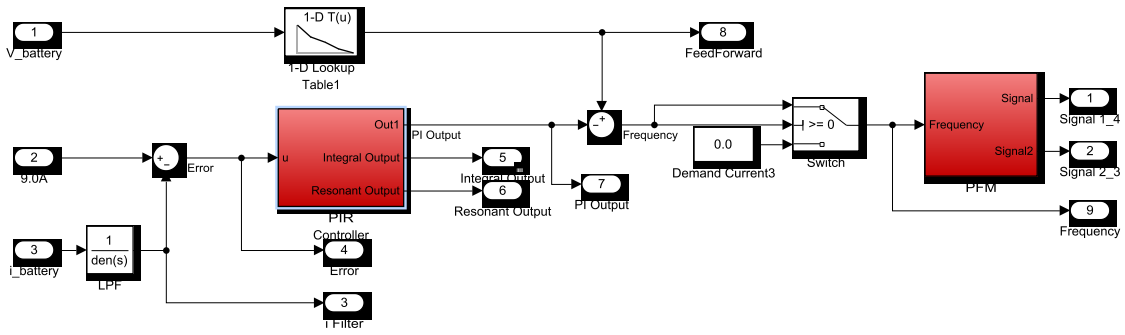

Fig. A-5. The sub-system of the controller of the DC-DC resonant converter

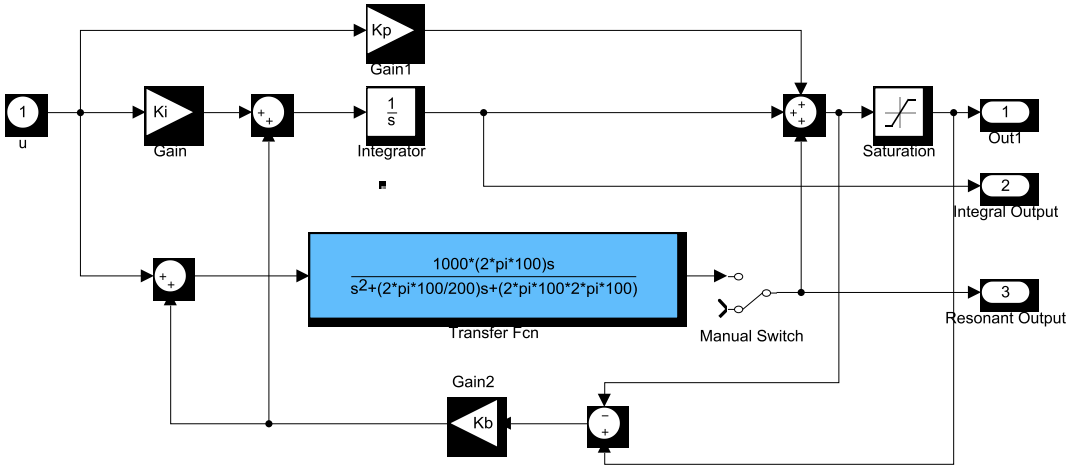

Fig. A-6. The sub-system of the PIR controller

APPENDIX B
Battery Testing System Hardware Configuration

The experimental tests have been implemented with the prototype illustrated in Chapter 2, Chapter 3 and Chapter 4. The battery and the safety protection system in the test are described as follows:

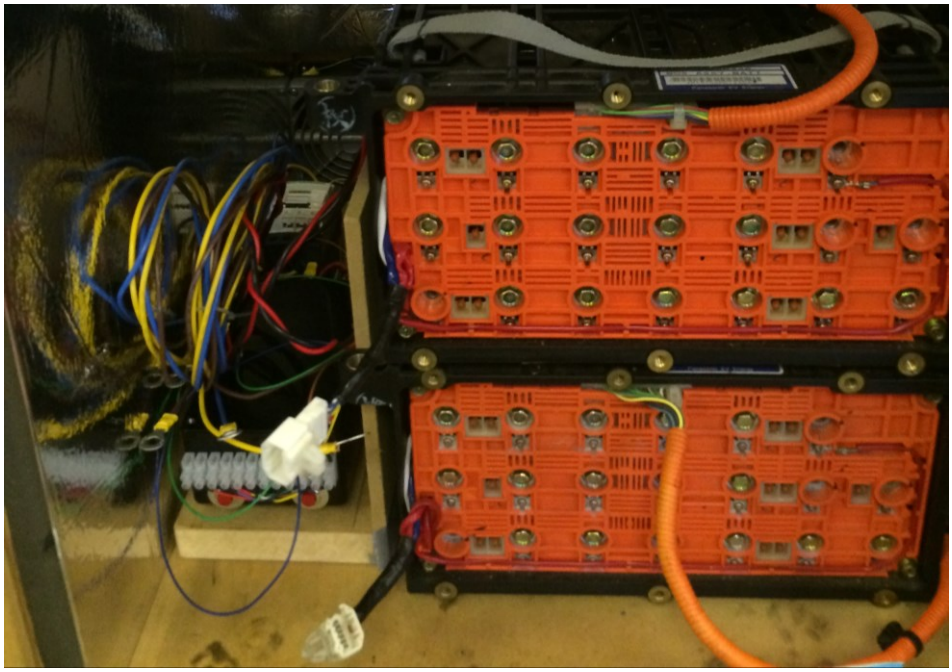

Fig. B-1. Overview of the battery pack and the protection system

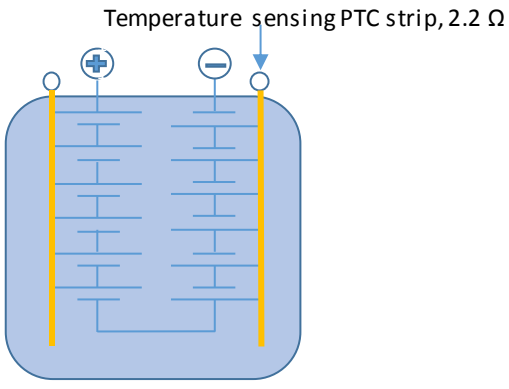

Fig. B-2. The schematic of one battery string in the battery pack

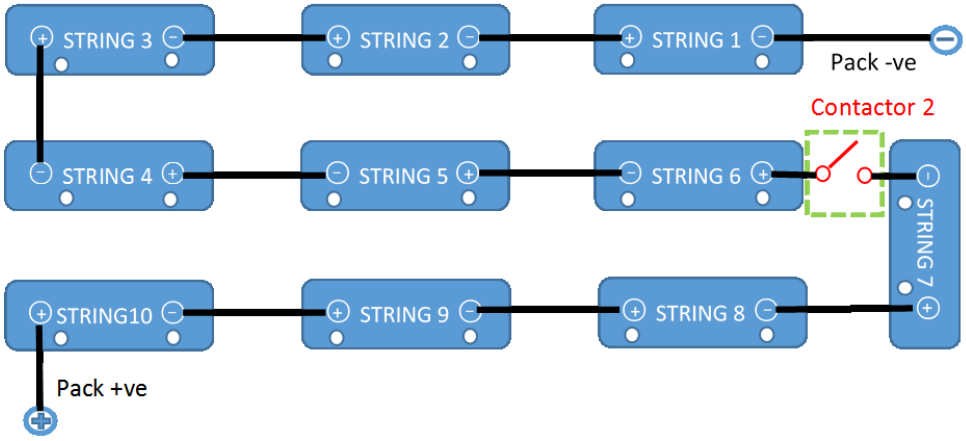

Fig. B-3. The schematic of one battery pack including 10 strings

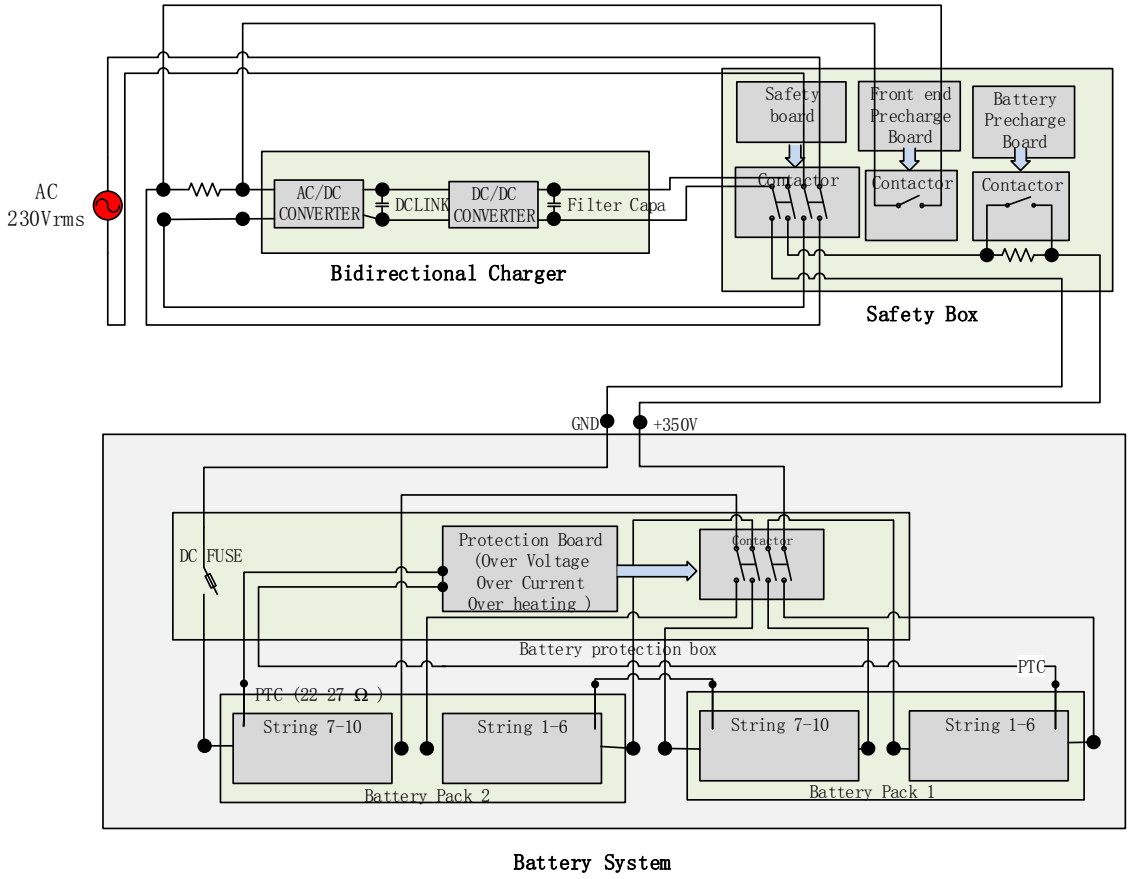

Fig. B-4. The schematic of the whole safety protection system

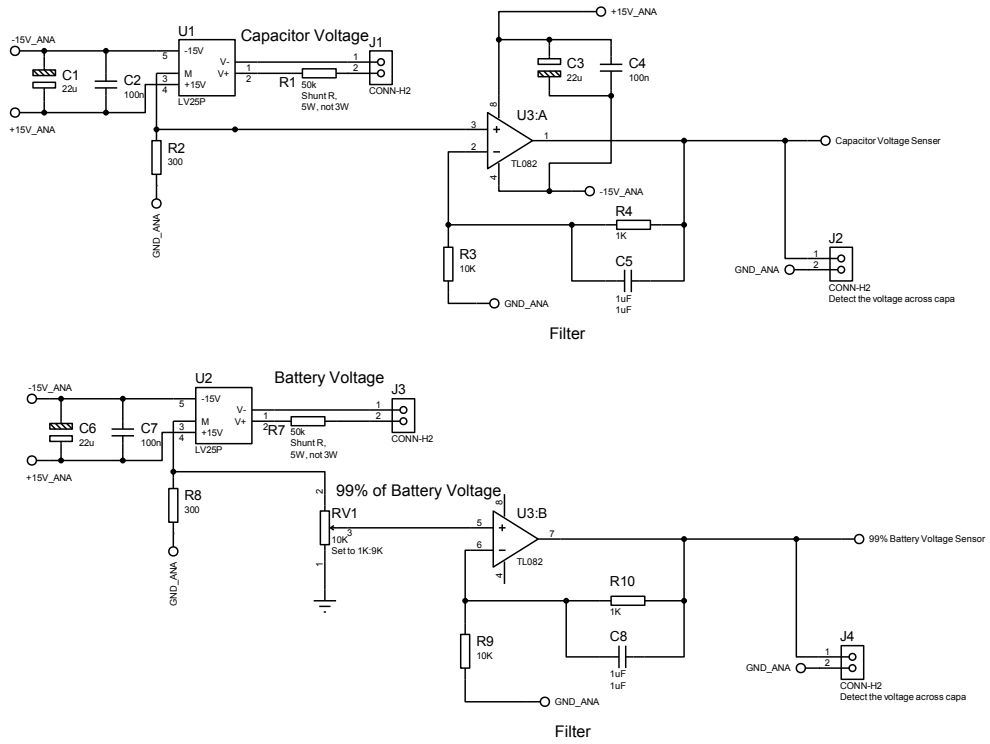

Fig. B-5. Battery pre-charge circuit schematic page 1/2

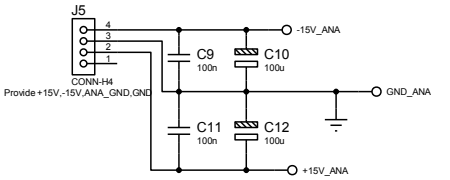

GND_ANA.is connected to GND.

Provide Power: +15V, -15V, ,ANA_GND, GND

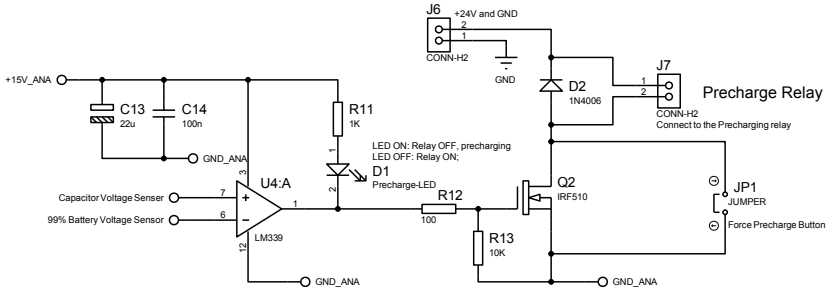

If Capacitor voltage is higher than 99% of Battery voltage, then output HIGH.
If output is HIGH, MOSFET turns on, Relay turns on. Precharge finish, LED off.
When press JP1, the relay is connected to 24V, relay turns on.

Fig. B-6. Battery pre-charge circuit schematic page 2/2

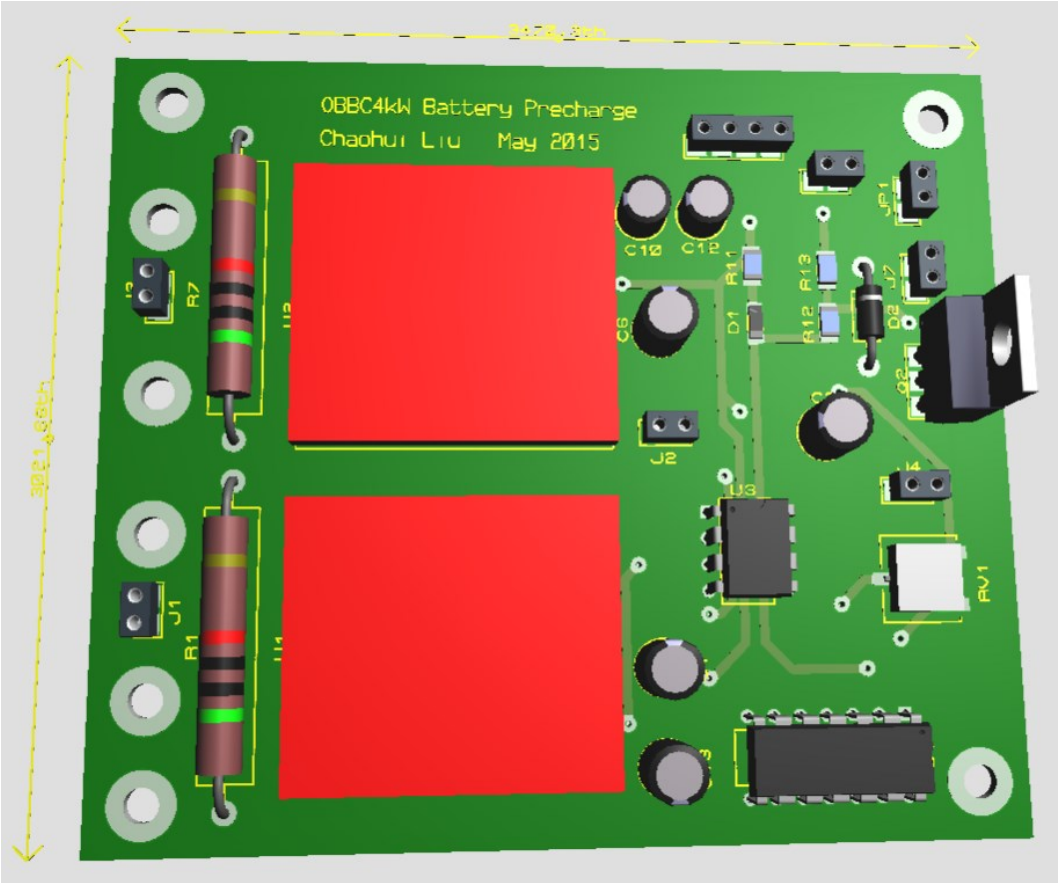

Fig. B-7. Battery pre-charge circuit 3-D overview

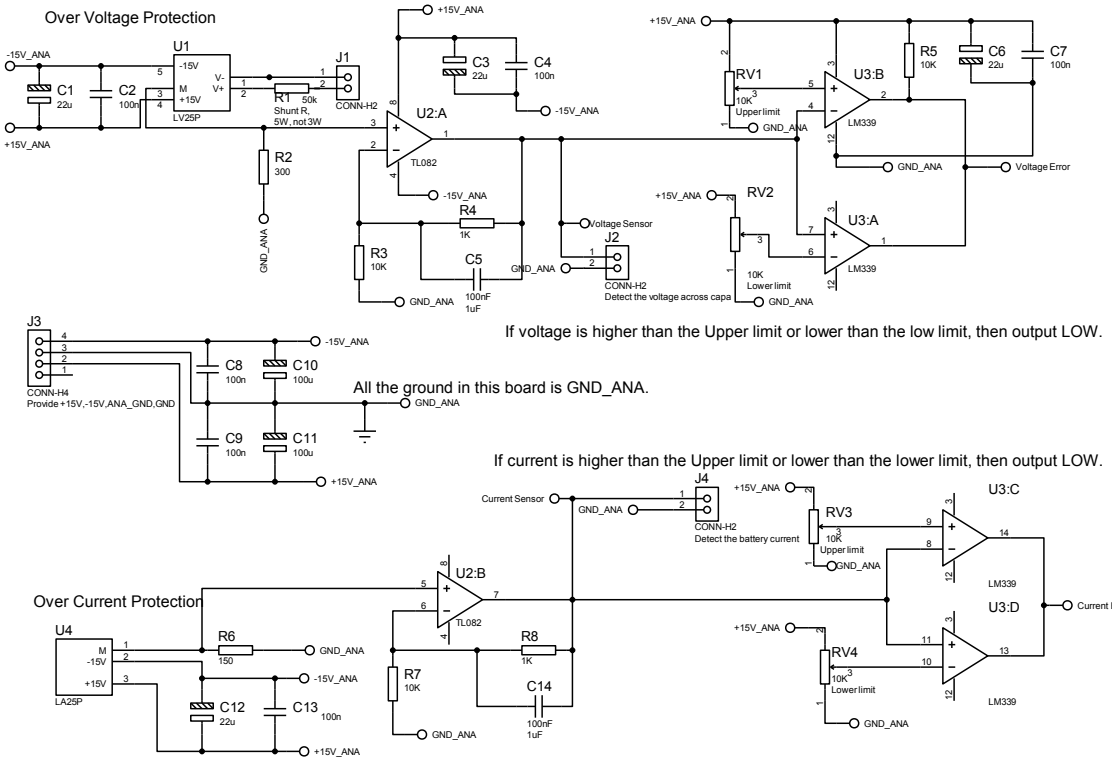

Fig. B-8. Battery test protection circuit schematic page 1/2

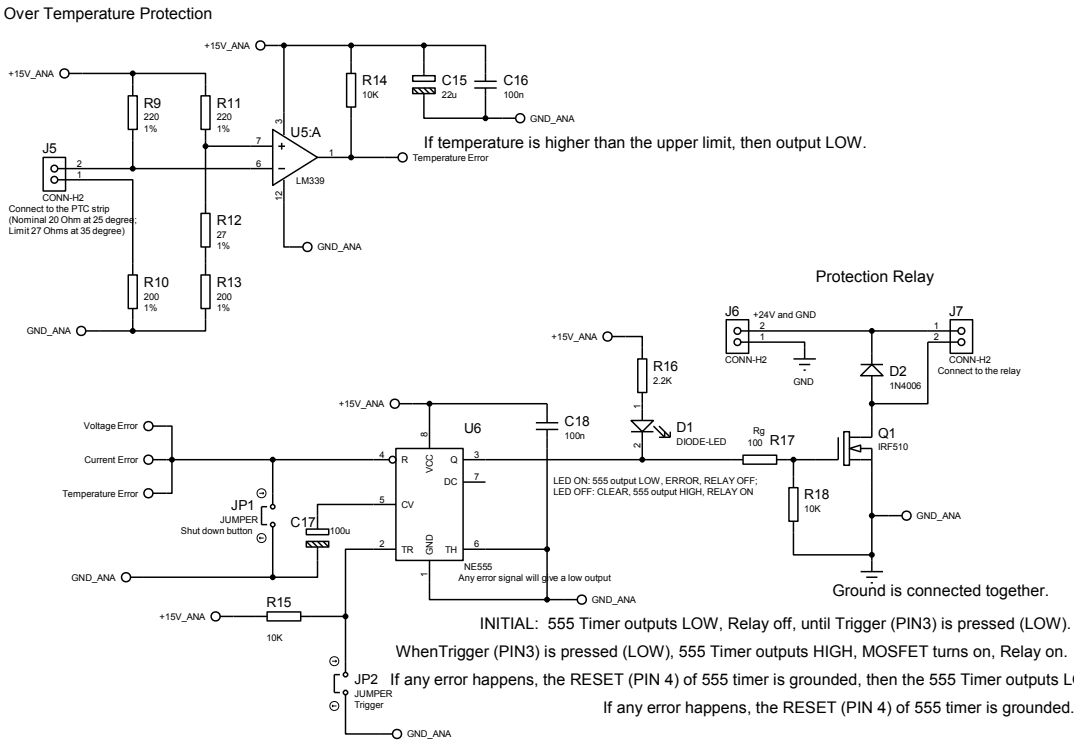

Fig. B-9. Battery test protection circuit schematic page 2/2

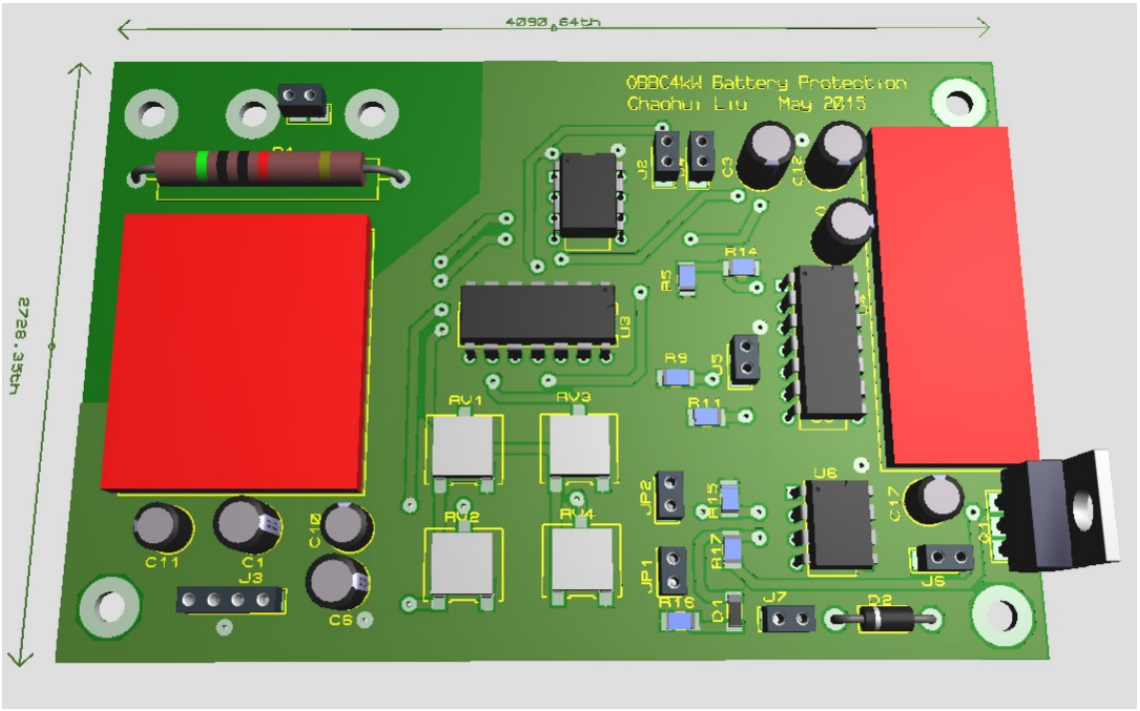

Fig. B-10. Battery test protection circuit 3-D overview

APPENDIX C LabVIEW FPGA Coding

National instrument Compact RIO 9082 is used as the processor due to the powerful real-time processing performance. The structure of the hardware has been illustrated in Chapter 4. This section describes the codes implemented in the graphical programming tool- LabVIEW FPGA.

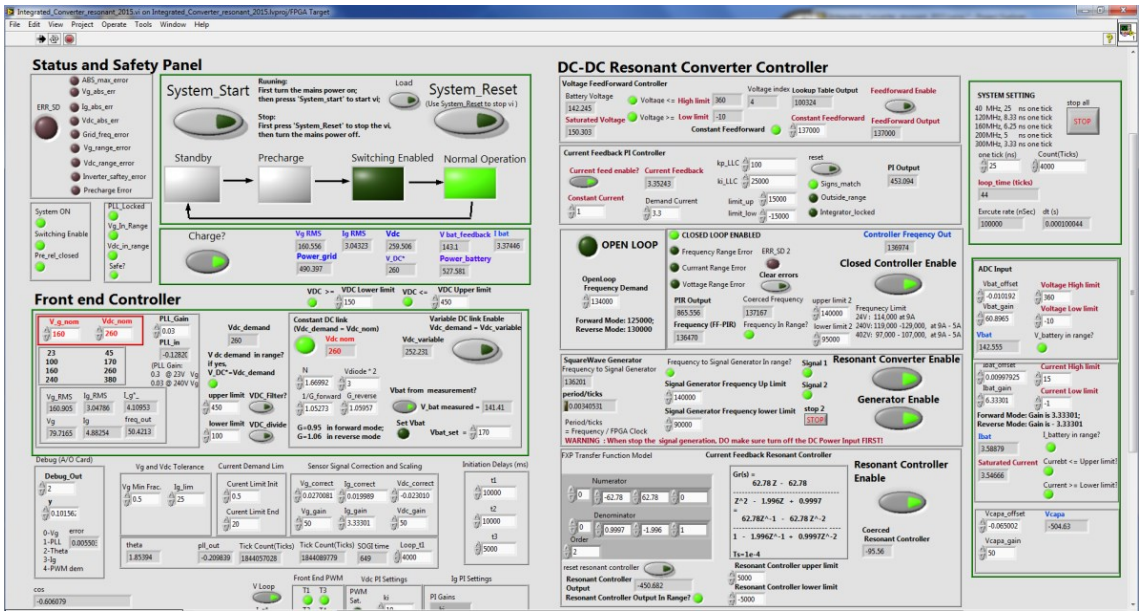

Fig. C-1. LabVIEW FPGA coding front panel

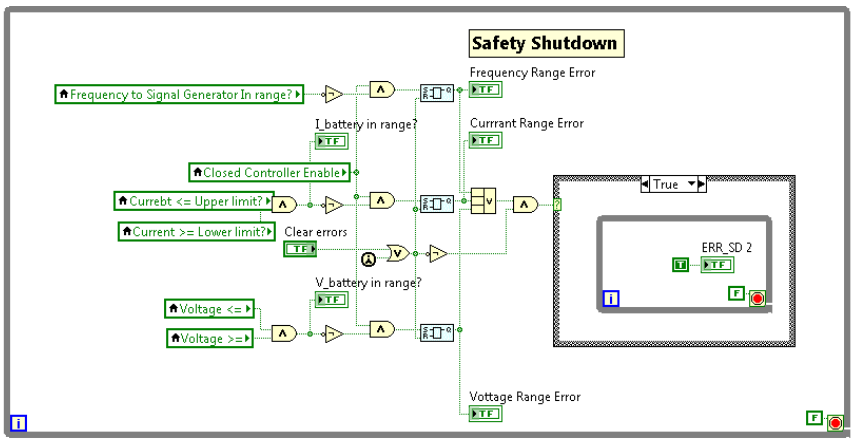

Fig. C-2. LabVIEW FPGA coding block diagram – Safety shutdown code

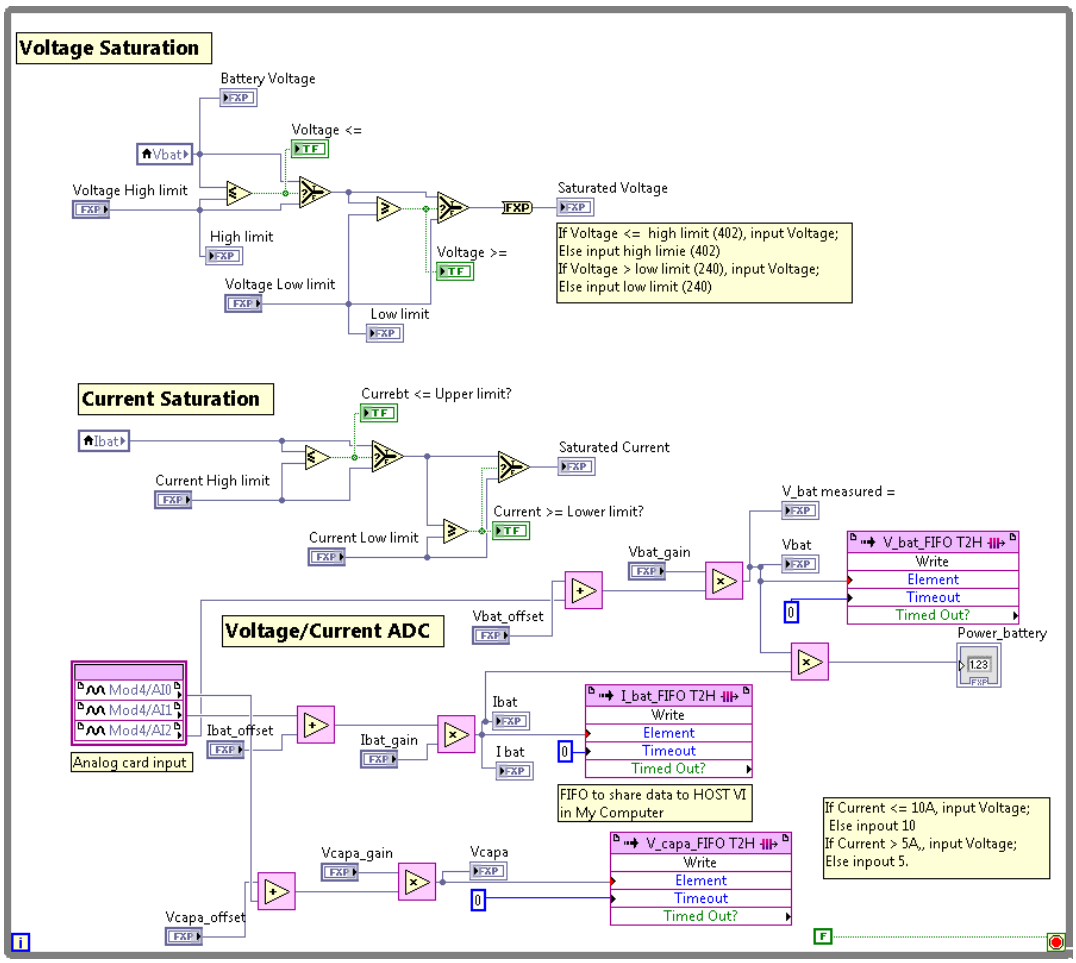

Fig. C-3. LabVIEW FPGA coding block diagram – Voltage/current ADC code

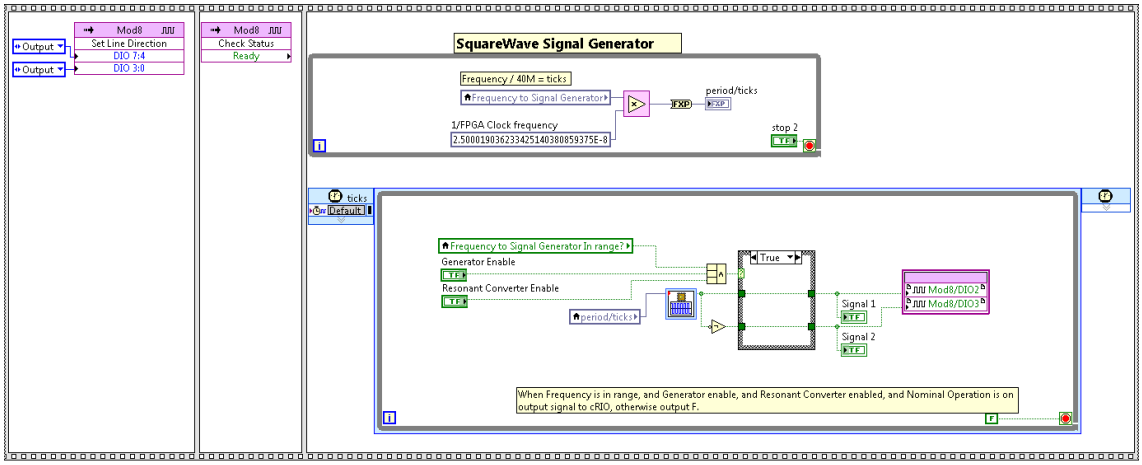

Fig. C-4. LabVIEW FPGA coding block diagram – Gate drive signal generator code

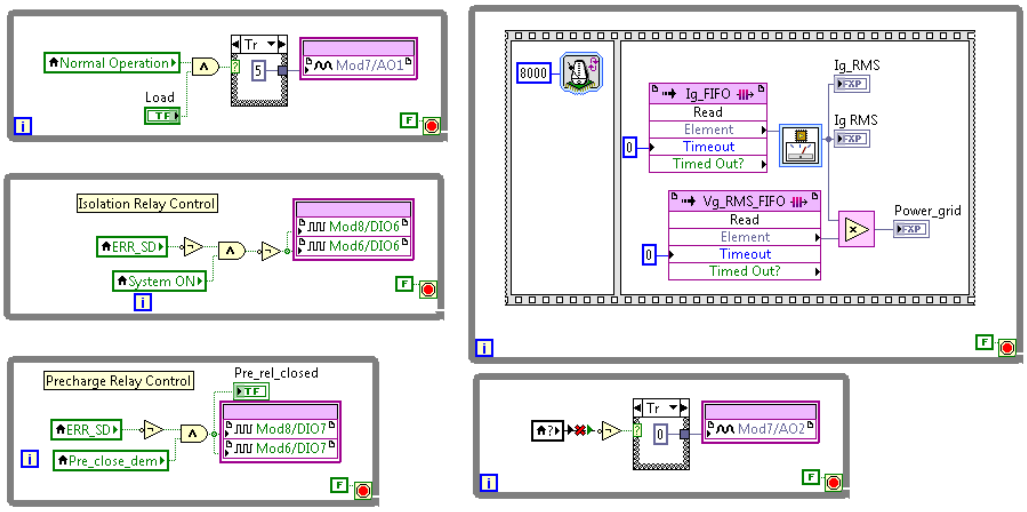

Fig. C-5. LabVIEW FPGA coding block diagram – Status monitoring code

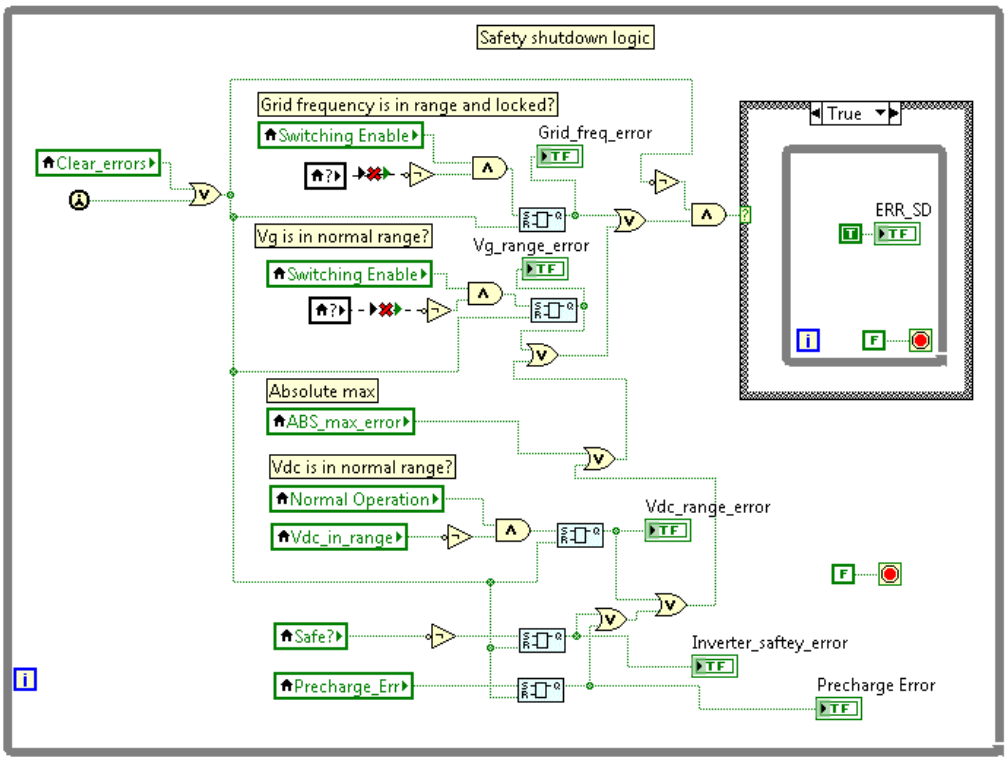

Fig. C-6. LabVIEW FPGA coding block diagram – Safety shutdown code

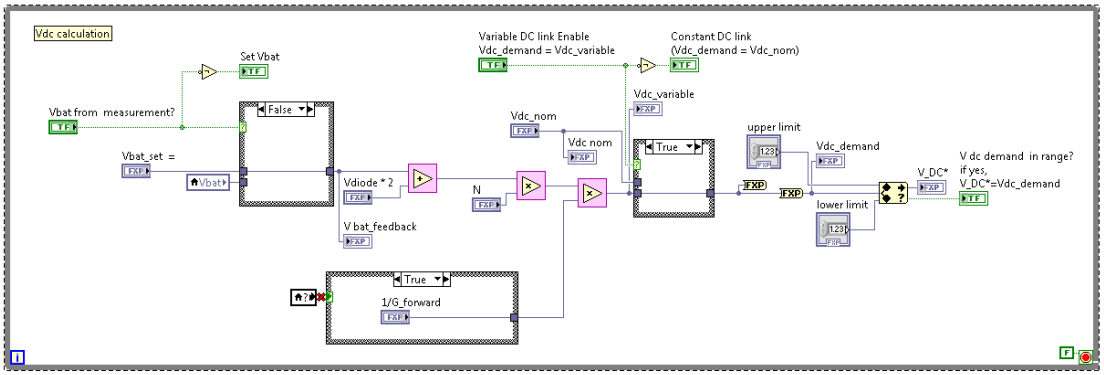

Fig. C-7. LabVIEW FPGA coding block diagram – Vdc calculation code

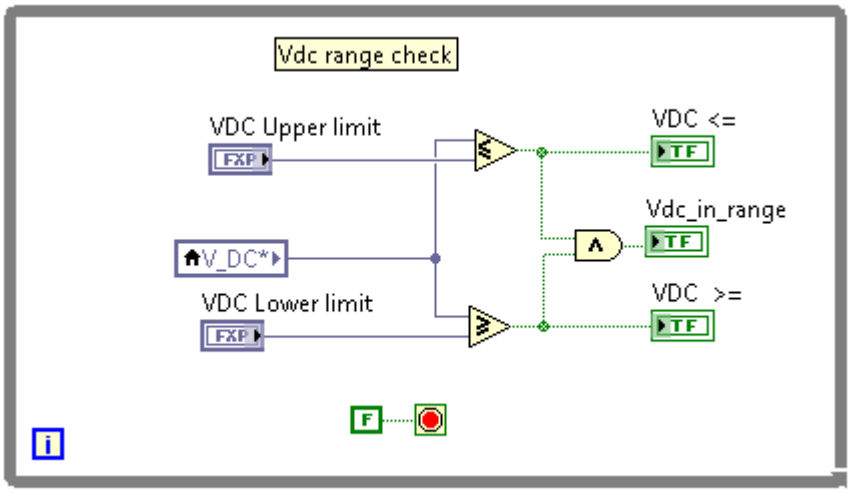

Fig. C-8. LabVIEW FPGA coding block diagram – Vdc range checking code

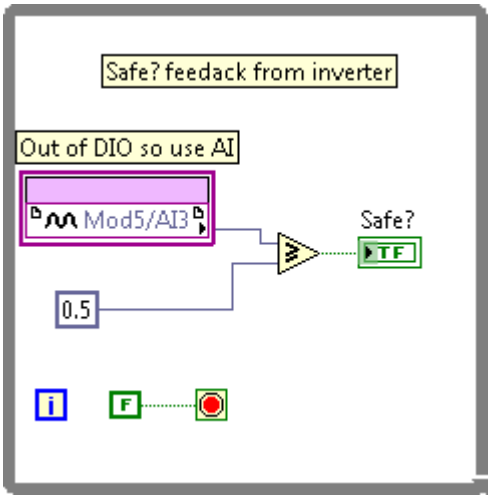

Fig. C-9. LabVIEW FPGA coding block diagram – Safe feedback code

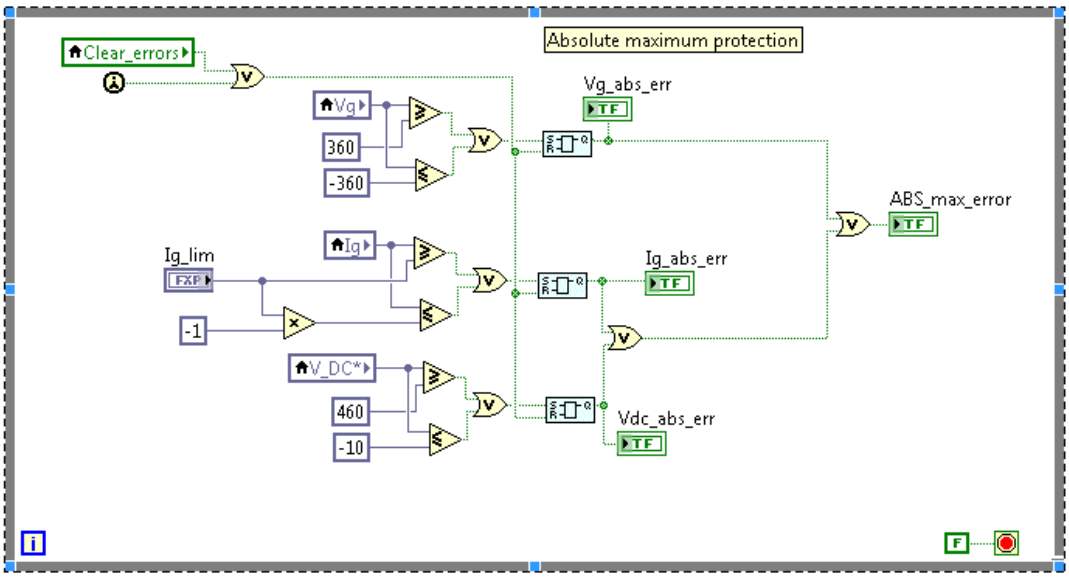

Fig. C-10. LabVIEW FPGA coding block diagram – Absolute maximum protection code

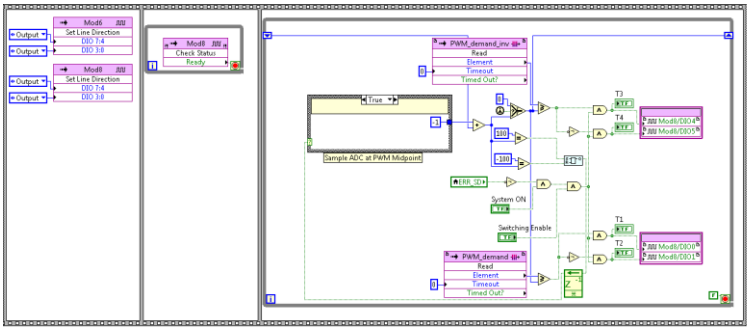

Fig. C-11. LabVIEW FPGA coding block diagram – PWM generator code

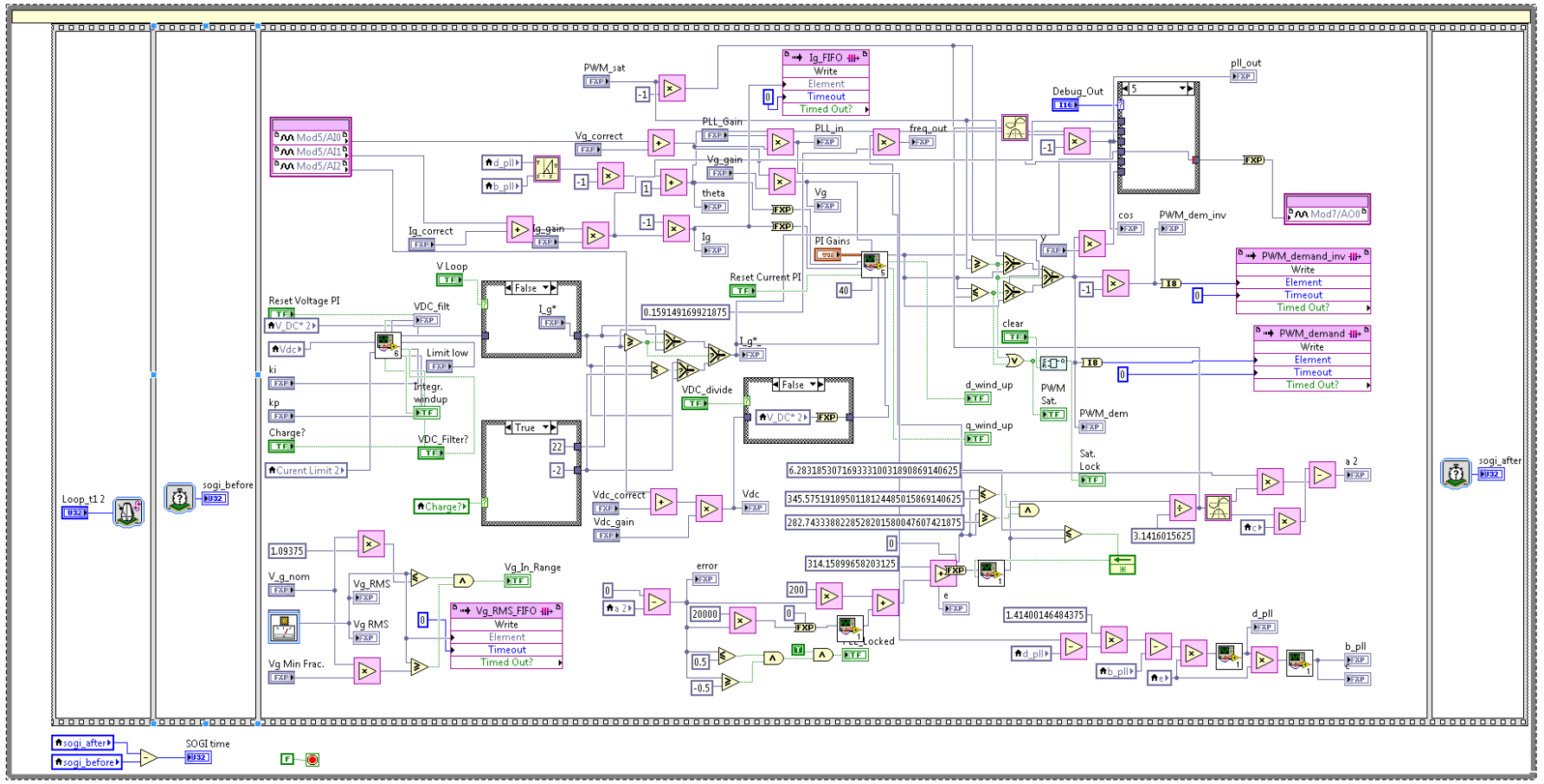

Fig. C-12. LabVIEW FPGA coding block diagram – Frontend converter controller code

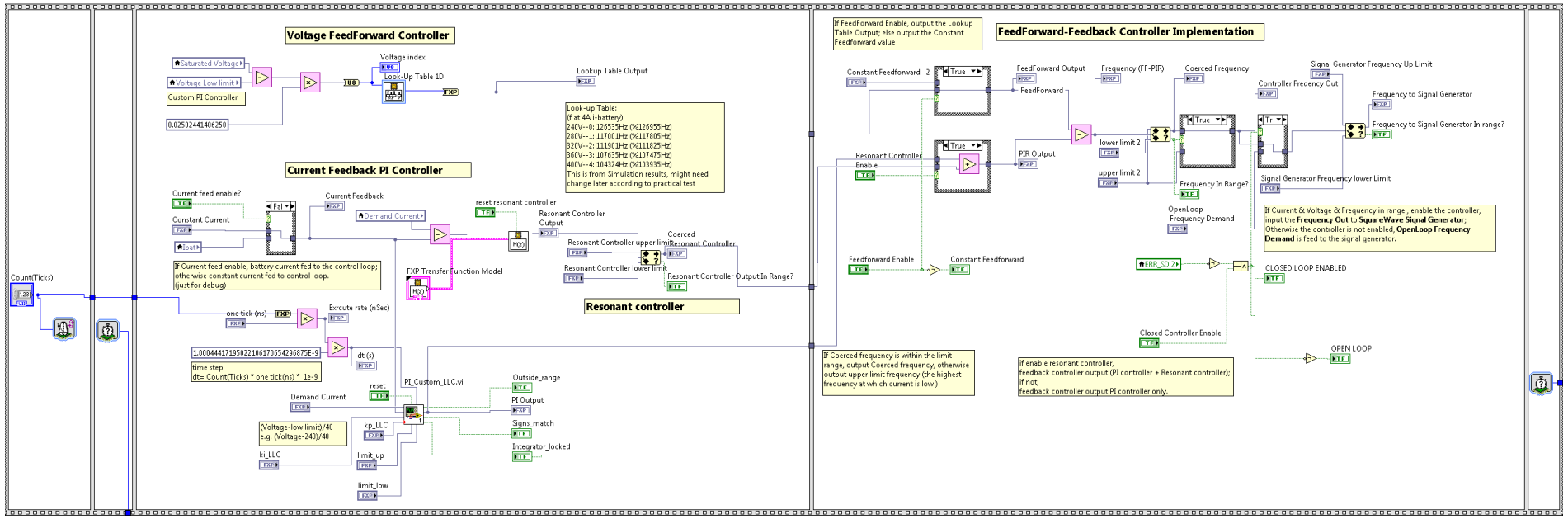

Fig. C-13. LabVIEW FPGA coding block diagram – DC-DC converter controller code

APPENDIX D
MATLAB Code for Power Loss Calculation

In order to evaluate the power loss in the converter, the practical method for quantifying the power loss distribution has been described in Chapter 3. This section lists the detailed MATLAB code of the calculation.

```
clear all;

%% Calculate the power loss in the OBBC converter
%   in the Forward mode
%=========================================================================
=====
%            1. DC-DC Converter power loss calculation in the Forward
mode
%    Based on Infineon's Application note
%    "MOSFET Power Losses Calculation Using the Data- Sheet
Parameters"
%    2016-06      created
%    2016-08      revised
%    2016-11      revised to apply the simulation results
%    2016-11.15   revised for application in the Forward mode
%=========================================================================
=====


%% 2. System Specification
%-------------------------------------------------------------------------
-----
%-------------------------------------------------------------------------
-----

% Define resoannt tank parameters
Ls  = 97.3e-6;              % Series inductor Ls =97.3uH
Lm  = 136.4e-6;             % Magnetic Inductor of Transformer is
136.4uH
N   = 1.66;                 % Transformer turns ratio is 15: 9 = 1.66,
in the simulation is 380/240 = 1.58

% LLC=0;  % if LLC -0, then load CLLC data for the calculation
  LLC =1; % if LLC = 1, then load LLC data for the calculation
  ZVS= 1;

%% 3. Load data from the M-file and assignment

% Four Simulation Conditions:
% Simulation CLLC forward at five power ratings:
% Simulation LLC forward at five power ratings:
% Simulation CLLC reverse at five power ratings:
% Simulation LLC reverse at five power ratings.

% Four Test Conditions:
```

```
% Test CLLC forward at two power ratings: 2KW and 4KW:
% Test LLC forward at two power ratings: 2KW and 4KW:
% Test CLLC reverse at two power ratings: 2KW and 4KW:
% Test LLC reverse at two power ratings: 2KW and 4KW:

% load the simulation data
%     if LLC ==0,
%     load Power_Loss_Simulation_CLLC_Forward;  % load the M-file from
the CLLC simulation results, Note this is not the test results
%     Power_Loss_Simulation_Forward =
Power_Loss_Simulation_CLLC_Forward
%     else
%     load Power_Loss_Simulation_LLC_Forward;   % load the M-file from
the LLC simulation results, Note this is not the test results
%     Power_Loss_Simulation_Forward =
Power_Loss_Simulation_LLC_Forward
%     end

% load the test data
if LLC ==0,
    load Power_Loss_Test_CLLC_Forward;  % load the M-file from the
CLLC simulation results, Note this is not the test results
    Power_Loss_Simulation_Forward = Power_Loss_Test_CLLC_Forward
    else
    load Power_Loss_Test_LLC_Forward;   % load the M-file from the LLC
simulation results, Note this is not the test results
    Power_Loss_Simulation_Forward = Power_Loss_Test_LLC_Forward
    end



    fsw  =  Power_Loss_Simulation_Forward(1,:);              %
Switching frequency;
    fsw  =  fsw *1000;

    V_DClink  = Power_Loss_Simulation_Forward(2,:);              % DC
Link Voltage in Simlation
    I_DClink  = Power_Loss_Simulation_Forward(3,:);              % DC
Link Current in Simlation
    V_Battery = Power_Loss_Simulation_Forward(4,:);              %
Battery Voltage in Simlation
    I_Battery = Power_Loss_Simulation_Forward(5,:);              %
Battery Current in Simlation

    ILs_rms   = Power_Loss_Simulation_Forward(6,:);              %
Primary side ILs RMS Current in Simlation
    Isec_rms  = Power_Loss_Simulation_Forward(7,:);              %
Secondary side Diode bridge RMS Current in Simlation

    Isw_off   = Power_Loss_Simulation_Forward(8,:);              %
Primary side MOSFET turn off current Current in Simlation
    ILs_peak  = Power_Loss_Simulation_Forward(9,:);              %
Primary side ILs measured (from waveforms) Peak Current in Simlation
    Isec_peak = Power_Loss_Simulation_Forward(10,:);             %
Secondary side Diode bridge Measured (from waveforms) Peak Current in
Simlation

    ILm_peak = Isw_off ;                                         % Lm
Peak current = Primary side MOSFET turn off current Current in
Simlation
```

```
%% 4. Define RoHM SiC MOSFET specific based on SCH2080KE datasheet

%-------------------------------------------------------------------
-----
%     Device data for RoHM SiC MOSFET
%     SCH2080KE N-channel SiC power MOSFET co-packaged with SiC-SBD
%-------------------------------------------------------------------
-----

% Device specification of MOSFET
RDS_on = 125e-3;            % Static drain-source on-state resistance
                            % 80 mOhm(typ), 117mOhm(max) at Tj = 25 C,
and 125Ohm (typ) at Tj = 125C, when VGS = 18V, ID = 10A;
                            % Read from datasheet Fig. 12, 13 and 14.

MOSFET_i_rt = 33e-9;        % MOSFET Turn-on delay tine is 37ns, and
rise time is 33 ns,
MOSFET_i_ft = 28e-9;        % MOSFET Turn-off delay time is 70ns, and
fall time is 28 ns;
% ???? need to add the rise time or not?

% Device specification of Diode
uD0 = 1.3;                  % Sic MOSFET diode Reverse volt drop is
1.3V read from table in Page 4
                            % 0.6V at VGS=0V and Is=10A read from
datasheet Fig. 22

RD = (1.3-0.7)/(10-0.01);   % Diode Resistance
                            % from datasheet curve Fig. 22
DIODE_trr = 37*1e-9;        % diode reverse recovery time is 37ns
DIODE_Qrr = 60*1e-9;        % diode reverse recovery charge is 60nC
DIODE_rrm = 2.4;            % peak reverse recovery current is 2.4A,
at IF=10A, VR=400V, di/dt=150A/us

% Gate Drive specification
U_plateau = 9.7;            % Gate plateau voltage is 9.7V
UDr = 12;                   % Gate Drive voltage +12 to -6
RG  = 6.3;                  % Gate input resistance is 6.3 Ohm

%% 5. Device Conduction Loss Calculation

   IDrms = ILs_rms;                     % the primary side MOSFET rms
current in the forward mode
   IFav  = Isec_rms*sqrt(2) * 2/pi;     % average DIODE current;
assumpt it is pure sinc wave  ($$ half cycle or one cycle?)
   IFrms = Isec_rms;                    % rms DIODE current;
($$ half cycle or one cycle?)

P_Con_MOS = RDS_on .* IDrms.^2 .* 2       % MOSFET Active Bridge
conduction loss during one cycle (2 bridges, 4 MOSFETs) ;

P_Con_Diode = (uD0 * IFav + RD * IFrms.^2) * 2   % Secondary side
Diode Rectifier Bridge conduction loss during one cycle (2 bridges, 4
diodes);

%% 6. Device Switchng Loss Calculation
%-----------------------------------------------------
% 6.1 Switching Losses Equations
%-----------------------------------------------------
```

```
% Equations
% Eon.M  = UDD * IDon * (tri + tfu)/2 + Qrr * UDD  $$
% Eoff.M = UDD * IDoff * (tru+tfi)/2 $$
% Eon.D  = (1/4) * Qrr * UDrr = (1/4) *Qrr *UDD$$
% Eoff.D = 0$$
% Psw.M  = (Eon.M + Eoff.M) * fsw$$
% Psw.D  = (Eon.D + Eoff.D) * fsw  $$

UDD = V_DClink
tri  = MOSFET_i_rt;                                % MOSFET current rise
time, read from datasheet

%-----------------------------------------------------
% 6.2 MOSFET Turn on switch loss
%     In ZVS, the MOSFET switching on loss is zero
%-----------------------------------------------------
% During MOSFET switching-on process, the worst case turn-on losses in
power MOSFET (Eon_M) can be calculated as
% the sum of
% the switch-on energy without taking the reverse recovery process
into account (Eon_M_i)
% and the switch-on energy caused by the reverse-recovery of the free-
wheeling diode (Eon_M_rr);



% Calculate tfu
% Two methods to calculate CGD for tfu
% Method 1:

CGD1 = 30e-12;
CGD2 = 700e-12;
IDon = Isw_off ;                                   % from simulation when
switch on, DC current
IGon = (UDr - U_plateau) / RG ;                    % gate current in turn
on process
tfu1 = (UDD - RDS_on*IDon) * CGD1 / IGon;          % voltage fall time
defined through the gate current and the capacitances CGD1;
tfu2 = (UDD - RDS_on*IDon) * CGD2 / IGon;          % voltage fall time
defiend through the gate current and CGD2;
tfu  = (tfu1 + tfu2) /2;                           % MOSFET voltage fall
time of the drain-source voltage from uDS=UDD to its on-state value
uDS=RDS_on*Ion, when turning on,

% Method 2:
Vds = UDD;
CGD  = 4319*exp(-1.39*Vds)+182*exp(-0.02*Vds);     % The polynomial
function of CGD against the drain–source voltage Vds
tfu  = (UDD - RDS_on*IDon) .* CGD / IGon;

Eon_M_i  = UDD .* IDon .* (tri+tfu)/2;             % switch-on energy
without taking the reverse recovery process into account (Eon_M_i)
Eon_M_rr = DIODE_Qrr .* UDD;                       % switch-on energy
caused by the reverse-recovery of the free-wheeling diode (Eon_M_rr)

% consider Zero Voltage Switching during MOSFET turning-on
if ZVS == 1
    Eon_M = 0;
else
    Eon_M  =  Eon_M_i + Eon_M_rr;
end
```

```
%-----------------------------------------------------
% 6.3 MOSFET Turn off switch loss (2 Methods)
%-----------------------------------------------------

% METHOD 1: Calculation with the capacitance

% During MOSFET switching-off process, there is no reverse recovery
IGoff   =  U_plateau / RG ;                         % gate current in
turn off process
tru1    = (UDD - RDS_on*IDon) * CGD1 / IGoff;       % voltage rise time
defined through the gate current and the capacitances CGD1;
tru2    = (UDD - RDS_on*IDon) * CGD2 / IGoff;       % voltage rise time
defined through the gate current and the capacitances CGD2;
tru     = (tru1 + tru2) /2;
tfi     = MOSFET_i_ft;                               % MOSFET current
fallingtime, read from datasheet.
IDoff   = Isw_off
Eoff_M = UDD .* IDoff .* (tru+tfi)/2;           % tru is voltage
rising time; tfi is current falling time;

% METHOD 2: Curve fitting from the datasheet

% Data points read from the Datasheet:
% Eoff_M = 26e-6;                                   % 26 uJ, read from
datasheet Fig. 19, 20, 21 when the battery voltage is 240V, IDoff =
10A;
% Eoff_M = 36e-6;                                   % 36 uJ, read from
datasheet Fig. 19, 20, 21 when the battery voltage is 400V, IDoff =
10A;

ID = Isw_off;
Eoff_M = 1e-6.*(0.0000922724653 .* (Vds.^2) + 0.0475102635693.*(Vds) +
3.4000415729136).*(0.2699799327533.* (ID.^2) -0.8702943202743.*(ID) +
48.8193577810183)/66

%-----------------------------------------------------%
% 6.4  Diode switch loss                              %
%-----------------------------------------------------%
% Primary side:
% During MOSFET switching-on process, the free wheeling diode turns
off, so the loss is mainly the reverse-recovery evergy,
% however, if the MOSFET is operating at ZVS, then the loss is zero.
Eon_D   = (1/4)*DIODE_Qrr * UDD;      % Reverse-recovery evergy

% Seondary side
% There is zero switching current turning off. so ideally, the diode
has no loss.

% Diode switch loss when MOSFET Turn off
% During MOSFET switching-off process, losses in the diode are
normally neglected
Eoff_D = 0;

%% 7. Core losses

%-----------------------------------------------------%
% 7.1 Core loss of Inductor (Material = 3C95)       %
%-----------------------------------------------------%
% core loss can be obtained from the core loss vs peak B curve in
datasheet
```

```
% Parameters
N_L = 24;                   % Inductor 24 turns, double winding 48 turns
Acore_E65 = 540e-6;         % 540 mm2
Ve_L =  79000*1e-9;         % 79000 mm^3

% Calculation
B_peak_L = Ls * ILs_peak / (Acore_E65 * N_L)    % Peak Flux density

Pv_L = 7.862 * (B_peak_L.^2.384) .* ((fsw*1e-3).^1.652) % Curve
fitting from the datasheet for 3C95, note fsw is kHz
P_core_L = Pv_L * Ve_L * 1e3                              % unit W

%-------------------------------------------------------%
% 7.2 Core loss of Transformer (Material  =  3C92)     %
%-------------------------------------------------------%

 N_Tx_pri = 15;             % Transformer primary side 15 turns,
double winding 30 turns
 N_Tx_sec = 9;              % Transformer secondary side 9 turns,
doubke winding 18 turns
 Acore_E59 =  353e-6;       % 353 mm2
 Ve_Tx  =  44000*1e-9;      % 79000 mm^3
 B_peak_Tx = Lm * ILm_peak / (Acore_E59 * N_Tx_pri)     % peak flux
density

 Pv_Tx_100kHz = 0.0253492764515 * (B_peak_Tx.^2 ) - 4.2232064705831 *
(B_peak_Tx) +  209.188306429935;     % 100 kHz swithing frequency
curve fitting
 Pv_Tx_200kHz = 0.0451985100246 * (B_peak_Tx.^2 ) - 4.1066513802761 *
(B_peak_Tx) +  133.9657955708089;    % 100 kHz swithing frequency
curve fitting

 Pv_Tx = Pv_Tx_100kHz ;                    % when the switching
freqyuency is close to 100 kHz;
 % Pv_Tx = Pv_Tx_200kHz ;                  % when the switching
freqyuency is close to 150-180 kHz;

 P_core_Tx = Pv_Tx * Ve_Tx * 1e3           % unit: KW * 1e3 = W

%% 8. Copper losses

%-------------------------------------------------------&
% 8.1 Defien the ac resiatance of Inductor             %
%-------------------------------------------------------%

R_L_ac = 0.01775 * exp(1.244e-05*fsw)    % Curve fitting from the
measured data from LCR meter, Data file is 151023155643.
P_copper_L = ILs_rms.^2 .* R_L_ac          % Copper loss of inductor

%-------------------------------------------------------&
% 8.2 Defien the ac resiatance of Transformer          %
%-------------------------------------------------------%

R_Tx_pri_ac =  0.005876 * exp(3.209e-05 * (fsw))  % Curve fitting from
the four scaled measured data from LCR meter at 90, 125 130 and 170
kHz. note the frequency is kHz
R_Tx_sec_ac =  0.001696 * exp(3.21e-05  * (fsw))  % Curve fitting from
the four scaled measured data from LCR meter at 90, 125 130 and 170
kHz. note the frequency is kHz

P_copper_Tx =  ILs_rms.^2 .* R_Tx_pri_ac + Isec_rms.^2 .* R_Tx_sec_ac
```

```
%% 9. Total loss

% Calculate the total losses
P_Con = P_Con_Diode + P_Con_MOS                % Conduction loss
consists loss on the mosfet in the primary side and diode in the
secondary side.
P_sw_MOS    = 4 * (Eon_M + Eoff_M) .* fsw
P_sw_Diode = 4 * (Eon_D + Eoff_D) .* fsw
P_sw        = (P_sw_MOS + P_sw_Diode)
P_loss_device = (P_sw + P_Con)

P_core        = P_core_L + P_core_Tx
P_copper      = P_copper_L + P_copper_Tx
P_loss_L      = P_core_L + P_copper_L
P_loss_Tx     = P_core_Tx + P_copper_Tx
P_loss_mag    = P_core_L  + P_core_Tx + P_copper_L + P_copper_Tx

P_loss_total = P_loss_device + P_loss_mag

Power_DClink  = V_DClink  .* I_DClink;     % DClink side Power in
Simulation
Power_Battery = I_Battery .* V_Battery;    % Battery Power in
Simulation
Power = Power_DClink                       % in forward mode, input
power is DC link power
efficiency = (1-(P_loss_total./Power))*100

Power_loss_Dist_Simulation_Forward(1,:)= P_Con_Diode
Power_loss_Dist_Simulation_Forward(2,:)= P_Con_MOS
Power_loss_Dist_Simulation_Forward(3,:)= P_Con
Power_loss_Dist_Simulation_Forward(4,:)= P_sw_MOS
Power_loss_Dist_Simulation_Forward(5,:)= P_sw_Diode
Power_loss_Dist_Simulation_Forward(6,:)= P_sw
Power_loss_Dist_Simulation_Forward(7,:)= P_loss_device
Power_loss_Dist_Simulation_Forward(8,:)= P_core_L
Power_loss_Dist_Simulation_Forward(9,:)= P_core_Tx
Power_loss_Dist_Simulation_Forward(10,:)= P_core
Power_loss_Dist_Simulation_Forward(11,:)= P_copper_L
Power_loss_Dist_Simulation_Forward(12,:)= P_copper_Tx
Power_loss_Dist_Simulation_Forward(13,:)= P_copper
Power_loss_Dist_Simulation_Forward(14,:)= P_loss_L
Power_loss_Dist_Simulation_Forward(15,:)= P_loss_Tx
Power_loss_Dist_Simulation_Forward(16,:)= P_loss_mag
Power_loss_Dist_Simulation_Forward(17,:)= P_loss_total
Power_loss_Dist_Simulation_Forward(18,:)= (Power*1e-3)
Power_loss_Dist_Simulation_Forward(19,:)= (fsw*1e-3)
Power_loss_Dist_Simulation_Forward(20,:)= efficiency

if LLC==0
    Power_loss_Dist_CLLC_Simulation_Forward =
Power_loss_Dist_Simulation_Forward
else
    Power_loss_Dist_LLC_Simulation_Forward =
Power_loss_Dist_Simulation_Forward
end

%% 10. Total loss Plot and Display

 % plot figures
figure
```

```
x = ['P_Con_MOS P_Con_Diode P_Con P_sw_MOS P_sw_Diode P_sw
P_loss_device P_core P_copper P_loss_mag P_loss_total']
P_loss = [ P_Con P_sw_MOS P_sw_Diode P_sw P_loss_device P_core
P_copper P_loss_mag P_loss_total]

bar([1:1:11], P_loss)
title ('Power distribution (W)')
ax = gca;

x = ['P_Con P_sw P_core P_copper P_loss_total']
power_loss(1,:) = [fsw; P_Con_MOS; P_Con_Diode; P_Con; P_sw_MOS;
P_sw_Diode; P_sw; P_loss_device; B_peak_L; P_core_L; B_peak_Tx;
P_core_Tx; P_core; P_copper_L; P_copper_Tx; P_copper; P_loss_mag;
P_loss_total]

figure
P_loss = [P_Con P_sw P_core P_copper P_loss_total]
bar([1:1:4], P_loss)
ax = gca;


grid on;
```

Table of Figure

List of Tables

REFERENCES

[1] M. Kesler, M. Kisacikoglu, and L. Tolbert, "Vehicle-to-Grid Reactive Power Operation Using Plug-in Electric Vehicle Bidirectional Off-Board Charger," *IEEE Transactions on Industrial Electronics,* vol. PP, pp. 1-1, 2014.

[2] J. C. Mukherjee and A. Gupta, "A Review of Charge Scheduling of Electric Vehicles in Smart Grid," *IEEE Systems Journal,* vol. 9, pp. 1541-1553, 2015.

[3] C. C. Chan, "An overview of electric vehicle technology," *Proceedings of the IEEE,* vol. 81, pp. 1202-1213, 1993.

[4] Z. Xiaohu, S. Lukic, S. Bhattacharya, and A. Huang, "Design and control of grid-connected converter in bi-directional battery charger for Plug-in hybrid electric vehicle application," in *Vehicle Power and Propulsion Conference, 2009. VPPC '09. IEEE*, 2009, pp. 1716-1721.

[5] Y. Ota, H. Taniguchi, T. Nakajima, K. M. Liyanage, J. Baba, and A. Yokoyama, "Autonomous Distributed V2G (Vehicle-to-Grid) Satisfying Scheduled Charging," *IEEE Transactions on Smart Grid,* vol. 3, pp. 559-564, 2012.

[6] U. K. Madawala and D. J. Thrimawithana, "A Bidirectional Inductive Power Interface for Electric Vehicles in V2G Systems," *IEEE Transactions on Industrial Electronics,* vol. 58, pp. 4789-4796, 2011.

[7] H. Liu, Z. Hu, Y. Song, and J. Lin, "Decentralized Vehicle-to-Grid Control for Primary Frequency Regulation Considering Charging Demands," *IEEE Transactions on Power Systems,* vol. 28, pp. 3480-3489, 2013.

[8] M. Yilmaz and P. T. Krein, "Review of the Impact of Vehicle-to-Grid Technologies on Distribution Systems and Utility Interfaces," *IEEE Transactions on Power Electronics,* vol. 28, pp. 5673-5689, 2013.

[9] M. Yilmaz and P. T. Krein, "Review of Battery Charger Topologies, Charging Power Levels, and Infrastructure for Plug-In Electric and Hybrid Vehicles," *IEEE Transactions on Power Electronics,* vol. 28, pp. 2151-2169, 2013.

[10] A. Westgeest and L. Brett, "Improving safety and performance testing for EV batteries," in *2013 World Electric Vehicle Symposium and Exhibition (EVS27)*, 2013, pp. 1-4.

[11] P. A. Cassani and S. S. Williamson, "Significance of Battery Cell Equalization and Monitoring for Practical Commercialization of Plug-In Hybrid Electric Vehicles," in *2009 Twenty-Fourth Annual IEEE Applied Power Electronics Conference and Exposition*, 2009, pp. 465-471.

[12] A. Khaligh and Z. Li, "Battery, Ultracapacitor, Fuel Cell, and Hybrid Energy Storage Systems for Electric, Hybrid Electric, Fuel Cell, and Plug-In Hybrid Electric Vehicles: State of the Art," *IEEE Transactions on Vehicular Technology,* vol. 59, pp. 2806-2814, 2010.

[13] P. Ramadass, B. Haran, R. White, and B. N. Popov, "Performance study of commercial LiCoO2 and spinel-based Li-ion cells," *Journal of Power Sources,* vol. 111, pp. 210-220, 9/23/ 2002.

[14] K. Nihal, "Rechargeable batteries and battery management systems design," in *IECON 2010 - 36th Annual Conference on IEEE Industrial Electronics Society*, 2010, pp. 1-2.

[15] J. T. Salihi, P. D. Agarwal, and G. J. Spix, "Induction Motor Control Scheme for Battery-Powered Electric Car (GM-Electrovair I)," *IEEE Transactions on Industry and General Applications,* vol. IGA-3, pp. 463-469, 1967.

[16] S. Jurkovic, K. M. Rahman, and P. J. Savagian, "Design, optimization and development of electric machine for traction application in GM battery electric vehicle," in *2015 IEEE International Electric Machines & Drives Conference (IEMDC)*, 2015, pp. 1814-1819.

[17] P. Leijen and N. Kularatna, "Developing a monitoring system for Toyota Prius battery-packs for longer term performance issues," in *2013 IEEE International Symposium on Industrial Electronics*, 2013, pp. 1-6.

[18] K. J. Kelly, M. Mihalic, and M. Zolot, "Battery usage and thermal performance of the Toyota Prius and Honda Insight during chassis dynamometer testing," in *Seventeenth Annual Battery Conference on Applications and Advances. Proceedings of Conference (Cat. No.02TH8576)*, 2002, pp. 247-252.

[19] W. Renhart, C. Magele, and B. Schweighofer, "FEM-Based Thermal Analysis of NiMH Batteries for Hybrid Vehicles," *IEEE Transactions on Magnetics,* vol. 44, pp. 802-805, 2008.

[20] A. Hoke, A. Brissette, K. Smith, A. Pratt, and D. Maksimovic, "Accounting for Lithium-Ion Battery Degradation in Electric Vehicle Charging Optimization," *IEEE Journal of Emerging and Selected Topics in Power Electronics,* vol. 2, pp. 691-700, 2014.

[21] J. R. M. D. Reyes, R. V. Parsons, and R. Hoemsen, "Winter Happens: The Effect of Ambient Temperature on the Travel Range of Electric Vehicles," *IEEE Transactions on Vehicular Technology,* vol. 65, pp. 4016-4022, 2016.

[22] O. Tremblay, L. A. Dessaint, and A. I. Dekkiche, "A Generic Battery Model for the Dynamic Simulation of Hybrid Electric Vehicles," in *2007 IEEE Vehicle Power and Propulsion Conference*, 2007, pp. 284-289.

[23] H. He, R. Xiong, X. Zhang, F. Sun, and J. Fan, "State-of-Charge Estimation of the Lithium-Ion Battery Using an Adaptive Extended Kalman Filter Based on an Improved Thevenin Model," *IEEE Transactions on Vehicular Technology,* vol. 60, pp. 1461-1469, 2011.

[24] H. S. Park, C. E. Kim, C. H. Kim, G. W. Moon, and J. H. Lee, "A Modularized Charge Equalizer for an HEV Lithium-Ion Battery String," *IEEE Transactions on Industrial Electronics,* vol. 56, pp. 1464-1476, 2009.

[25] A. Affanni, A. Bellini, G. Franceschini, P. Guglielmi, and C. Tassoni, "Battery choice and management for new-generation electric vehicles," *IEEE Transactions on Industrial Electronics,* vol. 52, pp. 1343-1349, 2005.

[26] S. Dey, B. Ayalew, and P. Pisu, "Combined estimation of State-of-Charge and State-of-Health of Li-ion battery cells using SMO on electrochemical model," in *2014 13th International Workshop on Variable Structure Systems (VSS)*, 2014, pp. 1-6.

[27] R. Milligan, T. Muneer, and I. Smith, "A comparative range approach using the Real World Drive Cycles and the Battery Electric Vehicle," in *2015 IEEE International Transportation Electrification Conference (ITEC)*, 2015, pp. 1-5.

[28] Y. Attia, A. Abdelrahman, M. Hamouda, and M. Youssef, "SiC devices performance overview in EV DC/DC converter: A case study in a Nissan Leaf," in *2016 IEEE Transportation Electrification Conference and Expo, Asia-Pacific (ITEC Asia-Pacific)*, 2016, pp. 214-219.

[29] W. Liangrong, L. Jianing, X. Guoqing, X. Kun, and S. Zhibin, "A novel battery charger for plug-in hybrid electric vehicles," in *Information and Automation (ICIA), 2012 International Conference on*, 2012, pp. 168-173.

[30] S. R. Osman, N. A. Rahim, and S. Jeyraj, "Single current sensor with multiple constant current charging method in solar battery charger," in *3rd IET International Conference on Clean Energy and Technology (CEAT) 2014*, 2014, pp. 1-5.

[31] Y. D. Lee and S. Y. Park, "Rapid charging strategy in the constant voltage mode for a high power Li-Ion battery," in *2013 IEEE Energy Conversion Congress and Exposition*, 2013, pp. 4725-4731.

[32] S. Li, C. Zhang, and S. Xie, "Research on Fast Charge Method for Lead-Acid Electric Vehicle Batteries," in *Intelligent Systems and Applications, 2009. ISA 2009. International Workshop on*, 2009, pp. 1-5.

[33] S. G. Abeyratne, P. S. N. Perera, H. S. Jayakody, S. M. K. B. Samarakoon, and R. R. S. De Bulathge, "Soft Switching fast charger for batteries used in Renewable Energy applications and electric vehicles," in *Industrial and Information Systems (ICIIS), 2012 7th IEEE International Conference on*, 2012, pp. 1-6.

[34] M. Chen and G. A. Rincon-Mora, "Accurate, Compact, and Power-Efficient Li-Ion Battery Charger Circuit," *IEEE Transactions on Circuits and Systems II: Express Briefs,* vol. 53, pp. 1180-1184, 2006.

[35] L. Yi-Hwa, T. Jen-Hao, and L. Yu-Chung, "Search for an optimal rapid charging pattern for lithium-ion batteries using ant colony system algorithm," *IEEE Transactions on Industrial Electronics,* vol. 52, pp. 1328-1336, 2005.

[36] S. A. Singh and S. S. Williamson, "Comprehensive review of PV/EV/grid integration power electronic converter topologies for DC charging applications," in *2014 IEEE Transportation Electrification Conference and Expo (ITEC)*, 2014, pp. 1-5.

[37] S. S. Williamson, A. K. Rathore, and F. Musavi, "Industrial Electronics for Electric Transportation: Current State-of-the-Art and Future Challenges," *IEEE Transactions on Industrial Electronics,* vol. 62, pp. 3021-3032, 2015.

[38] A. Dubey and S. Santoso, "Electric Vehicle Charging on Residential Distribution Systems: Impacts and Mitigations," *IEEE Access,* vol. 3, pp. 1871-1893, 2015.

[39] A. Khaligh and S. Dusmez, "Comprehensive Topological Analysis of Conductive and Inductive Charging Solutions for Plug-In Electric Vehicles," *IEEE Transactions on Vehicular Technology,* vol. 61, pp. 3475-3489, 2012.

[40] S. Dusmez and A. Khaligh, "Cost effective solutions to level 3 on-board battery chargers," in *Applied Power Electronics Conference and Exposition (APEC), 2012 Twenty-Seventh Annual IEEE*, 2012, pp. 2121-2127.

[41] M. Etezadi-Amoli, K. Choma, and J. Stefani, "Rapid-Charge Electric-Vehicle Stations," *IEEE Transactions on Power Delivery,* vol. 25, pp. 1883-1887, 2010.

[42] T. Kang, C. Kim, Y. Suh, H. Park, B. Kang, and D. Kim, "A design and control of bi-directional non-isolated DC-DC converter for rapid electric vehicle charging system," in *2012 IEEE International Conference on Information and Automation*, 2012, pp. 14-21.

[43] J. G. Pinto, V. Monteiro, H. Gonçalves, and J. L. Afonso, "Onboard Reconfigurable Battery Charger for Electric Vehicles With Traction-to-Auxiliary Mode," *IEEE Transactions on Vehicular Technology,* vol. 63, pp. 1104-1116, 2014.

[44] G. Y. Choe, J. S. Kim, B. K. Lee, W. Chung-Yuen, and L. Tea-Won, "A Bi-directional battery charger for electric vehicles using photovoltaic PCS systems," in *2010 IEEE Vehicle Power and Propulsion Conference*, 2010, pp. 1-6.

[45] M. A. Fasugba and P. T. Krein, "Gaining vehicle-to-grid benefits with unidirectional electric and plug-in hybrid vehicle chargers," in *2011 IEEE Vehicle Power and Propulsion Conference*, 2011, pp. 1-6.

[46] W. Su, H. Eichi, W. Zeng, and M. Y. Chow, "A Survey on the Electrification of Transportation in a Smart Grid Environment," *IEEE Transactions on Industrial Informatics,* vol. 8, pp. 1-10, 2012.

[47] E. Sortomme and M. A. El-Sharkawi, "Optimal Charging Strategies for Unidirectional Vehicle-to-Grid," *IEEE Transactions on Smart Grid,* vol. 2, pp. 131-138, 2011.

[48] E. Inoa and J. Wang, "PHEV Charging Strategies for Maximized Energy Saving," *IEEE Transactions on Vehicular Technology,* vol. 60, pp. 2978-2986, 2011.

[49] W. Kempton and J. Tomić, "Vehicle-to-grid power fundamentals: Calculating capacity and net revenue," *Journal of Power Sources,* vol. 144, pp. 268-279, 2005.

[50] J. Gallardo-Lozano, M. I. Milanés-Montero, M. A. Guerrero-Martínez, and E. Romero-Cadaval, "Three-phase bidirectional battery charger for smart electric vehicles," in *2011 7th International Conference-Workshop Compatibility and Power Electronics (CPE)*, 2011, pp. 371-376.

[51] International Organization for Standardization (ISO). *ISO 6469-3:2011 Electrically propelled road vehicles -- Safety specifications -- Part 3: Protection of persons against electric shock* Available: http://www.iso.org/iso/catalogue_detail?csnumber=45479

[52] UL. (2016, 10 December). *UL 2231-1 Standard for Safety for Personnel Protection Systems for Electric Vehicle (EV) Supply Circuits: General Requirements*. Available: https://standardscatalog.ul.com/standards/en/standard_2231-1_2

[53] S. Y. Kim, H. S. Song, and K. Nam, "Idling Port Isolation Control of Three-Port Bidirectional Converter for EVs," *IEEE Transactions on Power Electronics,* vol. 27, pp. 2495-2506, 2012.

[54] S. Pala and S. P. Singh, "Design, modeling and implementation of Bi-directional buck and boost converter," in *2012 IEEE 5th India International Conference on Power Electronics (IICPE)*, 2012, pp. 1-6.

[55] A. Nasiri, Z. Nie, S. B. Bekiarov, and A. Emadi, "An On-Line UPS System With Power Factor Correction and Electric Isolation Using BIFRED Converter," *IEEE Transactions on Industrial Electronics,* vol. 55, pp. 722-730, 2008.

[56] C. Qiao and K. M. Smedley, "A topology survey of single-stage power factor corrector with a boost type input-current-shaper," *IEEE Transactions on Power Electronics,* vol. 16, pp. 360-368, 2001.

[57] M. T. Zhang, M. M. Jovanovic, and F. C. Lee, "Analysis and evaluation of interleaving techniques in forward converters," *IEEE Transactions on Power Electronics,* vol. 13, pp. 690-698, 1998.

[58] J. Y. Lin, P. J. Liu, and C. Y. Yang, "A Dual-Transformer Active-Clamp Forward Converter With Nonlinear Conversion Ratio," *IEEE Transactions on Power Electronics,* vol. 31, pp. 4353-4361, 2016.

[59] X. Peng, Y. Mao, W. Pit-Leong, and F. C. Lee, "Design of 48 V Voltage regulator modules with a novel integrated magnetics," *IEEE Transactions on Power Electronics,* vol. 17, pp. 990-998, 2002.

[60] M. Jain, M. Daniele, and P. K. Jain, "A bidirectional DC-DC converter topology for low power application," *IEEE Transactions on Power Electronics,* vol. 15, pp. 595-606, 2000.

[61] C. Gould, K. Colombage, J. Wang, D. Stone, and M. Foster, "A comparative study of on-board bidirectional chargers for electric vehicles to support vehicle-to-grid power transfer," in *2013 IEEE 10th International Conference on Power Electronics and Drive Systems (PEDS)*, 2013, pp. 639-644.

[62] G. Hua and F. C. Lee, "Soft-switching techniques in PWM converters," *IEEE Transactions on Industrial Electronics,* vol. 42, pp. 595-603, 1995.

[63] G. Y, L. Z, H. L, Q. Z, and H. G, "Three-level LLC series resonant DC/DC converter," *IEEE Transactions on Power Electronics,* vol. 20, pp. 781-789, 2005.

[64] W. Chen, P. Rong, and Z. Lu, "Snubberless Bidirectional DC-DC Converter With New CLLC Resonant Tank Featuring Minimized Switching Loss," *IEEE Transactions on Industrial Electronics,* vol. 57, pp. 3075-3086, 2010.

[65] G. Oggier, G. O. García, and A. R. Oliva, "Modulation Strategy to Operate the Dual Active Bridge DC-DC Converter Under Soft Switching in the Whole Operating Range," *IEEE Transactions on Power Electronics,* vol. 26, pp. 1228-1236, 2011.

[66] M. N. Kheraluwala, R. W. Gascoigne, D. M. Divan, and E. D. Baumann, "Performance characterization of a high-power dual active bridge," *IEEE Transactions on Industry Applications,* vol. 28, pp. 1294-1301, 1992.

[67] G. G. Oggier, G. O. GarcÍa, and A. R. Oliva, "Switching Control Strategy to Minimize Dual Active Bridge Converter Losses," *IEEE Transactions on Power Electronics,* vol. 24, pp. 1826-1838, 2009.

[68] M. H. Ryu, H. S. Kim, J. W. Baek, H. G. Kim, and J. H. Jung, "Effective Test Bed of 380-V DC Distribution System Using Isolated Power Converters," *IEEE Transactions on Industrial Electronics,* vol. 62, pp. 4525-4536, 2015.

[69] T. Jiang, X. Chen, J. Zhang, and Y. Wang, "Bidirectional LLC resonant converter for energy storage applications," in *2013 Twenty-Eighth Annual IEEE Applied Power Electronics Conference and Exposition (APEC)*, 2013, pp. 1145-1151.

[70] X. Xie, Z. Zhao, C. Zhao, J. M. Zhang, and Z. Qian, "Analysis and Optimization of LLC Resonant Converter With a Novel Over-Current Protection Circuit," *IEEE Transactions on Power Electronics,* vol. 22, pp. 435-443, 2007.

[71] R. Liu and C. Q. Lee, "The LLC-type series resonant converter-variable switching frequency control," in *Proceedings of the 32nd Midwest Symposium on Circuits and Systems*, 1989, pp. 509-512 vol.1.

[72] K. Siri and C. Q. Lee, "Constant switching frequency LLC-type series resonant converter," in *Circuits and Systems, 1989., Proceedings of the 32nd Midwest Symposium on*, 1989, pp. 513-516 vol.1.

[73] C. J and W. A. F., "Analytic solutions for LLCC parallel resonant converter simplify use of twoand three-element converters," *IEEE Transactions on Power Electronics,* vol. 13, pp. 235-243, 1998.

[74] G. Y, L. Z, and Q. Z, "Three level LLC series resonant DC/DC converter," in *2004 Nineteenth Annual IEEE Applied Power Electronics Conference and Exposition (APEC)*, 2004, pp. 1647-1652 Vol.3.

[75] L. Gang, Y. Jang, M. Jovanovic, and J. Q. Zhang, "Implementation of a 3.3-kW DC-DC Converter for EV On-Board Charger Employing Series-Resonant Converter with Reduced-Frequency-Range Control," *IEEE Transactions on Power Electronics,* vol. PP, pp. 1-1, 2016.

[76] H. Zeng, N. Gonzalez-Santini, Y. Yu, S. Yang, and F. Peng, "Harmonic Burst Control Strategy for Full-Bridge Series Resonant Converter-Based EV Charging," *IEEE Transactions on Power Electronics,* vol. PP, pp. 1-1, 2016.

[77] R. Oruganti and F. C. Lee, "State-plane analysis of parallel resonant converter," in *1985 IEEE Power Electronics Specialists Conference*, 1985, pp. 56-73.

[78] Z. Cao, J. Tao, N. Fröhleke, and J. Böcker, "Dynamical modeling for series-parallel resonant converter under optimized modulation," in *2013 Twenty-Eighth Annual IEEE Applied Power Electronics Conference and Exposition (APEC)*, 2013, pp. 1391-1398.

[79] Z. Cao, F. H. Nzeugang, N. Fröhleke, and J. Böcker, "A comparative study of series-parallel resonant converter by using different modulation strategies," in *IECON 2011 - 37th Annual Conference of the IEEE Industrial Electronics Society*, 2011, pp. 1006-1011.

[80] A. A. Aboushady, S. J. Finney, B. W. Williams, and K. H. Ahmed, "Steady state analysis of the phase-controlled LCC-type series-parallel resonant converter operating above resonance," in *2013 Twenty-Eighth Annual IEEE Applied Power Electronics Conference and Exposition (APEC)*, 2013, pp. 2125-2131.

[81] B. Yang, F. C. Lee, A. J. Zhang, and H. Guisong, "LLC resonant converter for front end DC/DC conversion," in *Applied Power Electronics Conference and Exposition, 2002. APEC 2002. Seventeenth Annual IEEE*, 2002, pp. 1108-1112 vol.2.

[82] C. Gould, C. M. Bingham, D. A. Stone, and M. P. Foster, "CLL resonant converters with output short-circuit protection," *Electric Power Applications, IEE Proceedings -,* vol. 152, pp. 1296-1306, 2005.

[83] C. Gould, D. A. Stone, M. P. Foster, and C. Bingham, "State-variable modelling of CLL resonant converters," in *Second International Conference on Power Electronics, Machines and Drives (PEMD 2004).* 2004, pp. 214-219 Vol.1.

[84] C. H. Chang, C. Hung-Liang, C. En-Chih, C. Chun-An, and C. Hung-Yi, "Modeling and design of the LLC resonant converter used in solar array simulator," in *2012 7th IEEE Conference on Industrial Electronics and Applications (ICIEA)*, 2012, pp. 653-658.

[85] G. Pledl, M. Tauer, and D. Buecherl, "Theory of operation, design procedure and simulation of a bidirectional LLC resonant converter for vehicular applications," in *2010 IEEE Vehicle Power and Propulsion Conference*, 2010, pp. 1-5.

[86] F. Krismer, J. Biela, and J. W. Kolar, "A comparative evaluation of isolated bi-directional DC/DC converters with wide input and output voltage range," in *Fourtieth IAS Annual Meeting. Conference Record of the 2005 Industry Applications Conference, 2005.*, 2005, pp. 599-606 Vol. 1.

[87] N. M. L. Tan, T. Abe, and H. Akagi, "Topology and application of bidirectional isolated dc-dc converters," in *8th International Conference on Power Electronics - ECCE Asia*, 2011, pp. 1039-1046.

[88] G. Liu, D. Li, J. Q. Zhang, B. Hu, and M. L. Jia, "Bidirectional CLLC resonant DC-DC converter with integrated magnetic for OBCM application," in *2015 IEEE International Conference on Industrial Technology (ICIT)*, 2015, pp. 946-951.

[89] J. H. Jung, H. S. Kim, M. H. Ryu, and J. W. Baek, "Design Methodology of Bidirectional CLLC Resonant Converter for High-Frequency Isolation of DC Distribution Systems," *IEEE Transactions on Power Electronics,* vol. 28, pp. 1741-1755, 2013.

[90] P. He and A. Khaligh, "Comprehensive Analyses and Comparison of 1kW Isolated DC-DC Converters for Bidirectional EV Charging Systems," *IEEE Transactions on Transportation Electrification,* vol. PP, pp. 1-1, 2016.

[91] J. S. Lai, L. Zhang, Z. Zahid, N. H. Tseng, C. S. Lee, and C. H. Lin, "A high-efficiency 3.3-kW bidirectional on-board charger," in *2015 IEEE 2nd International Future Energy Electronics Conference (IFEEC)*, 2015, pp. 1-5.

[92] J. Y. Lee and B. M. Han, "A Bidirectional Wireless Power Transfer EV Charger Using Self-Resonant PWM," *IEEE Transactions on Power Electronics,* vol. 30, pp. 1784-1787, 2015.

[93] C. Liu, J. Wang, K. Colombage, C. Gould, B. Sen, and D. Stone, "Current ripple reduction in 4kW LLC resonant converter based battery charger for electric vehicles," in *2015 IEEE Energy Conversion Congress and Exposition (ECCE)*, 2015, pp. 6014-6021.

[94] Q. Kejun, Z. Chengke, Y. Yue, and M. Allan, "Temperature effect on electric vehicle battery cycle life in Vehicle-to-grid applications," in *Electricity Distribution (CICED), 2010 China International Conference on*, 2010, pp. 1-6.

[95] O. Satilmis and E. Mese, "Investigating DC link current ripple and PWM modulation methods in Electric Vehicles," in *Electric Power and Energy Conversion Systems (EPECS), 2013 3rd International Conference on*, 2013, pp. 1-6.

[96] T. J. Liang and J. H. Lee, "Novel High-Conversion-Ratio High-Efficiency Isolated Bidirectional DC-DC Converter," *IEEE Transactions on Industrial Electronics,* vol. 62, pp. 4492-4503, 2015.

[97] D. Patil and V. Agarwal, "Compact ON Board Single Phase EV Battery Charger with Novel Low Frequency Ripple Compensator and Optimum Filter Design," *IEEE Transactions on Vehicular Technology,* vol. PP, pp. 1-1, 2015.

[98] S. S. Nag, S. Mishra, and A. Joshi, "A Passive Filter Building Block for Input or Output Current Ripple Cancellation in a Power Converter," *IEEE Journal of Emerging and Selected Topics in Power Electronics,* vol. PP, pp. 1-1, 2015.

[99] T. Shimizu, Y. Jin, and G. Kimura, "DC ripple current reduction on a single-phase PWM voltage-source rectifier," *IEEE Transactions on Industry Applications,* vol. 36, pp. 1419-1429, 2000.

[100] K. J, P. N, L. D, and H. D, "A simple control scheme for DC output ripple voltage suppression in BIFRED with a small-sized energy storage capacitor," in *30th Annual Conference of IEEE Industrial Electronics Society, 2004. IECON 2004*, 2004, pp. 779-783 Vol. 1.

[101] S. Fukuda and T. Yoda, "A novel current-tracking method for active filters based on a sinusoidal internal model [for PWM invertors]," *IEEE Transactions on Industry Applications,* vol. 37, pp. 888-895, 2001.

[102] J. Miret, M. Castilla, J. Matas, J. M. Guerrero, and J. C. Vasquez, "Selective Harmonic-Compensation Control for Single-Phase Active Power Filter With High Harmonic Rejection," *IEEE Transactions on Industrial Electronics,* vol. 56, pp. 3117-3127, 2009.

[103] D. N. Zmood and D. G. Holmes, "Stationary frame current regulation of PWM inverters with zero steady-state error," *IEEE Transactions on Power Electronics,* vol. 18, pp. 814-822, 2003.

[104] C. Liu, W. Chen, F. Blaabjerg, and D. Xu, "Optimized design of resonant controller for stator current harmonic compensation in DFIG wind turbine systems," in *2012 Twenty-Seventh Annual IEEE Applied Power Electronics Conference and Exposition (APEC*, 2012, pp. 2038-2044.

[105] J. Wang, B. Ji, X. Lu, X. Deng, F. Zhang, and C. Gong, "Steady-State and Dynamic Input Current Low-Frequency Ripple Evaluation and Reduction in Two-Stage Single-Phase Inverters With Back Current Gain Model," *IEEE Transactions on Power Electronics,* vol. 29, pp. 4247-4260, 2014.

[106] L. Cao, K. H. Loo, and Y. M. Lai, "Frequency-Adaptive Filtering of Low-Frequency Harmonic Current in Fuel Cell Power Conditioning Systems," *IEEE Transactions on Power Electronics,* vol. 30, pp. 1966-1978, 2015.

[107] Y. Du, D. D. C. Lu, G. M. L. Chu, and W. Xiao, "Closed-Form Solution of Time-Varying Model and Its Applications for Output Current Harmonics in Two-Stage PV Inverter," *IEEE Transactions on Sustainable Energy,* vol. 6, pp. 142-150, 2015.

[108] F. Deng and Z. Chen, "Elimination of DC-Link Current Ripple for Modular Multilevel Converters With Capacitor Voltage-Balancing Pulse-Shifted Carrier PWM," *IEEE Transactions on Power Electronics,* vol. 30, pp. 284-296, 2015.

[109] G. Grandi, J. Loncarski, and O. Dordevic, "Analysis and Comparison of Peak-to-Peak Current Ripple in Two-Level and Multilevel PWM Inverters," *IEEE Transactions on Industrial Electronics,* vol. 62, pp. 2721-2730, 2015.

[110] K. H. Leung, K. H. Loo, and Y. M. Lai, "Unity-Power-Factor Control Based on Precise Ripple Cancellation for Fast-Response PFC Preregulator," *IEEE Transactions on Power Electronics,* vol. 31, pp. 3324-3337, 2016.

[111] C. Eun-Seok, S. Byong-Chul, K. Hag-Wone, C. Kwan-Yuhl, H. Soon-Sang, and B. Byung-Dug, "120Hz output voltage ripple reduction of LLC resonant converter using resonant controller," in *Telecommunications Energy Conference (INTELEC), 2012 IEEE 34th International*, 2012, pp. 1-7.

[112] C. Xi, M. Mengyin, D. Shanxu, C. Wen, and C. Changsong, "Low frequency ripple propagation analysis in LLC resonant converter based on signal modulation-demodulation theory and reduction based on PIR control strategy," in *Energy Conversion Congress and Exposition (ECCE), 2013 IEEE*, 2013, pp. 5390-5394.

[113] H. Hong, "FHA-based voltage gain function with harmonic compensation for LLC resonant converter," in *Applied Power Electronics Conference and Exposition (APEC), 2010 Twenty-Fifth Annual IEEE*, 2010, pp. 1770-1777.

[114] Z. U. Zahid, J. S. J. Lai, X. K. Huang, S. Madiwale, and J. Hou, "Damping impact on dynamic analysis of LLC resonant converter," in *Applied Power Electronics Conference and Exposition (APEC), 2014 Twenty-Ninth Annual IEEE*, 2014, pp. 2834-2841.

[115] C. Buccella, C. Cecati, H. Latafat, P. Pepe, and K. Razi, "Observer-based Control of LLC DC/DC Resonant Converter Using Extended Describing Functions," *IEEE Transactions on Power Electronics,* vol. PP, pp. 1-1, 2014.

[116] B. Yang, "Topology investigation of front end DC/DC converter for distributed power system," PhD, Electrical and Computer Engineering, Virginia Polytechnic Institute and State University, Blacksburg, Virginia, 2003.

[117] T. Olivier and D. Louis-A, "Experimental Validation of a Battery Dynamic Model for EV Applications," *World Electric Vehicle Journal,* vol. 3, 2009.

[118] J. A. Short, D. G. Infield, and L. L. Freris, "Stabilization of Grid Frequency Through Dynamic Demand Control," *IEEE Transactions on Power Systems,* vol. 22, pp. 1284-1293, 2007.

[119] M. Cheng, J. Wu, S. Galsworthy, N. Jenkins, and W. Hung, "Availability of load to provide frequency response in the great Britain power system," in *Power Systems Computation Conference (PSCC), 2014*, 2014, pp. 1-7.

[120] D. T. Gladwin, C. R. Gould, D. A. Stone, and M. P. Foster, "Viability of 'second-life' use of electric and hybridelectric vehicle battery packs," in *Industrial Electronics Society, IECON 2013 - 39th Annual Conference of the IEEE*, 2013, pp. 1922-1927.

[121] C. Liu, J. Wang, K. Colombage, C. Gould, and B. Sen, "A CLLC resonant converter based bidirectional EV charger with maximum efficiency tracking," in *8th IET International Conference on Power Electronics, Machines and Drives (PEMD 2016)*, 2016, pp. 1-6.

[122] Z. Hu, Y. Qiu, Y. F. Liu, and P. C. Sen, "A Control Strategy and Design Method for Interleaved LLC Converters Operating at Variable Switching Frequency," *IEEE Transactions on Power Electronics,* vol. 29, pp. 4426-4437, 2014.

[123] J. Deng, S. Li, S. Hu, C. C. Mi, and R. Ma, "Design Methodology of LLC Resonant Converters for Electric Vehicle Battery Chargers," *IEEE Transactions on Vehicular Technology,* vol. 63, pp. 1581-1592, 2014.

[124] M. P. Foster, C. R. Gould, A. J. Gilbert, D. A. Stone, and C. M. Bingham, "Analysis of CLL Voltage-Output ResonantConverters Using Describing Functions," *IEEE Transactions on Power Electronics,* vol. 23, pp. 1772-1781, 2008.

[125] J. F. Lazar and R. Martinelli, "Steady-state analysis of the LLC series resonant converter," in *Applied Power Electronics Conference and Exposition, 2001. APEC 2001. Sixteenth Annual IEEE*, 2001, pp. 728-735 vol.2.

[126] A. J. Gilbert, D. A. Stone, C. M. Bingham, and M. P. Foster, "Design of an LCC current-output resonant converter for use as a constant current source," in *Power Electronics and Applications, 2007 European Conference on*, 2007, pp. 1-6.

[127] Z. U. Zahid, Z. M. Dalala, R. Chen, B. Chen, and J. S. Lai, "Design of Bidirectional DC-DC Resonant Converter for Vehicle-to-Grid (V2G) Applications," *IEEE Transactions on Transportation Electrification,* vol. 1, pp. 232-244, 2015.

[128] M. Z. Youssef and P. K. Jain, "Design and Performance of a Resonant LLC 48V Voltage Regulator Module with a Self-sustained Oscillation Controller," in *Applied Power Electronics Conference, APEC 2007 - Twenty Second Annual IEEE*, 2007, pp. 141-147.

[129] A. Hillers, D. Christen, and J. Biela, "Design of a Highly efficient bidirectional isolated LLC resonant converter," in *Power Electronics and Motion Control Conference (EPE/PEMC), 2012 15th International*, 2012, pp. DS2b.13-1-DS2b.13-8.

[130] J. Jee-Hoon, K. Ho-Sung, K. Jong-Hyun, R. Myoung-Hyo, and B. Ju-Won, "High efficiency bidirectional LLC resonant converter for 380V DC power distribution system using digital control scheme," in *Applied Power Electronics Conference and Exposition (APEC), 2012 Twenty-Seventh Annual IEEE*, 2012, pp. 532-538.

[131] C. Chien-Hsuan, C. Hung-Liang, C. En-Chih, C. Chun-An, and C. Hung-Yi, "Modeling and design of the LLC resonant converter used in solar array simulator," in *Industrial Electronics and Applications (ICIEA), 2012 7th IEEE Conference on*, 2012, pp. 653-658.

[132] G. Ivensky, S. Bronshtein, and A. Abramovitz, "Approximate Analysis of Resonant LLC DC-DC Converter," *Power Electronics, IEEE Transactions on,* vol. 26, pp. 3274-3284, 2011.

[133] G. Pledl, M. Tauer, and D. Buecherl, "Theory of operation, design procedure and simulation of a bidirectional LLC resonant converter for vehicular applications," in *Vehicle Power and Propulsion Conference (VPPC), 2010 IEEE*, 2010, pp. 1-5.

[134] L. Byoung-Hee, K. Moon-Young, K. Chong-Eun, P. Ki-Bum, and M. Gun-Woo, "Analysis of LLC Resonant Converter considering effects of parasitic components," in *Telecommunications Energy Conference, 2009. INTELEC 2009. 31st International*, 2009, pp. 1-6.

[135] B. R. Lin, J. J. Chen, and C. L. Yang, "Analysis and implementation of dual-output LLC resonant converter," in *Industrial Technology, 2008. ICIT 2008. IEEE International Conference on*, 2008, pp. 1-6.

[136] M. A. C. Belhadj, A. Ales, A. Zaoui, Z. Chebbat, J. L. Schanen, and J. Roudet, "Analytical model of DC-DC converters based on switching impedances and EMI sources," in *2016 International Symposium on Electromagnetic Compatibility - EMC EUROPE*, 2016, pp. 750-755.

[137] A. Bhargava, D. Pommerenke, K. W. Kam, F. Centola, and C. W. Lam, "DC-DC Buck Converter EMI Reduction Using PCB Layout Modification," *IEEE Transactions on Electromagnetic Compatibility,* vol. 53, pp. 806-813, 2011.

[138] T. Mofan, H. Yuan, W. Kangping, X. Yang, H. Lang, S. Jingjing, *et al.*, "EMI modeling and experiment of a GaN based LLC half-bridge converter," in *Power Electronics and ECCE Asia (ICPE-ECCE Asia), 2015 9th International Conference on*, 2015, pp. 1961-1966.

[139] S. Park, H. A. Huynh, and S. Kim, "Analysis of EMI reduction methods of DC-DC buck converter," in *2015 10th International Workshop on the Electromagnetic Compatibility of Integrated Circuits (EMC Compo)*, 2015, pp. 92-96.

[140] H. Wang, S. Dusmez, and A. Khaligh, "Maximum Efficiency Point Tracking Technique for LLC Based PEV Chargers through Variable DC Link Control," *IEEE Transactions on Industrial Electronics,* vol. PP, pp. 1-1, 2014.

[141] M. H. Bierhoff and F. W. Fuchs, "Semiconductor losses in voltage source and current source IGBT converters based on analytical derivation," in *Power Electronics Specialists Conference, 2004. PESC 04. 2004 IEEE 35th Annual*, 2004, pp. 2836-2842 Vol.4.

[142] S. Inoue and H. Akagi, "A Bidirectional DC-DC Converter for an Energy Storage System With Galvanic Isolation," *IEEE Transactions on Power Electronics,* vol. 22, pp. 2299-2306, 2007.

[143] F. Krismer and J. W. Kolar, "Accurate Power Loss Model Derivation of a High-Current Dual Active Bridge Converter for an Automotive Application," *IEEE Transactions on Industrial Electronics,* vol. 57, pp. 881-891, 2010.

[144] F. Musavi, W. Eberle, and W. G. Dunford, "A High-Performance Single-Phase Bridgeless Interleaved PFC Converter for Plug-in Hybrid Electric Vehicle Battery Chargers," *IEEE Transactions on Industry Applications,* vol. 47, pp. 1833-1843, 2011.

[145] B. S. Bhangu, P. Bentley, D. A. Stone, and C. M. Bingham, "Nonlinear observers for predicting state-of-charge and state-of-health of lead-acid batteries for hybrid-electric vehicles," *IEEE Transactions on Vehicular Technology,* vol. 54, pp. 783-794, 2005.

[146] Y. Cao, S. Tang, C. Li, P. Zhang, Y. Tan, Z. Zhang, *et al.*, "An Optimized EV Charging Model Considering TOU Price and SOC Curve," *IEEE Transactions on Smart Grid,* vol. 3, pp. 388-393, 2012.

[147] Y. Du, S. M. Lukic, B. S. Jacobson, and A. Q. Huang, "Modulation Technique to Reverse Power Flow for the Isolated Series Resonant DC-DC Converter With Clamped Capacitor Voltage," *IEEE Transactions on Industrial Electronics,* vol. 59, pp. 4617-4628, 2012.

[148] X. Wang, C. Jiang, B. Lei, H. Teng, H. K. Bai, and J. L. Kirtley, "Power-Loss Analysis and Efficiency Maximization of a Silicon-Carbide MOSFET-Based Three-Phase 10-kW Bidirectional EV Charger Using Variable-DC-Bus Control," *IEEE Journal of Emerging and Selected Topics in Power Electronics,* vol. 4, pp. 880-892, 2016.

[149] S. Sheng and B. Lehman, "A simple variable step size method for maximum power point tracking using commercial current mode control DC-DC regulators," in *2016 IEEE Applied Power Electronics Conference and Exposition (APEC)*, 2016, pp. 2286-2291.

[150] T. Konjedic, L. Korosec, M. Truntic, C. Restrepo, M. Rodic, and M. Milanovic, "DCM-Based Zero-Voltage Switching Control of a Bidirectional DC-DC Converter With Variable Switching Frequency," *IEEE Transactions on Power Electronics,* vol. 31, pp. 3273-3288, 2016.

[151] T. Jiang, J. Zhang, X. Wu, K. Sheng, and Y. Wang, "A Bidirectional LLC Resonant Converter With Automatic Forward and Backward Mode Transition," *IEEE Transactions on Power Electronics,* vol. 30, pp. 757-770, 2015.

[152] A. Stadler, R. Huber, T. Stolzke, and C. Gulden, "Analytical Calculation of Copper Losses in Litz-Wire Windings of Gapped Inductors," *IEEE Transactions on Magnetics,* vol. 50, pp. 81-84, 2014.

[153] M. Etemadrezaei and S. M. Lukic, "Coated-Strand Litz Wire for Multi-Megahertz Frequency Applications," *IEEE Transactions on Magnetics,* vol. 52, pp. 1-11, 2016.

[154] R. Y. Zhang, J. K. White, J. G. Kassakian, and C. R. Sullivan, "Realistic litz wire characterization using fast numerical simulations," in *2014 IEEE Applied Power Electronics Conference and Exposition - APEC 2014*, 2014, pp. 738-745.

[155] L. D. Ferraro and F. G. Capponi, "Aluminium Multi-Wire for High-Frequency Electric Machines," in *2007 IEEE Industry Applications Annual Meeting*, 2007, pp. 89-93.

[156] K. Mori, S. Yamaguchi, A. Higasiura, and K. Higuchi, "Development of parallel array multiple wire strip," in *Proceedings:Electrical Electronics Insulation Conference and Electrical Manufacturing & Coil Winding Conference*, 1995, pp. 247-251.

[157] M. v. d. Geest, H. Polinder, J. A. Ferreira, and D. Zeilstra, "Stator winding proximity loss reduction techniques in high speed electrical machines," in *2013 International Electric Machines & Drives Conference*, 2013, pp. 340-346.

[158] R. C. Chang, C. K. Chen, C. Y. Wang, and Y. Y. Tzou, "Calculation of losses and temperature rise for high frequency transformer under forced-air convection," in *IECON 2010 - 36th Annual Conference on IEEE Industrial Electronics Society*, 2010, pp. 1-6.

[159] M. A. Eit, F. Bouillault, C. Marchand, and G. Krebs, "2-D Reduced Model for Eddy Currents Calculation in Litz Wire and Its Application for Switched Reluctance Machine," *IEEE Transactions on Magnetics,* vol. 52, pp. 1-4, 2016.

[160] I. Petrov, M. Polikarpova, P. Ponomarev, P. Lindh, and J. Pyrh?nen, "Investigation of additional AC losses in tooth-coil winding PMSM with high electrical frequency," in *2016 XXII International Conference on Electrical Machines (ICEM)*, 2016, pp. 1841-1846.

[161] Q. Wang, X. Zhang, R. Burgos, D. Boroyevich, A. White, and M. Kheraluwala, "Design considerations for a high efficiency 3 kW LLC resonant DC/DC transformer," in *2015 IEEE Energy Conversion Congress and Exposition (ECCE)*, 2015, pp. 5454-5461.

[162] I. Schmale, B. Gleich, O. Mende, and J. Borgert, "On the design of human-size MPI drive-field generators using RF Litz wires," in *2015 5th International Workshop on Magnetic Particle Imaging (IWMPI)*, 2015, pp. 1-1.

[163] J. R. Sibue, G. Meunier, J. P. Ferrieux, J. Roudet, and R. Periot, "Modeling and Computation of Losses in Conductors and Magnetic Cores of a Large Air Gap Transformer Dedicated to Contactless Energy Transfer," *IEEE Transactions on Magnetics,* vol. 49, pp. 586-590, 2013.

[164] A. Stadler, "The optimization of high frequency inductors with litz-wire windings," in *2013 International Conference-Workshop Compatibility And Power Electronics*, 2013, pp. 209-213.

[165] A. Stadler and C. Gulden, "Copper losses of litz-wire windings due to an air gap," in *2013 15th European Conference on Power Electronics and Applications (EPE)*, 2013, pp. 1-7.

[166] S. Wang and D. G. Dorrell, "Copper Loss Analysis of EV Charging Coupler," *IEEE Transactions on Magnetics,* vol. 51, pp. 1-4, 2015.

[167] C. R. Sullivan, "Computationally efficient winding loss calculation with multiple windings, arbitrary waveforms, and two-dimensional or three-dimensional field geometry," *IEEE Transactions on Power Electronics,* vol. 16, pp. 142-150, 2001.

[168] CEDRAT. (2013). *Flux v11.1.2 user manual*. Available: http://www.cedrat.com/en/software/flux.html